

**Integrated SQUID Magnetometers with  
YBa<sub>2</sub>Cu<sub>3</sub>O<sub>7</sub> Grain Boundary Josephson Junctions  
for Biomagnetic Applications**

Dissertation  
zur Erlangung des Doktorgrades  
des Fachbereichs Physik  
der Universität Hamburg

vorgelegt von  
Stefan Krey  
aus Hamburg

Hamburg  
1999

*... it is a rare example of actually getting everything you pay for in physics, without being short changed.*

J.R. Gribbin on superconductivity in  
*In Search of Schrödingers Cat*,  
Bantam Books, 1984

## Abstract

Integrated dc SQUID magnetometers made of the high temperature superconductor  $\text{YBa}_2\text{Cu}_3\text{O}_7$  are experimentally investigated with regard to biomagnetic applications. Both step-edge as well as bicrystal Josephson junctions are used. The pickup loop is an essential part for the sensitive coupling of external signals into the SQUID magnetometer. Three different ways for the coupling are investigated. The most simple way is the direct connection of the pickup loop to the SQUID. Although the efficiency of this method is low, it allows the fabrication of the device from a single superconducting layer. A magnetic field resolution of  $\sqrt{S_B} = 38 \text{ fT}/\sqrt{\text{Hz}}$  is achieved. A significant better field resolution is obtained with magnetometers from multilayers. Two different multilayer magnetometers are investigated: the inductively coupled magnetometer with monolithically integrated flux transformer and the multiloop magnetometer. An optimization of the multiloop layout results in an effective flux capturing area of  $2.31 \text{ mm}^2$ . Noise measurements yield a white noise level of  $\sqrt{S_B} = 17 \text{ fT}/\sqrt{\text{Hz}}$  and  $\sqrt{S_B} = 60 \text{ fT}/\sqrt{\text{Hz}}$  at 1 Hz. Biomagnetic measurements demonstrate the practical application. A signal-to-noise ratio of 28 is obtained in a real-time magnetocardiogram, which is already adequate for many clinical applications. A great challenge is the operation of magnetometers from high temperature superconductors in unshielded environment, where magnetic noise signals have to be suppressed by several orders of magnitude. Methods for the noise rejection are demonstrated by using electronic first order gradiometer schemes. The investigation of the low-frequency noise in static magnetic fields yields no higher values for multilayer magnetometers compared to conventional single-layer devices. A reduction of the low-frequency noise of field cooled magnetometers is obtained by reducing the maximum linewidth in the magnetometer layout. This also enhances the magnetometer linearity. A new type of magnetic field sensor is introduced. It is based on a serial array of 105 Josephson junctions on a bicrystal substrate. To increase the sensitivity of the array, it is embedded in flux focusing areas. The junction parameters exhibit a high homogeneity throughout the array. A field resolution of  $\sqrt{S_B} = 1.2 \text{ pT}/\sqrt{\text{Hz}}$  is obtained.

## Inhaltsangabe

Im Hinblick auf biomagnetische Anwendungen werden integrierte dc SQUID Magnetometer aus dem Hochtemperatursupraleiter  $\text{YBa}_2\text{Cu}_3\text{O}_7$  experimentell untersucht. Als Josephson-Kontakte werden sowohl Stufenkontakte als auch Bikristall-Kontakte eingesetzt. Ein wesentlicher Bestandteil eines SQUID Magnetometers ist die Einkoppelschleife für eine empfindliche Einkopplung externer Signale in das SQUID. Drei unterschiedliche Arten einer solchen Einkopplung werden untersucht. Eine sehr einfache Möglichkeit ist die direkte Verbindung der Einkoppelschleife an das SQUID. Die Effizienz dieser Methode ist gering, sie ermöglicht aber die Herstellung des Bauelements aus einer einzigen supraleitenden Schicht. Es wird damit eine Feldauflösung von  $\sqrt{S_B} = 38 \text{ fT}/\sqrt{\text{Hz}}$  erzielt. Eine deutlich bessere Feldauflösung läßt sich mit Magnetometern in Mehrlagentechnologie erreichen. Zwei unterschiedliche Mehrlagenbauelemente werden untersucht: Das induktiv gekoppelte Magnetometer mit vollständig integriertem Flußtransformator und das Mehrschleifen-Magnetometer. Durch eine Optimierung des Mehrschleifen-Layouts wird eine effektive Aufnehmerfläche von  $2.31 \text{ mm}^2$  erreicht. Rauschmessungen ergeben eine Feldauflösung von  $\sqrt{S_B} = 17 \text{ fT}/\sqrt{\text{Hz}}$  im weißen Rauschen und  $\sqrt{S_B} = 60 \text{ fT}/\sqrt{\text{Hz}}$  bei 1 Hz. Die praktische Anwendung der Magnetometer wird anhand von biomagnetischen Messungen demonstriert. Das erreichte Signal-Rausch Verhältnis von 28 in einem Echtzeit-Magnetokardiogramm ist bereits für viele klinische Anwendungen ausreichend. Eine große Herausforderung stellt der Betrieb von Magnetometern aus Hochtemperatursupraleitern in unabgeschirmter Umgebung dar. Magnetische Störsignale müssen um mehrere Größenordnungen unterdrückt werden. Anhand von elektronischen Gradiometern 1. Ordnung werden Methoden zur Störsignalunterdrückung demonstriert. Untersuchungen des niederfrequenten Rauschens bei Abkühlung in statischen Magnetfeldern ergeben keine höheren Werte für die Mehrlagenbauelemente im Vergleich zu herkömmlichen Einlagen-Magnetometern. Eine Reduktion des niederfrequenten Rauschens von im Feld gekühlten Magnetometern kann durch eine Verkleinerung der maximalen Strukturbreite im Layout erreicht werden. Dies verbessert gleichfalls die Linearität des Bauelements. Es wird ein neuartiger Magnetfeldsensor vorgestellt, der auf einer Serienschaltung von 105 Josephson-Kontakten auf einem Bikristall-Substrat basiert. Um seine Feldauflösung zu erhöhen, wird dieser mit zusätzlichen flußkonzentrierenden Flächen versehen. Es wird eine hohe Homogenität der Kontaktparameter innerhalb des Sensors beobachtet. Im Gegensatz zu SQUIDs ermöglicht er auch die Messung von Absolutfeldern. Es wird eine Feldauflösung von  $\sqrt{S_B} = 1.2 \text{ pT}/\sqrt{\text{Hz}}$  erreicht.

# Contents

<b>1</b>	<b>Introduction</b>	<b>5</b>
<b>2</b>	<b>Josephson junctions and dc SQUIDS</b>	<b>9</b>
2.1	Superconductivity . . . . .	9
2.2	The Josephson effects . . . . .	12
2.3	The RCSJ model of the Josephson junction . . . . .	15
2.4	Noise in Josephson junctions . . . . .	17
2.5	Grain boundary Josephson junctions from $\text{YBa}_2\text{Cu}_3\text{O}_7$ . . . . .	20
2.6	The dc SQUID . . . . .	25
2.7	Noise in dc SQUIDS . . . . .	28
<b>3</b>	<b>DC SQUID magnetometer design</b>	<b>33</b>
3.1	Directly coupled dc SQUID magnetometers . . . . .	35
3.2	Inductively coupled magnetometers with integrated flux transformer . . . .	39
3.3	Multiloop magnetometers . . . . .	41
3.4	Summary . . . . .	43
<b>4</b>	<b>Experimental</b>	<b>45</b>
4.1	Preparation of multilayer magnetometers with step-edge Josephson junctions	45
4.2	Preparation of single-layer magnetometers with bicrystal Josephson junctions	48
4.3	Measurement techniques . . . . .	49
<b>5</b>	<b>Integrated dc SQUID magnetometers</b>	<b>53</b>
5.1	Samples . . . . .	53
5.1.1	Directly coupled magnetometers . . . . .	53
5.1.2	Inductively coupled magnetometers . . . . .	62
5.1.3	Multiloop magnetometers . . . . .	67
5.1.4	Temperature dependence of the effective area . . . . .	74
5.1.5	Summary . . . . .	77
5.2	Low noise operation with additional positive feedback (APF) . . . . .	79

5.3	Biomagnetic measurements . . . . .	84
5.4	Unshielded measurements . . . . .	90
5.5	Noise characterization in static magnetic fields . . . . .	95
5.5.1	Low-frequency noise of multilayer $\text{YBa}_2\text{Cu}_3\text{O}_7$ magnetometers in static magnetic fields . . . . .	96
5.5.2	Low-frequency noise and linearity of a directly coupled magnetome- ter with small linewidths in static magnetic fields . . . . .	100
<b>6</b>	<b>Josephson junction serial array magnetometers</b>	<b>107</b>
<b>7</b>	<b>Summary and conclusions</b>	<b>115</b>

# 1 Introduction

At present, the superconducting quantum interference device (SQUID) is the most sensitive sensor for magnetic flux. Its operation principle as a flux-to-voltage converter is based on the Josephson effects and the flux quantization, two unique phenomena of superconductivity. Almost every physical quantity that can be converted into a magnetic flux can be very sensitively measured with a SQUID. Currently, SQUIDs are most widely used in biomagnetic systems measuring the magnetic fields from the human heart or brain. These systems benefit from the SQUID's extreme sensitivity over a broad frequency range and its small size. Today, all biomagnetic systems in clinical use are still based on SQUIDs manufactured from low temperature superconductors requiring expensive refrigeration with liquid helium. The discovery of the high temperature superconductivity in the copper oxides by Bednorz and Müller [1] in 1986 has started a rush on this new field of research, and only one year later  $\text{YBa}_2\text{Cu}_3\text{O}_7$  was discovered as the first material being superconducting at liquid nitrogen temperature [2]. This has been a great step forward, because liquid nitrogen is much cheaper and easier to handle than liquid helium. Today,  $\text{YBa}_2\text{Cu}_3\text{O}_7$  is still the most widely used and technologically best controlled high temperature superconductor. But one has also to cope with difficulties arising from the complex chemical structure of the high temperature superconductors. Superconductivity in the copper oxides is anisotropic. This requires a high degree of crystalline orientation throughout the device and complicates the preparation of multilayer structures. Furthermore, it must be stated that a reliable and cost-effective way for the preparation of Josephson junctions, the basic elements of SQUIDs, has not been found, yet.

This thesis describes the development of SQUID sensors based on  $\text{YBa}_2\text{Cu}_3\text{O}_7$  for biomagnetic applications, in particular for magnetocardiography. Magnetocardiography is the noninvasive measurement of magnetic signals generated by the electrical activity of the human heart. The low strength of these signals and the high information content at low frequencies makes high demands on the sensor's intrinsic low-frequency noise level and on the suppression of external noise sources. Magnetic fields are only weakly detected by a bare SQUID as a mainly flux sensing device. Therefore pickup loop structures are connected to the SQUID which convert a magnetic field signal into a flux signal for the

SQUID. Such a combination is called a SQUID magnetometer. Pickup loops for SQUIDs from the metallic low temperature superconductors are easily fabricated from solid superconducting wires. Various gradiometer configurations are employed, which are only sensitive to spatial gradients of the magnetic field. Thus, homogeneous contributions of environmental magnetic noise are highly rejected. On the contrary, there is not yet a suitable interconnect technology for SQUIDs and wires from high temperature superconductors. SQUID and pickup loop must be prepared from epitaxial thin-films and both are either integrated on a single chip or they reside on different substrates tightly pressed together in a so-called flip-chip configuration. In this thesis, only integrated magnetometers are described, in which pickup loop and SQUID are monolithically integrated on one substrate, employing single-layer as well as multilayer technology. The discussed magnetometers are exclusively based on grain boundary Josephson junctions, which is currently the most reliable and successful approach for Josephson junctions in high temperature superconductors.

Chapter 2 introduces the fundamental principles of superconductivity, Josephson junctions and SQUIDs, which are necessary for the understanding of the experimental results. The different magnetometer concepts treated in this thesis, and the design rules for their practical layout, are presented in Chapter 3. Chapter 4 briefly describes the fabrication of the magnetometers and the measurement techniques for their characterization. The physical properties of the fabricated samples are investigated in the first section of Chapter 5, which closes with a short summary. Section 5.2 describes a method for the low-noise direct readout of SQUID magnetometers and its application to one of the fabricated devices. Some biomagnetic measurements are presented in Section 5.3. The subsequent sections refer to problems that arise when SQUID magnetometers from high temperature superconductors are operating in unshielded environment. Section 5.4 treats methods for the cancellation of environmental magnetic noise, and Section 5.5 describes noise measurements on devices cooled in static magnetic fields. Chapter 6 introduces a new magnetometer concept based on a serial array of Josephson junctions combined with flux focusers. A summary of this thesis is presented in Chapter 7.

Most results of this thesis have already been published or submitted for publication. Chapters 5 and 6 mainly consist of the reprinted publications [P3], [P4], [P7], [P10] and [P11], each with a short introduction into the specific theme.

- [P1] O. Dössel, B. David, R. Eckart, D. Grundler, S. Krey, *High- $T_c$  SQUID Magnetometers for Magnetocardiography*, Proceedings of 2<sup>nd</sup> Workshop on HTS Applications and New Materials, University of Twente, Enschede, The Netherlands, May 8-10, 1995, Ed. Dave H. A. Blank.



- 
- [P2] B. David, D. Grundler, S. Krey, V. Doormann, R. Eckart, J. P. Krumme, G. Rabe, and O. Dössel, *High- $T_c$  SQUID magnetometers for biomagnetic measurements*, Supercond. Sci. Technol. **9**, A96-A99 (1996).
  - [P3] D. Drung, E. Dantsker, F. Ludwig, H. Koch, R. Kleiner, J. Clarke, S. Krey, D. Reimer, B. David and O. Dössel, *Low noise  $YBa_2Cu_3O_{7-x}$  SQUID magnetometers operated with additional positive feedback*, Appl. Phys. Lett. **68**, 1856 (1996).
  - [P4] M. Schilling, S. Krey, and R. Scharnweber, *Biomagnetic measurements with an integrated  $YBa_2Cu_3O_7$  magnetometer in a hand-held cryostat*, Appl. Phys. Lett. **69**, 2749 (1996).
  - [P5] K.-O. Subke, S. Krey, H. Burkhardt, D. Reimer, and M. Schilling, *Process Optimization for High Yield of  $YBa_2Cu_3O_7$  Ramp-Edge Josephson Junctions with  $PrBa_2Cu_3O_7$  Barriers*, Proceedings of the 6<sup>th</sup> International Superconductive Electronics Conference (ISEC '97), June 25-28, 1997, Berlin, Germany, Eds. H. Koch and S. Knappe.
  - [P6] S. Krey, K.-O. Subke, D. Reimer, M. Schilling, R. Scharnweber, and B. David, *Integrated  $YBa_2Cu_3O_7$  Magnetometers for Biomagnetic Applications*, Applied Superconductivity, **5**, 213 (1998).
  - [P7] S. Krey, B. David, R. Eckart, and O. Dössel, *Low noise operation of integrated  $YBa_2Cu_3O_7$  magnetometers in static magnetic fields*, Appl. Phys. Lett. **72**, 3205 (1998).
  - [P8] K.-O. Subke, S. Krey, H. Burkhardt, A. Bartold, and M. Schilling, *Technology for  $YBa_2Cu_3O_7$  SNS- and SIS-Josephson Junctions*, IEEE Trans. Appl. Supercond. **9**, 3125 (1999).
  - [P9] S. Krey, O. Brüggmann, H. Burkhardt, and M. Schilling, *Noise Properties of  $YBa_2Cu_3O_7$  Josephson Junction Array Magnetometers*, IEEE Trans. Appl. Supercond. **9**, 3401 (1999).
  - [P10] S. Krey, O. Brüggmann, and M. Schilling, *Highly sensitive magnetometers based on  $YBa_2Cu_3O_7$  Josephson junction arrays*, Appl. Phys. Lett. **74**, 293 (1999).
  - [P11] S. Krey, H.-J. Barthelmess, and M. Schilling, *Low-frequency noise and linearity of  $YBa_2Cu_3O_7$  dc superconducting quantum interference device magnetometers in static magnetic fields*, submitted to J. Appl. Phys.



## 2 Josephson junctions and dc SQUIDS

### 2.1 Superconductivity

Superconductivity is named after the striking property of many materials showing perfect dc conductivity below a critical temperature  $T_c$  which is specific for the material. The microscopic origin of this pure quantum mechanical phenomenon is the formation of pairs of two conduction electrons having opposite momentum and spin (Cooper pairs) [3]. In the classical low- $T_c$  superconductors the pairing is mediated by an electron-phonon interaction, whereas the pairing mechanism in the high temperature superconductors (HTS) is still unveiled. The spatial extent of the pair correlation can be several orders of magnitude larger than the interatomic distance and is characterized by the coherence length  $\xi$ . Due to the quasi-boson character of the Cooper pairs, they are allowed to condensate into a common ground state, which can be described by a single macroscopic wave function

$$\psi(\mathbf{r}, t) = \sqrt{n_C(\mathbf{r})} e^{i\phi(\mathbf{r}, t)}, \quad (2.1)$$

where  $n_C(\mathbf{r})$  is the Cooper pair density and  $\phi(\mathbf{r}, t)$  a common phase, both depending on the position  $\mathbf{r}$ . The phase  $\phi(\mathbf{r}, t)$  evolves in time at the angular frequency  $2E_F/\hbar$ , where  $E_F$  is the Fermi energy. A consequence of the long-range phase coherence of the superconducting state and the requirement that  $\psi(\mathbf{r}, t)$  be single-valued, is the quantization of magnetic flux in a closed superconducting ring: The magnetic flux inside a hole surrounded by a superconductor is quantized in units of the magnetic flux quantum  $\Phi_0 = h/(2e)$ . This flux remains constant until the superconductivity is destroyed in one part of the ring. A further peculiar property of superconductors is the displacement of magnetic flux, when the sample is cooled below  $T_c$  (Meissner-Ochsenfeld effect). One distinguishes between two kinds of superconductors: Type I superconductors completely expel the magnetic flux into the surface regions, thus behave like perfect diamagnets, as long as the applied field is below a critical value  $B_c$ . At  $B_c$  there is an abrupt transition to the normal state. Type II superconductors behave the same way below a critical field  $B_{c1}$ . At higher fields however, there is no sharp transition, but flux partially penetrates the sample

(mixed state) in the form of normal conducting flux vortices (Abrikosov vortices), each carrying a single flux quantum. Above an upper critical field  $B_{c2}$ , the entire sample becomes normal conducting. The distance over which the magnetic field falls to zero inside a superconductor is called the London penetration depth  $\lambda_L$  [4]. The type of superconductor is determined by whether the coherence length is large (Type I) or small (Type II) compared to  $\lambda_L$ . Since the upper critical field of Type II superconductors can be much higher than in Type I superconductors, Type II materials are of much more practical importance. Most alloys and compounds and also all high temperature superconductors are of Type II, whereas pure elementary metals are often Type I superconductors. The binding energy of a Cooper pair is given by the superconducting energy gap  $2\Delta$ , where  $\Delta$  is a function of the temperature [5]. Excitation energies larger than  $2\Delta$  will break the Cooper pair into two single electrons (quasiparticles). At  $T > 0$ , there always exists a normal component of quasiparticles, due to thermal excitations. Since Cooper pairs carry the charge  $2e$ , they will be accelerated in an electric field. Their maximum kinetic energy limits the current density in the superconductor to a critical value  $J_c$ . Because the diamagnetic behavior of a superconductor is produced by shielding currents flowing inside the penetration depth, superconductivity can be destroyed in high magnetic fields, when the shielding currents exceed the critical value. An intensely discussed peculiarity of HTS is their unconventional symmetry of the superconducting gap function, which appears to be predominantly of  $d_{x^2-y^2}$  type [6].

## The high temperature superconductor $\text{YBa}_2\text{Cu}_3\text{O}_7$

At present, the ceramic compound  $\text{YBa}_2\text{Cu}_3\text{O}_{7-\delta}$  is the technologically best controlled and most widely used HTS. Its transition temperature  $T_c$  reaches 93 K, but strongly depends on the oxygen deficiency  $\delta$ . The highest  $T_c$  values are obtained for  $\text{YBa}_2\text{Cu}_3\text{O}_{7-\delta}$  with  $\delta \approx 0.1$ , which is therefore commonly referred to as  $\text{YBa}_2\text{Cu}_3\text{O}_7$ . The crystal structure is orthorhombic with the lattice constants  $a = 3.82 \text{ \AA}$ ,  $b = 3.88 \text{ \AA}$  and  $c = 11.68 \text{ \AA}$  [7]. Figure 2.1 displays a schematic view of this structure. It can be considered as three stacked perovskite cells. Due to this structure, the coherence length  $\xi$  and the critical current density are highly anisotropic. The coherence length in  $ab$ -direction is about  $\xi_{ab} = 1.5 \text{ nm}$  at  $T = 0 \text{ K}$ , whereas the length  $\xi_c$  along the  $c$ -axis is typically an order of magnitude shorter [8]. The current transport takes mainly place in the copper-oxygen (CuO) planes along the  $ab$ -direction, where the CuO-chains act as charge reservoirs for the hole-like charge carriers. For this reason, thin-film devices from  $\text{YBa}_2\text{Cu}_3\text{O}_7$  are usually prepared from epitaxially grown  $c$ -axis oriented thin-films, where the  $c$ -axis is perpendicular to the substrate surface. Typical critical current densities in  $ab$ -direction

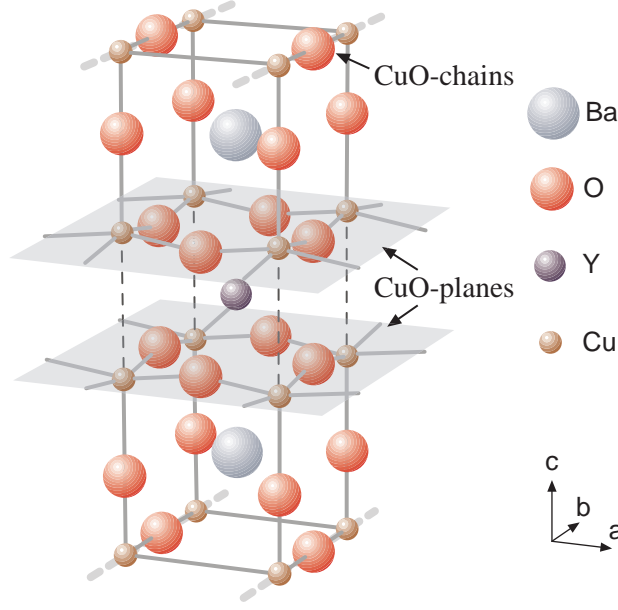


FIGURE 2.1: Atomic structure of  $\text{YBa}_2\text{Cu}_3\text{O}_7$ . The lattice constants are  $a = 3.82 \text{ \AA}$ ,  $b = 3.88 \text{ \AA}$  and  $c = 11.68 \text{ \AA}$ .

are  $J_c > 10^6 \text{ A/cm}^2$ . The thin-films are deposited at high temperatures of  $750 \dots 800^\circ\text{C}$  in their tetragonal phase  $\text{YBa}_2\text{Cu}_3\text{O}_6$ . The transition into the orthorhombic phase takes place when the sample is cooled to room temperature in oxygen atmosphere. Above  $T_c$ , the conductivity of  $\text{YBa}_2\text{Cu}_3\text{O}_7$  is metallic like, whereas the tetragonal  $\text{YBa}_2\text{Cu}_3\text{O}_6$  is semiconducting. The temperature dependent London penetration depth of  $\text{YBa}_2\text{Cu}_3\text{O}_7$  can be described by

$$\lambda_L(T) = \lambda_L(0) / \sqrt{1 - \left(\frac{T}{T_c}\right)^\alpha}, \quad (2.2)$$

where  $\alpha = 4$  for the empirical two-fluid formula of Gorter and Casimir [5,9]. More recently, the exponent  $\alpha = 2$  has been found to be more adequate for patterned  $\text{YBa}_2\text{Cu}_3\text{O}_7$  thin-films [10]. Hence, this exponent is used for the calculations in this thesis. The low-temperature value  $\lambda_L(0)$  is about  $150 \text{ nm}$  in  $ab$ -direction, but it depends on the film quality [11–13]. Since  $\lambda_L > \xi$ ,  $\text{YBa}_2\text{Cu}_3\text{O}_7$  is a Type II superconductor.

For the substrate and intermediate layers in multilayer devices, the perovskite  $\text{SrTiO}_3$  is used. The lattice constant  $a = 3.91 \text{ \AA}$  matches well with the  $\text{YBa}_2\text{Cu}_3\text{O}_7$  structure, which is a prerequisite for a heteroepitaxial growth with low stress [14]. The thermal expansion coefficient is also well matched and prevents cracks in the material, caused by the large difference between the deposition temperature and the operation temperature. A major drawback of  $\text{SrTiO}_3$  is its large and temperature dependent dielectric constant of about  $\epsilon_r \approx 2000$  at  $T = 77 \text{ K}$  and the large loss tangent [15–18], which makes it impracticable for high-frequency devices, e.g. HTS filters or resonators. Due to large parasitic capacitances,

$LC$  resonances in SQUID devices are found at low frequencies and at voltage values in the usual range of operation. These  $LC$  resonances may severely reduce the performance of a SQUID.

## 2.2 The Josephson effects

The basic active element of superconducting electronics is the Josephson junction consisting of two weakly coupled superconducting electrodes [19]. In the classical Josephson junction the coupling is realized by a thin insulating layer, acting as a tunneling barrier [20]. If the barrier thickness does not significantly exceed the coherence length  $\xi$ , phase coherence evolves between the pair wavefunctions of both electrodes across the barrier. As a consequence, Cooper pairs will tunnel through the insulation and a nondissipative current will flow across the junction. The time evolution of the superconducting states at both sides of the barrier is described by the time-dependent Schrödinger equation for each electrode

$$i\hbar \frac{\partial \psi_1}{\partial t} = U_1 \psi_1 + K \psi_2 \quad (2.3)$$

$$i\hbar \frac{\partial \psi_2}{\partial t} = U_2 \psi_2 + K \psi_1, \quad (2.4)$$

where  $U_{1,2}$  are the potential energies of both states, and  $K$  is a measure for the interaction energy between them. Starting from this set of equations and the macroscopic wave function (2.1), the two fundamental Josephson relations are obtained after a short calculation [21]

$$J = J_0 \sin \phi \quad (2.5)$$

$$\frac{\partial \phi}{\partial t} = \frac{2e}{\hbar} V, \quad (2.6)$$

where  $\phi = \theta_1 - \theta_2$  is the phase difference between both wavefunctions,  $J$  is the current density in the junction,  $J_0$  the critical current density of the junction, and  $V$  the voltage across the junction. Both equations entirely describe the dynamics of the Josephson junction. From (2.6) we see that the phase  $\phi$  will be constant when there is no voltage across the junction. Then a constant current flows through the junction, according to (2.5). This is called the *dc Josephson effect*. Second, if one forces the current to exceed the critical value  $J_0$ , a voltage drop  $V$  occurs across the junction. In this case, the Josephson relations can be combined to

$$J(t) = J_0 \sin \left( \frac{2eV}{\hbar} t + \phi_0 \right), \quad (2.7)$$

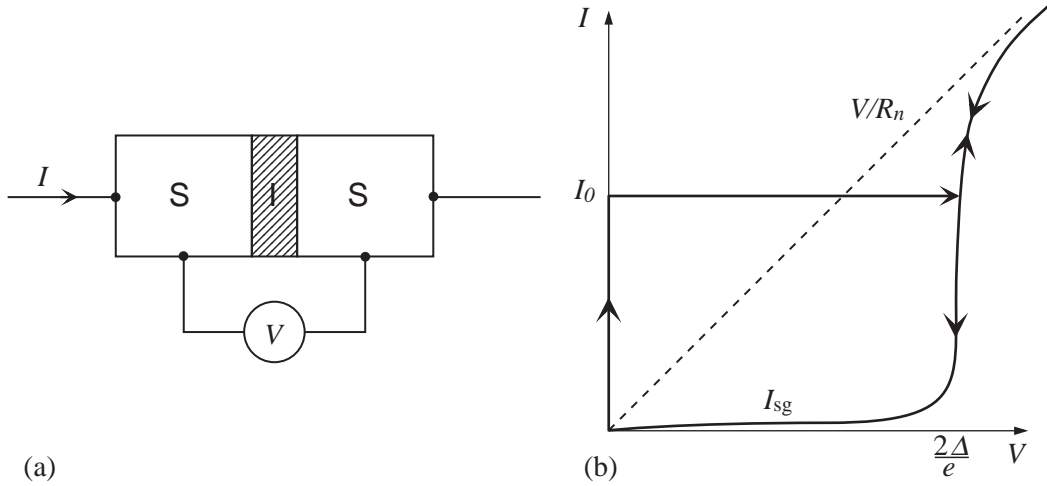


FIGURE 2.2: (a) Schematic representation of a symmetric SIS tunnel junction and (b) its current-voltage characteristic.  $R_n$  is the normal state resistance for high voltages and  $I_{sg}$  denotes the subgap current from tunneling quasiparticles.

where  $\phi_0$  is the integration constant of (2.6). Hence, the supercurrent  $J$  oscillates at the frequency

$$f_J = \frac{2e}{h}V, \quad (2.8)$$

which is called the *ac Josephson effect*. The Josephson frequency is  $f_J = 484 \text{ MHz} \times V/\mu\text{V}$ , therefore the Josephson junction can be considered as a microwave device. One may prove the ac Josephson effect by impressing a rf signal in the microwave range on the junction. The interaction of the Josephson oscillations with the rf field leads to constant voltage steps at integer multiples of the signal frequency in the current-voltage characteristic (Shapiro steps) [22]. A schematic representation of a symmetric superconductor-insulator-superconductor (SIS) Josephson tunnel-junction is given in Fig. 2.2(a). In general, the Josephson frequency by far exceeds the bandwidth of the connections to the measurement equipment, hence only mean voltages are measured in the quasi-static (dc) current-voltage characteristic. The typical characteristic of a SIS Josephson junction at low temperatures is shown in Fig. 2.2(b). For  $V = 0$  a nondissipative current of tunneling Cooper pairs flows through the junction. However, if the current is raised above the critical value  $I_0$ , the Cooper pairs will break and the junction becomes resistive on the branch of tunneling quasiparticles. A steep current increase on this branch occurs at the gap voltage  $V = 2\Delta/e$ . For  $T > 0$  there are always quasiparticles whose tunneling current causes the low conductivity below the gap voltage (subgap current). Hence, there are two current states below the gap voltage, and the characteristic is hysteretic. Hysteretic characteristics are typically found for Josephson tunnel junctions from the classical low- $T_c$  superconductors. Because the hysteresis is unwanted for most practical applications, it

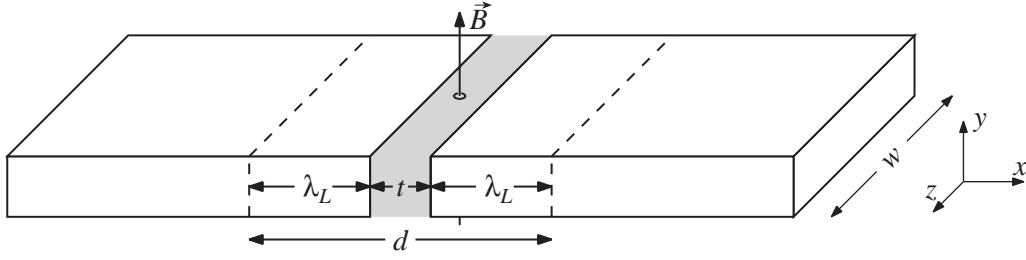


FIGURE 2.3: Model of a planar-type Josephson tunnel junction.

is usually suppressed by damping the junction with a parallel resistor. Common high- $T_c$  Josephson junctions show no hysteresis, because of a high subgap leakage current. According to the *intrinsically shunted junction* (ISJ) model, this current is caused by a high density of localized electronic defect states inside the barrier, providing an intrinsic resistive shunt for the quasiparticles. The quasiparticle transport is dominated by resonant tunneling *via* the localized states [23–25]. Although the Josephson effects have been first deduced for a tunneling barrier, they are also present in general weak link junctions. For instance, the barrier may also consist of a normal conductor. A detailed survey on HTS Josephson junctions is given in [26].

If a magnetic field  $B$  passes through a planar Josephson junction of the type shown in Fig. 2.3, the phase difference  $\phi$  and therefore the current density will no longer be spatially constant along the junction, but modulated perpendicular to the field direction [5]. In the most simple case of a homogeneous barrier and a junction width  $w$  much narrower than the Josephson penetration depth ( $w < 4\lambda_J$ )

$$\lambda_J = \left( \frac{\hbar}{2e\mu_0 J_0 d} \right)^{\frac{1}{2}}, \quad (2.9)$$

the critical current as a function of the magnetic flux through the junction is given by

$$I_0(\Phi) = I_0(0) \left| \frac{\sin(\pi\Phi/\Phi_0)}{\pi\Phi/\Phi_0} \right|, \quad (2.10)$$

where  $\Phi = Bwd$ ,  $d = t + 2\lambda_L$ , and  $t$  is the electrode separation. This relation also implies a sinusoidal current-phase relation. It is known from optics as the intensity distribution of light from Fraunhofer diffraction by a single slit. The  $I_0$  vs  $B$  curve is therefore commonly referred to as the Fraunhofer pattern of a Josephson junction. Figure 2.4 shows a plot of the Fraunhofer pattern and the current density distributions for different flux states in the junction.  $I_0(B)$  may be written as

$$I_0(B) = \left| \int_{-\infty}^{\infty} J_0(z) e^{i\beta z} dz \right|, \quad (2.11)$$

where  $\beta = 2\pi dB/\Phi_0$  and  $J_0(z) = \int J_0(y, z) dy$ . Thus,  $I_0(B)$  is the magnitude of the complex Fourier transform of the  $y$ -integrated critical current density along the  $z$ -direction.



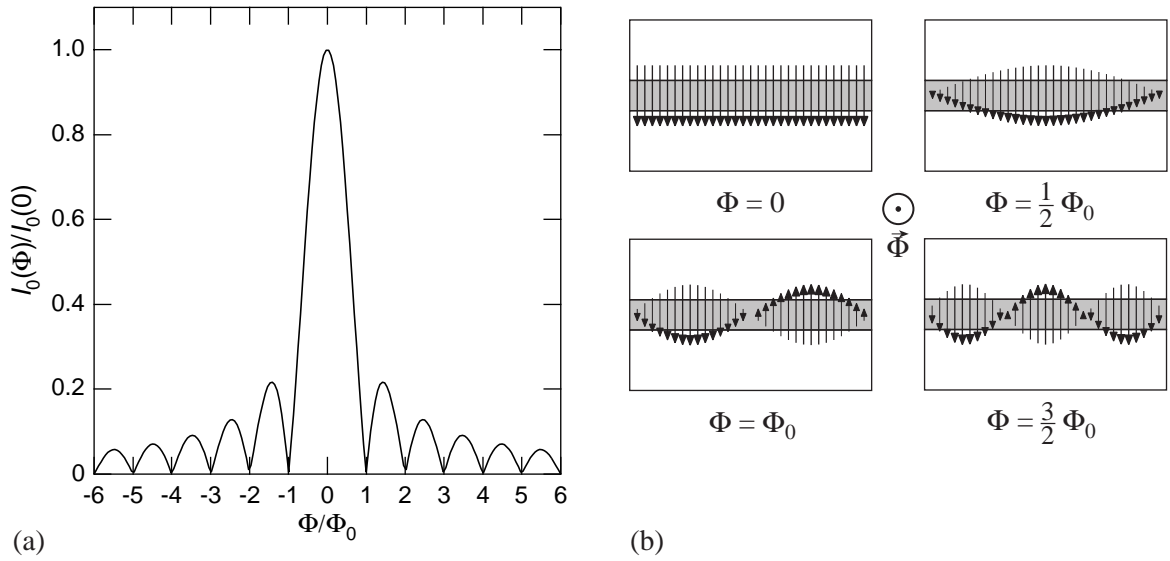


FIGURE 2.4: (a) Dependence of the critical current on the applied magnetic flux for a Josephson junction with spatially homogeneous critical current density (Fraunhofer pattern). (b) Effect of the applied flux on the current distribution in a homogeneous Josephson junction.

The extent to which the actual dependence fits (2.10) is a measure for the junction's lateral homogeneity. However, the critical current density distribution  $J_0(z)$  cannot be obtained by the inverse Fourier transformation of  $I_0(B)$ , because of the lack of phase information. The distance between the minima and the side-lobes of the Fraunhofer pattern equals  $\Phi_0 = BA$ , from which an effective junction area  $A$  may be deduced<sup>1</sup>. In planar-type Josephson junctions this is usually larger than the geometrical area  $wd$ , due to the Meissner-Ochsenfeld effect in the adjacent electrodes, which focuses flux into the junction area [27].

## 2.3 The RCSJ model of the Josephson junction

As mentioned in Section 2.2, the hysteresis of a Josephson junction is usually damped for practical reasons, either with an external resistor or intrinsically in the case of HTS. The dynamics of such a junction can be well described by the *resistively and capacitively shunted junction* (RCSJ) model introduced by Stewart and McCumber [28, 29]. Figure 2.5(a) gives the electrical representation of this model. The cross  $J$  symbolizes the Josephson tunnel junction described by the two Josephson relations (2.5) and (2.6).  $R_n$  is

<sup>1</sup>In a more strict sense, one should speak of an effective flux density in the geometrical junction area. However, the latter cannot be easily determined, and the concept of an effective flux sensing area is customary.

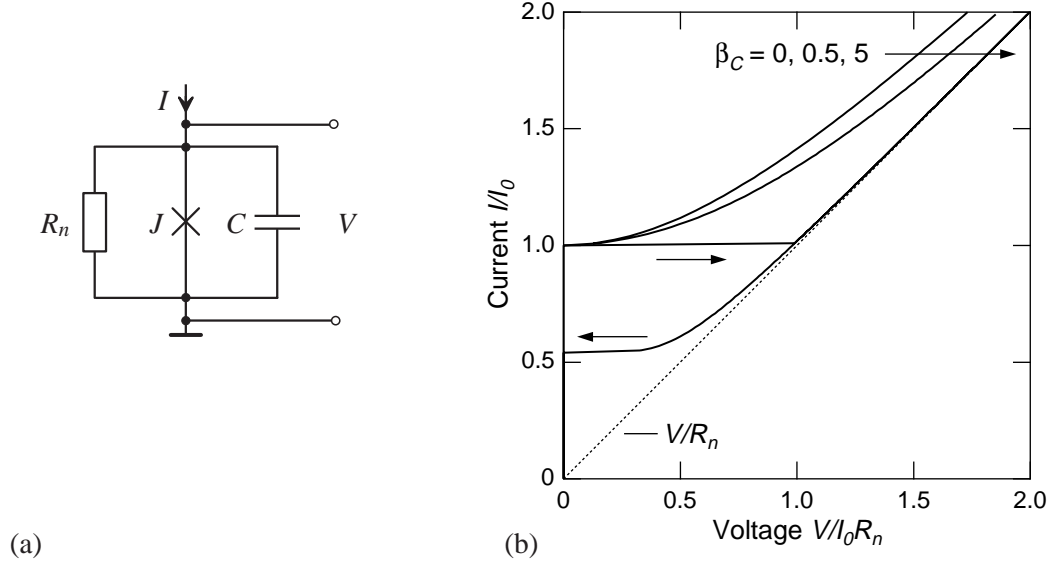


FIGURE 2.5: (a) Equivalent circuit for a Josephson junction according to the RCSJ model. (b) Effect of the junction capacitance on the  $IV$  characteristic.

the normal conducting shunt and  $C$  accounts for displacement currents in the junction's capacitance. The differential equation for this circuit and the current source  $I$  is

$$I = \frac{V}{R_n} + I_0 \sin \phi + C \frac{\partial V}{\partial t}. \quad (2.12)$$

Introducing the second Josephson relation (2.6), this can be written as

$$\frac{I}{I_0} = \sin \phi + \frac{1}{\omega_c} \frac{\partial \phi}{\partial t} + \frac{\beta_C}{\omega_c^2} \frac{\partial^2 \phi}{\partial t^2}, \quad (2.13)$$

with the characteristic frequency  $\omega_c = 2eI_0 R_n / \hbar$  and the dimensionless McCumber-parameter

$$\beta_C = \omega_c R_n C = \frac{2e}{\hbar} I_0 R_n^2 C. \quad (2.14)$$

$\beta_C$  is the ratio of the resistance  $R_n$  and the capacitive reactance  $1/\omega_c C$ . It determines the shape of the current-voltage ( $IV$ ) characteristic and the damping of the hysteresis. Usually, (2.13) must be solved numerically with the voltage  $V = \langle (\hbar/2e) \partial \phi / \partial t \rangle$  averaged in time to obtain the  $IV$  characteristic. It is found that the junction is overdamped for  $\beta_C < 1$ , so that there is no hysteresis. With increasing  $\beta_C$  the  $IV$  characteristic approaches the resistance line  $I = V/R_n$ , due to increased shorting of the Josephson oscillations. For  $\beta_C > 1$  the characteristic becomes hysteretic. For an example, Fig. 2.5(b) shows three solutions of the RCSJ model for the values  $\beta_C = 0, 0.5$  and  $5$ . The resistance line is obtained for  $\beta_C = \infty$ . In the most simple case where  $C = 0$ , (2.13) can also be solved analytically, and one obtains

$$\begin{aligned} V &= 0 && \text{for } I < I_0, \quad \text{and} \\ V &= R_n \sqrt{I^2 - I_0^2} && \text{for } I > I_0. \end{aligned} \quad (2.15)$$

In all solutions of the RCSJ model, the  $IV$  curve asymptotically approaches the resistance line for high voltages. However, Josephson junctions from HTS often show an excess current  $I_{\text{ex}}$ , so that the asymptotic line of the  $IV$  curve is displaced parallel to the resistance line by the amount of  $I_{\text{ex}}$ . Thus,  $I_{\text{ex}}$  may be expressed as [30]

$$I_{\text{ex}} = \lim_{V \rightarrow \infty} \left( I - \frac{V}{R_n} \right). \quad (2.16)$$

The excess current is not included in the simple RCSJ model, and its origin in HTS Josephson junctions is still unclear. One possible mechanism is the pair-quasiparticle conversion (Andreev reflection) at the junction interfaces that opens up an additional conductance channel [30]. Foglietti *et al.* [31] modelled the excess current by using a nonsinusoidal current-phase relation instead of the first Josephson relation. They found that the RCSJ model may still be a relatively good approximation for the experimental data, when the corrected critical current  $I'_0 = I_0 - I_{\text{ex}}$  is used, and when  $I_{\text{ex}}$  is small compared to  $I_0$ . However, the sinusoidal current-phase relation of (2.5) has been well confirmed for the step-edge and  $24^\circ$  bicrystal Josephson junctions treated in this thesis [32–34]. In contrast, a nonsinusoidal current-phase relation has been reported for symmetrical  $45^\circ$  bicrystal Josephson junctions, which is attributed to the  $d_{x^2-y^2}$  symmetry of the  $\text{YBa}_2\text{Cu}_3\text{O}_7$  order parameter [35]. A further cause of excess current may be self-field effects in wide Josephson junctions ( $w > 4\lambda_J$ ) [36].

## 2.4 Noise in Josephson junctions

### Frequency-independent noise

At finite temperature, the lower limit of the junction noise is set by the thermal noise in the shunt resistance  $R_n$ . The statistical motion of the unpaired charge carriers in the resistor provides an additional current source with a frequency-independent current noise spectral density [37]

$$S_I = \frac{4k_B T}{R_n}, \quad (2.17)$$

where  $k_B$  is the Boltzmann constant and  $T$  the temperature. If the thermal energy is of the order of the Josephson coupling energy  $E_J = \hbar I_0 / (2e)$ , the noise current temporarily

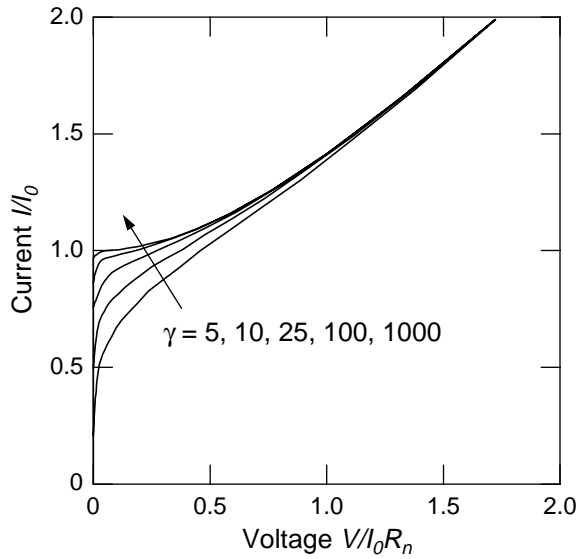


FIGURE 2.6:  $IV$  characteristics for different values of the noise parameter  $\gamma$ .

disrupts the phase coupling of both junction electrodes, at which the phase slips by  $2\pi$  and a voltage drop occurs [38]. The normalized barrier height for this phase slip process is defined by the ratio of the Josephson coupling energy  $E_J$  and the thermal energy  $k_B T$

$$\gamma = \frac{E_J}{k_B T} = \frac{I_0 \Phi_0}{2\pi k_B T}. \quad (2.18)$$

The nonzero time-averaged voltage leads to a noise-rounded  $IV$  characteristic around  $V = 0$ , even at bias currents lower than the critical current. The degree of rounding increases with decreasing  $\gamma$  [39].  $IV$  characteristics for different values of  $\gamma$  are displayed in Fig. 2.6. At low bias currents, the thermal fluctuations give also rise to an additional temperature dependent junction resistance which shows up as a characteristic foot-structure at  $T_c$  in the resistance-temperature curve [40]. The voltage noise spectral density at frequencies much less than the Josephson frequency is given by [41, 42]

$$S_V = \left[ 1 + \frac{1}{2} \left( \frac{I_0}{I} \right)^2 \right] \frac{4k_B T R_d^2}{R_n}, \quad (2.19)$$

where  $R_d = (\partial V / \partial I)_I$  is the dynamic resistance of the noise-rounded  $IV$  characteristic at the bias current  $I$ . The term  $\frac{1}{2}(I_0/I)^2$  accounts for noise contributions from around the Josephson frequency, which are mixed down into the low-frequency regime by the inherent nonlinearity of the Josephson junction [43].

## 1/f noise

Noise measurements on Josephson junctions generally reveal much higher noise values than expected from thermal noise. This excess noise is frequency dependent and its spectral density typically increases towards low frequencies as  $1/f$ . A typical voltage

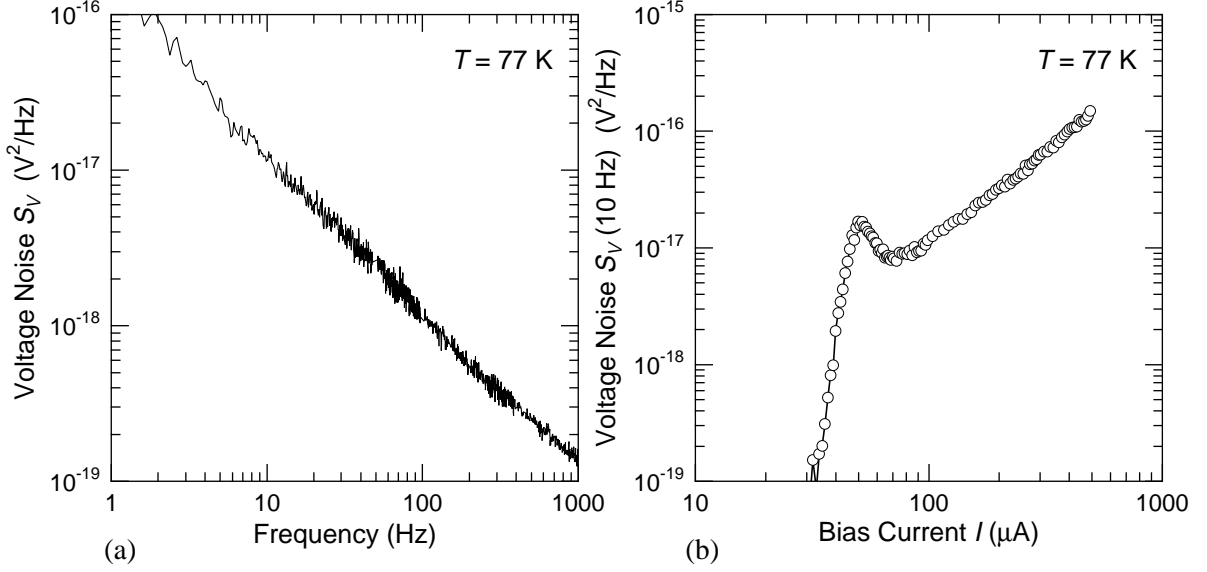


FIGURE 2.7: (a) Voltage noise of a  $6\text{ }\mu\text{m}$  wide step-edge Josephson junction at a bias current of  $50\text{ }\mu\text{A}$ . (b) Low-frequency noise at  $10\text{ Hz}$  of the same junction depending on the bias current.

noise spectrum of a  $6\text{ }\mu\text{m}$  wide step-edge Josephson junction from a  $\text{YBa}_2\text{Cu}_3\text{O}_7$  thin-film is depicted in Fig. 2.7(a). A clear  $1/f$  behavior is found. Figure 2.7(b) shows the low-frequency noise at  $10\text{ Hz}$  as a function of the applied bias current [44]. One finds a sharp noise maximum near  $I_0$ , which is attributed to critical current fluctuations  $\delta I_0$ . After a minimum, the noise quadratically increases with  $I$ , where resistance fluctuations  $\delta R_n$  dominate. For the voltage noise spectral density one finds [45]

$$S_V = (V - R_d I)^2 \left| \frac{\delta I_0}{I_0} \right|^2 + V^2 \left| \frac{\delta R_n}{R_n} \right|^2 + 2C(0) (V - R_d I) V \left| \frac{\delta I_0}{I_0} \right| \left| \frac{\delta R_n}{R_n} \right|, \quad (2.20)$$

with the normalized critical current fluctuations  $|\delta I_0/I_0|^2 = (S_I(f)/I_0^2)_{I \simeq I_0}$ , the normalized resistance fluctuations  $|\delta R_n/R_n|^2 = (S_R(f)/R_n^2)_{I \gg I_0}$ , and  $C(0)$  the cross-correlation coefficient between  $\delta I_0$  and  $\delta R_n$ . Uncorrelated fluctuations yield  $C(0) = 0$ , whereas it is  $C(0) = 1$  and  $C(0) = -1$  for fully in-phase and anti-phase correlation, respectively. Correlation measurements of the voltage noise in HTS grain boundary junctions near  $I_0$  and for  $I \gg I_0$  have revealed that both fluctuations are anti-correlated [44, 46]. This is explained within the framework of the ISJ model. Unpaired electrons can cross the barrier *via* the localized electronic defect states, and fluctuations in  $S_V$  are caused by the trapping and release at these states [47, 48]. A trapped electron increases the barrier height, which increases the normal state resistance and decreases the junction's critical current. Hence, fluctuations in  $I_c$  and  $R_n$  are expected to be fully anti-correlated [49, 50]. Typical values of  $|\delta I_0/I_0|$  at  $1\text{ Hz}$  and  $T = 77\text{ K}$  are  $(0.5 \dots 3) \times 10^4/\sqrt{\text{Hz}}$  [51–56].

An additional source of  $1/f$  noise may be the trapping and release of flux quanta in the Josephson junction, but this can be distinguished from the above source by the much larger noise amplitude [57].

## 2.5 Grain boundary Josephson junctions from $\text{YBa}_2\text{Cu}_3\text{O}_7$

All devices described in this thesis, except for the IMPUC magnetometer in publication [P4] of Section 5.3, are based on artificial grain boundary Josephson junctions from  $\text{YBa}_2\text{Cu}_3\text{O}_7$  thin-films, either created by a steep step in the substrate (step-edge junction) or on a bicrystalline substrate (bicrystal junction). A third type, not treated in this work, is the biepitaxial grain boundary junction, where one junction electrode is grown on top of a template layer, usually yielding an asymmetric  $45^\circ$  (001) tilt grain boundary.

A grain boundary can be regarded as the junction of two tilted parts or grains in a crystal. Recent studies gave evidence that  $\text{YBa}_2\text{Cu}_3\text{O}_7$  grain boundaries consist of a spatially inhomogeneous but continuous insulating barrier containing a high density of localized defect states [25, 45, 58]. Grain boundaries in HTS materials exhibit pronounced Josephson effects, due to the fact that the superconducting coherence length  $\xi$  approximately equals the natural width of the boundary of about 1–2 nm. The microscopic origin for the weak link character is still unclear. A reduced oxygen content, a high degree of oxygen disorder, or stress effects may be possible reasons. According to the ISJ model, a suppression of the local energy gap function within a distance of about 0.4 nm at the junction interfaces must be considered, which is due to pair weakening by Coulomb repulsion at the localized sites [23, 59]. The main transport mechanisms across the barrier are direct tunneling and resonant tunneling *via* the defect states. The ISJ model predicts the scaling relation  $J_0\rho_n \propto J_0^{1/2}$  for the critical current density  $J_0$  and the specific normal state resistance  $\rho_n$  of the Josephson junction. It is found that most types of grain boundary junctions fit into this relation [25]. An alternative junction model has been proposed by Moeckly *et al.* [60], where the junction consists of a network of superconducting filaments partially shunting the normal conducting barrier. Although this model also predicts the scaling behavior of  $J_0$  and  $\rho_n$ , it fails to explain the correlation between critical current and resistance fluctuations.

A different approach for HTS Josephson junctions are artificial barriers from thin insulating, normal conducting or semiconducting materials between the superconducting electrodes. Usually, the ramp-edge geometry is employed to take advantage of the larger coherence length in *ab*-direction. In contrast to the step-edge or bicrystal grain boundary junction, a more demanding two-level preparation process must be used [61]. In a first step, a bottom superconducting layer and an insulating layer are deposited. After the

patterning of the bottom electrode from these layers, the barrier and the superconductor for the top electrode are *in situ* deposited, forming a ramp over the bottom electrode. Varying the ramp angle and the barrier thickness allows the adjustment of the junction parameters. However, their reproducibility depends strongly on the homogeneity of the barrier, its epitaxial quality, and the transparency of the interfaces. The IMPUC device in Section 5.3 is based on ramp-edge junctions employing an artificial barrier of semiconducting  $\text{PrBa}_2\text{Cu}_3\text{O}_7$ .

### Step-edge grain boundary junctions

Figure 2.8 depicts the growth of a  $c$ -axis oriented  $\text{YBa}_2\text{Cu}_3\text{O}_7$  thin-film over a step-edge in a  $\text{SrTiO}_3$  substrate for two different step angles  $\alpha$ . Depending on  $\alpha$ , structurally different grain boundaries are obtained [62–64]. For  $\alpha$  sufficiently larger than  $45^\circ$ ,  $\text{YBa}_2\text{Cu}_3\text{O}_7$  grows with a  $90^\circ$  tilt  $c$ -axis orientation at the edge, and two symmetrical grain boundaries of (103) orientation, inclined roughly  $45^\circ$  to the film surface, are formed at the top and at the bottom of the edge. Both have approximately similar critical current densities of about  $10^4$  to  $10^5 \text{ A/cm}^2$ . More shallow steps with  $\alpha < 40^\circ \dots 45^\circ$  do not produce any grain boundaries, and microbridges exhibit no Josephson effects. At steep steps with  $\alpha \gtrsim 70^\circ$ , again a  $90^\circ$  tilt grain is found. However, this grain is thinner than for the more shallow step, and the bottom grain boundary is dominated by a basal-plane-faced (010)(001) type with a significant lower critical current than for the (103) type. Because of the presence of at least two grain boundaries, whose transport properties strongly depend on the step profile and its microstructure, one usually finds a large spread of the Josephson junction parameters. For practical applications steep steps are preferred, because of the single dominating grain boundary and its lower critical current [63]. The transport properties can be adjusted in a limited range by the step angle  $\alpha$ , and by the ratio of the step height and the film thickness. The weaker coupling of the bottom grain boundary is compatible with the experimental observation that the

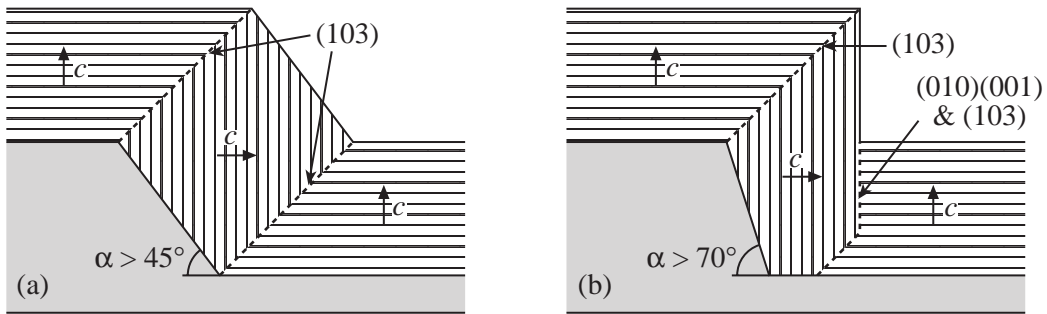


FIGURE 2.8: The growth of a  $\text{YBa}_2\text{Cu}_3\text{O}_7$  thin-film over step-edges with different step-angles  $\alpha$ .

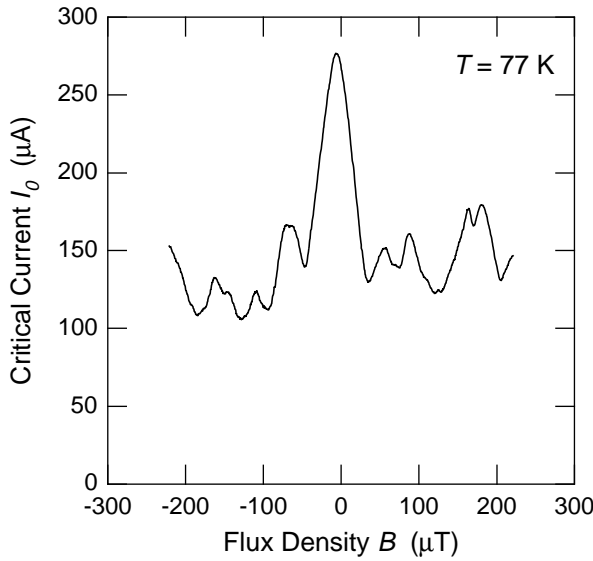


FIGURE 2.9:  $I_0$  versus  $B$  dependence of a  $6\text{ }\mu\text{m}$  wide step-edge Josephson.

junction's transport properties strongly depend on the microstructure at the bottom edge of the step. Structural irregularities, due to the complicated growth mechanism and introduced by the fabrication process are found from the nm- up to the  $\mu\text{m}$ -range [25, 62, 65]. These inhomogeneities often result in strongly irregular Fraunhofer patterns. Figure 2.9 shows a typical example of an  $I_0(B)$  dependence for a  $6\text{ }\mu\text{m}$  wide step-edge Josephson junction. Although a predominant center lobe is measured, deviations from the ideal pattern (refer to Fig. 2.4) are clearly visible. The pattern is neither symmetric nor periodic and indicates a spatially nonuniform critical current density. The effective junction area, calculated from the distances of the first minima to the center lobe, is about  $48\text{ }\mu\text{m}^2$ . This is roughly 10 times the estimated geometrical area. The increase is due to the flux-focusing effect of the electrodes enhancing the local magnetic field at the grain boundary [27]. In this measurement, the magnetic field was applied perpendicular to the substrate surface. For a different direction, a smaller effective area is expected, because of the predominant (010)(001) grain boundary [63]. Another striking feature of this Fraunhofer pattern is the reduced modulation depth. There is a residual level of excess current of about 38% of the maximum critical current that is not influenced by the magnetic field. Excess currents are often observed with step-edge Josephson junctions [63, 64]. The microscopic origin is not yet clear, but it is presumably also related to the irregular microstructure of the step-edge.

It must be noted, that the above mentioned angle dependence of the step-edge microstructure only applies to step-edge junctions on  $\text{SrTiO}_3$  substrates. On  $\text{MgO}$  substrates, Josephson junctions are already obtained with step angles considerably less than  $45^\circ$  [66].



## Bicrystal grain boundary junctions

Devices employing bicrystal Josephson junctions have to be prepared on bicrystal substrates. These are manufactured from two halves of a single-crystal which are fused together with a certain misorientation angle to form a bicrystal. A schematic sketch of a HTS thin-film on a symmetric (001) tilt bicrystal substrate is given in Fig. 2.10. The misorientation angle  $\theta$  can be arbitrarily chosen. When an epitaxial  $\text{YBa}_2\text{Cu}_3\text{O}_7$  thin-film grows on top of the bicrystal substrate, the misorientation angle is transferred into the film and thus forms a grain boundary. A Josephson junction is simply fabricated from this film by patterning a microbridge across the grain boundary line. Several groups have experimentally investigated the transport characteristics in dependence on the angle  $\theta$  [67–69]. They found that the critical current density decreases about exponentially with increasing  $\theta$ , most likely caused by an increase of the thickness of the disordered region around the grain boundary [26]. Therefore, the critical current of bicrystal Josephson junctions can be varied over several orders of magnitude by changing  $\theta$ .

Typical current-voltage characteristics of narrow bicrystal Josephson junctions are close to those calculated according to the RCSJ model. In particular, excess currents are much lower than in step-edge junctions. The magnetic field dependence of the critical current is mostly found to be very similar to the ideal Fraunhofer pattern of a spatially homogeneous Josephson junction. However, there are still deviations that indicate a certain degree of spatial inhomogeneity. A typical example of an  $I_0(B)$  characteristic for a  $4\mu\text{m}$  wide bicrystal Josephson junction is shown in Fig. 2.11(a). The similarity to the ideal pattern

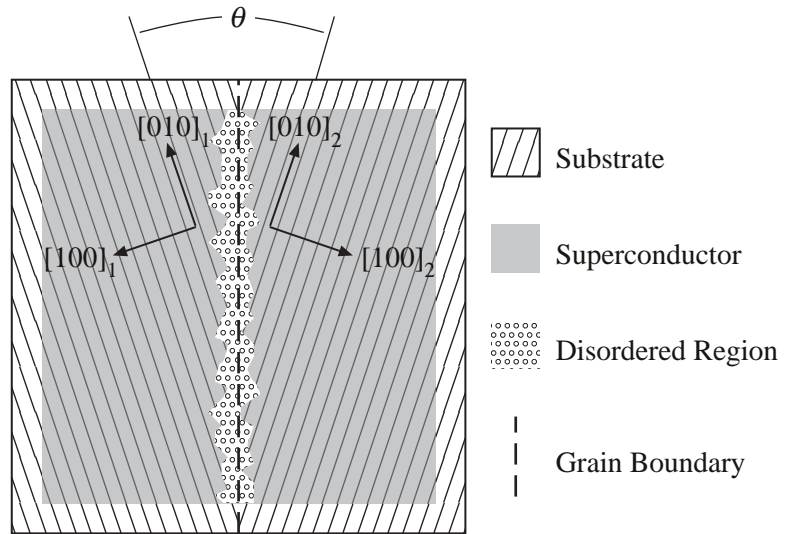


FIGURE 2.10: Schematic sketch of a HTS thin-film on a symmetric bicrystalline substrate with misorientation angle  $\theta$ . The grain boundary is indicated by the vertical dashed line.

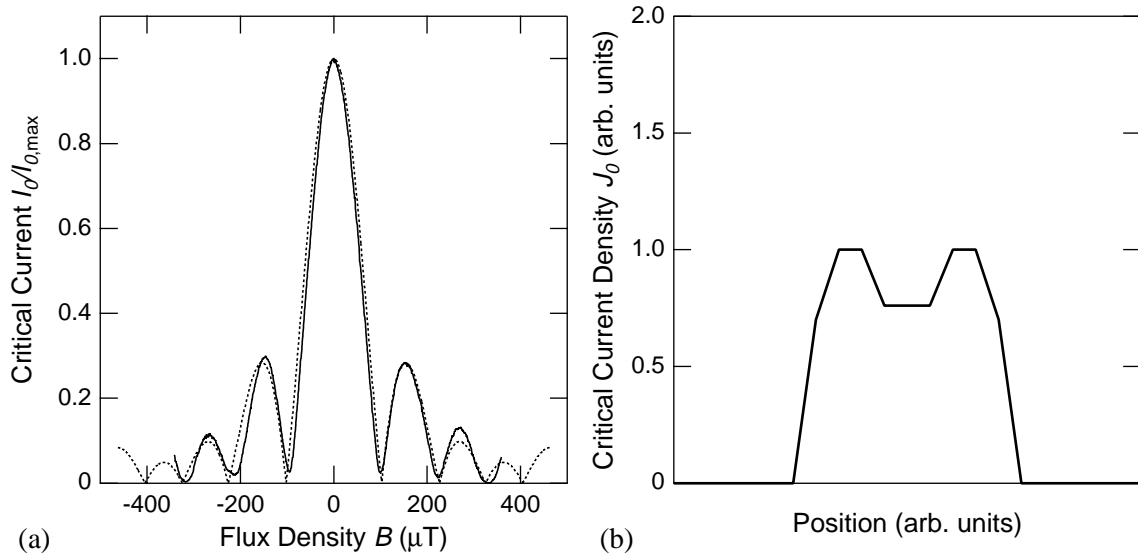


FIGURE 2.11: (a) Fraunhofer pattern of a  $4\mu m$  wide bicrystal Josephson junction at 77 K. The dotted line is a fit obtained with the critical current density profile shown in (b).

in Fig. 2.4 is obvious, however the first side lobes have an elevated height, which points to the fact that the critical current density is increased at the junction edges. Figure 2.11(b) shows an estimated current density profile, which yields a good agreement between the calculated Fraunhofer pattern and the measured one. Increased critical current densities at the edges of HTS Josephson junctions are often observed, which is most likely caused by a better oxygen loading of the edges. By using Low Temperature Scanning Electron Microscopy (LTSEM), Gerdemann *et al.* [65] investigated the spatial variation of the critical current distribution in different types of HTS grain boundary Josephson junctions. The results clearly demonstrate that bicrystal Josephson junctions by far show the best homogeneity compared to step-edge and biepitaxial junctions. The two major drawbacks of using bicrystal substrates are their high price<sup>2</sup> due to the complicated fabrication process, and the fact that the placement of the junctions is restricted to the grain boundary line.

Josephson junctions based on large-angle grain boundaries, in particular asymmetric junctions with a misorientation angle of  $\theta = 45^\circ$ , show  $I_0(B)$  characteristics which are very different from the Fraunhofer pattern. The maxima of the symmetric  $I_0(B)$  patterns occur at fields far aside of  $B = 0$ . This anomalous magnetic field dependence is attributed to the predominant  $d_{x^2-y^2}$  symmetry component of the  $YBa_2Cu_3O_7$  order parameter and

<sup>2</sup>At present, the price of a  $SrTiO_3$  bicrystal substrate is about ten times the price of a single-crystal substrate.

the faceted microstructure of the grain boundary [70, 71]. Both may lead to a local  $\pi$  phase shift between the two wave functions at the boundary, and thus to a sign reversal of the local Josephson current. This effect is strongest for a  $45^\circ$  misorientation angle.

## 2.6 The dc SQUID

A dc SQUID is essentially a superconducting ring, disrupted by two nonhysteretic Josephson junctions. Figure 2.12(a) displays the equivalent circuit for a dc SQUID according to the RCSJ model [42]. The operation of the dc SQUID is based on the Josephson effects and the long-range phase coherence in the SQUID loop inductance  $L$ . The term *interference* in the acronym SQUID essentially describes the interference between the two branch currents  $i_1$  and  $i_2$ , due to the phase coupling. For the dc SQUID, the coupling is described by

$$2\pi \frac{\Phi}{\Phi_0} - \delta_1 + \delta_2 = 2\pi n, \quad n = 0, 1, 2, \dots, \quad (2.21)$$

where  $\delta_{1,2}$  are the phase differences across the junctions and  $\Phi$  is the total magnetic flux in the SQUID inductance  $L$ . The total current through the SQUID is the sum of the currents  $i_1$  and  $i_2$ . Their difference gives rise to a circulating current  $i_{\text{circ}}$  in the ring. Therefore, the total flux in the SQUID loop consists of the external flux  $\Phi_{\text{ext}}$  and a self-induced component  $Li_{\text{circ}}$ . These relations and (2.5) lead to a dependence of the SQUID's critical current on the external magnetic flux that is depicted in Fig. 2.12(b). The maximum critical current  $2I_0$  is obtained for integer flux quanta  $\Phi_{\text{ext}} = n\Phi_0$ , and minimal values are found for  $\Phi_{\text{ext}} = (n + \frac{1}{2})\Phi_0$ . Consequently, the average voltage across the SQUID will also modulate with the period  $\Phi_0$ , when a bias current  $I_b$  slightly larger than  $2I_0$  is

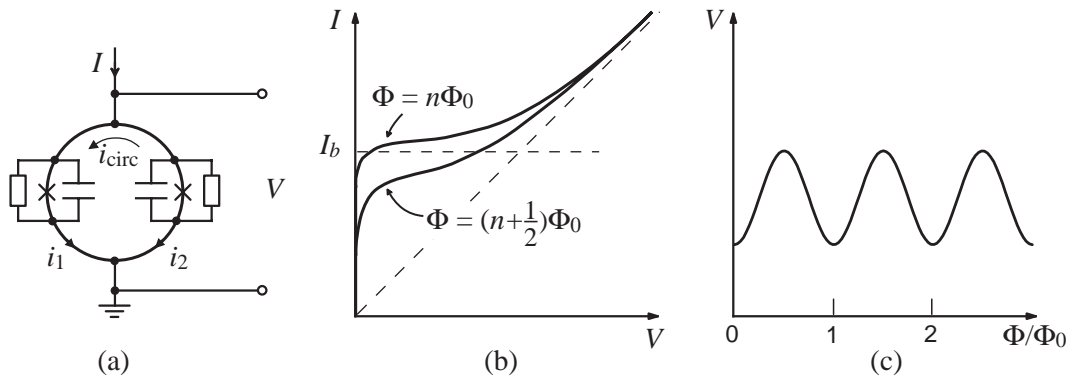


FIGURE 2.12: (a) Equivalent circuit of a dc SQUID according to the RCSJ model. (b)  $IV$  characteristic of a dc SQUID. Both extremal curves for  $\Phi = n\Phi_0$  and  $\Phi = (n + \frac{1}{2})\Phi_0$  are depicted, including noise rounding. (c) Voltage modulation of the SQUID as a function of the applied magnetic flux at constant bias current  $I_b > 2I_0$ .

applied. As depicted in Fig. 2.12(c), the voltage modulation is typically sinusoidal for HTS SQUIDS, due to noise rounding. Deviations from the sinusoidal shape can originate from the interaction of the Josephson oscillations with parasitic ac impedances, in particular with the input structures of SQUID magnetometers. These effects will be described in the following sections in more detail. To obtain the complete dynamics of the dc SQUID, one must numerically solve a set of four coupled differential equations, one for each branch current using (2.12), one for the phase coupling condition (2.21), and one for the voltage across the SQUID using the second Josephson relation (2.6). The influence of noise can be taken into account with two independent current noise sources in parallel with the Josephson junctions [72].

Although one can measure magnetic flux with a SQUID by counting flux quanta, the maximum field resolution and linearity is obtained, if the SQUID is operated in a small range of the flux-voltage characteristic, where the transfer function

$$V_\Phi = \left( \frac{\partial V}{\partial \Phi} \right)_I \quad (2.22)$$

is maximal. This is usually realized with a feedback control by a so-called flux-locked loop (FLL) circuit, as is described in Section 4.3 in more detail. In this case, the SQUID can be considered as a linear flux-to-voltage converter with the transfer function  $V_\Phi$ . For a sinusoidal peak-to-peak voltage modulation  $\Delta V$  the transfer function is  $V_\Phi = \pi \Delta V / \Phi_0$ . The maximum modulation of the critical current, hence the maximum voltage modulation, strongly depends on the SQUID inductance  $L$ . For small inductances, the current modulation can nearly be  $2I_0$ . With larger inductances, however, the modulation is limited by screening through the self-induced flux  $Li_{\text{circ}}$ . One defines the modulation parameter

$$\beta_L = \frac{2LI_0}{\Phi_0} \quad (2.23)$$

as the ratio of the maximal screenable flux  $LI_0$  and the largest self-induced flux  $\Phi_0/2$  [73]. For minor noise rounding, the voltage modulation may be estimated with [72, 74, 75]

$$\Delta V \simeq \frac{I_0 R_d}{1 + \beta_L}, \quad (2.24)$$

where  $R_d$  is the dynamic resistance of each Josephson junction. This relation is well confirmed for dc SQUIDS from low- $T_c$  superconductors. However, HTS dc SQUIDS exhibit a much stronger decrease of modulation with increasing inductance, which is attributed to the influence of thermal noise [76–78]. The typical operation temperature for SQUIDS from the classic metallic superconductors is the boiling temperature 4.2 K of helium, which is about 45% of the critical temperature of niobium devices (9.2 K). In contrast, devices from  $\text{YBa}_2\text{Cu}_3\text{O}_7$  are usually operated in liquid nitrogen ( $T = 77$  K) at about 88% of their

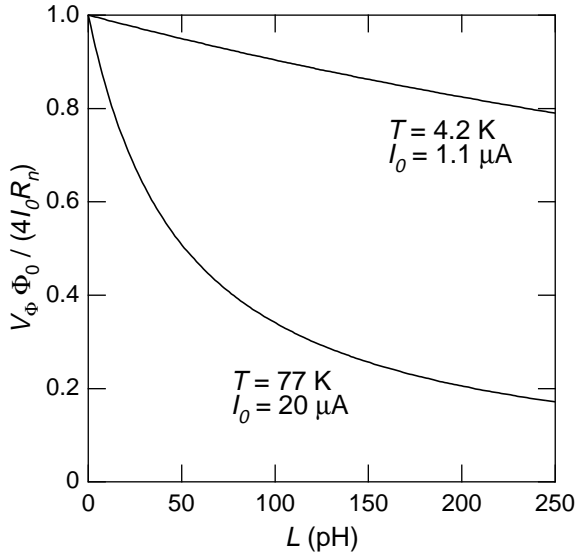


FIGURE 2.13: Dependence of the reduced transfer function on the SQUID inductance  $L$  for the operation temperatures 4.2 K and 77 K. The critical currents are chosen to obtain the same noise parameter  $\gamma$ .

critical temperature. Hence, much more thermal fluctuations are present, which affect the phase coherence in the SQUID loop. Enpuku *et al.* found that the thermal noise degrades the transfer function mainly through the noise flux inside the SQUID inductance [77, 79]. The total thermal flux noise integrated over all frequencies  $\Phi_N = \langle \delta \Phi_n^2 \rangle^{\frac{1}{2}} = \sqrt{k_B T L}$  should be significantly less than the flux quantum  $\Phi_0$ . This condition limits the inductance of HTS devices at 77 K to about 200 pH where  $\Phi_N = 0.22 \Phi_0$ . From numerical simulations, the following relation has been obtained [77]

$$V_\Phi = 4 \frac{I_0 R_n}{\Phi_0 (1 + \beta_L)} \exp\left(\frac{-3.5 \pi^2 \Phi_N^2}{\Phi_0^2}\right). \quad (2.25)$$

This dependence of  $V_\Phi$  on the SQUID inductance is shown in Fig. 2.13 for the temperatures 4.2 K and 77 K. The critical currents were chosen to obtain the same noise parameter  $\gamma \simeq 6$ .

Transfer functions predicted by (2.25) represent an upper limit. The experimental data for HTS SQUIDs are well below this limit, though they follow (2.25) qualitatively [80]. Several reasons are discussed to explain this observation: The transfer function may be reduced, due to asymmetric Josephson junctions. However, quite large asymmetries must be present for a significant reduction, especially for larger  $\beta_L$  [72]. The SQUID inductance is often calculated from the SQUID geometry, therefore errors may occur in the estimation of  $L$ . In particular, its kinetic part can be underestimated, for it strongly depends on the quality of the superconducting thin-film [13]. A more likely reason are microwave resonances in the SQUID loop, which cause a distortion of the current-voltage characteristic. An example of this effect is given in Section 5.1.1. A further source of error can be the estimation of the critical current, if the  $IV$  characteristic is strongly noise-rounded [81], or if there is a large amount of excess current [30].

## 2.7 Noise in dc SQUIDS

The magnetic field resolution of a SQUID is limited by noise from environmental electromagnetic sources and by noise sources in the SQUID itself, in particular the junction noise discussed in Section 2.4 and the flux noise from the motion of Abrikosov vortices in the superconducting film. The total noise is measured as voltage noise across the SQUID, which is expressed by its spectral density  $S_V(f)$  in units  $V^2/\text{Hz}$ . Since the SQUID is basically a magnetic flux sensor, the voltage noise is usually converted into the equivalent flux noise with the spectral density

$$S_\Phi(f) = \frac{S_V(f)}{V_\Phi^2}. \quad (2.26)$$

An additional figure of merit, mainly used for SQUID optimization calculations, is the energy resolution  $\varepsilon = S_\Phi/(2L)$ , which accounts for both the flux noise and the flux input coupling through the SQUID inductance  $L$ . However, low values with  $\varepsilon$  near the quantum limit are only found for very small values of  $L$ . Since real world signals are flux densities, larger sensors, and which is therefore inevitable, larger inductances must be used. Extensive numerical calculations on the thermal noise in SQUIDS at 4.2 K were taken out by Tesche and Clarke [72], employing the RCSJ model. They found an optimum noise performance for the SQUID parameter  $\beta_L \approx 1$ , and a normal state resistance  $R_n$  as large as possible. These results still apply to SQUIDS from HTS [80]. The noise-rounding parameter  $\gamma$  should exceed 5, which is equivalent to a minimal critical current of  $I_0 = 16 \mu\text{A}$  per junction at 77 K [42]. An optimum set of parameters for SQUIDS at 77 K is given by  $I_0 = 20 \mu\text{A}$  and  $L = 50 \text{ pH}$ . For HTS SQUIDS, the McCumber-parameter  $\beta_C$  may be slightly larger than one, where the junction's hysteresis is still suppressed by the thermal fluctuations and the  $LC$  resonance causes a larger voltage modulation [82–84].

Usually, one distinguishes between two different parts of a SQUID noise spectrum: The frequency-independent (“white”) noise at higher frequencies, and the low-frequency (“ $1/f$ ”) noise, which typically scales as  $1/f^\alpha$  with the frequency  $f$  and some exponent  $\alpha$ .

### Frequency-independent noise

The lower limit of the frequency-independent SQUID noise is set by the phase-slip process due to the thermal noise current in the junction resistance  $R_n$ . An estimation for the voltage noise spectral density across a SQUID is obtained from a simple model [72], where the total noise current in the SQUID is divided into two independent parts. One flows through both resistors in parallel ( $R = R_n/2$ ), yielding a voltage noise spectral density  $S_I R_d^2$  across the SQUID's dynamic resistance  $R_d$ . The second circulates over

both resistors ( $R = 2R_n$ ) and generates flux noise with the spectral density  $S_I L^2$  in the SQUID inductance  $L$ . It is converted into voltage noise by the transfer function  $V_\Phi$ . Using  $S_I = \eta 4k_B T / R$ , where  $\eta = 1 + \frac{1}{2}(I_0/I)^2$  is the mixing factor described in Section 2.4 one obtains

$$S_V = \eta R_d^2 \frac{4k_B T}{R_n/2} + \eta L^2 V_\Phi^2 \frac{4k_B T}{2R_n}. \quad (2.27)$$

An estimation using typical HTS SQUID parameters and the reduced transfer function (2.25) shows that the flux noise term is about one order of magnitude smaller than the first term and can thus be neglected. Using (2.26) and (2.27) one obtains

$$S_\phi = 8\eta \frac{k_B T}{R_n} \frac{R_d^2}{V_\Phi^2} \quad (2.28)$$

for the flux noise spectral density. Hence, for a low-noise SQUID a large transfer function is needed, which requires a low inductance.

## Low-frequency noise

Most applications are not limited by the white noise level of the SQUID sensor but affected by its  $1/f$  noise. Magnetocardiography and also some geophysical experiments require a maximum field resolution in the frequency range  $1 \dots 200$  Hz, hence the  $1/f$  corner frequency should be at the lower end of this range. The predominant sources of low-frequency noise in SQUIDs are the current noise in the Josephson junctions and the thermally activated motion of Abrikosov vortices [85]. Both the occupation of a localized defect state in the junction barrier and the trapping of a vortex at a pinning center, can in general be described by a two-level fluctuator (TLF) model. The TLF generates a random train of voltage pulses (random telegraph signal) with amplitude  $\delta V$ , where the pulse lengths are given by the average lifetimes  $\tau_o$  and  $\tau_u$  for the occupied and the unoccupied state, respectively. The lifetimes strongly depend on the temperature

$$\tau_i = \tau_{i0} \exp\left(\frac{E_a}{k_B T}\right), \quad i = o, u, \quad (2.29)$$

where  $1/\tau_{i0}$  is an attempt frequency and  $E_a$  the activation energy. This type of noise signal produces a Lorentzian voltage noise spectrum [54, 86]

$$S_V(f) = \delta V^2 \frac{\tau_{\text{eff}}^2}{(\tau_o + \tau_u)^2} \frac{\tau_{\text{eff}}}{1 + (2\pi f \tau_{\text{eff}})^2}, \quad (2.30)$$

which is nearly frequency-independent below the corner frequency  $1/\tau_{\text{eff}} = 1/\tau_o + 1/\tau_u$  and proportional to  $1/f^2$ , above. The superposition of many statistically independent TLFs with a flat distribution of energy barriers yields a spectrum  $S_V \propto 1/f$ . A stronger

frequency dependence  $S_V \propto 1/f^\alpha$  with exponents  $\alpha > 1$  is mainly found for ambient noise.

The amount of  $1/f$  noise from vortex motion strongly depends on the residual field  $B_0$  in which the SQUID is cooled through its transition temperature, and also on the crystallographic quality of the involved superconducting thin-films [87–89]. Since the number of vortices in the superconducting film is proportional to  $B_0$ ,  $S_\Phi$  is expected to scale linearly with  $B_0$ , presuming an uncorrelated vortex motion. Noise measurements on field cooled SQUID magnetometers will be discussed in Section 5.5 in detail.

In the well-shielded and zero-field-cooled case, the noise generated by vortex motion in SQUIDS from state-of-the-art *c*-axis oriented  $\text{YBa}_2\text{Cu}_3\text{O}_7$  thin-films can be usually neglected. In this case, the dominating  $1/f$  noise source is the current noise from randomly trapped charge carriers in the junction barrier. An estimation for the noise level is obtained with a similar model as the one describing the white noise [90]. The current noise is divided into two independent parts, where the first one describes in-phase fluctuations of the critical currents of both junctions. They produce fluctuations of the mean voltage across the current biased SQUID. The second part describes anti-phase fluctuations, which generate flux noise in the SQUID loop. The common current bias is  $I \simeq I_0$ , where the maximum transfer function is obtained. Hence, the resistance fluctuations can be neglected. Using the RCSJ model, one obtains [91]

$$S_V(f) = \frac{1}{2}[(V - R_d I)^2 + (L I_0 V_\Phi)^2] \frac{S_I(f)}{I_0^2}, \quad (2.31)$$

where  $S_I(f)$  is the spectral density of the critical current fluctuations. The first term is given by the in-phase fluctuations and the second one by the anti-phase fluctuations. Provided that the flux-voltage curve is symmetric, the in-phase part can be completely suppressed, when the SQUID is operated in the common flux-locked loop (FLL) mode with flux modulation and lock-in detection. Then, the residual flux noise spectral density is given by

$$S_\Phi(f) = \frac{1}{2}(L I_0)^2 |\delta I_0 / I_0|^2, \quad (2.32)$$

using  $|\delta I_0 / I_0|^2 = S_I(f) / I_0^2$ . Thus, measuring the flux noise with flux modulation, one obtains an estimation for the normalized critical current fluctuations in the Josephson junctions. A total suppression of the current noise is obtained with additional bias current modulation, where the bias current is periodically reversed [90, 92]. Since the sign of the circulating noise current is reversed during one period, the voltage signal averages to zero after integration in the FLL electronics, provided that the modulation frequency is considerably higher than the  $1/f$  corner frequency. In a direct readout FLL electronics without flux modulation, both in-phase and anti-phase fluctuations are not suppressed.



However, a modulation scheme using bias reversal may also be applied for a total suppression of the critical current fluctuations. This is treated in Section 5.2 in more detail. Consequently, by applying the bias current reversal method, a residual amount of  $1/f$  noise can be attributed to ambient noise penetrating the shields or to vortex motion, provided that the SQUID characteristics have the necessary symmetry and the SQUID electronics is properly adjusted. A more detailed description of both types of SQUID FLL electronics is given in Section 4.3.



### 3 DC SQUID magnetometer design

A bare SQUID is basically a flux-to-voltage converter. As noted in Section 2.6, the SQUID inductance of a HTS SQUID is limited to a value of about 200 pH or less. Hence, the SQUID loop itself cannot be made arbitrarily large, so that the magnetic field resolution of a bare SQUID is insufficient for many applications. For this reason, large area flux collecting antennas in the form of pickup loops are employed to convert the magnetic flux density signal  $B$  effectively into a magnetic flux signal  $\Phi$  for the SQUID. This combination of flux collecting pickup loop and SQUID is called a *SQUID magnetometer*. The efficiency of the pickup loop is described by the ratio of the effective flux in the SQUID and the applied flux density. This characteristic quantity is called the effective area of a SQUID magnetometer

$$A_{\text{eff}} = \frac{\partial \Phi}{\partial B} \quad (3.1)$$

Figure 3.1 schematically shows the operation principle of a SQUID magnetometer. It follows that the field resolution of a SQUID magnetometer is basically determined by the effective flux collecting area  $A_{\text{eff}}$  and the transfer function  $V_{\Phi}$  of the SQUID. Several schemes for the input coupling in SQUID magnetometers have been developed, which are schematically depicted in Fig. 3.2. They will be discussed in the following.

The most simple way of coupling an antenna to a SQUID is the direct signal injection with a large-area pickup loop galvanically connected parallel to the SQUID loop [76, 93]. Although the efficiency of this solution is comparatively poor due to the substantial

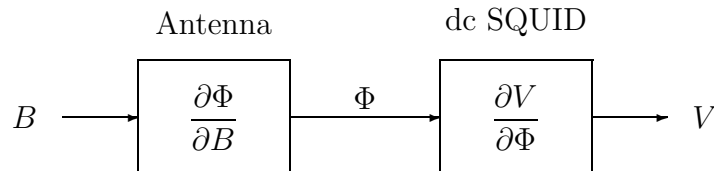


FIGURE 3.1: Principle of operation of a SQUID magnetometer.

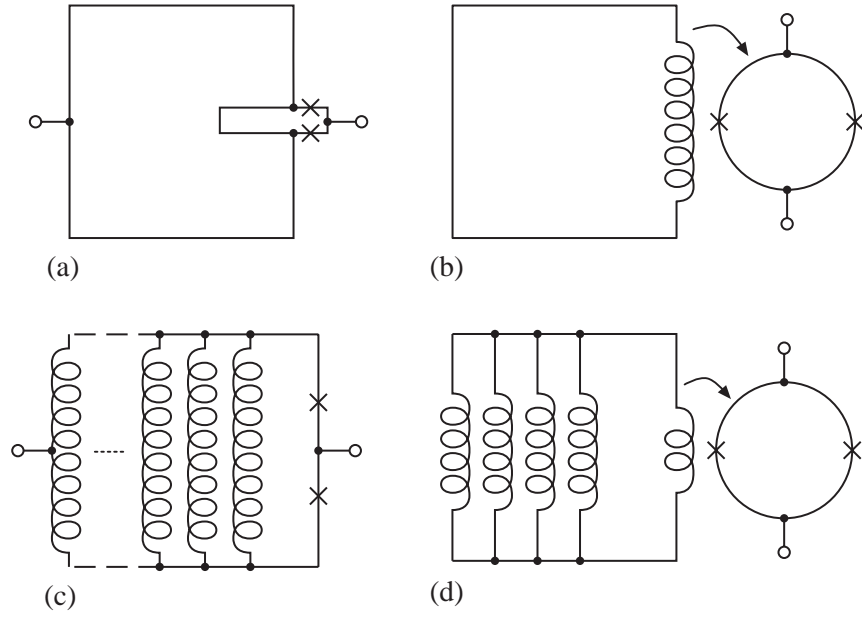


FIGURE 3.2: Coupling schemes of dc SQUID magnetometers: (a) directly coupled magnetometer, (b) inductively coupled magnetometer, (c) multiloop magnetometer, (d) magnetometer with integrated multiloop pickup coil (IMPUC).

inductance mismatch, this configuration is widely used for HTS SQUID magnetometers, because it can be realized with a single superconducting layer.

A more efficient solution is the inductive coupling of the pickup loop to the SQUID loop *via* a spiral input coil. Pickup loop and input coil have matched inductances, yielding a much better coupling between pickup loop and SQUID. Usually, the flux transformer design of Ketchen and Jaycox [94–96] is employed, where the SQUID loop is shaped like a square washer with a planar multiturn input coil patterned on top of it. The washer layout keeps the SQUID inductance low, but provides enough space for the windings of the input coil. Transformer coupled magnetometers from low temperature superconductors usually employ a solid wire-wound pickup loop that is galvanically connected to the thin-film input coil integrated on the SQUID chip. Hence, the pickup loop may be easily designed in a gradiometer configuration adapted to measure the first or second order spatial derivative of the magnetic field for a good suppression of homogeneous signals from distant noise sources. Unfortunately, there is not yet a suitable interconnect technology for HTS wires and thin-films, so that pickup loop and input coil have to be integrated on one substrate for inductively coupled HTS magnetometers. However, both can be separate from the SQUID, which may reside on a different substrate. This flip-chip arrangement [88, 97, 98] has the advantage that the SQUID can be fabricated in a more simple single-layer process with higher yield. Good magnetometer properties can be obtained by choosing the optimum combination of SQUID-chip and antenna-chip. The

major drawback of this setup is the complicated adjustment of the input coil onto the SQUID washer. In this work, only monolithically *integrated* magnetometers are discussed.

A completely different approach is the multiloop magnetometer, which was originally developed in 1971 by Zimmerman [99] in solid niobium technology. Later, this concept was redesigned for LTS and HTS thin-film technology by Drung *et al.* [100, 101]. In the multiloop magnetometer one cannot distinguish between SQUID and pickup loop, for the SQUID loop itself is enlarged to be the pickup loop. From inductance considerations it is clear that this cannot be done with a single loop. But with several pickup loops connected in parallel, the SQUID inductance can be kept low enough to ensure low-noise operation. Flux transformer coupled multiloop SQUIDs are described by Carelli *et al.* [102, 103].

A combination of the multiloop approach with the inductively coupled design is the magnetometer with an integrated multiloop pickup coil (IMPUC). As in the Ketchen-Jaycox scheme, a multiturn input coil is employed, but fewer turns are used due to the lower inductance of the multiloop pickup coil. The IMPUC concept was successfully introduced with ramp-edge Josephson junctions by Scharnweber *et al.* [104, 105]. An IMPUC magnetometer based on bicrystal Josephson junctions is discussed by Subke *et al.* [61, 106].

The following sections give the design considerations for the practical layout of directly and inductively coupled magnetometers, and for the multiloop magnetometer.

### 3.1 Directly coupled dc SQUID magnetometers

The general design of a directly coupled magnetometer is shown in Fig. 3.3. In this configuration, the shielding current  $I$  generated in the pickup loop by an applied field  $B$  is directly injected into the SQUID inductance  $L$ . In the field  $B$  the flux inside the pickup loop of a directly coupled magnetometer is given by

$$\Phi_p = BA_p = (L_p + kL)I, \quad (3.2)$$

where  $A_p$  is the effective flux sensing area of the pickup loop and  $L_p$  is the pickup loop inductance.  $kL$  is the fraction of the SQUID inductance in which the shielding current is injected. The flux in the SQUID loop consists of a part due to the external field and a second part generated by the shielding current

$$\Phi_S = BA_S + kLI. \quad (3.3)$$

Then the effective flux sensing area  $A_{\text{eff}} = \Phi_S/B$  of the magnetometer becomes

$$A_{\text{eff}} = A_S + \frac{kL}{L_p + kL}A_p. \quad (3.4)$$

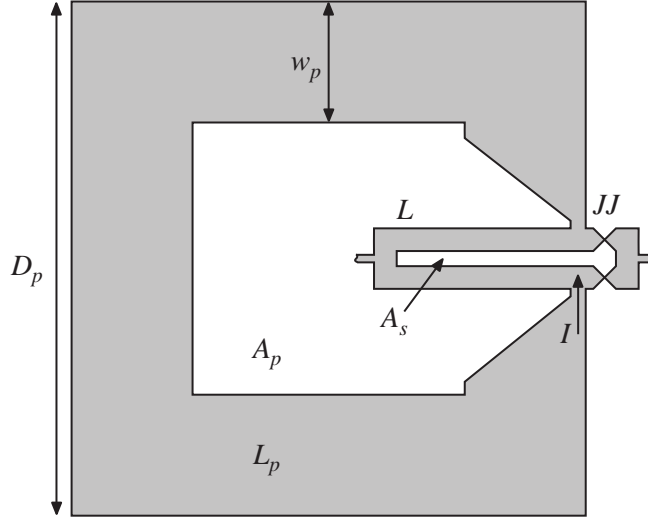


FIGURE 3.3: Schematic of a directly coupled dc SQUID magnetometer. The large pickup loop inductance  $L_p$  is galvanically connected to the SQUID inductance  $L$ .  $JJ$  marks the Josephson junctions.

Typically, it is  $L_p \gg L$ , so that the term  $kL$  in the denominator may be neglected. The large mismatch between both inductances causes a comparatively low field resolution of the directly coupled magnetometer. A much better efficiency is obtained with multilayer magnetometers to the disadvantage of a more complicated preparation process. They will be discussed in the following sections. A good approximation for the inductance of the square washer pickup loop is given by [101]

$$L_p = 2 \frac{\mu_0}{\pi} (D_p - w_p) \left[ \ln \left( \frac{32}{\pi} \frac{D_p - w_p}{w_p} \right) - 2 \right]. \quad (3.5)$$

This formula is a special case ( $N = 4$ ) of (3.26) in Section 3.3 for the inductance of a polygonal pickup loop. Due to the large relative dielectric constant  $\varepsilon_r$  of the used  $\text{SrTiO}_3$  substrates, the capacitance and inductance of the SQUID loop cannot be treated as lumped elements, but the loop must be considered as a transmission line with distributed parameters [17]. The capacitance per unit length of a symmetrical coplanar stripline is given by [107]

$$C' = \frac{1}{2} \varepsilon_0 (\varepsilon_r + 1) \frac{K(k')}{K(k)}, \quad (3.6)$$

where  $K(k)$  is the complete elliptic integral of first kind,  $k = s/(s+2w)$  and  $k' = \sqrt{1-k^2}$ . With the phase velocity  $v_p = c \sqrt{2/(\varepsilon_r + 1)}$ , the impedance of the coplanar stripline  $Z_{\text{CS}} = 1/(v_p C')$  becomes

$$Z_{\text{CS}} = \frac{\sqrt{\mu_0/\varepsilon_0}}{\sqrt{\frac{1}{2}(\varepsilon_r + 1)}} \frac{K(k)}{K(k')}. \quad (3.7)$$

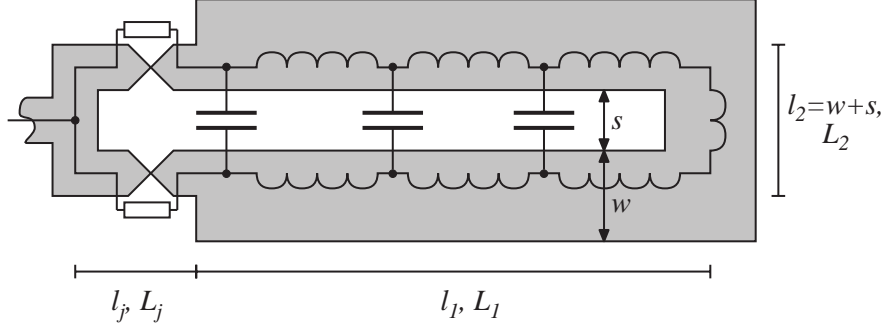


FIGURE 3.4: Layout of the SQUID loop of the directly coupled magnetometer and its equivalent circuit model.

The constants  $\mu_0$  and  $\varepsilon_0$  are the vacuum permeability and vacuum permittivity, respectively, and  $c = 1/\sqrt{\varepsilon_0\mu_0}$  is the vacuum velocity of light. The SQUID loop is similar to the so-called hairpin resonator used in HTS microwave filter circuits [108]. It is bounded by the large impedance change at the Josephson junctions, thus the fundamental mode corresponds to a half wavelength along the total length of the resonator  $l_r \approx 2l_1 + l_2$ , yielding a resonance frequency of

$$f_0 = \frac{v_p}{2l_r} = \frac{c}{2l_r} \sqrt{\frac{2}{\varepsilon_r + 1}}. \quad (3.8)$$

Distortions of the current-voltage characteristic due to these stripline resonances will be discussed in Section 5.1.1. The inductance per unit length is  $L' = Z/v_p$ , and with (3.7) one obtains

$$L_1 = \mu_0 l_1 \frac{K(k)}{K(k')} \quad (3.9)$$

for the inductance of a coplanar stripline. The small contribution  $L_j$  from the Josephson junctions may also be calculated in this way. The inductance  $L_2$  of the single connecting part of both legs in the SQUID loop can be calculated with [109]

$$L_2 = \frac{\mu_0}{2\pi} l_2 \left( \ln \frac{2l_2}{w + t} + \frac{1}{2} \right), \quad (3.10)$$

where  $t$  is the thickness of the thin-film. Thus far, no superconducting properties were involved in the inductance calculations. However, for structural dimensions of the order of the London penetration depth, significant contributions from the kinetic inductance must be considered. The kinetic inductance  $L_k$  in a conductor of volume  $V$  is defined by [5]

$$\frac{1}{2} L_k I^2 = \frac{1}{2} \mu_0 \lambda_L^2 \int_V J^2 dV, \quad (3.11)$$

where  $I$  is the total current and  $J$  the local current density in the conductor. The kinetic inductance is not a superconductivity induced effect, for it is solely caused by the inertia

of the charge carriers. However, the kinetic inductance of normal conductors is usually negligible, because of the short mean free path length of the electrons [110]. Consequently, the contribution from the unpaired electrons in a superconductor can also be neglected. Because HTS devices are usually operated near  $T_c$ ,  $\lambda_L$  and thus the kinetic inductance can become quite large and may not be neglected. Assuming a spatially constant current density, the kinetic inductance of a stripline of length  $l$ , width  $w$ , and thickness  $t$  is obtained from (3.11) as

$$L_k(T) = \mu_0 l \frac{\lambda_L(T)^2}{wt}. \quad (3.12)$$

In the typical parameter range, the error is negligible compared to more elaborate formulas taking the actual current distribution into account [111, 112]. Finally, the complete inductance  $L$  of the SQUID loop structure in Fig. 3.4 becomes

$$L = L_1 + L_2 + L_j + L_k. \quad (3.13)$$

The effective area of the square washer pickup loop is approximately given by the geometrical mean of the total area  $A_t$  and the area of the center hole  $A_h$

$$A_p = a \sqrt{A_t A_h} = a D_p (D_p - 2w_p), \quad (3.14)$$

where  $a$  is about 1.1 [113]. The effective SQUID loop area may be calculated in the same way, but due to the narrow linewidths the London penetration depth has to be taken into account.

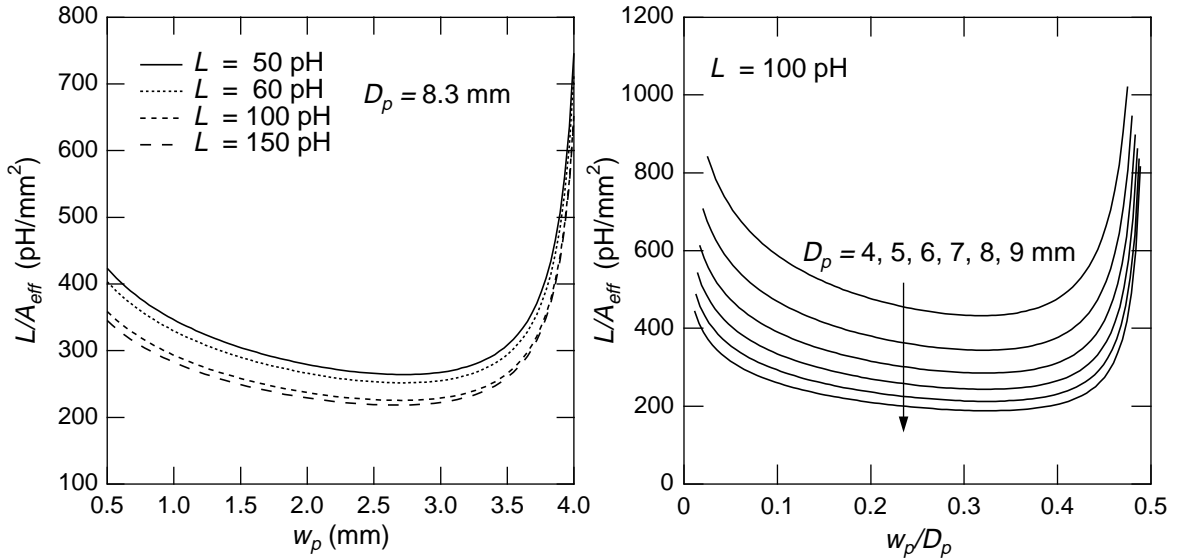


FIGURE 3.5: Determination of the optimum pickup loop width  $w_p$  of a directly coupled magnetometer: (a) For a pickup loop size of  $D_p = 8.3$  mm a nearly inductance independent optimum of  $w_p \simeq 2.7$  mm is found. (b) The optimum ratio of pickup loop width and pickup loop size is  $w_p/D_p \simeq 1/3$ , roughly independent from  $D_p$ .



With the above results an optimum pickup loop linewidth can be calculated if one uses the ratio  $L/A_{\text{eff}}$  as the optimization criterion. Magnetic flux is coupled most efficiently into the magnetometer where  $L/A_{\text{eff}}$  is minimal. Figure 3.5(a) shows the results for several practical inductances and a pickup loop size of  $D_p = 8.3$  mm. A nearly inductance independent optimum at  $w_p = 2.7$  mm is found. Figure 3.5(b) depicts the ratio  $L/A_{\text{eff}}$  as a function of the ratio of the pickup loop width  $w_p$  and the pickup loop size  $D_p$ . The optimum is found at about  $w_p = D_p/3$ , roughly independent from the pickup loop size.

## 3.2 Inductively coupled magnetometers with integrated flux transformer

A schematic representation of the inductively coupled magnetometer is shown in Fig. 3.6. A pickup loop of inductance  $L_p$  is connected to a spiral input coil inductance  $L_i$  prepared on top of a square washer SQUID for a tight coupling. In this layout, the washer also serves as a return path for the input coil, saving a third superconducting layer. The inductance of the square washer SQUID is given by  $L = L_h + L_{\text{sl}}$ , where  $L_h$  is the contribution from

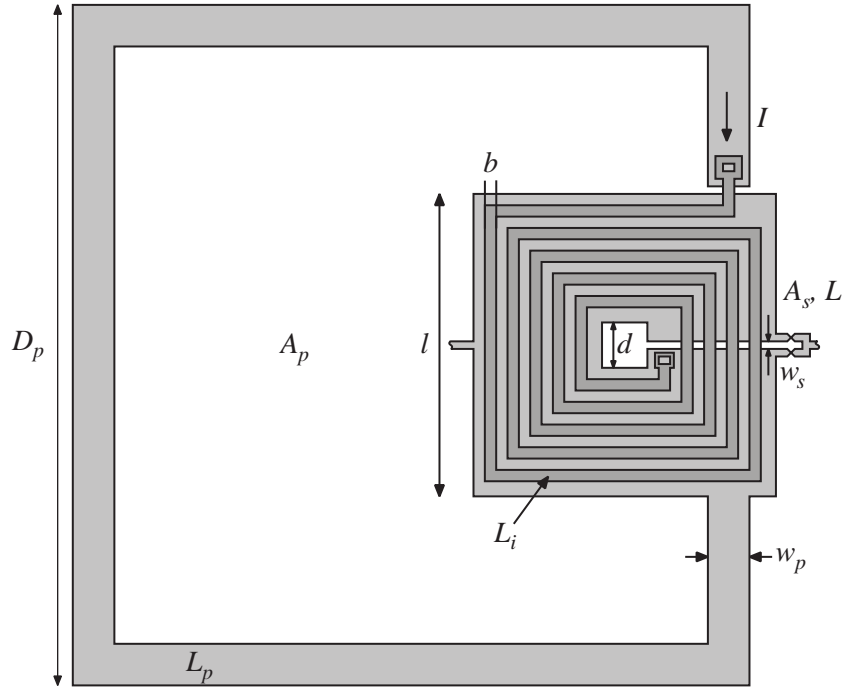


FIGURE 3.6: Schematic of an inductively coupled dc SQUID magnetometer. The pickup loop inductance  $L_p$  is connected to the input coil inductance  $L_i$  prepared on top of a square washer SQUID. The washer also serves as a return path for the input coil, saving a third superconducting layer. This requires a via contact near the center hole. A second via connects the outermost input coil winding to the pickup loop.

the center hole and  $L_{\text{sl}}$  the contribution from the slit. The hole inductance is usually estimated with [95]

$$L_h = 1.25 \mu_0 d, \quad (3.15)$$

where  $d$  is the sidelength of the square washer hole. This equation is the result of a three-dimensional numerical calculation for superconducting thin-films and holds for a hole size less than the washer linewidth. The slit inductance can be calculated with the formula (3.9) for a coplanar stripline. In the inductively coupled magnetometer, the kinetic part of the SQUID inductance has no effect on the coupling efficiency, because no flux couples to it. This is in contrast to the directly coupled magnetometer, where the shielding current in the pickup loop is directly injected into the SQUID inductance. In both cases, however, the kinetic contribution affects the SQUID performance *via* the modulation parameter  $\beta_L$ . If the SQUID is coupled to a superconducting input circuit with a pickup loop inductance  $L_p$  and an input coil inductance  $L_i$ , the low-frequency inductance of the SQUID washer is reduced to an effective inductance

$$L' = L \left( 1 - k^2 \frac{L_i}{L_p + L_i} \right). \quad (3.16)$$

This is due to a screening effect of the superconducting load, which acts as a groundplane for the SQUID loop [95,114]. The coupling constant  $k$  is defined by the mutual inductance  $M = k\sqrt{L_i L}$  between the input coil and the washer inductance. The reduced inductance usually results in an increased voltage modulation of the screened SQUID, compared to a bare SQUID washer of the same size. In turn, also the input coil inductance is reduced by the SQUID washer [75,115].

In zero field, flux quantization in the input circuit of the transformer-coupled magnetometer leads to

$$\Phi_p = BA_p + (L_p + L_i)I = 0, \quad (3.17)$$

where  $B$  is the applied magnetic field,  $A_p$  is the effective area of the pickup loop, and  $I$  is the shielding current. The comparatively small flux in the area of the input coil is neglected. The flux signal  $\Phi_S$  coupled to the SQUID washer is determined by the shielding current  $I$ , the mutual inductance  $M$ , and the effective area  $A_S$  of the SQUID washer

$$\Phi_S = BA_S - MI. \quad (3.18)$$

Here, the winding direction of the input coil is chosen in such way that the external flux and the flux due to the shielding current have the same direction. For the effective flux collecting area  $A_{\text{eff}} = \Phi_S/B$  of the magnetometer one obtains

$$A_{\text{eff}} = A_S + \frac{M}{L_p + L_i} A_p, \quad (3.19)$$

where the areas  $A_S$  and  $A_p$  may be calculated with (3.14).

In the case of strong coupling, a current  $I$  in the input coil of  $n$  turns will induce a reverse image current  $nI$  into the SQUID washer. Thus, the mutual inductance between input coil and SQUID is  $M \simeq nL$ . The input coil inductance becomes [94]

$$L_i = L_{\text{SL}} + n^2 L, \quad (3.20)$$

where  $L_{\text{SL}}$  is the stripline inductance of the input coil on top of the square washer that acts as a superconducting groundplane. The second term arises from the image currents in the washer which couple back to the input coil. There is no simple analytical expression for the inductance of a superconducting square spiral coil. However, an estimation is given by the formula for a superconducting stripline on a groundplane [116]

$$L_{\text{SL}} = \frac{\mu_0 l}{w} \left( h + \lambda_L \coth\left(\frac{t_1}{\lambda_L}\right) + \lambda_L \coth\left(\frac{t_2}{\lambda_L}\right) \right) \quad \text{for } w \gg h, \quad (3.21)$$

where  $w$  is the width of the stripline,  $h$  is its distance away from the groundplane, and  $t_1, t_2$  are the thicknesses of both superconducting layers. Here, the mutual inductances between the windings are neglected. For typical layouts,  $L_{\text{SL}}$  is much smaller than  $n^2 L$  and may therefore be neglected.

### 3.3 Multiloop magnetometers

The basic relations for the design and optimization of thin-film multiloop magnetometers are discussed in Refs. [101, 117] in detail and will only be summarized in the following.

The common layout of a thin-film multiloop magnetometer is an equilateral polygon with  $N$  sides and  $N$  spokes. Figure 3.7 schematically shows this cart-wheel like shape for  $N = 8$ . To obtain a flux state  $\Phi$  in the multiloop SQUID, this flux must be coupled to each one of the  $N$  loops. Therefore the effective flux collecting area of the multiloop device is given by  $A_p/N$ , where  $A_p$  is the area of the polygonal pickup loop. Furthermore, this area has to be reduced by the parasitic area  $A_s$  of one spoke. Hence,

$$A_{\text{eff}} = \frac{A_p}{N} - A_s. \quad (3.22)$$

Again, the pickup loop area  $A_p$  is calculated as the geometrical mean from outer dimension  $D_p$  and inner dimension  $D_p - 2w_p$ , but now for an equilateral polygon:

$$A_p = \frac{N}{4} \tan\left(\frac{\pi}{4}\right) D_p (D_p - 2w_p). \quad (3.23)$$

The parasitic area covered by one spoke is given by

$$A_s = \frac{1}{2} (D_p - w_p) d_{s,\text{eff}}, \quad (3.24)$$

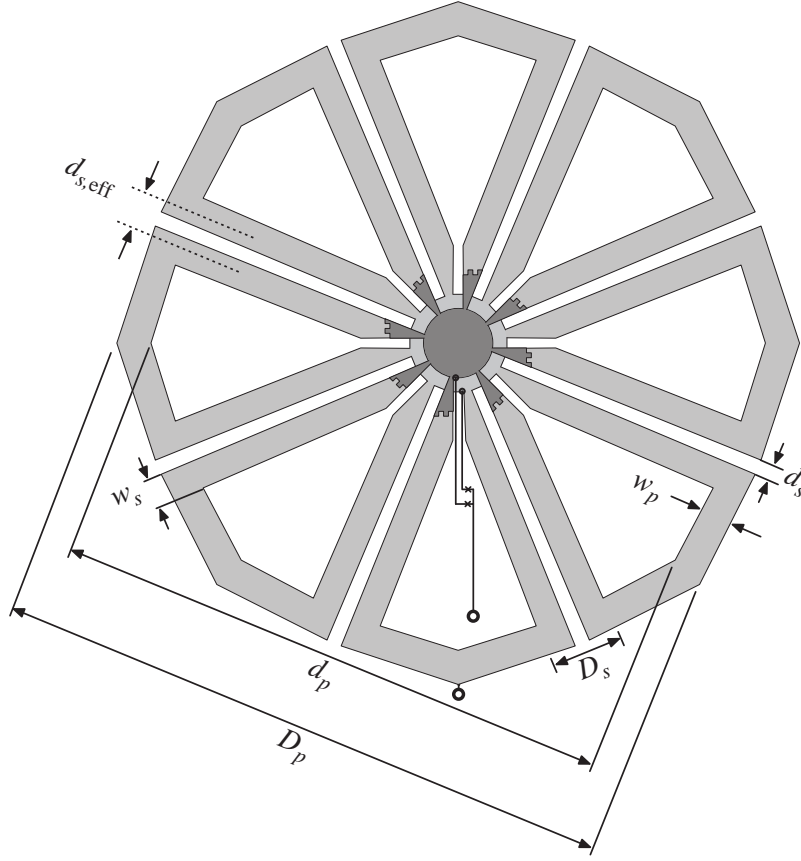


FIGURE 3.7: Schematic of a multiloop magnetometer with 8 pickup loops. The darker area is fabricated from the top superconducting layer.

where  $d_{s,eff}$  is an effective slitwidth, accounting for flux focusing into the slit and the London penetration depth [101].

The inductance of a multiloop magnetometer consists of contributions from the inductance  $L_p$  of the polygonal pickup loop, the inductance  $L_s$  from the spokes and the parasitic inductance  $L_j$  from the leads to the Josephson junctions and the junctions themselves. The inductance of a single loop is given by  $L_p/N + L_s$ . For the complete device with  $N$  loops in parallel one obtains

$$L = \frac{L_p}{N^2} + \frac{L_s}{N} + L_j. \quad (3.25)$$

An estimation for the inductance  $L_p$  is obtained from the inductance of a circular conductor loop of radius  $r$

$$L_p = \mu_0 r \left[ \ln \left( \frac{16r}{w_p} \right) - 2 \right] \quad (3.26)$$

if one replaces its circumference by the mean polygon circumference

$$2\pi r = N \tan \left( \frac{\pi}{N} \right) (D_p - w_p). \quad (3.27)$$

The spoke inductance  $L_s$  can be calculated with the formula (3.9) for a coplanar stripline. A good approximation for a spoke slit width  $d_s$  smaller than the linewidth  $w_s$  is given by [101]

$$L_s = \mu_0 l \frac{\pi}{2 \ln(4D_s/d_s)}, \quad (3.28)$$

where  $l$  is the length of the spoke and  $D_s = 2w_s + d_s$  the total spoke width. The flux contribution in the magnetometer due to the spokes is strongly reduced by the large mutual inductance between the adjoining loops. A current in one spoke line causes an oppositely equal flux in both adjoining loops and thus no net flux in the SQUID. Only the small amount of stray flux in the slit between the spoke lines causes a flux contribution. Hence, this slit should be made as narrow as possible. Accordingly, the inductance of the spoke is mainly determined by the spoke slit width. From (3.22) follows that the effective area of a multiloop magnetometer is roughly given by the area of one loop. Opening of single loops does not change the effective area of the device, but only increases its inductance [118].

### 3.4 Summary

Figure 3.8 summarizes the results of calculations made in accordance to the previous sections. It shows the attainable effective area for the three investigated magnetometer layouts depending on the SQUID inductance. The calculations were made for pickup loop sizes between 4 and 9 mm, suitable for the most common substrate size of  $10 \times 10 \text{ mm}^2$ .

Obviously, only a comparatively low effective area can be obtained with the directly coupled magnetometer, which results from the direct signal injection and the large inductance mismatch between pickup loop and SQUID loop. Typical devices show effective areas considerably less than  $1 \text{ mm}^2$ , i.e. less than 1% of the pickup loop area. The main advantage of this magnetometer design is the ease of fabrication in a simple single layer process. According to (3.4), the effective area increases nearly linear with the SQUID inductance. The calculations have been made for the pickup loop linewidth  $w_p = D_p/3$ .

With the inductively coupled layout, a larger effective area over a broad inductance range is obtained as the result of the matched inductances. For an 8 mm device of  $L = 100 \text{ pH}$  an effective area of about  $2 \text{ mm}^2$  is calculated, which is roughly 4 times the effective area of a directly coupled magnetometer of the same size and inductance. The curves were calculated for an optimal inductance matching ( $L_p = L_i$ ) and a coupling constant  $k = 0.9$ .

The inductance of a multiloop magnetometer is mainly determined by the number of the loops. The effective area depends much stronger on the SQUID inductance than in the other magnetometer types. Practical effective areas, comparable to those of inductively

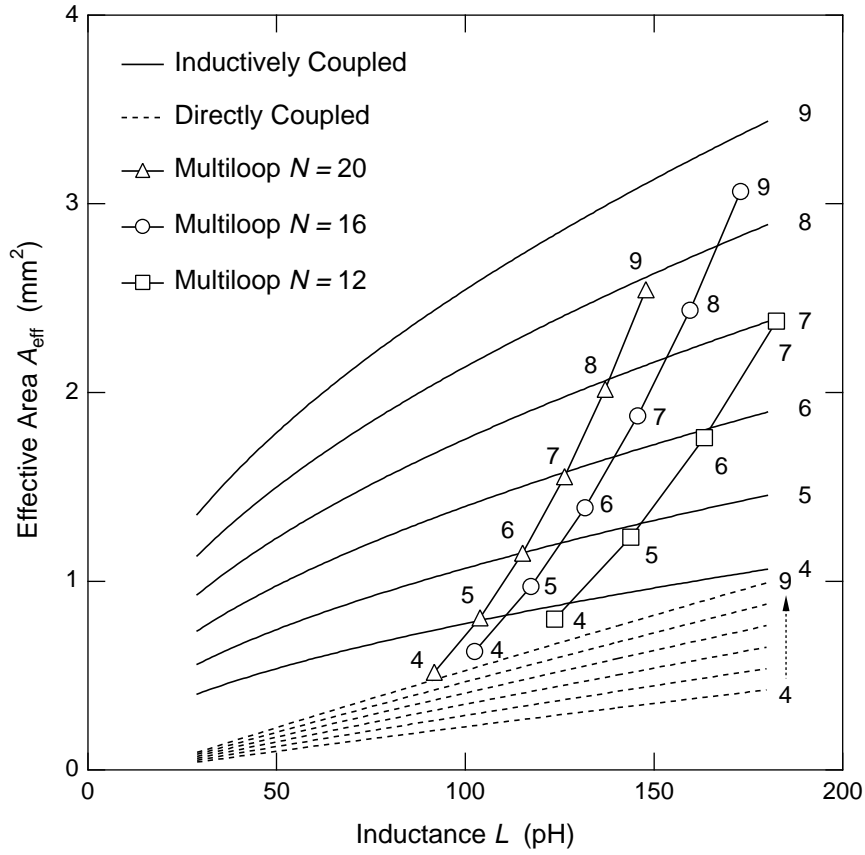


FIGURE 3.8: Attainable effective area depending on the SQUID inductance for inductively coupled, directly coupled, and multiloop devices. The numbers indicate the pickup loop size  $D_p$  in mm. The multiloop data are presented for 3 different numbers of loops.

coupled magnetometers, are only obtained with inductances  $> 100$  pH. Lower inductances require high loop numbers, so that the fraction of the parasitic spoke area in (3.22) gets adversely increased. For a HTS multiloop magnetometer, the loop number  $N = 16$  yields a good compromise between a reasonable effective area and a sufficiently low SQUID inductance. A pickup loop size of  $D_p = 7$  mm results in an effective area of  $1.9 \text{ mm}^2$  and a SQUID inductance of 146 pH. About one half of this inductance is due to the spokes and one third due to the polygonal pickup loop. For each point in Fig. 3.8, pickup loop width and spoke width have been adjusted to yield the minimum of the ratio  $L/A_{\text{eff}}$ . This optimization procedure will be treated in more detail in Section 5.1.3.

## 4 Experimental

This chapter describes the preparation processes used for the fabrication of multilayer and single-layer magnetometers based on the superconductor  $\text{YBa}_2\text{Cu}_3\text{O}_7$ . Since the work described in this thesis was carried out in two laboratories, different methods were used for the thin-film deposition. The multilayer devices based on step-edge Josephson junctions were prepared using rf magnetron sputtering, whereas pulsed laser deposition was used for the single-layer magnetometers on bicrystal substrates. Both methods are well established since many years, and the distinction presented here was not driven by any technological considerations. A more detailed review on the various processes commonly involved in the preparation of HTS multilayer magnetometers is given by Wellstood *et al.* [119]. The chapter closes with a brief description of the measurement techniques used for measuring the dc characteristics and noise spectra of the devices.

### 4.1 Preparation of multilayer magnetometers with step-edge Josephson junctions

The multilayer magnetometers described in this thesis are based on two superconducting  $\text{YBa}_2\text{Cu}_3\text{O}_7$  layers and an intermediate  $\text{SrTiO}_3$  layer for their insulation. Both types of thin-films are deposited by off-axis rf magnetron sputtering. On optimized sputtering conditions, the transition temperature of unpatterned  $\text{YBa}_2\text{Cu}_3\text{O}_7$  thin-films is 88 K with a critical current density of about  $2 \times 10^6 \text{ A/cm}^2$ . Usually, the films are smooth and without outgrows or impurity phases. The fabrication process of a multilayer device involves four thin-film depositions and four photolithographic steps [120].

First, a layer of about 150 nm  $\text{YBa}_2\text{Cu}_3\text{O}_7$  is *in situ* deposited together with a thin cap-layer of 25 nm  $\text{SrTiO}_3$  on top of it. Usually, the upper  $\text{YBa}_2\text{Cu}_3\text{O}_7$  layer in a multi-level device is of poorer quality, due to the complex growth mechanism and many involved preparation steps. This introduces weak pinning centers for flux vortices and thus sources of low-frequency noise [88, 89]. For this reason, the large superconducting areas of the pickup loops are prepared from the bottom  $\text{YBa}_2\text{Cu}_3\text{O}_7$  film directly grown on the sub-

strate. The cap-layer protects this film during the subsequent photolithographic process and improves the epitaxial growth of the 200 nm  $\text{SrTiO}_3$  insulating layer deposited on top of it. The step-edge and the vias to the bottom  $\text{YBa}_2\text{Cu}_3\text{O}_7$  layer are patterned in two successive photolithographic steps into the insulating layer. The vias come in the second place, since they are more sensitive to environmental influences than the step. The  $3\text{ }\mu\text{m}$  wide Josephson junctions would degrade during subsequent film depositions. Therefore, they are patterned from the upper  $\text{YBa}_2\text{Cu}_3\text{O}_7$  film deposited at last. Furthermore, the input coil of the inductively coupled device and the central interconnection of the pickup loops in the multiloop magnetometer are patterned from the top superconducting layer.

The patterning of the thin-films is done by conventional photolithography and Ar-ion beam etching. The ion beam has an energy of 350–400 eV and a current density of about  $3\text{ mA/cm}^2$ . To prevent the sample from overheating during the etch process, it is watercooled and the ion-beam is pulsed. The endpoint detection is done visually with a microscope, watching the color change of the luminescence sent out by the excited sputtered material near the substrate surface ( $\text{YBa}_2\text{Cu}_3\text{O}_7$ : green,  $\text{SrTiO}_3$ : blue). The photomasks are designed in a way that a slight overetching does not affect the device operation. Two different mask steps are necessary to pattern the step-edge and the via contacts. In order to avoid large-angle grain boundaries at the crossovers and to increase the geometrical cross-sections along the  $\text{YBa}_2\text{Cu}_3\text{O}_7$  *ab*-planes for high current densities in the vias, flat angles are needed at the edges of these structures. This is achieved by a combination of resist bakeout on a hotplate and etching under flat incidence [120]. On the contrary, the step-edge has to be very steep to form a suitable grain boundary for a Josephson junction. A fixed vertical incidence of the ion beam leads to a strong redeposition of the sputtered material at the step-edge, yielding a rough edge and a poor quality of the Josephson junctions. It was found that the redeposition can be prevented, when the ion beam is swept by  $\pm 20^\circ$  along the step-edge. To obtain low-ohmic contacts, the contact pads are *in situ* covered with about 50 nm Ag by dc sputtering through a shadow mask right after a short cleaning of the surface by Ar-ion beam etching. The photoresist is removed with a thoroughly cleaning procedure of rinsings in acetone and propanol in an ultrasonic bath.

The thin-film deposition is done by off-axis rf magnetron sputtering in an  $\text{Ar}/\text{O}_2$  atmosphere. The  $\text{YBa}_2\text{Cu}_3\text{O}_7$  films are deposited at the temperature  $785^\circ\text{C}$  and 100 W rf power. The background pressure is 30 Pa at a partial pressure ratio  $p_{\text{Ar}}/p_{\text{O}_2} = 2 : 1$ . The conditions for the  $\text{SrTiO}_3$  deposition are:  $T = 750^\circ\text{C}$ ,  $p = 10\text{ Pa}$ ,  $p_{\text{Ar}}/p_{\text{O}_2} = 1 : 1$  and  $P_{\text{rf}} = 200\text{ W}$ . After the deposition, the device is cooled with a defined temperature profile in 500 mbar  $\text{O}_2$ . During the process, the substrate is glued to the heater with silver paste to obtain a good and reproducible thermal contact.



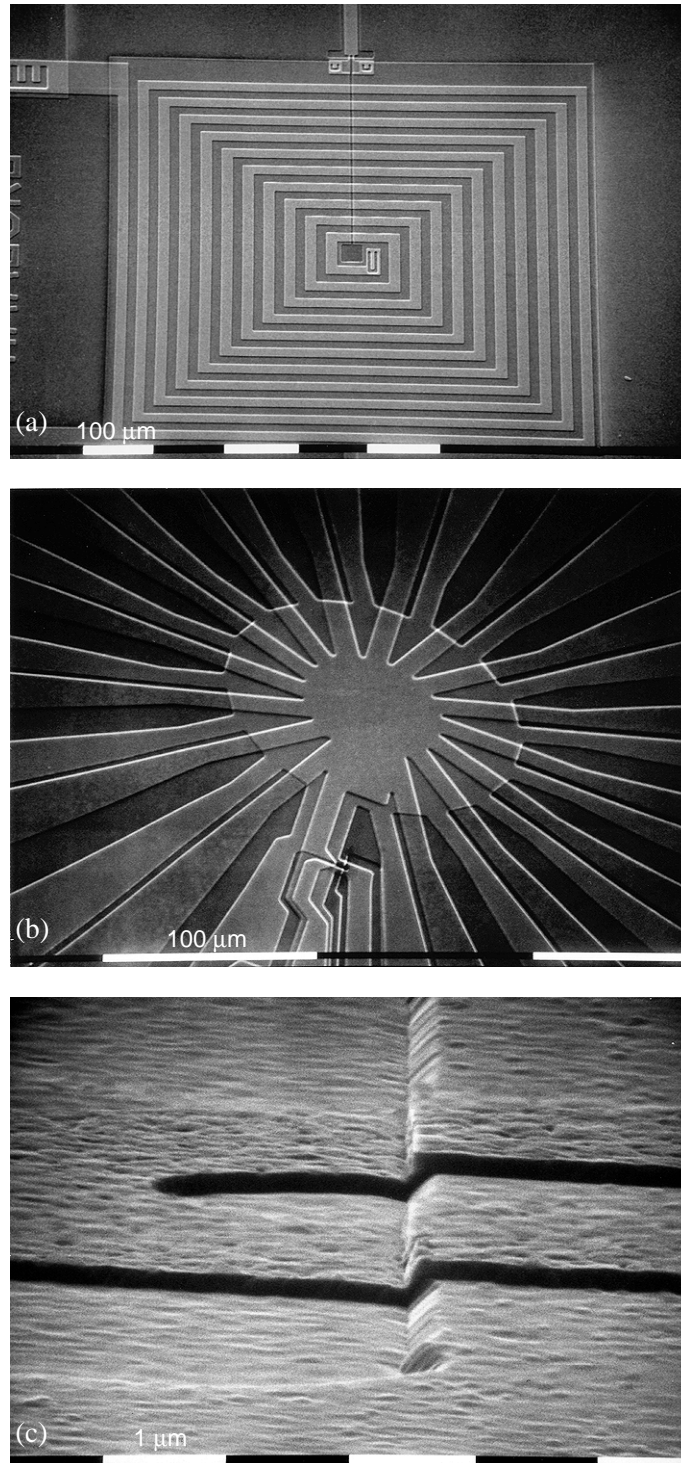


FIGURE 4.1: Scanning Electron Microscope images of multilayer devices: (a) Square washer of an inductively coupled magnetometer with integrated input coil. (b) Central part of a multiloop magnetometer including the step-edge Josephson junctions. (c) Step-edge Josephson junctions of a multiloop magnetometer.

Figure 4.1 shows Scanning Electron Microscopy (SEM) images of different multilayer magnetometers. In Fig. 4.1(a), the square washer of an inductively coupled magnetometer can be seen. Clearly visible is the small *via* that connects the innermost turn of the input coil to the washer. The connection of the outermost turn to the input loop is partly shown in the upper left. Two further vias in the upper middle connect the Josephson junctions in the top layer with the square washer in the bottom layer. Figure 4.1(b) shows the central overlap region of a multiloop magnetometer where all loops are connected. One side of the loops is connected in the bottom layer and the other one in the top layer. For  $N$  loops at least  $N$  *vias* are required, which cannot be seen in the picture. Also visible are the Josephson junctions and their leads. Figure 4.1(c) shows the two step-edge Josephson junctions of a multiloop magnetometer. All films are smooth and without outgrows.

## 4.2 Preparation of single-layer magnetometers with bicrystal Josephson junctions

A comprehensive survey on the pulsed laser deposition process and preparation methods used for the single-layer bicrystal devices is given by Heinsohn *et al.* [121] and Subke *et al.* [61, 122, 123]. Therefore, this process is only briefly summarized in the following. Only one  $\text{YBa}_2\text{Cu}_3\text{O}_7$  deposition step is involved, since only single-layer devices have been prepared on bicrystal substrates.

The  $\text{YBa}_2\text{Cu}_3\text{O}_7$  thin-film is deposited, using a 248 nm KrF Excimer laser with a pulse rate of 3 Hz and a pulse energy adjusted to about 1 J. The energy density at the surface of the  $\text{YBa}_2\text{Cu}_3\text{O}_7$  target is about  $2 \text{ J/cm}^2$ . For the target, a stoichiometric polycrystalline pellet with a diameter of 20 mm is used. It is prepared from the powdery precursors by a calcination and sintering process, which is also described in [61] in detail. The substrate is glued to the heater with silver paste and its temperature of about  $815^\circ\text{C}$  is controlled contactless using a pyrometer. The deposition takes place in a background pressure of 8 Pa  $\text{O}_2$ . After the deposition, the recipient is flooded with  $\text{O}_2$  to normal pressure, and the substrate is kept at about  $500^\circ\text{C}$  for 120 minutes before it is cooled to room temperature. Typical values for the critical temperature and critical current density are  $T_c = 89 \text{ K}$  and  $J_c > 10^6 \text{ A/cm}^2$ , respectively.

The bicrystal line is not visible under a microscope, so it must be marked to allow the adjustment of the photomask. This is done with 5% hydrofluoric acid (HF) at the substrate border after covering the rest of the substrate surface with a protective layer of photoresist. HF preferably etches  $\text{SrTiO}_3$  at lattice defects and grain boundaries, therefore the grain boundary line becomes visible. Unfortunately,  $\text{YBa}_2\text{Cu}_3\text{O}_7$  is not

etched by HF and must be removed with 2.5% diluted nitric acid ( $\text{HNO}_3$ ), beforehand. After this procedure the photoresist mask can be adjusted, so that the microbridges for the Josephson junctions cross the grain boundary. Finally, the magnetometer device is patterned by Ar-ion etching in a parallel-plate reactor. In contrast to ion-beam etching, the etch process in a parallel-plate reactor is highly isotropic, so that steep edges cannot be obtained. However, this is no disadvantage for the preparation of bicrystal or ramp-edge Josephson junctions. The Ar-plasma in the parallel-plate reactor cannot be pulsed and a large amount of heat is transferred to the photoresist, despite a cooled base plate. In addition, much UV radiation is present during the etch process. Both leads to a strong cross-polymerization of the photoresist, which prevents its removal by acetone or propanol. For multilayer devices, it is absolutely necessary that these residues are removed before depositing the subsequent layer. This is therefore routinely done with a treatment in an oxygen plasma. Since the plasma treatment has also a beneficial effect on the critical current density of the  $\text{YBa}_2\text{Cu}_3\text{O}_7$  films, it is performed after each  $\text{YBa}_2\text{Cu}_3\text{O}_7$  deposition.

### 4.3 Measurement techniques

For optimum temperature stability, almost all measurements are made in liquid nitrogen at 77 K. Temperature dependent measurements are either made in a helium-flow cryostat or a heatable can in a liquid-helium dewar. In all cases, the device is shielded against ambient magnetic fields at least by one double-walled Cryoperm shield.

The dc characteristics of the devices are measured using a standard low-noise operational amplifier with an input voltage noise of  $\sqrt{S_V} = 4 \text{ nV}/\sqrt{\text{Hz}}$  and an amplification of 1000. A bias current up to 10 mA is supplied by a low-noise current source which can be modulated by a delta generator. For differential measurements with a lock-in amplifier a sine wave may be added. Noise measurements on single Josephson junctions are made with a transformer-coupled low-noise amplifier with a white input noise level of about  $\sqrt{S_V} = 150 \text{ pV}/\sqrt{\text{Hz}}$  [44]. Magnetic flux in the sample is generated by a small coil, which is supplied by the same type of current source. The coil has been calibrated against a Helmholtz coil in the magnetically shielded room of Philips Hamburg. The magnetic flux density inside the Helmholtz coil was checked with a commercial fluxgate sensor and the measured value differed by less than 1 % from the calculated value. The calibration was confirmed by further measurements at the PTB Berlin.

SQUIDs and SQUID magnetometers are usually operated with a so-called flux-locked loop (FLL) electronics, where the SQUID signal is integrated and fed back to the SQUID via a resistor  $R_f$  and a coil  $L_f$ . In this feedback control, the SQUID is used as a null-detector of magnetic flux, and the sensor's linearity range is enhanced from fractions of

a flux quantum up to several hundreds of flux quanta. The voltage across the feedback resistor  $R_f$  is proportional to the signal flux  $\Phi_{\text{sig}}$ . Noise spectra are recorded with a Fast Fourier Transform (FFT) signal analyzer at the output of the FLL electronics. In practice, there are two main variations of SQUID FLL electronics: The FLL circuit with flux modulation and lock-in detection, and the directly coupled FLL electronics. In the first type, the flux in the SQUID is modulated by  $\Phi_0/2$  between the points of maximum transfer function in the flux-voltage characteristic. The signal is obtained after demodulation and integration. Due to the modulation method, a resonant tank circuit or step-up transformer can be used to increase the voltage signal at the preamplifier input. Thus, even SQUIDS with a small voltage modulation can be measured with negligible noise contribution from the preamplifier. The low-frequency properties of the preamplifier's input stage like temperature drift,  $1/f$  noise, or offset voltage do not affect the measured signal, since this is mixed up to higher frequencies. Figure 4.2(a) shows a simplified schematic of a FLL electronics with flux modulation. The flux modulation scheme is depicted in Fig. 4.2(b). In the directly coupled FLL electronics (Fig. 4.2(c)), the input stage is dc coupled to the SQUID. Since no tank circuit or transformer is used, an ultra low-noise preamplifier with excellent low-frequency properties is necessary [124]. State-of-the-art components still require SQUIDS with a voltage modulation of more than about  $5\text{ }\mu\text{V}$ . The main advantages of this electronics are the very large sensor bandwidth, which may easily reach several MHz [125,126], and the possibility of additional positive feedback (APF) [100]. With APF, the slope on one side of the  $V$ - $\Phi$  curve is increased to obtain an enhanced transfer function. This is done with only two additional passive components, the resistor  $R_a$  and the coil  $L_a$ , across the SQUID. The APF method cannot be applied with flux modulation, because the modulation between both operation points on opposite sides of the  $V$ - $\Phi$  curve would average out the APF effect. The first measurements employing the APF method with HTS magnetometers are described in Section 5.2. The simplicity of this electronics enables very compact multichannel systems at low costs. In both types of electronics an additional bias current modulation scheme can be used to suppress the  $1/f$  noise component from critical current fluctuations in the Josephson junctions [90,92,127,128]. A comprehensive survey on the fundamentals of SQUID readout electronics is given in [129].

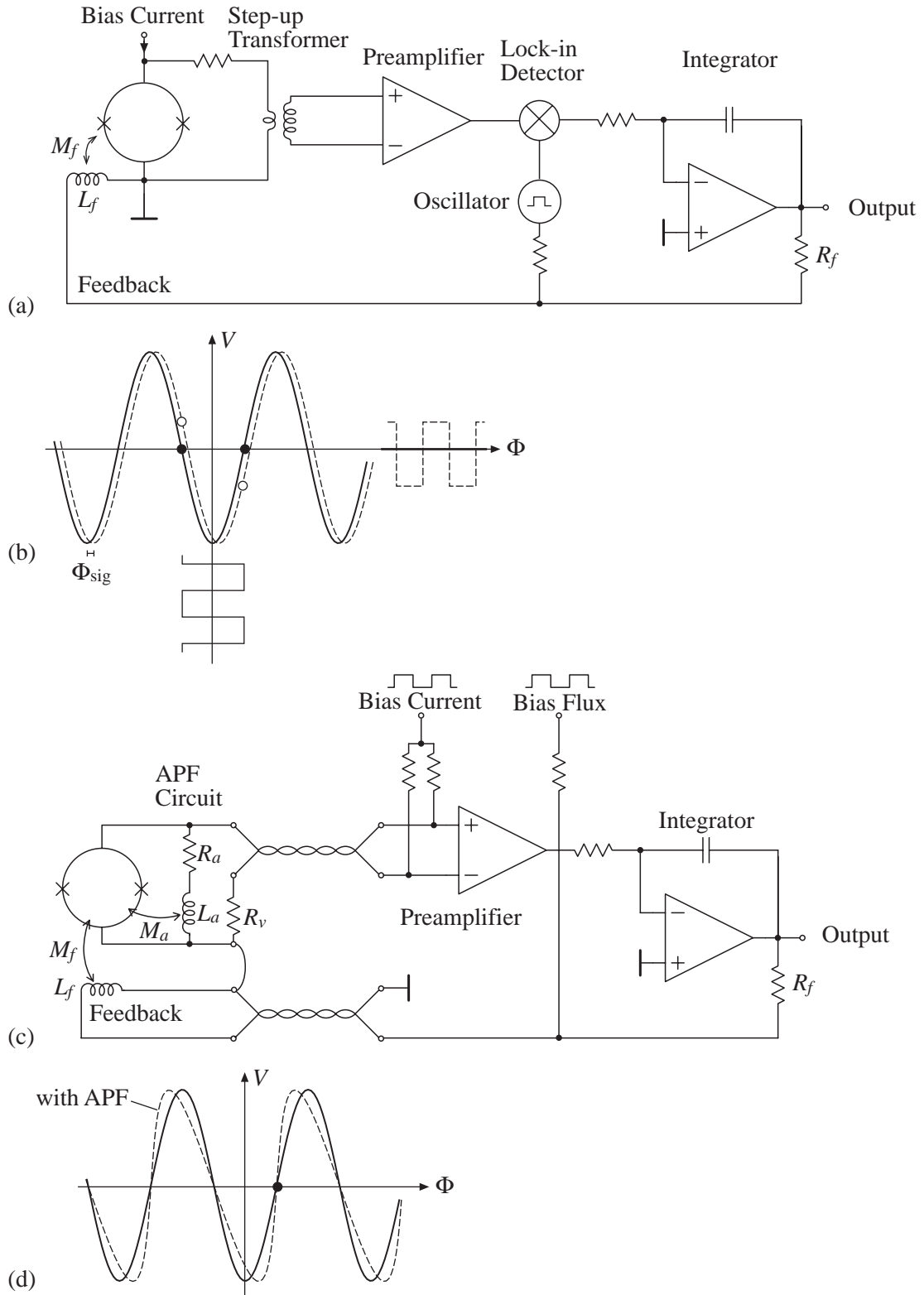


FIGURE 4.2: (a) Schematic of a flux-locked loop (FLL) circuit with flux modulation and lock-in detection. (b) Principle of flux modulation. The dashed curve is shifted by the external signal  $\Phi_{\text{sig}}$ . (c) Directly coupled FLL circuit with APF components  $R_a$  and  $L_a$ . (d) Effect of the APF circuit on the flux-voltage characteristic.



## 5 Integrated dc SQUID magnetometers

This chapter describes the geometrical parameters and electrical characteristics of the fabricated samples of directly coupled, inductively coupled, and multiloop magnetometers. Due to the less demanding single-layer preparation process for directly coupled magnetometers, some statistical information is obtained about their parameter dependencies. Some attention is paid to microwave resonances in the magnetometer structures, which may seriously deteriorate the magnetometer performance. Furthermore, the temperature dependence of the effective area of all three magnetometer types is discussed.

The publication [P3] in Section 5.2 reports the first measurements on HTS SQUID magnetometers employing the APF method combined with bias current modulation. In addition, high quality magnetocardiograms are presented. Further biomagnetic measurements have been made with a miniature hand-held cryostat and an IMPUC magnetometer. They are described in publication [P4] of Section 5.3. In Section 5.4, measurements made in unshielded environment and methods for ambient noise rejection are reviewed. The following sections refer to the problem of increased low-frequency noise in field-cooled HTS magnetometers. The publication [P7] of Section 5.5.1 reports noise measurements on two multilayer magnetometers in various cooling fields, and Section 5.5.2 describes a method for enhancing the noise performance and linearity of field-cooled directly coupled magnetometers.

### 5.1 Samples

#### 5.1.1 Directly coupled magnetometers

Directly coupled magnetometers have been fabricated from single epitaxial layers of  $\text{YBa}_2\text{Cu}_3\text{O}_7$ . The films are prepared by pulsed laser deposition on symmetrical (100)  $\text{SrTiO}_3$  bicrystal substrates with  $24^\circ$  misorientation angle. Film thicknesses between 100 nm and 150 nm are used. The substrate size is  $10 \times 10 \text{ mm}^2$ .

Figure 5.1 shows the magnetometer layout and a photograph of the area around the SQUID loop. The layout is similar to the one introduced by Lee *et al.*, having a square

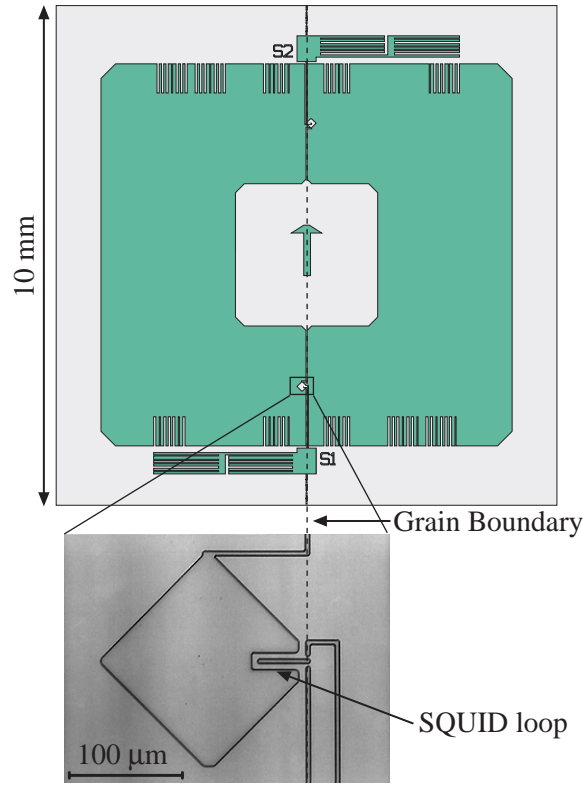


FIGURE 5.1: (a) Layout of the directly coupled magnetometer. (b) Photograph of the central part around the SQUID loop.

washer type pickup loop with the outer dimensions  $8.6 \times 8 \text{ mm}^2$  and an inner hole size of  $3 \times 3 \text{ mm}^2$ . The width of the Josephson junctions is nominally  $2 \mu\text{m}$ . Three layouts have been used, which mainly differ in the length of the SQUID loop and thus in the SQUID inductance. In each layout, two SQUIDs are connected to the pickup loop, which can be characterized separately. Thus, better device statistics are obtained with less preparation steps, and one can select the SQUID with better performance after a first characterization.

Table 5.1 shows the SQUID loop lengths and the calculated inductances and effective areas for the three different layouts. The inductance values include the kinetic contribution for a film thickness of 120 nm, a critical temperature  $T_c = 88 \text{ K}$  and an operation temperature of 77 K. Figure 5.2 shows experimental results at 77 K for the effective area of several directly coupled SQUID magnetometers in dependence on the SQUID inductance. Although there is a considerable spread among the samples, a good agreement is found with the theoretical prediction calculated from the formulas in Section 3.1. The spread is attributed to variations in the photolithographic process and the film quality. The dimensions of the SQUID loop are not much larger than the best attainable linewidth in the photolithography process ( $1 \mu\text{m}$ ), thus even a slight error in the exposure has a large effect on the linewidth of the SQUID loop and its inductance. Although the kinetic inductance



TABLE 5.1: SQUID loop length and the calculated values of inductance and effective area for the three investigated layouts of directly coupled SQUID magnetometers.

Layout	SQUID length ( $\mu\text{m}$ )	Inductance (pH)	Effective Area ( $\text{mm}^2$ )
DSC1	46	57	0.249
	86	102	0.495
DSC2	126	146	0.737
	146	168	0.855
DSC3	39	49	0.203
	39	49	0.203

has been taken into account using the individual critical temperatures in formulas (2.2) and (3.12), this gives only a rough estimation of the actual values.

Voltage modulation values between  $5\mu\text{V}$  and  $40.5\mu\text{V}$  are obtained. As is discussed in Section 2.6, the voltage modulation strongly depends on the modulation parameter  $\beta_L$ , which is illustrated by Fig. 5.3(a). A strong decrease of the voltage modulation is found for an increasing modulation parameter. As expected, maximum modulation is obtained for low values around  $\beta_L = 1$ . Figure 5.3(b) shows the reduced voltage modulation  $\Delta V/(I_0 R_n)$  as a function of the SQUID inductance and compared to the theory by Enpuku *et al.* [77, 79]. The mean critical current of all investigated samples

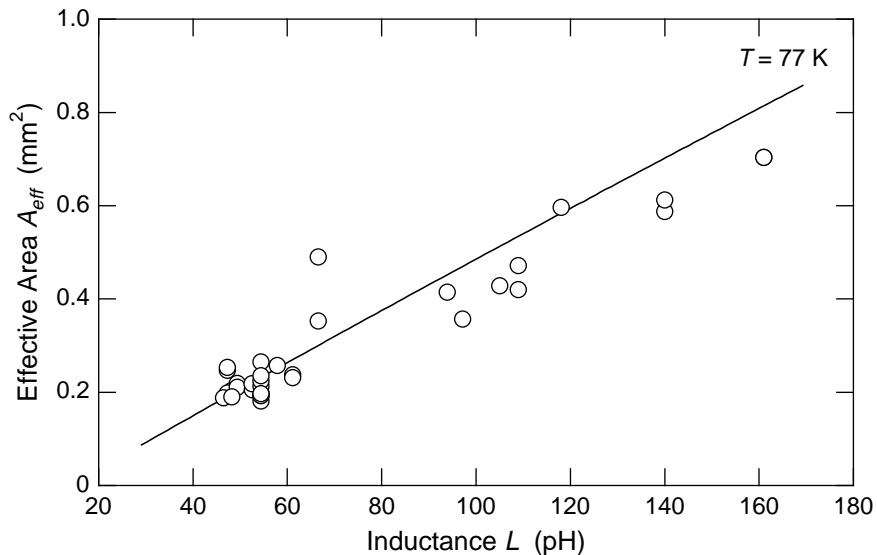


FIGURE 5.2: Effective area of directly coupled magnetometers as a function of the SQUID inductance. The straight line is the calculated dependence for a pickup loop dimension  $D_p = 8.3\text{ mm}$ . The kinetic contributions of the inductances were estimated, using the individual  $T_c$  values of the magnetometers.

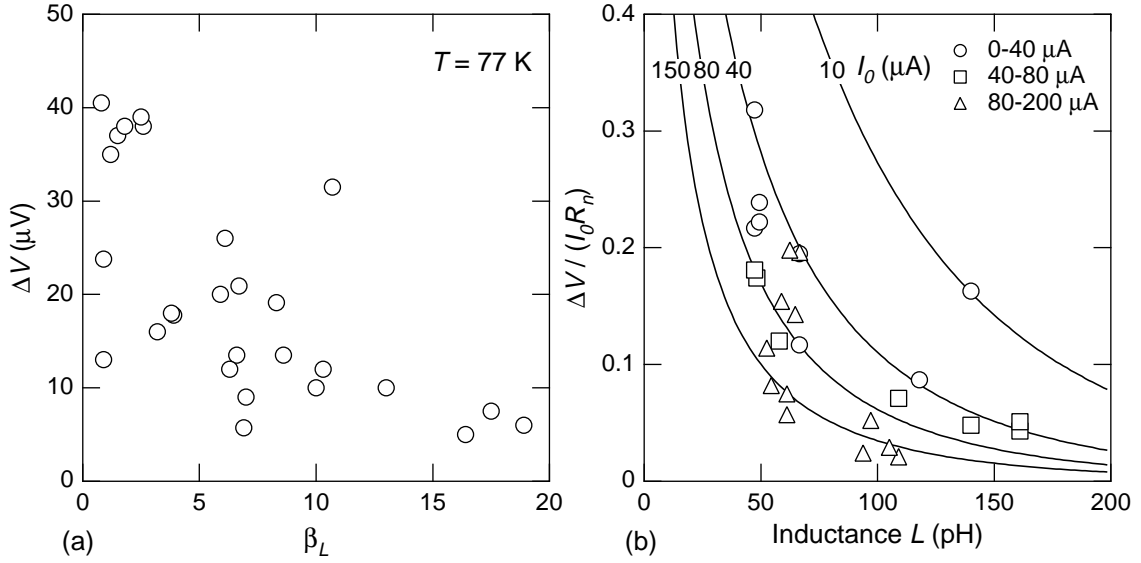


FIGURE 5.3: (a) Voltage modulation of directly coupled SQUID magnetometers as a function of the modulation parameter  $\beta_L$ . (b) Reduced voltage modulation as a function of the SQUID inductance and in comparison to the theory by Enpuku *et al.* (lines) [77]. The different symbols denote the quoted critical current ranges.

is  $84\text{ }\mu\text{A}$ . Since all experimental values of  $\Delta V / (I_0 R_n)$  are scattered around the line for  $I_0 = 80\text{ }\mu\text{A}$ , a good overall agreement between theory and experiment is found. Also the tendency of a higher voltage modulation obtained with lower junction critical currents is reflected. The mean characteristic voltage of the investigated samples is  $I_0 R_n = 175\text{ }\mu\text{V}$  with a standard deviation of  $1\sigma = 45\text{ }\mu\text{V}$ . This is in good agreement with data found in the literature [69, 130]. Higher voltage modulations in the investigated inductance range are expected for smaller critical currents which, however, depend mainly on the quality of the bicrystal grain boundary and can only be controlled by the film thickness and junction width. Since the kinetic inductance contribution becomes adversely large for a film thickness less than about  $100\text{ nm}$ , a reduced junction width is favorable, but limited by the resolution of the photolithography process. A further, but less controllable, way to reduce the critical current is the annealing of the device at an elevated temperature in an oxygen free (e.g. argon) atmosphere. Due to a higher oxygen mobility at grain boundaries, oxygen will leave the thin-film preferably at the Josephson junctions decreasing their critical current. This method has been investigated with a device, which already exhibited a reduced critical current and an increased normal resistance four months after fabrication, presumably due to an improper handling. In Fig. 5.4, the device parameters are depicted after three additional annealing steps at  $200^\circ\text{C}$  in Ar atmosphere (10 min. at  $200^\circ\text{C}$  and 10 min. cool-down). The former tendency was continued with the first annealing step. Besides the characteristic voltage, also the voltage modulation was significantly

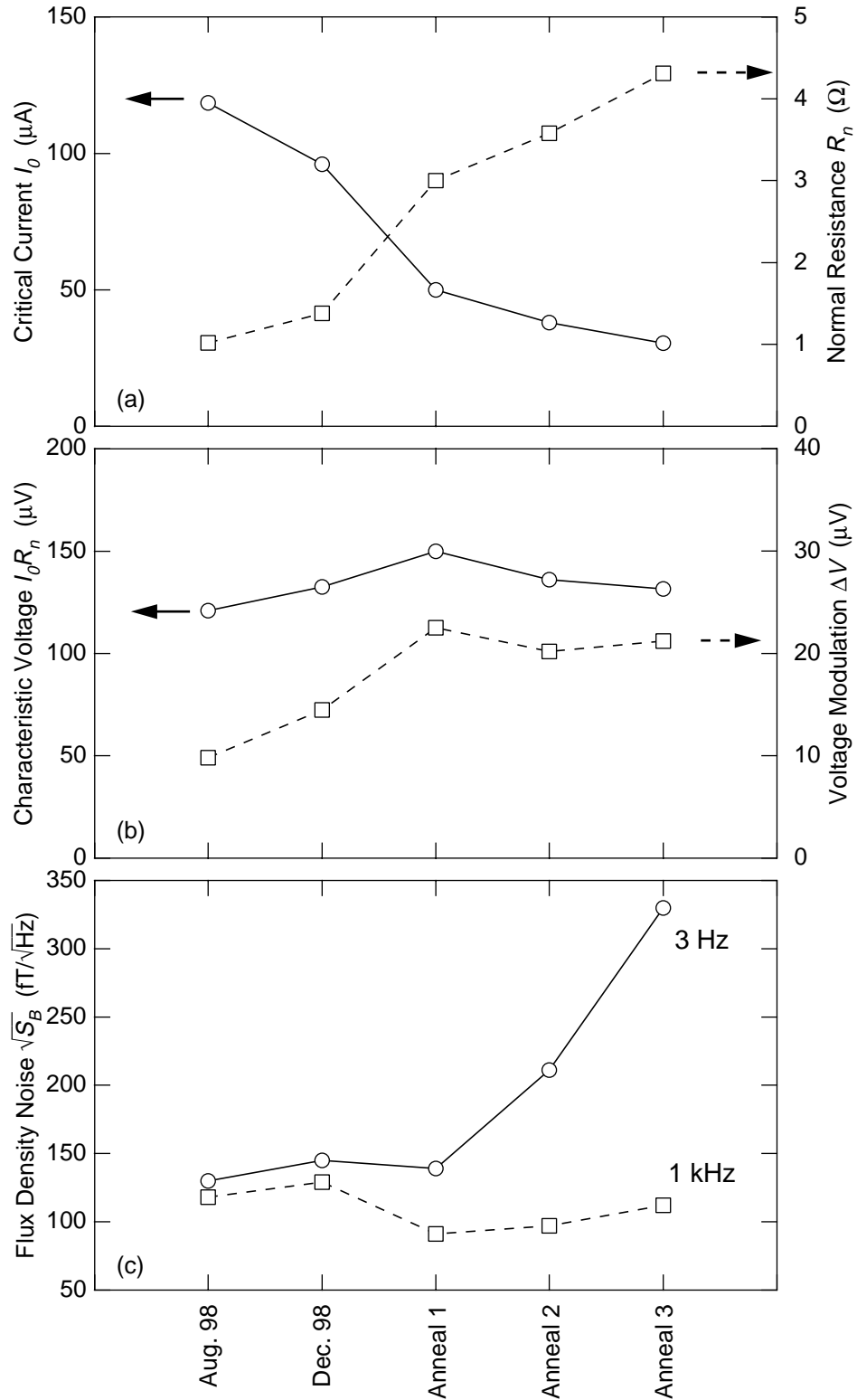


FIGURE 5.4: Change of magnetometer characteristics after four months of handling and after three annealing steps at 200°C in Ar-atmosphere. (a) Critical current and normal resistance, (b) characteristic voltage and voltage modulation, (c) low-frequency and white flux density noise.

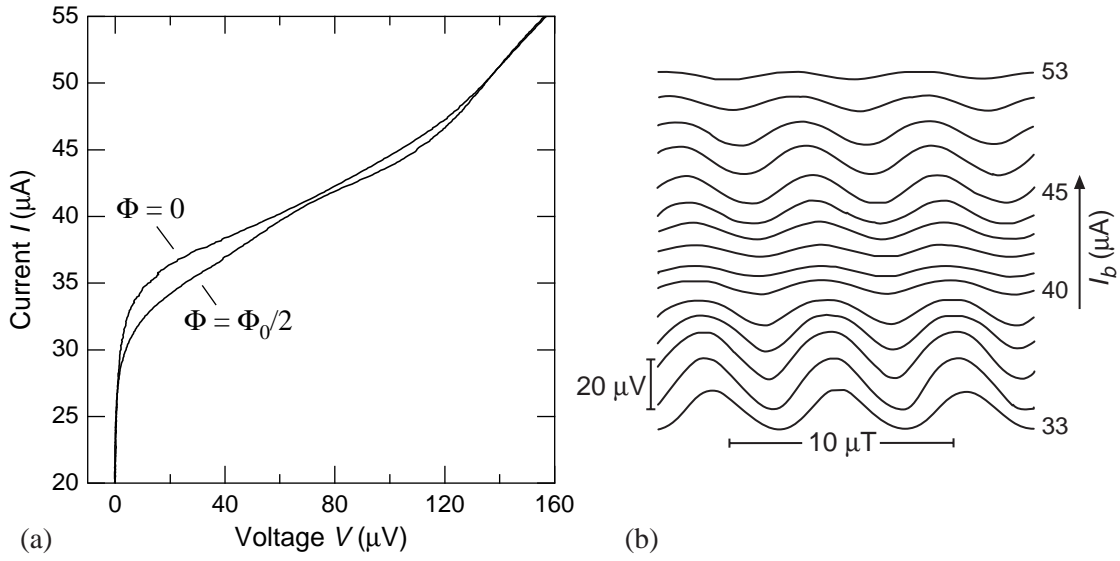


FIGURE 5.5: (a) Current-voltage characteristic with applied flux  $\Phi = 0$  and  $\Phi = \Phi_0/2$  for a directly coupled SQUID magnetometer. (b) Flux-voltage characteristic for the same device at different bias currents  $I_b$ .

increased, yielding a reduced white noise level. However, the second and third annealing steps reduced  $I_0 R_n$  again, and the low-frequency noise became markedly increased. Hence, the superconducting film must have been damaged more seriously. Further investigations on this method should be made to prove, whether the junction characteristics can be controlled in a predictable way.

In Fig. 5.3 can be seen that the values for the voltage modulation exhibit a remarkable spread. The most likely source of the observed large variations are resonances of the current oscillations from the the ac Josephson effect in the SQUID loop. This causes a distortion of the current-voltage characteristic. Figure 5.5(a) depicts the current-voltage characteristic of a directly coupled magnetometer without applied flux and with the applied flux  $\Phi = \Phi_0/2$ , where the critical current is maximally reduced. In the latter case, one observes a broad resonant current increase at around  $76 \mu\text{V}$ , which narrows both branches and leads to a reduced voltage modulation at bias currents around  $42 \mu\text{A}$ , as is depicted in Fig 5.5(b). Even a crossing of both branches is possible, which would lead to zero voltage modulation at this point. For the given device, the total length of the stripline resonator is  $l_r = 115 \mu\text{m}$ . Assuming a dielectric constant of  $\epsilon_r = 2000$  for the  $\text{SrTiO}_3$  substrate, the fundamental resonance frequency becomes  $f_0 = 41 \text{ GHz}$  and the resonance voltage is  $V_0 = 85 \mu\text{V}$ , which is in reasonable agreement with the experimental value. The deviation is attributed to the rough estimation of  $\epsilon_r$  and to the influence of the current leads connecting the SQUID loop with the pickup loop. Similar distortions of the current-voltage characteristic have been observed in almost all fabricated devices.

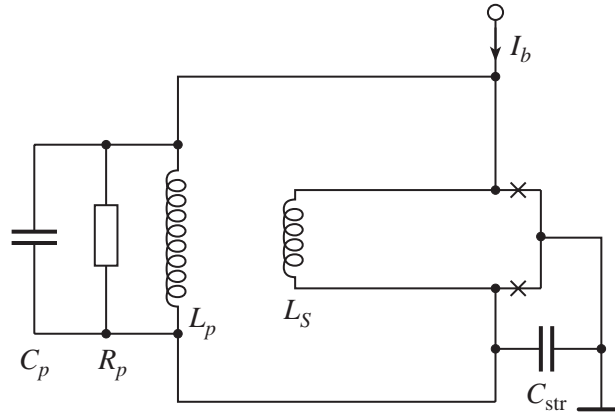


FIGURE 5.6: A simplified circuit model of a directly coupled SQUID magnetometer taking into account the parasitic capacitances  $C_p$  and  $C_{\text{str}}$ .  $R_p$  represents the rf loss of  $C_p$  and  $L_S$  is the SQUID inductance.

A consequence of microwave resonances in the pickup loop are distortions of the flux-voltage characteristic. Figure 5.6 shows the equivalent circuit of a parallel  $L_p$ - $C_p$ - $R_p$  resonant circuit connected to the SQUID inductance  $L_S$ .  $L_p$  is the pickup loop inductance,  $C_p$  the stray capacitance across the pickup loop, and  $R_p$  represents the rf loss of the substrate. It has been shown theoretically and in extensive numerical simulations that resonances in the input circuit of a SQUID magnetometer can cause a distortion of the flux-voltage curve, when there are stray capacitances forming additional capacitive current paths from the input circuit to the current source. The extra currents produce additional magnetic flux in the SQUID inductance and cause a capacitive feedback [130, 131]. In Fig. 5.6,  $C_{\text{str}}$  schematically indicates such a capacitive current path between pickup loop and current source. Figure 5.7 depicts the flux-voltage characteristics of two SQUIDs with identical layout, symmetrically connected to the same pickup loop. It is found that the  $V$ - $\Phi$  curves for SQUID S1 are smooth and nearly sinusoidal, whereas the curves for SQUID S2 are strongly distorted on one side. Since the corresponding parasitic impedances are the same for both SQUIDs, the strength of the resonances must severely depend on the SQUID parameters  $I_0$  and  $R_n$ . These are  $I_0 = 17 \mu\text{A}$  and  $R_n = 7.5 \Omega$  for S1 and  $I_0 = 26 \mu\text{A}$  and  $R_n = 6.2 \Omega$  for S2. It is correspondingly found for all types of integrated SQUID magnetometers, that devices with higher critical currents exhibit more pronounced distortions of their  $V$ - $\Phi$  curves than comparable devices with lower critical currents, but higher  $R_n$  values. There is not yet a simple model which predicts the amount of distortion from the magnetometer parameters, thus numerical simulations taking into account the parasitic parameters have to be done. Numerical simulations by Enpuku *et al.* [17, 131] confirm the strong influence of the junction parameters that is found above.

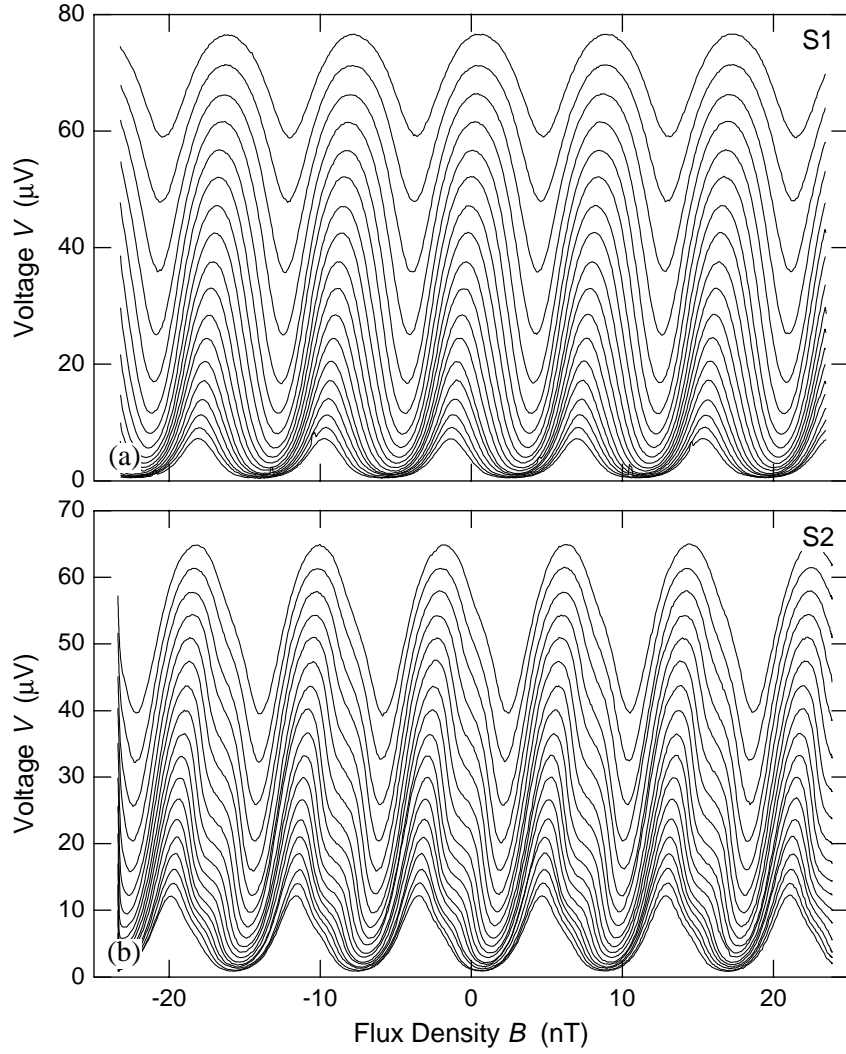


FIGURE 5.7: Voltage modulation versus applied magnetic field at 77 K for two SQUIDs (S1, S2) directly coupled to the same pickup loop. The curves have been recorded at equidistant bias currents  $I_b = 34 \dots 51 \mu\text{A}$  for S1 and  $I_b = 54 \dots 67 \mu\text{A}$  for S2. The maximum voltage modulations are  $\Delta V = 40.5 \mu\text{V}$  and  $\Delta V = 35.0 \mu\text{V}$  for S1 and S2, respectively. The modulation curves for S2 exhibit distortions on one side, due to resonances of the Josephson oscillations in the pickup loop. The resonances are more damped, when the pickup loop is operated with S1.

An asymmetric flux-voltage characteristic has an adverse effect on noise measurements, if one uses the flux modulation technique. Because of the reduced transfer coefficients at one operating point, a smaller SQUID signal is obtained after integration in the FLL circuit. As a consequence, a higher noise level is measured when compared to a similar device with symmetric flux-voltage curve. When a resonant curve is present, it is therefore favorable to use a directly coupled FLL electronics with only a single point of operation that can be set to the one with maximum transfer coefficient.

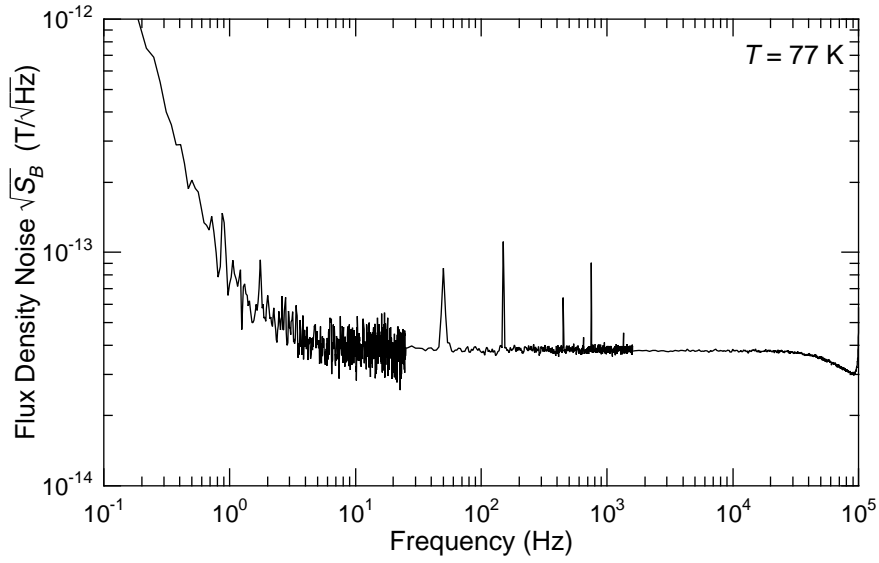


FIGURE 5.8: Flux density noise spectrum of a directly coupled magnetometer, measured in a shielded room. The white noise level is  $\sqrt{S_B} = 38 \text{ fT}/\sqrt{\text{Hz}}$  at 1 kHz and the low frequency noise is  $\sqrt{S_B} = 80 \text{ fT}/\sqrt{\text{Hz}}$  at 1 Hz. The spectrum has been measured with bias reversal.

Figure 5.8 shows a flux density noise spectrum for a directly coupled SQUID magnetometer. It has been recorded at  $T = 77 \text{ K}$  in zero field in the Berlin Magnetically Shielded Room (BMSR) at the PTB Berlin, using a directly coupled FLL electronics with 100 kHz bias current reversal. At 1 kHz a white noise level of  $\sqrt{S_B} = 38 \text{ fT}/\sqrt{\text{Hz}}$  including the preamplifier noise is obtained. The low-frequency noise is  $\sqrt{S_B} = 80 \text{ fT}/\sqrt{\text{Hz}}$  at 1 Hz, which already includes a significant amount of ambient noise. The  $1/f$  corner frequency is 4.5 Hz, and the 3 dB bandwidth about 100 kHz. The device is the same as SQUID S1 of Fig. 5.7(a), having a voltage modulation of  $\Delta V = 40.5 \mu\text{V}$ . The calculated SQUID inductance is  $L = 47 \text{ pH}$  and the critical current is  $I_0 = 17 \mu\text{A}$ , yielding a nearly optimum modulation parameter  $\beta_L = 0.8$ . Figure 5.9 summarizes the measured white flux noise values for all fabricated directly coupled SQUID magnetometers as a function of their inductance. A clear increase in flux noise is found for increasing SQUID inductance, which could be well fitted with a linear dependence. Typical flux noise values for 50 pH SQUIDs are below  $10 \mu\Phi_0/\sqrt{\text{Hz}}$ . However, they are more than one order of magnitude higher than the values calculated from (2.25) and (2.28). Furthermore, the values fit less satisfying to these dependencies than to a linear function of  $L$ . As a consequence, no optimum inductance value can be derived from these data for a lowest flux density noise level, since both effective area and flux noise depend linearly on  $L$ . The large difference between the calculated noise level and the experimental results has already been noticed by Enpuku *et al.* [78] and is comprehensively discussed by Koelle *et al.* [80]. No systematic trends have been found as functions of the SQUID parameters. The discrepancies may be

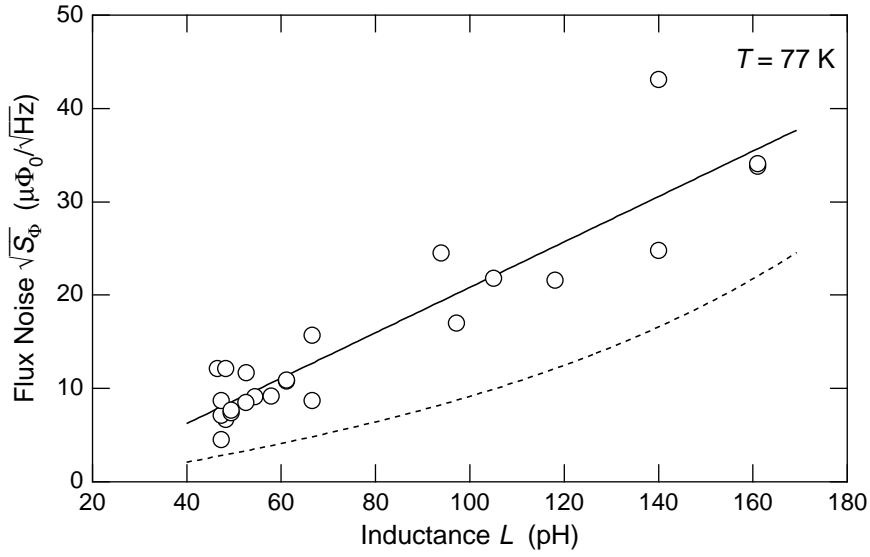


FIGURE 5.9: White flux noise of directly coupled magnetometers as a function of the SQUID inductance. The straight line is a linear fit to the data. The dashed line has been calculated according to the Eqs. (2.25) and (2.28). It already includes the factor  $\times 10$  suggested by Enpuku *et al.* in Ref. [78].

attributed to imperfect junctions, wrongly estimated parameters, or what is most likely in the present case, the microwave resonances discussed above. Furthermore, some amount of excess noise from environmental sources and the FLL electronics cannot be ruled out.

### 5.1.2 Inductively coupled magnetometers

A schematic representation of an inductively coupled magnetometer has been given in Fig. 3.6. The actual layout includes two square washers, each with a monolithically integrated multiturn input coil in the top superconducting layer. Both input coils are individually shunted and connected to the same pickup loop of nearly substrate size. Since the shunt acts as a small pickup loop, both SQUIDs can first be characterized at reduced sensitivity. By measuring the effective area of the shunted magnetometer, one can find out, whether the input coil functions properly. Then, the SQUID with better performance is coupled to the full-size pickup loop by scribing the respective shunt. In all cases, opening the shunt reduced the voltage modulation of the SQUID. This is attributed to an inductance increase of the SQUID washer according to (3.16) [117].

Figure 5.10 displays a microscope image of the square washer of an inductively coupled magnetometer with integrated input coil and an intact shunt. The geometrical parameters of the inductively coupled magnetometer are given in Table 5.2. The pickup loop is not quadratic, but has two indentations for the SQUIDs and the bond pads. A practical pickup loop area  $A_p = 54 \text{ mm}^2$  is estimated from the geometrical mean of the outer and





FIGURE 5.10: Microscope image of the square washer of an inductively coupled magnetometer with a multitrans input coil integrated in the top superconducting layer. The sidelength of the square washer is  $700\ \mu\text{m}$ . The upper part of the picture shows the superconducting shunt.

inner area of the pickup loop, according to (3.14). The calculated inductance of the pickup loop is  $L_p = 15\ \text{nH}$ . Following the equations in Section 3.2, the inductances  $L_h = 48\ \text{pH}$  and  $L_{sl} = 92\ \text{pH}$  are calculated for the washer hole and slit, respectively. Thus, the total inductance of the bare SQUID washer is  $L = 140\ \text{pH}$ . With (3.20) and (3.21), an input coil inductance of  $L_i = 17\ \text{nH}$  is calculated, yielding a good inductance match between pickup loop and input coil. A coupling constant  $k = 0.84$  has been derived from the measurement of the mutual inductance between the input coil and the SQUID washer at  $T = 4.2\ \text{K}$  [132]. Using this value, a screened SQUID inductance  $L' = 88\ \text{pH}$  is obtained with (3.16). The calculation of the effective area with (3.19) yields  $A_{\text{eff}} = 1.73\ \text{mm}^2$ .

TABLE 5.2: Geometrical parameters of the inductively coupled SQUID magnetometer.

Washer sidelength	$l$	700	$\mu\text{m}$
Washer hole sidelength	$d$	30	$\mu\text{m}$
Washer slitlength	$l_s$	335	$\mu\text{m}$
Washer slitwidth	$w_s$	2.5	$\mu\text{m}$
Pickup loop width	$w_p$	0.6	mm
Pickup loop sidelength	$D_p$	8.8	mm
Number of input coil turns	$n$	$10\frac{1}{2}$	
Width of input coil	$b$	16	$\mu\text{m}$

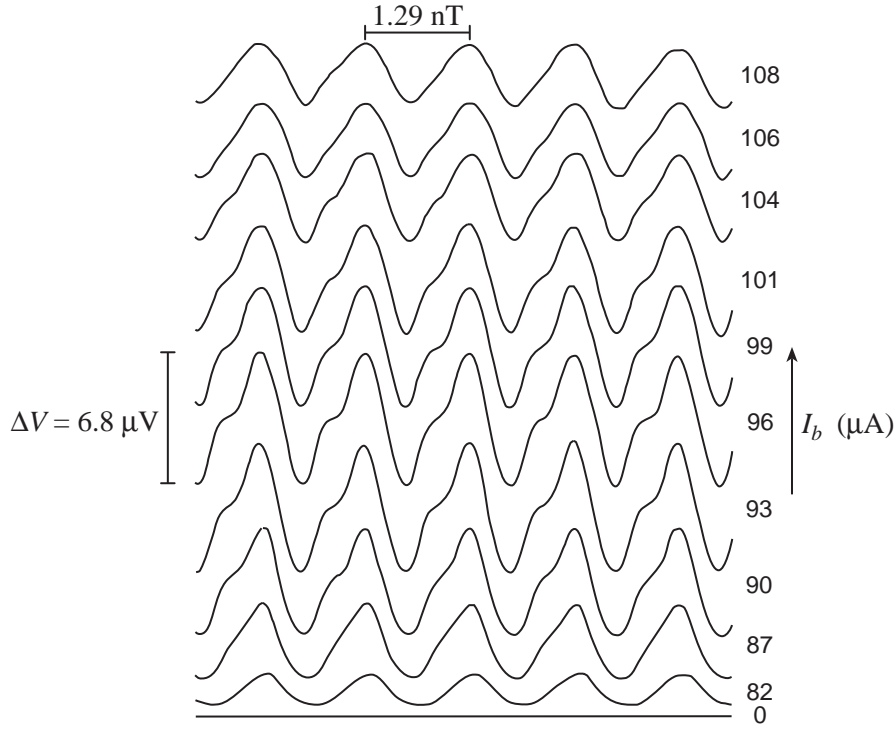


FIGURE 5.11: Voltage versus flux curves at different bias currents for an inductively coupled SQUID magnetometer at  $T = 77$  K. The curves show a pronounced distortion on the positive slope due to microwave resonances in the input circuit of the device.

Figure 5.11 shows the voltage modulation of an inductively coupled magnetometer with step-edge Josephson junctions at  $T = 77$  K. A maximum modulation of  $\Delta V = 6.8 \mu\text{V}$  is obtained at the bias current  $I_b = 96 \mu\text{A}$ . The junction's critical current and normal resistance of this sample are  $I_0 = 42 \mu\text{A}$  and  $R_n = 2.6 \Omega$ , respectively. It must be noted that the value for the critical current includes some amount of excess current, as has been observed for all investigated devices based on step-edge Josephson junctions. After opening the shunt, the field period  $B/\Phi$  reduced from  $10.7 \text{ nT}/\Phi_0$ , a typical value for directly coupled magnetometers, to  $1.29 \text{ nT}/\Phi_0$ . This yields an effective area  $A_{\text{eff}} = \Phi/B = 1.60 \text{ mm}^2$ , which is close to the theoretical value of  $1.73 \text{ mm}^2$ . Details of further devices with the same layout are discussed in Refs. [51, 117, 132].

The flux-voltage curves in Fig. 5.11 show a pronounced distortion on the positive slope. This distortion is due to  $LC$  resonances in the parallel circuit of SQUID washer and input coil, which is schematically shown in Fig. 5.12. The resonance frequency is determined by the input coil inductance  $L_i$ , the capacitance  $C_i$  between input coil and SQUID washer, and the rf loss  $R_i$  of the capacitance  $C_i$ . Hilgenkamp [36] calculated the frequency dependent complex impedance for the actual layout of a similar magnetometer and found a large number of resonant states between 80 MHz up to 70 GHz, corresponding to a voltage range of  $0.2 \dots 140 \mu\text{V}$ . Therefore, distortions of the flux-voltage curve can be

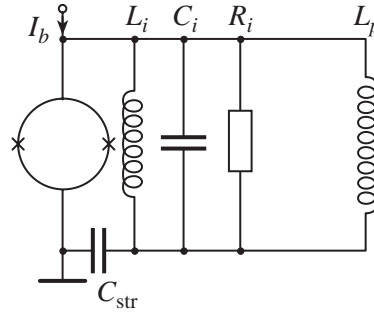


FIGURE 5.12: Simplified circuit model of an inductively coupled SQUID magnetometer taking into account the parasitic capacitances  $C_i$  and  $C_{str}$ .  $R_i$  represents the rf loss of  $C_i$  and  $L_p$  is the inductance of the pickup loop.

found in the whole range of operation of HTS SQUIDs. A distortion of the flux-voltage curve from the input coil resonances can only occur, if the rf voltage produced by the resonant circuit generates magnetic flux in the input coil. For this, a closed current path to the current source must be present, which is provided by the connection of the input coil to the SQUID washer and a parasitic capacitance  $C_{str}$  between the input coil and the ground of the SQUID [133, 134]. There are several ways to prevent the distortion of the flux-voltage curve. One can choose a different material with a smaller dielectric constant than  $\text{SrTiO}_3$  for the insulation layer between the washer and input coil. This will shift the input coil resonances to higher frequencies and out of the range of operation. Insulating materials, such as  $\text{MgO}$ ,  $\text{LaAlO}_3$ ,  $\text{NdGaO}_3$ ,  $\text{CeO}_2$  and others can be used [119], but due to a larger lattice mismatch, the epitaxial quality of the upper superconducting layer might get reduced. An increased low-frequency noise would be the result. One can also introduce a third superconducting layer to provide an insulated return path from the inner turn of the input coil to the pickup loop. However, at the current state of technology, this additional layer and the involved processing steps may also lead to a reduced film quality and a higher noise level. The resonances can also be suppressed with a damping resistor, either between washer and input coil, or in parallel with the SQUID inductance. Values about  $0.1\ \Omega$  must be used, for not to increase the white noise level by the Johnson noise [36]. However, for the deposition of metallic thin-film resistors on  $\text{YBa}_2\text{Cu}_3\text{O}_7$ , a very clean *in situ* technology is necessary to provide reliable low-resistance superconductor-metal contacts. It should be further noted that all investigated inductively coupled magnetometers exhibited a smooth flux-voltage curve before the superconducting shunt was opened. Hence, also the pickup loop inductance influences the strength of the resonances. After opening the shunt, all devices exhibited distortions of their flux-voltage curve, in particular at temperatures below 77 K. Smooth flux-voltage curves could be attributed to noise rounding, either at elevated temperatures, but also at 77 K if the device had a very small critical current [117].

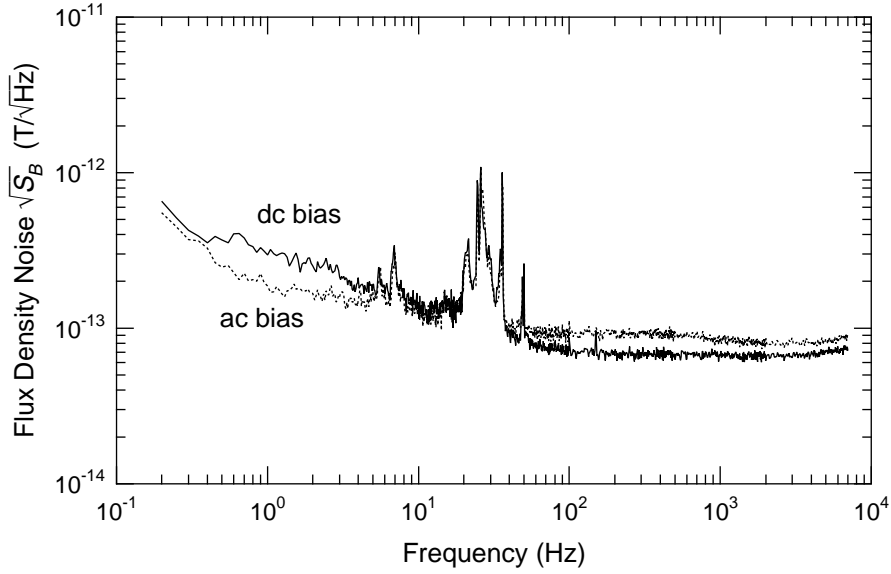


FIGURE 5.13: Noise spectra of an inductively coupled magnetometer recorded at  $T = 77$  K in zero field. The spectra have been recorded both with static bias current (dc bias) and with bias current reversal (ac bias).

The magnetic flux density noise of the investigated inductively coupled magnetometer is shown in Fig. 5.13. The spectra have been recorded with a flux-modulation type FLL electronics, both with static bias current and bias current reversal. Using static bias, a white noise level of  $\sqrt{S_B} = 66 \text{ fT}/\sqrt{\text{Hz}}$  at 1 kHz is measured, which raises to  $85 \text{ fT}/\sqrt{\text{Hz}}$  with bias reversal. This effect is attributed to the resonant flux-voltage curve, which prevents the optimal adjustment of the bias current modulation scheme. Also the static bias measurements are affected by the asymmetry of the flux voltage curve. A measurement with a directly coupled FLL electronics with the working point properly adjusted on the smooth side of the curve would presumably have yielded lower white noise values. Using bias current modulation, the low-frequency noise at 1 Hz could be reduced from  $\sqrt{S_B} = 300 \text{ fT}/\sqrt{\text{Hz}}$  to  $190 \text{ fT}/\sqrt{\text{Hz}}$ , indicating that the static bias value includes some amount of current noise from the Josephson junctions. There still remains some frequency-dependent noise that can be either attributed to environmental noise or to flux motion in the  $\text{YBa}_2\text{Cu}_3\text{O}_7$  films. Although the measurements were performed in a shielded room with an additional mumetal shield surrounding the magnetometer, many lines around 25 Hz are present in the spectra. They originate from mechanical vibrations of the experimental setup in the residual field penetrating the shields. Hence, it is likely that the remaining frequency-dependent contribution is also caused by ambient noise. Figure 5.25 in Section 5.4 gives an impression of the amount of ambient noise present outside of the shields. The low-frequency noise from flux motion of this particular device cooled in static magnetic fields is studied in detail in publication [P7] in Section 5.5.

### 5.1.3 Multiloop magnetometers

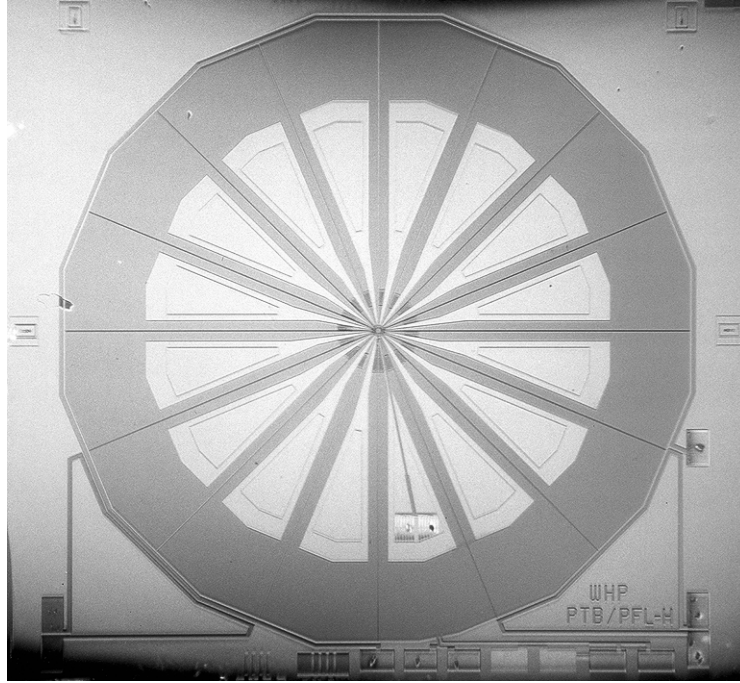


FIGURE 5.14: Microscope image of a multiloop magnetometer of WH3 layout. The outer diameter of the polygonal pickup loop is 8.5 mm.

Three different layouts for HTS multiloop magnetometers have been investigated. Their most important design parameters are summarized in Table 5.3. Figure 5.14 shows a microscope image of a practical multiloop magnetometer of WH3 layout. Magnetometers of the WH1 layout have also been fabricated by Reimer *et al.* [135,136], employing ramp-edge Josephson junctions, and Ludwig *et al.* [137], employing bicrystal grain boundary junctions. In the WH2 layout, the width of the pickup loop is enlarged to reduce its inductance contribution. By this means, the calculated SQUID inductance is reduced by

TABLE 5.3: Design parameters of multiloop dc SQUID magnetometers.

Layout		WH1	WH2	WH3	
Diameter	$D_p$	7	8.5	8.5	mm
Number of loops	$N$	16	16	16	
Pickup loop width	$w_p$	400	1350	1094	$\mu\text{m}$
Spoke width	$D_s$	404	404	278	$\mu\text{m}$
Spoke slitwidth	$d_s$	4	4	4	$\mu\text{m}$
SQUID inductance	$L$	145	134	146	pH
Effektive area	$A_{\text{eff}}$	1.77	2.03	2.35	$\text{mm}^2$
$B/\Phi = 1/A_{\text{eff}}$		1.17	1.02	0.880	$\text{nT}/\Phi_0$

TABLE 5.4: Experimental parameters of the investigated multiloop devices at  $T = 77$  K.

Device	Layout	$\Delta V$ ( $\mu$ V)	$I_0$ ( $\mu$ A)	$R_n$ ( $\Omega$ )	$B/\Phi$ (nT/ $\Phi_0$ )	$A_{\text{eff}}$ (mm <sup>2</sup> )
#290	WH1	4.4	20	5.7	1.16	1.78
#291	WH1	5.8	56	2.9	1.16	1.78
#327	WH2	8.5	56	4.8	1.14	1.81
#327 <sup>a</sup>	WH2	11.5	20	8.3	1.14	1.81
#366	WH3	6.9	13	5.3	0.897	2.31
#407	WH3	13.5	6.0	12.7	0.895	2.31

<sup>a</sup>After annealing

about 8 %. A detailed study of the transport and noise properties of step-edge multiloop magnetometers of WH1 and WH2 layout is given in Ref. [117]. Table 5.4 summarizes the experimental data for the multiloop magnetometers treated in this section. The mean experimental value for the effective area of WH1 devices is  $A_{\text{eff}} = 1.78 \text{ mm}^2$ , which agrees well with the calculated value in Table 5.3. However, for the WH2 layout, a mean value of  $1.85 \text{ mm}^2$  is found, which is about 9 % below the predicted value. Figure 3.8 shows, that a larger effective area can be expected from an optimized combination of pickup loop width and spoke width. For this reason, the WH3 layout was designed to yield the maximum effective area for the diameter of the WH2 layout and the inductance of the WH1 layout.

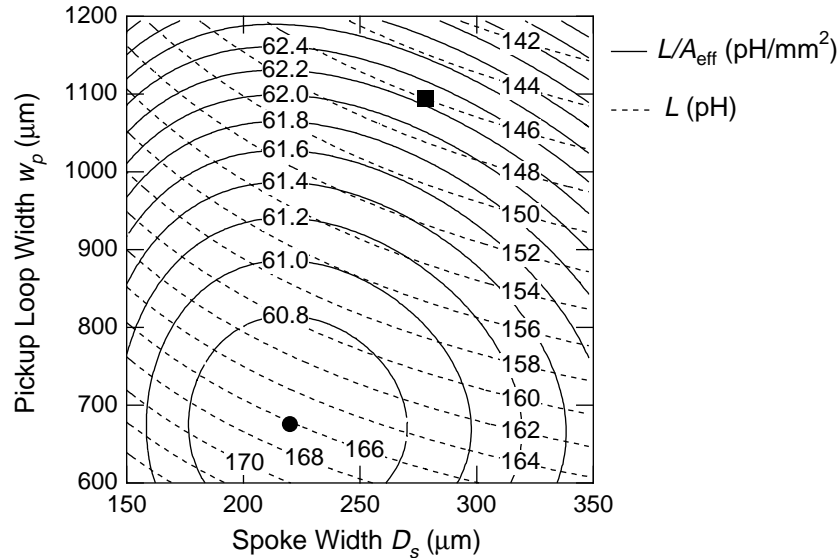


FIGURE 5.15: Dependence of the ratio  $L/A_{\text{eff}}$  and inductance  $L$  on the pickup loop width  $w_p$  and the spoke width  $D_s$  for a multiloop magnetometer with a diameter of 8.5 mm. The optimum combination of  $w_p$  and  $D_s$  is marked with the circle. To keep the inductance at 146 pH, the parameters marked with the square were chosen.

The ratio  $L/A_{\text{eff}}$  is used as the optimization criterion in a similar way as is described in Section 3.1 for the directly coupled magnetometer. Figure 5.15 shows the results of the calculations. A real optimum of  $L/A_{\text{eff}}$  is found for the parameters  $D_s = 220 \mu\text{m}$  and  $w_p = 676 \mu\text{m}$ . However, these values yield a very large SQUID inductance of about 166 pH. Therefore, the SQUID inductance was held fixed at  $L = 146 \text{ pH}$ , at which the lowest value of  $L/A_{\text{eff}}$  is found for  $D_s = 278 \mu\text{m}$  and  $w_p = 1094 \mu\text{m}$ . For these dimensions, an effective area  $A_{\text{eff}} = 2.35 \text{ mm}^2$  is calculated. Two devices have been prepared with WH3 layout, both having a measured effective area of  $A_{\text{eff}} = 2.31 \text{ mm}^2$ . Thus, a very good agreement is obtained with the calculated value.

Figure 5.16 shows the flux-voltage and current-voltage characteristics of the WH3-#407 multiloop magnetometer. The flux-voltage curves are well periodic and a maximum voltage modulation of  $13.5 \mu\text{V}$  is obtained. The large phase shift with respect to the sign of the bias current is attributed to the magnetic flux from the bias current leads coupled to the SQUID. The critical current and normal resistance at 77 K are  $I_0 = 6.0 \mu\text{A}$  and  $R_n = 12.7 \Omega$ , respectively. This yields a comparatively low characteristic voltage of  $I_0 R_n = 76.2 \mu\text{V}$ . The average value for multilayer magnetometers employing step-edge junctions is found to be  $I_0 R_n = 109 \mu\text{V}$  with a standard deviation of  $1\sigma = 80 \mu\text{V}$  [117]. This  $I_0 R_n$  value is lower than for the investigated devices with bicrystal junctions, although the critical currents of the step-edge devices usually include a larger amount of excess current. Furthermore, the spread is larger for step-edge junctions. This reflects the more variable microstructure of step-edge junctions compared to bicrystal junctions.

The temperature dependence of the critical current and the voltage modulation of the multiloop magnetometer WH3-#407 is shown in Fig. 5.17. At lower temperatures, an approximately linear behavior of  $I_0(T)$  is found, which is explained within a SIS-like junction model with a high density of defect states. According to this model, a quadratic behavior is expected at temperatures near  $T_c$  [51]. The modulation voltage closely follows the temperature dependence of the critical current. All fabricated devices employing grain boundary Josephson junctions exhibit a nearly temperature independent normal resistance.

Despite a slight asymmetry, the flux-voltage curves in Fig. 5.16(a) appear smooth, because of the low critical current and the accordingly large noise rounding. At lower temperatures, however, distortions are found, which are similar to the ones described in the previous sections. Figure 5.18 displays some flux-voltage curves for this device at different temperatures. Again, the distortion is only found on one side of the flux-voltage curve. The magnetometer #327 exhibited a comparatively high junction critical current and a distorted flux-voltage curve already at 77 K. For this reason, the device was treated with an annealing procedure, similar to the one described in Section 5.1.1, to reduce the

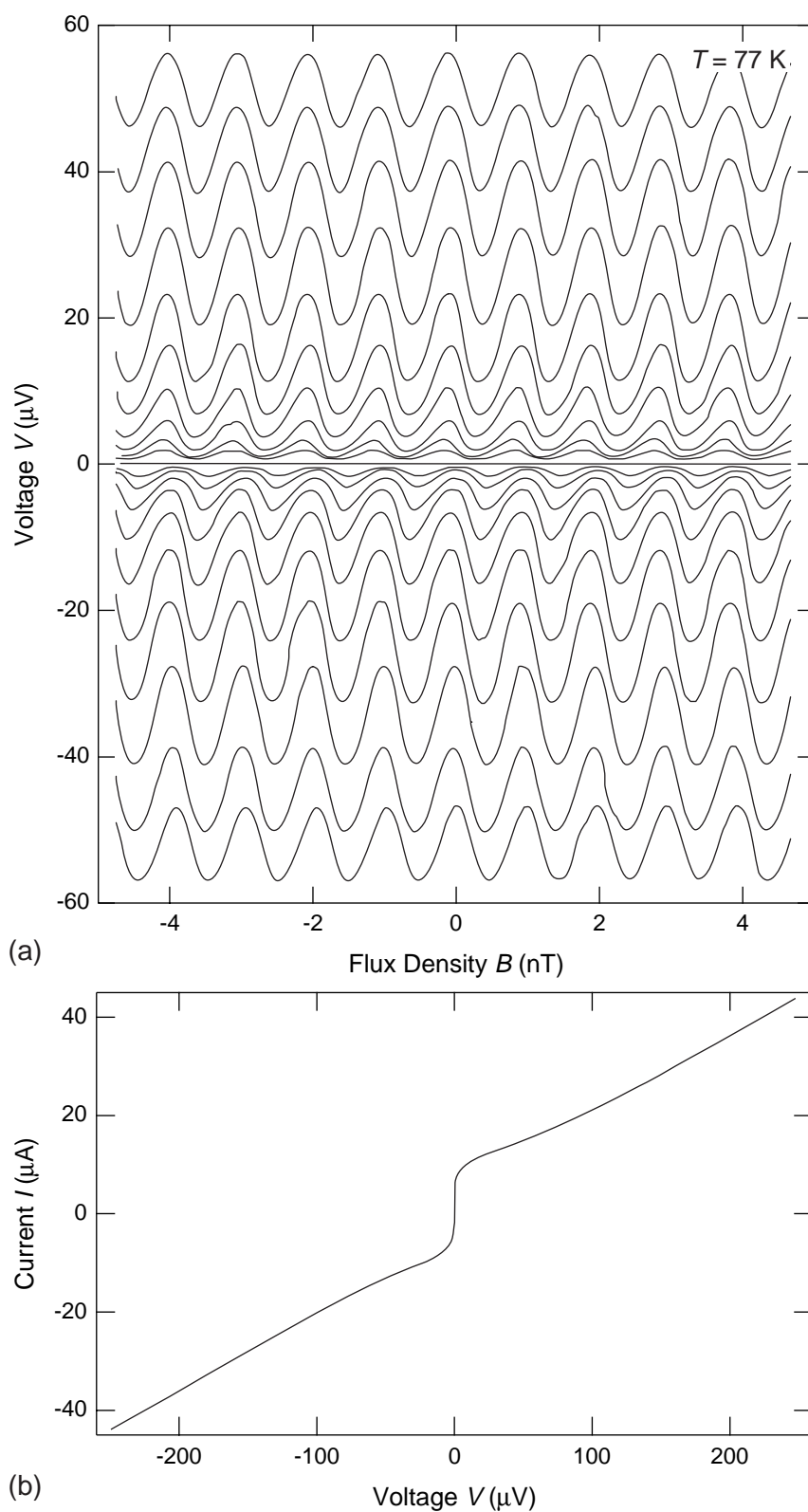


FIGURE 5.16: (a) Flux-voltage curves of the multiloop magnetometer WH3-#407 for different bias currents in the range  $I_b = -15 \dots 15 \mu\text{A}$ . The maximum voltage modulation is  $\Delta V = 13.5 \mu\text{V}$ . (b) Current-voltage characteristic at  $T = 77 \text{ K}$ .



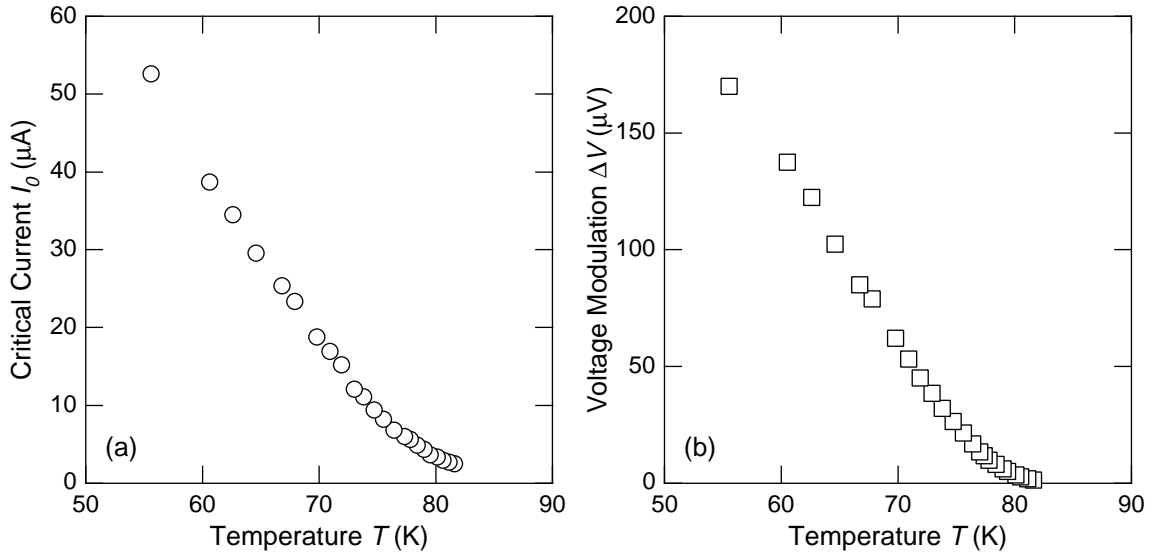


FIGURE 5.17: Temperature dependence of the (a) critical current and the (b) voltage modulation of the multiloop magnetometer WH3-#407.

junction's critical current. The magnetometer was heated for 25 minutes to 200°C in 10 mbar Ar and was afterwards cooled with N<sub>2</sub> at normal pressure to room temperature. The results are illustrated by Fig. 5.19. The critical current has been reduced from 56  $\mu$ A to 20  $\mu$ A and the voltage modulation has significantly increased from 8.5  $\mu$ V to 11.5  $\mu$ V, presumably due to the lower  $\beta_L$  parameter. It must be noted that the high  $I_0 R_n$  value of formerly 269  $\mu$ V has been reduced to 166  $\mu$ V. However, for practical applications it is more important that the flux-voltage curves have become smooth and nearly sinusoidal at 77 K. Thus, the new bias point is now obviously out of the range of the microwave resonances.

Flux density noise spectra of two multiloop magnetometers are depicted in Fig. 5.20. They have been measured at Philips Hamburg, either using a superconducting shield of the HTS Bi<sub>2</sub>Sr<sub>2</sub>CaCu<sub>2</sub>O<sub>8</sub> (BSCCO 2212) [138], or a double-walled metallic Cryoperm shield closely surrounding the magnetometer. The BSCCO shield was additionally surrounded by a single Cryoperm cylinder. Comparing the measurements for both types of shields, one finds that an increased white noise level is obtained with the metallic shield, which is attributed to its thermal Johnson noise [139]. A significantly lower white noise level is found with the BSCCO shield. For the devices WH2-#327 and WH3-#366, the values  $\sqrt{S_B} = 17 \text{ fT}/\sqrt{\text{Hz}}$  and  $29 \text{ fT}/\sqrt{\text{Hz}}$  in the white noise regime are measured, respectively. However, a large amount of  $1/f$  noise is found with the BSCCO shield, which is attributed to the motion of weakly pinned flux lines in the shield. No reduction of this noise could be achieved, even when the BSCCO shield was surrounded with a further Cryoperm shield,

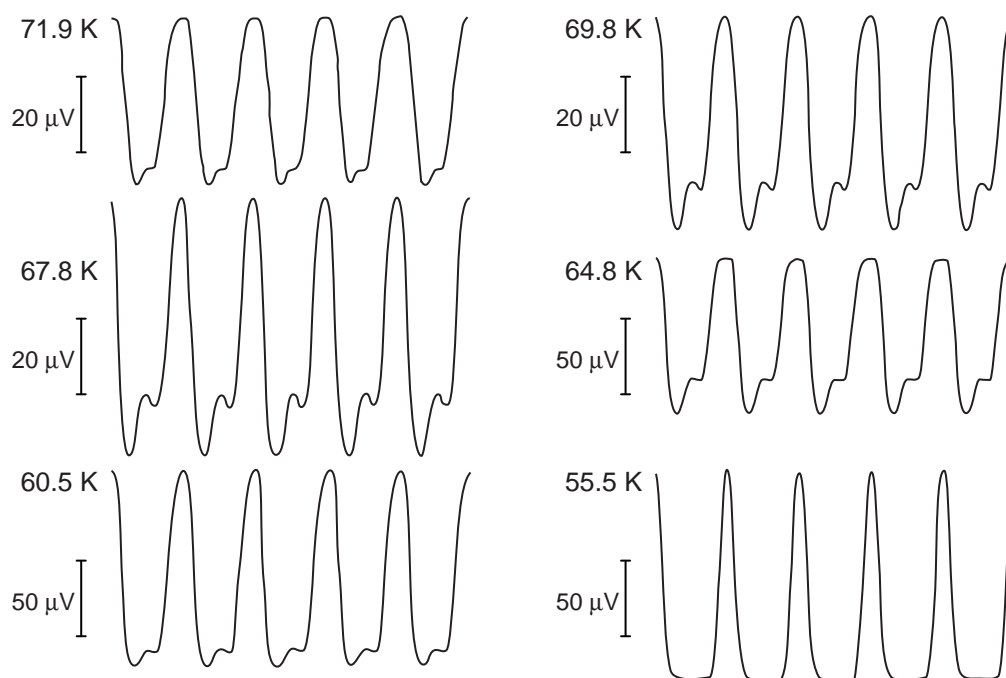


FIGURE 5.18: Resonance structures in the flux-voltage curves of the multiloop magnetometer WH3-#407 at various temperatures.

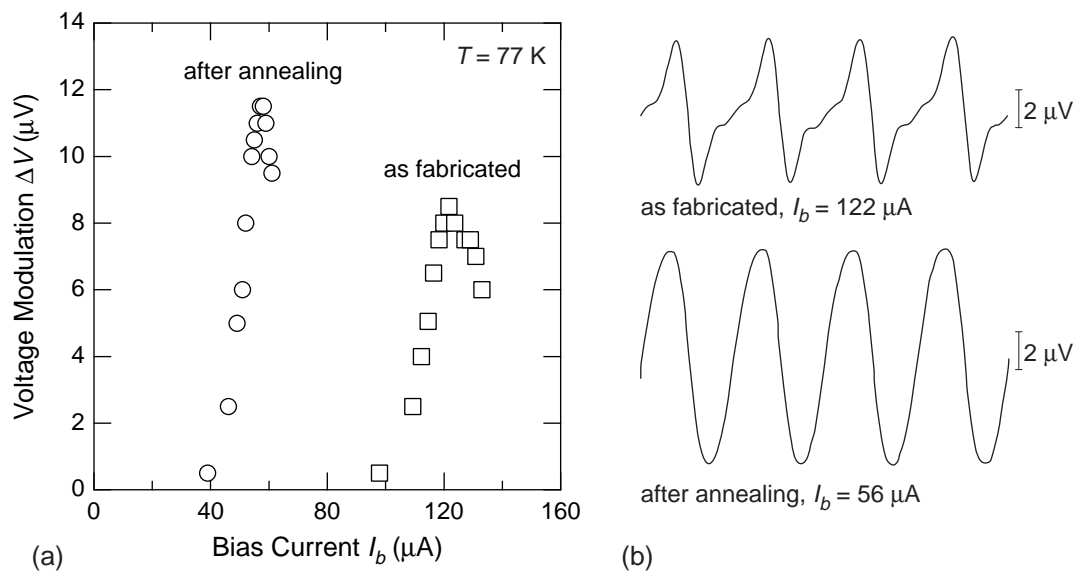


FIGURE 5.19: (a) Voltage modulation of the magnetometer WH2-#327 as a function of the bias current before and after annealing. (b) Shape of flux-voltage curves before and after annealing.

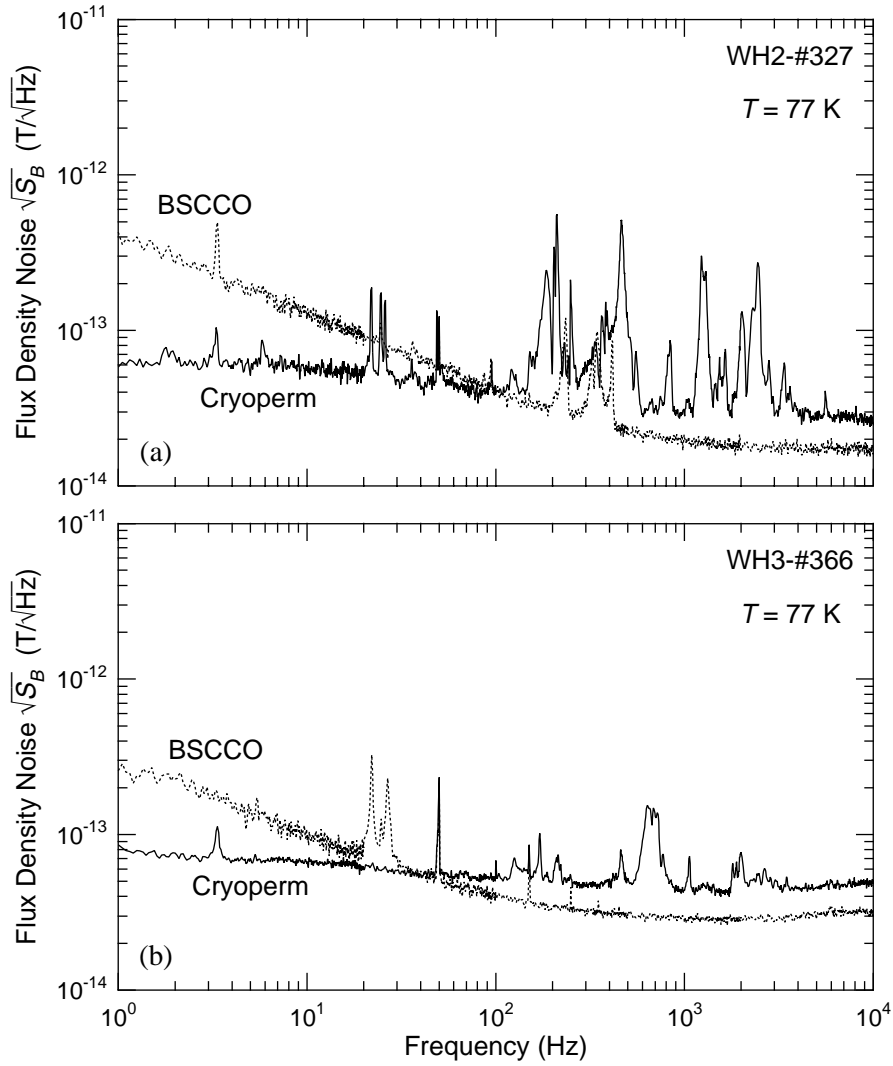


FIGURE 5.20: Flux density noise spectra of two multiloop magnetometers measured with different shields: A superconducting BSCCO shield and a triple Cryoperm shield. The superconducting shield induces a large amount of  $1/f$  noise, whereas the metallic shield increases the frequency-independent noise. All measurements have been made using bias current modulation.

or when it was cooled inside a shielded room. Since the flux noise from the shield is detected like an external signal, no noise reduction can be obtained with modulation schemes. Hence, the low-frequency noise of the magnetometers had to be characterized with the metallic shield. Using bias current modulation, the values  $\sqrt{S_B} = 60 \text{ fT}/\sqrt{\text{Hz}}$  and  $81 \text{ fT}/\sqrt{\text{Hz}}$  at 1 Hz are measured for the devices WH2-#327 and WH3-#366, respectively. These noise values still include the thermal noise component from the shield. All noise measurements have been made with bias current modulation to suppress the  $1/f$  noise component from critical current fluctuations in the Josephson junctions.

The white noise level of magnetometer WH2-#327 is comparable to the one reported by Ludwig *et al.* [88] for a multiloop magnetometer employing bicrystal Josephson junctions. The authors also report an increased noise level when using a metallic shield instead of a superconducting  $\text{YBa}_2\text{Cu}_3\text{O}_7$  shield. However, their  $\text{YBa}_2\text{Cu}_3\text{O}_7$  shield, based on a thick-film of  $\text{YBa}_2\text{Cu}_3\text{O}_7$  on yttria stabilized zirconia, exhibited a much better low-frequency behavior.

#### 5.1.4 Temperature dependence of the effective area

The effective area of HTS magnetometers depends on the temperature as a consequence of the temperature dependent London penetration depth  $\lambda_L(T)$ . For example, Fig. 5.21 shows the temperature dependence of the effective area of the WH3-type multiloop magnetometer #407. The effective area slightly decreases with increasing temperature. A reduction of 1.3% is measured between 55 K and 82 K. This is attributed to a pure geometrical effect of the temperature dependent London penetration depth, which widens the slits between the pickup loops. Thus, the stray flux into the slits increases and the effective flux capturing area of the magnetometer gets reduced. Since the effect is small, the temperature dependence of the effective area may be well fitted with a linear dependence on the London penetration depth

$$\begin{aligned} A_{\text{eff}}(T) &= a + b \frac{\lambda_L(T)}{\lambda_L(0)} \\ &= a + b / \sqrt{1 - \left(\frac{T}{T_c}\right)^2}, \end{aligned} \quad (5.1)$$

where  $a$  and  $b$  are constants. The solid line in Fig. 5.21 shows a fit of this model to the experimental data. The resulting value for the temperature independent part of the effective area is  $a = 2.35 \text{ mm}^2$ . Thus, an excellent agreement is found, if one compares this value with the theoretical one in Table 5.3, for which no temperature dependent effects have been considered. Measurements on devices with the other layouts WH1 and WH2 yield very similar results for the slope  $b$ .

Figure 5.22 summarizes results for all magnetometer types treated in this thesis. However, the data for the directly coupled magnetometer have been taken from a paper by ter Brake *et al.* [140]. For a better comparison, the effective area is normalized to the low-temperature value  $A_{\text{eff}}(0) = a + b$ . In all cases, the temperature dependence can be well fitted with a linear dependence on  $\lambda_L(T)$  in the way shown above for the multiloop magnetometer. The value  $b$  is negative for the multiloop and the IMPUC device, since an increasing temperature results in an increase of the stray flux into the spoke slits,

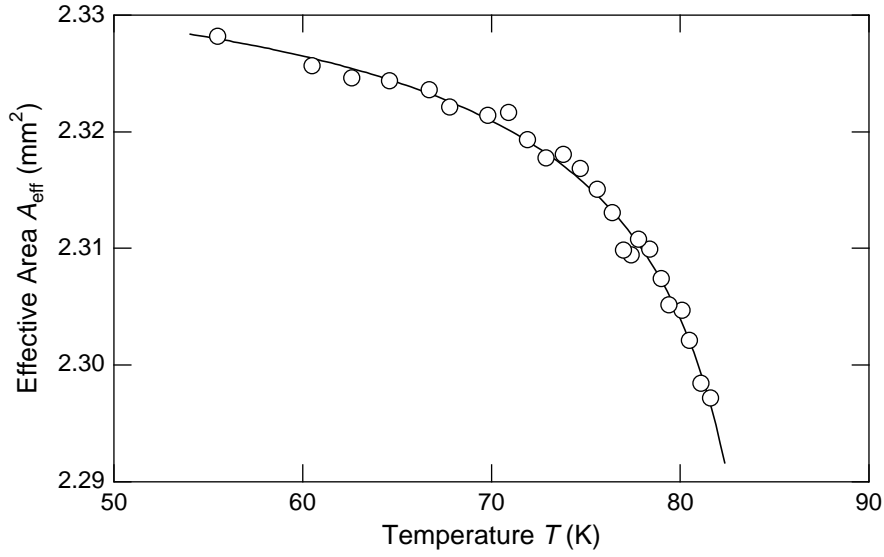


FIGURE 5.21: Temperature dependence of the effective area of a WH3-type multiloop magnetometer. The solid line is a fit to the data.

which is lost for the pickup loops. In contrast, the effective area of the inductively coupled magnetometer becomes larger with increasing temperature. This is attributed to the widening of the washer slit and hole increasing the mutual inductance between input coil and washer. Obviously, this effect is of less importance for the IMPUC device. Therefore a magnetometer with vanishing coefficient  $b$  might be obtained with an optimized layout. The multiloop magnetometer is the least temperature sensitive device. This is due to the fact that its sensitivity is mainly determined by the large-area pickup loops, but not by small structures with dimensions of the order of  $\lambda_L(T)$ . This also explains the good reproducibility of the effective area of multiloop magnetometers and the good agreement with the theoretical values. The effective area of the directly coupled magnetometer shows the largest variation with the temperature. Here, the SQUID loop is of very small size and its inductance is therefore strongly affected by the London penetration depth, both geometrically and by the kinetic inductance contribution. Since the effective area is nearly proportional to the SQUID loop inductance, it similarly varies with the temperature.

The temperature dependence of the effective area is a serious issue when the magnetometer is operating in a magnetic field  $B_0$  like the earth's field of about  $50 \mu\text{T}$ , since temperature fluctuations will produce an apparent magnetic field noise

$$\sqrt{S_B}(f) = B_0 \alpha(T) \sqrt{S_T}(f), \quad \text{where} \quad (5.2)$$

$$\alpha(T) = \frac{1}{A_{\text{eff}}(T)} \frac{\partial A_{\text{eff}}(T)}{\partial T}. \quad (5.3)$$

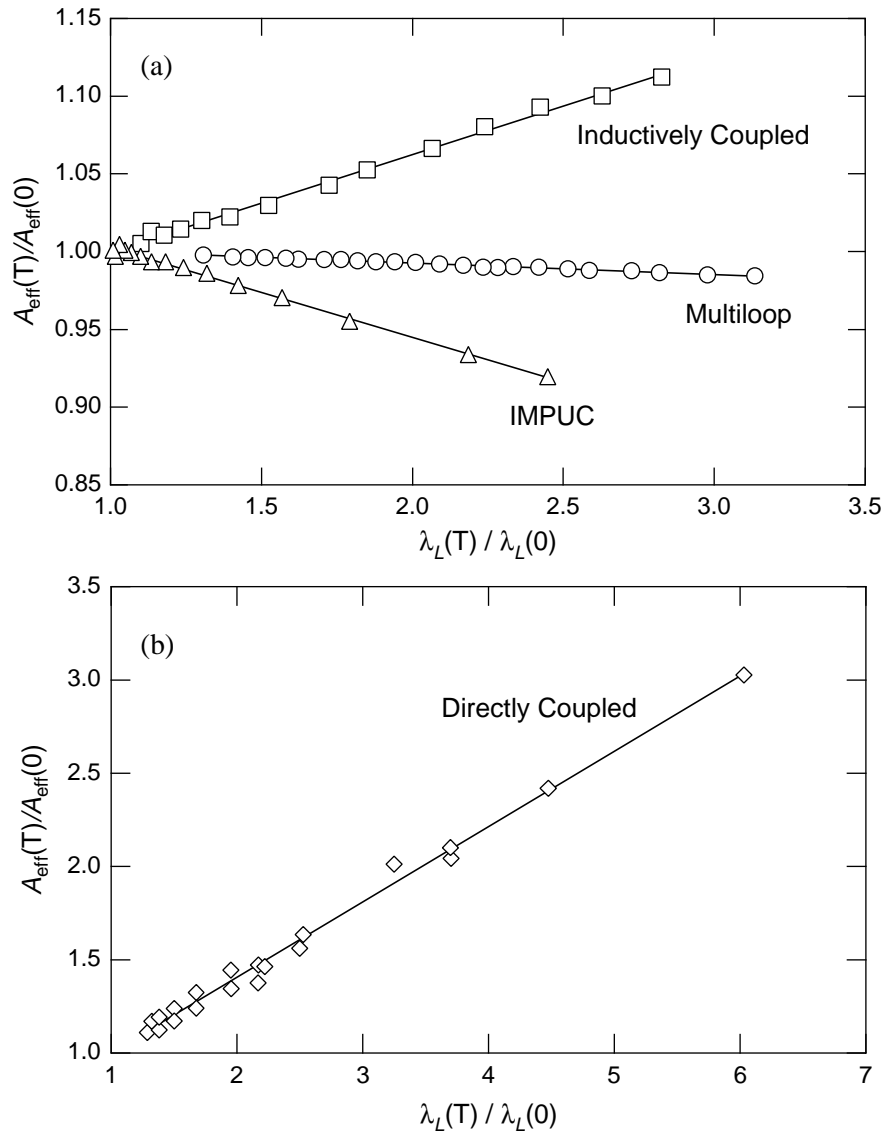


FIGURE 5.22: Effective area of integrated magnetometers as a function of the London penetration depth. For a better comparison, the effective area is normalized to the low-temperature value. The values in (b) are taken from Ref. [140]. The lines are linear fits to the data.

$\sqrt{S_T}(f)$  is the spectral density of the temperature fluctuations. The coefficient  $\alpha(T)$  can be obtained from (5.1)

$$\alpha(T) = \frac{b}{A_{\text{eff}}(T)} \left(1 - \frac{T^2}{T_c^2}\right)^{-\frac{3}{2}} \frac{T}{T_c^2}. \quad (5.4)$$

Table 5.5 summarizes the results obtained from the data in Fig. 5.22. It also gives the maximum allowed peak-to-peak temperature fluctuations  $\delta T_{\text{pp}}$  calculated for a static magnetic field of  $B_0 = 50 \mu\text{T}$  and an apparent magnetic field noise level of 1 pT peak-to-peak. It follows that a temperature stability in the  $\mu\text{K}$  range is required for the operation at 77 K in the earth's field. Directly coupled magnetometers require the highest temperature stability with fluctuations less than 1  $\mu\text{K}$  peak-to-peak. The requirement for the multiloop magnetometer is about 30 times less stringent. The temperature stability may be realized with a sufficiently large thermal buffer with good thermal contact to the magnetometer, so that the corner frequency of the thermal fluctuations is reduced below the frequency range of interest. The requirements on temperature stability are less stringent when the earth's magnetic field is compensated.

TABLE 5.5: Parameters  $b$  and  $\alpha(77 \text{ K})$  that have been obtained from a fit of the temperature dependent effective area to Eq. (5.1). The last column gives the peak-to-peak temperature fluctuations yielding an apparent magnetic field noise of 1 pT peak-to-peak in a static field of  $B_0 = 50 \mu\text{T}$  at  $T = 77 \text{ K}$ .

Type	$b$ ( $\text{mm}^2$ )	$\alpha(77 \text{ K})$ ( $10^{-3} \text{ K}^{-1}$ )	$\delta T_{\text{pp}}$ ( $\mu\text{K}$ )
Directly Coupled	0.0411	27.1	0.74
Inductively coupled	0.0981	6.64	3.0
Multiloop	-0.0128	-0.861	23
IMPUC	-0.0578	-10.0	2.0

### 5.1.5 Summary

Three different types of integrated  $\text{YBa}_2\text{Cu}_3\text{O}_7$  magnetometers have been investigated: The directly coupled, the inductively coupled, and the multiloop magnetometer. All devices have been operating in liquid nitrogen at 77 K.

The directly coupled magnetometers have been fabricated in a comparatively simple single-layer process on  $24^\circ$  bicrystal substrates. Low flux density noise levels of  $\sqrt{S_B}(1 \text{ kHz}) = 38 \text{ fT}/\sqrt{\text{Hz}}$  and  $\sqrt{S_B}(1 \text{ Hz}) = 80 \text{ fT}/\sqrt{\text{Hz}}$  have been obtained. The effective area is about  $0.2 \text{ mm}^2$  for a SQUID inductance of about 50 pH and a pickup loop

size of 8.3 mm. Larger effective areas are linearly obtained with higher SQUID inductances. All parameters of the directly coupled magnetometers show a large spread among the samples. The large variations in the effective area are attributed to the small linewidth of the SQUID loop and the large kinetic contribution to its inductance. A smaller spread is expected for thicker films, which will be used in future devices. Also the amplitude of voltage modulation shows large variations. As expected from the theory, the largest voltage modulation is obtained with a modulation parameter  $\beta_L \approx 1$ , requiring junction critical currents of about  $20 \mu\text{A}$  in a SQUID of 50 pH inductance. In contrast, the average critical current of the investigated samples is  $84 \mu\text{A}$ . Even higher values are expected for thicker films. For this reason, an annealing method has been investigated to reduce the junction critical currents. With this, the critical currents can be reduced, but the low-frequency noise of the magnetometer may get affected. Lower critical currents from the beginning are expected with bicrystals employing  $30^\circ$  grain boundaries [69]. This will be investigated in the future. Using  $30^\circ$  bicrystals, Beyer *et al.* [130] has obtained a white noise level as low as  $\sqrt{S_B} = 24 \text{ fT}/\sqrt{\text{Hz}}$  at 1 kHz due to an extraordinarily large voltage modulation of  $54 \mu\text{V}$ . This noise level is already close to the values obtained with the best multilayer magnetometers. An even lower value of  $14 \text{ fT}/\sqrt{\text{Hz}}$  at 1 kHz has been obtained by Cantor *et al.* [141] using a large  $19 \times 19 \text{ mm}^2$  pickup loop on a  $2 \times 2 \text{ cm}^2$  bicrystal. The general tendency found for the inductance dependency of the voltage modulation is in good agreement with the theory. However, the measured amplitudes are generally somewhat lower than the calculated ones. This is mainly attributed to distortions of the current-voltage characteristic due to microwave resonances in the SQUID loop. A maximum voltage modulation of  $\Delta V = 40.5 \mu\text{V}$  has been measured.

The fabrication of the inductively coupled and the multiloop magnetometers requires a more demanding multilevel process. Based on step-edge Josephson junctions, multiloop magnetometers have been fabricated that have flux density noise levels of  $\sqrt{S_B} = 29 \text{ fT}/\sqrt{\text{Hz}}$  and  $\sqrt{S_B} = 17 \text{ fT}/\sqrt{\text{Hz}}$  in the white noise regime, and low-frequency noise levels of  $\sqrt{S_B}(1 \text{ Hz}) = 81 \text{ fT}/\sqrt{\text{Hz}}$  and  $\sqrt{S_B}(1 \text{ Hz}) = 60 \text{ fT}/\sqrt{\text{Hz}}$ , respectively. A maximum voltage modulation of  $13.5 \mu\text{V}$  has been obtained with a multiloop magnetometer of 146 pH SQUID inductance. The effective area of the multiloop magnetometer has been increased to  $A_{\text{eff}} = 2.31 \text{ mm}^2$  by means of an optimization of the pickup loop linewidth and the spoke linewidth. This is the largest effective area reported so far for a HTS SQUID magnetometer of comparable size [142, 143].

The lowest white noise level in a monolithically integrated HTS multilayer device has been reported by Drung *et al.* [81] for an inductively coupled magnetometer based on bicrystal Josephson junctions. Although this device exhibited a strongly resonant flux-voltage characteristic, a white noise level of  $\sqrt{S_B} = 8.6 \text{ fT}/\sqrt{\text{Hz}}$  could be achieved by



using a directly coupled FLL electronics and APF. A comparable noise level has been obtained with a bicrystal multiloop magnetometer fabricated by the Berkeley group [137]. A detailed comparison of this device with the step-edge multiloop magnetometer WH1-#291 of Section 5.1.3 is given in publication [P3], which is included in the following Section 5.2.

All integrated SQUID magnetometers can show distorted flux-voltage characteristics, which are attributed to microwave resonances in the pickup loop and to the adversely large dielectric constant of the used  $\text{SrTiO}_3$  substrates. These resonances lead to an increased noise level, when the magnetometer is operated in a flux-modulation type FLL electronics. It has been demonstrated that the resonances can be removed by changing the Josephson junction parameters in an annealing process. In every case, the resonances occur only on one side of the flux-voltage characteristic. Thus, an operation with a directly coupled FLL electronics is always possible, without deterioration of the noise level.

The effective area of HTS magnetometers depends on the temperature. This makes demands on the temperature stabilization when the magnetometer is operated in an ambient magnetic field. The temperature dependence is largely different for the various magnetometer types. The lowest temperature dependence is found for the multiloop magnetometer and the largest is found for the directly coupled magnetometer. Furthermore, the multiloop magnetometer exhibits the best correspondence between the calculated effective area and the experimental value. This parameter is also very reproducible.

## 5.2 Low noise operation with additional positive feedback (APF)

Many biomagnetic applications require SQUID magnetometers with a low noise level down to frequencies of 1 Hz or lower. Low-frequency  $1/f$  noise from vortex motion in the superconducting films is measured like an external signal and can only be reduced by taking precautions in the magnetometer design and by maintaining a high quality of the involved thin-films. This topic is discussed in more detail in Section 5.5. In contrast,  $1/f$  noise from critical current fluctuations can be electronically suppressed by using the bias reversal scheme described in Section 4.3. The direct readout FLL electronics has been originally designed for biomagnetic multichannel systems employing low- $T_c$  magnetometers, where current noise is generally not a serious issue. Hence, bias reversal was not implemented in the early versions of this electronics. The advent of high quality HTS magnetometers with noise levels suitable for biomagnetic measurements makes multichannel systems of HTS magnetometers now possible. However, due to the high  $1/f$  noise level

of current HTS Josephson junctions, bias current modulation is inevitably necessary. To make the direct readout FLL electronics suitable for HTS magnetometers, Drung implemented a bias reversal scheme, which is also compatible with the APF method [127]. The noise reduction has been successfully demonstrated with a low- $T_c$  magnetometer employing Nb/Si<sub>x</sub>N<sub>y</sub>/Nb junctions with a high level of excess noise. The first operation of HTS magnetometers employing bias reversal and APF is reported in the following publication. Three magnetometers from YBa<sub>2</sub>Cu<sub>3</sub>O<sub>7</sub>-SrTiO<sub>3</sub>-YBa<sub>2</sub>Cu<sub>3</sub>O<sub>7</sub> multilayers have been investigated: An inductively coupled flip-chip magnetometer and a multiloop magnetometer, both fabricated on bicrystal substrates by the Berkeley group, and the step-edge multiloop magnetometer #291 (refer to Section 5.1.3) fabricated at Philips Hamburg. High quality real-time magnetocardiograms demonstrate their applicability in biomagnetic measurements. Very low white noise levels of  $\sqrt{S_B} = 10 \text{ fT}/\sqrt{\text{Hz}}$  and  $16.2 \text{ fT}/\sqrt{\text{Hz}}$  have been obtained with the Berkeley devices. A somewhat higher value of  $30 \text{ fT}/\sqrt{\text{Hz}}$  has been measured with the step-edge magnetometer. This is due to its comparatively low voltage modulation, which was further reduced by the load of the APF circuit. However, this magnetometer exhibits the lowest low-frequency noise level of  $94 \text{ fT}/\sqrt{\text{Hz}}$  at 1 Hz, including an environmental contribution of about  $50 \text{ fT}/\sqrt{\text{Hz}}$ . To illustrate the low noise values, high quality magnetocardiograms have been recorded. One of them is discussed in the following section.

## Low noise $\text{YBa}_2\text{Cu}_3\text{O}_{7-x}$ SQUID magnetometers operated with additional positive feedback

D. Drung, E. Dantsker,<sup>a)</sup> F. Ludwig, and H. Koch

*Physikalisch-Technische Bundesanstalt, Abbestr. 2-12, 10587 Berlin, Germany*

R. Kleiner and John Clarke

*Department of Physics, University of California, Berkeley, and Materials Sciences Division, Lawrence Berkeley National Laboratory, Berkeley, California 94720*

S. Krey and D. Reimer

*Institute of Applied Physics, University of Hamburg, Jungiusstrasse 11, 20355 Hamburg, Germany*

B. David and O. Doessel

*Philips Research Laboratories, Dept. Technical Systems, Roentgenstrasse 24-26, 22335 Hamburg, Germany*

(Received 9 October 1995; accepted for publication 29 January 1996)

Three magnetometers based on dc superconducting quantum interference devices (SQUIDs) fabricated from  $\text{YBa}_2\text{Cu}_3\text{O}_{7-x}$  have been operated in a magnetically shielded room using a flux-locked loop involving additional positive feedback with bias current reversal. Two of these devices, integrated multiloop dc SQUIDs with outer diameters of 7 mm, achieved white noise levels of  $10 \text{ fT}/\sqrt{\text{Hz}}$  for bicrystal junctions and  $30 \text{ fT}/\sqrt{\text{Hz}}$  for step-edge junctions. The third magnetometer involved a flux transformer with a  $10 \times 10 \text{ mm}^2$  pickup coil connected to a 16-turn input coil which was inductively coupled to a bicrystal SQUID. This device achieved a white noise of  $16.2 \text{ fT}/\sqrt{\text{Hz}}$ . High quality magnetocardiograms were obtained without signal averaging.

© 1996 American Institute of Physics. [S0003-6951(96)02013-8]

To operate a dc superconducting quantum interference device (SQUID) in a flux-locked loop one commonly applies an oscillating magnetic flux and demodulates the voltage across it.<sup>1</sup> An alternative scheme, additional positive feedback (APF),<sup>2</sup> involves no such modulation, enabling one to construct lower cost and more compact multichannel systems. This scheme has been used successfully in several multichannel systems involving low-transition temperature ( $T_c$ ) SQUIDs. The lack of modulation in the original APF scheme means that low-frequency critical current or resistance fluctuations in the Josephson junctions<sup>3</sup> are not suppressed; however, in high quality low- $T_c$  junctions the influence of these fluctuations is often negligible compared with other sources of low-frequency noise. In contrast, critical current fluctuations are the dominant source of low-frequency noise in high- $T_c$  dc SQUIDs and one must inevitably use a bias current reversal scheme to reduce them.<sup>3</sup> Recently, an APF scheme with bias reversal has been developed and successfully tested with low- $T_c$  multiloop SQUIDs.<sup>4</sup> In this letter, we report the use of bias reversal in an APF flux-locked loop to reduce the low-frequency noise in high- $T_c$  SQUID magnetometers, and demonstrate the use of these devices to obtain high quality magnetocardiograms in a magnetically shielded room.

For this study, we used two integrated multiloop magnetometers and one flip-chip magnetometer. The multiloop magnetometers have an outer diameter of 7 mm and consist of 16 pickup loops connected in parallel across two junctions to form a SQUID with an inductance  $L$  of about  $145 \text{ pH}$ .<sup>5,6</sup> One of these devices was fabricated at Philips Hamburg using a  $\text{YBa}_2\text{Cu}_3\text{O}_{7-x}$ - $\text{SrTiO}_3$ - $\text{YBa}_2\text{Cu}_3\text{O}_{7-x}$  (YBCO-STO-

YBCO) multilayer process with step-edge junctions.<sup>7</sup> The other multiloop device and the flip-chip magnetometer were fabricated at the University of California, Berkeley and Lawrence Berkeley National Laboratory using a YBCO-STO-YBCO multilayer process with bicrystal junctions.<sup>8</sup> The flip-chip magnetometer consists of a flux transformer with a  $10 \times 10 \text{ mm}^2$  pickup loop connected to a 16-turn input coil that is inductively coupled to a  $500 \text{ }\mu\text{m}$  square washer SQUID with bicrystal junctions.<sup>8,9</sup> The flux transformer and SQUID are pressed together with a  $3\text{-}\mu\text{m}$ -thick mylar foil between them. The crossover was aligned to cover about 75% of the length of the slit in the SQUID washer (type A/C in Ref. 9), thus providing a ground plane to reduce the self-inductance of the SQUID to about  $30 \text{ pH}$ . The parameters of the magnetometers are listed in Table I.

The APF circuit consists of a resistor  $R_a$  and a coil  $L_a$  in series, connected in parallel with the SQUID (Fig. 1). A constant bias current  $I_b$  maintains a voltage  $V$  across the SQUID which is equal to the bias voltage  $V_b$  if the SQUID is at its working point. A small increase in the magnetic flux  $\Phi$  in the SQUID produces a small change in  $V$ . The resulting current change in the APF circuit induces an additional flux in the SQUID via the mutual inductance  $M_a$  between the APF coil and the SQUID, thereby increasing the flux-to-voltage transfer function to  $V_\Phi = \partial V / \partial \Phi = V_{\Phi,i} / (1 - G_a)$ , where  $V_{\Phi,i}$  is the intrinsic transfer function without APF (i.e., with  $R_a \rightarrow \infty$ ) and

$$G_a = (M_a + \partial \Phi / \partial I) V_{\Phi,i} / R_a \lesssim 1 \quad (1)$$

is the APF gain.<sup>10</sup> Note that with APF the bias current must be increased by  $\Delta I_b = V_b / R_a$  compared to the case without APF in order to have identical working points. The spectral density of the total flux noise with APF at frequency  $f$  is given by<sup>10</sup>

<sup>a)</sup>On leave from the University of California, Berkeley, CA.

TABLE I. Parameters and performance of high- $T_c$  magnetometers with additional positive feedback operated inside a magnetically shielded room. The noise was measured with bias reversal (values in parentheses with static bias).

Magnetometer type	Flip-chip	Multiloop	Multiloop
Junction technology	bicrystal	bicrystal	step-edge
Pickup coil shape	square	circular	circular
Pickup coil size $D_p$	10	7	7
Sensitivity $B/\Phi$	2.7	1.24	1.23
SQUID inductance $L$	$\approx 30$	$\approx 145$	$\approx 145$
Mutual inductance $M_a$	330	840	1050
APF resistance $R_a$	12	34	8.7
Junction resistance $R$	1.8	13	3
Bias current $I_b$	186	11	111
Bias voltage $V_b$	32	24	$\approx 30$
Voltage swing $2\delta V$	21.5	17.5	4.7
$V_\Phi = \partial V / \partial \Phi$	$\approx 900$	$\approx 700$	$\approx 125$
$-\partial \Phi / \partial I = R_{\text{dyn}} / V_\Phi$	$\approx 0.03$	...	0.12
$\sqrt{S_{B,i}(\text{white})}^a$	14.4 (13)	8.8 (7.7)	26 (22.5)
$\sqrt{S_B(\text{white})}^a$	16.2 (15)	10 (9)	30 (27)
$\sqrt{S_B(1 \text{ kHz})}$	16.3 (35)	13 (22) <sup>b</sup>	31 (32)
$\sqrt{S_B(100 \text{ Hz})}$	17.8 (91)	53 (74) <sup>b</sup>	34.6 (57)
$\sqrt{S_B(1 \text{ Hz})}^c$	135 (850)	110 (280)	94 (800)

<sup>a</sup>Measured with bias reversal at 5 kHz (with static bias at 20 kHz).

<sup>b</sup>Deteriorated due to a random telegraph signal.

<sup>c</sup>Includes environmental noise contribution of  $\approx 50 \text{ fT}/\sqrt{\text{Hz}}$ .

$$S_\Phi(f) = S_{\Phi,i}(f) + 4k_B T R_a (G_a / V_{\Phi,i})^2 + S_{V,\text{amp}}(f) / V_\Phi^2 + S_{I,\text{amp}}(f) (\partial \Phi / \partial I)^2. \quad (2)$$

Here,  $S_{\Phi,i}(f)$  is the intrinsic flux noise spectral density of the SQUID without APF,  $4k_B T R_a$  is the Nyquist voltage noise of the APF resistor,  $S_{V,\text{amp}}(f)$  and  $S_{I,\text{amp}}(f)$  are spectral densities of the voltage and current noise of the preamplifier,  $-\partial \Phi / \partial I = R_{\text{dyn}} / V_\Phi$  is the current sensitivity<sup>11</sup> (i.e., current-to-flux transfer function at constant SQUID voltage), and  $R_{\text{dyn}} = \partial V / \partial I$  is the dynamic resistance of the SQUID. Equation (2) shows that APF reduces the effects of the preamplifier voltage noise by increasing  $V_\Phi$ , whereas the effect of the current noise remains unchanged since  $-\partial \Phi / \partial I$  is not affected by APF.<sup>11</sup> The bandwidth of the enhanced transfer function, given by the bandwidth of the APF circuit  $f_a = R_a / 2\pi L_a$  divided by  $V_\Phi / V_{\Phi,i}$ , is  $(1 - G_a) R_a / 2\pi L_a$ . Typically, we choose  $G_a \approx 0.9$  as a good compromise between low noise and high bandwidth.

The SQUID was connected directly to the preamplifier (Analog Devices AD797), which has white voltage and cur-

rent noise levels of  $1 \text{ nV}/\sqrt{\text{Hz}}$  and  $2 \text{ pA}/\sqrt{\text{Hz}}$  with  $1/f$  noise corner frequencies of about 7 and 270 Hz, respectively. For all the magnetometers we used a 7-turn APF coil ( $L_a \approx 3 \mu\text{H}$ ) and a single-turn feedback coil of 0.05 mm diam, varnish-insulated Cu wire. The metal film APF resistor was selected for each SQUID to make  $G_a \approx 0.9$ . The current noise of the preamplifier is sufficiently low so that it was not necessary to reduce  $-\partial \Phi / \partial I$  by bias current feedback (BCF).<sup>11</sup> To minimize the number of wires between 77 K and room temperature we measured the SQUID voltage in a two-terminal configuration. The bias voltage  $V_b$  was generated by passing a bias current  $I_b$  through a cooled metal film resistor  $R_V$ . The deviation between the SQUID and bias voltages was amplified, integrated, and fed back as a current into the feedback coil. For the magnetometers used here, the feedback range was between  $\pm 60$  and  $\pm 90 \text{ nT}$ , and the 3 dB bandwidth of the flux-locked loop was between 40 and 200 kHz. The feedback electronics are described in detail elsewhere.<sup>4</sup>

The SQUID probe was inserted into a low-noise bi-magnetic dewar filled with liquid nitrogen, with a separation of about 13 mm between the magnetometer and the outer end of the dewar. The system was operated in the Berlin magnetically shielded room (BMSR).<sup>12</sup> The sensitivity  $B/\Phi$  ( $B$  is the flux density) was measured using a calibrated 20-cm-diam Helmholtz coil. The  $V-\Phi$  characteristics of the flip-chip and step-edge multiloop magnetometers are shown inset in Fig. 2, along with their magnetic flux density noise measured with both static bias current and bias reversal at 15 kHz (flip-chip) or 9 kHz (multiloop). The basic parameters of the  $V-\Phi$  characteristics (voltage swing  $2\delta V$  and transfer function  $V_\Phi$ ) and the noise at selected frequencies are also listed in Table I. With static bias the APF scheme does not suppress critical current fluctuations of the two junctions that are in phase, so that the low-frequency noise is higher than with the flux modulation scheme,<sup>3</sup> which does suppress these fluctuations. With bias reversal, both in-phase and out-of-phase fluctuations are suppressed,<sup>4</sup> and the low-frequency noise is strongly reduced, as is evident in Fig. 2 for frequencies below a few kHz. We see that at 1 Hz the noise contains a noticeable contribution from the ambient magnetic field noise inside the shielded room. With bias reversal the white noise of the flip-chip, bicrystal multiloop, and step-edge multiloop magnetometers was 16.2, 10, and  $30 \text{ fT}/\sqrt{\text{Hz}}$ , respectively; in each case with a static bias the white noise was slightly lower. From Eqs. (1) and (2), we estimated that the intrinsic white SQUID noise levels  $\sqrt{S_{B,i}}$  are typically 14% lower than the total white noise levels  $\sqrt{S_B}$  mainly due to the Nyquist noise of the APF resistor (Table I).

At frequencies between a few Hz and about 1 kHz the noise of the bicrystal multiloop magnetometer was seriously degraded by a random telegraph signal (RTS) with an amplitude of about  $9 \times 10^{-3} \Phi_0$  ( $\Phi_0$  is the flux quantum) which could not be removed by repeated thermal cycling. We believe this RTS was caused by a defect that developed in the eight months of storage since the original testing of the device.<sup>6</sup> To determine the noise in the absence of the RTS we measured a noise spectrum from pulse-free time traces using the "manual preview" averaging mode of our HP

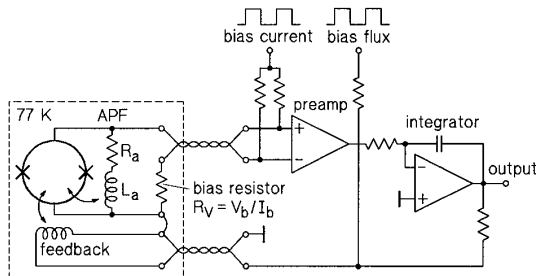


FIG. 1. APF flux-locked loop. The Josephson junctions are indicated by crosses on the SQUID loop.

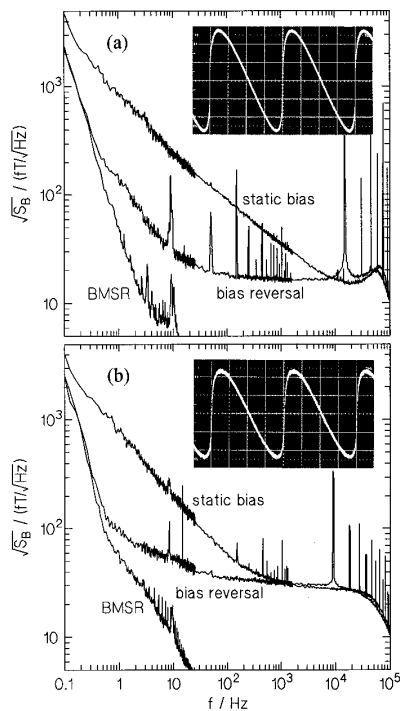


FIG. 2. Noise spectra (a) of the flip-chip magnetometer and (b) of the step-edge multiloop magnetometer measured in the magnetically shielded room. The background noise in the shielded room (curves "BMSR") was measured with a low- $T_c$  system at the corresponding positions. The lines in the spectrum are due to mechanical vibrations, power line interference, and bias reversal operation. The insets show the  $V$ - $\Phi$  characteristics with a horizontal scale of  $0.25 \Phi_0/\text{div}$  and a vertical scale of (a)  $4 \mu\text{V}/\text{div}$  and (b)  $1 \mu\text{V}/\text{div}$ .

35665A spectrum analyzer. This selective averaging reduced the noise with bias reversal by a factor of 5 to 10.5  $\text{fT}/\sqrt{\text{Hz}}$  at 100 Hz.

To illustrate the low noise achievable with these high- $T_c$  magnetometers operated with APF, in Fig. 3 we show two magnetocardiograms recorded from a healthy male volunteer with the flip-chip magnetometer (a) and step-edge multiloop magnetometer (b). The low noise levels (about 2 and 3 pT peak-to-peak in a 200 Hz bandwidth for the flip-chip and multiloop devices) demonstrate an excellent signal-to-noise ratio in a single-shot cardiogram. The quality of these biomagnetic measurement data demonstrates that high- $T_c$  magnetometers have now reached a noise level that would be adequate for many clinical applications.

In summary, we have used APF to operate high- $T_c$  SQUID magnetometers with low noise and a bandwidth of up to 200 kHz. Two of these magnetometers were used to obtain high quality magnetocardiograms in a magnetically shielded room.

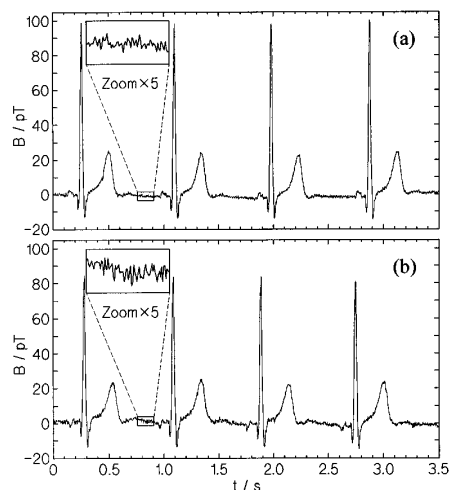


FIG. 3. Real-time trace of a magnetocardiogram measured in the magnetically shielded room without power line filters with (a) the flip-chip magnetometer and (b) the step-edge multiloop magnetometer. The measurement bandwidth is 0.016–200 Hz.

The authors thank S. Jurthe and H. Matz for developing parts of the SQUID electronics. One of us (E.D.) thanks the members of the PTB for their hospitality during his visit. The work in Berlin was partially supported by BMBF Contract Nos. 13N6398 and 13N6435, that at Philips Hamburg was supported by BMBF Contract No. 13N5709 3, and that in Berkeley by the Director, Office of Energy Research, Office of Basic Energy Sciences, Materials Sciences Division of the U.S. Department of Energy under Contract No. DE-AC03-76SF00098.

- <sup>1</sup> J. Clarke, W. M. Goubau, and M. B. Ketchen, *J. Low Temp. Phys.* **25**, 99 (1976).
- <sup>2</sup> D. Drung, R. Cantor, M. Peters, H. J. Scheer, and H. Koch, *Appl. Phys. Lett.* **57**, 406 (1990).
- <sup>3</sup> R. H. Koch, J. Clarke, W. M. Goubau, J. M. Martinis, C. M. Pegrum, and D. J. Van Harlingen, *J. Low Temp. Phys.* **51**, 207 (1983).
- <sup>4</sup> D. Drung, *Appl. Phys. Lett.* **67**, 1474 (1995).
- <sup>5</sup> D. Drung, S. Knappe, and H. Koch, *J. Appl. Phys.* **77**, 4088 (1995).
- <sup>6</sup> F. Ludwig, E. Dantsker, R. Kleiner, D. Koelle, J. Clarke, S. Knappe, D. Drung, H. Koch, N. McN. Alford, and T. W. Button, *Appl. Phys. Lett.* **66**, 1418 (1995).
- <sup>7</sup> B. David, D. Grundler, R. Eckart, F. Fanghänel, J. P. Krumme, V. Doormann, and O. Doessel, *Supercond. Sci. Technol.* **7**, 287 (1994).
- <sup>8</sup> F. Ludwig, D. Koelle, E. Dantsker, D. T. Nemeth, A. H. Miklich, J. Clarke, and R. E. Thomson, *Appl. Phys. Lett.* **66**, 373 (1995).
- <sup>9</sup> E. Dantsker, F. Ludwig, R. Kleiner, J. Clarke, M. Teepe, L. P. Lee, N. McN. Alford, and T. Button, *Appl. Phys. Lett.* **67**, 725 (1995).
- <sup>10</sup> D. Drung, in *SQUID Sensors: Fundamentals, Fabrication and Applications*, NATO ASI Series, edited by H. Weinstock (Kluwer, Dordrecht, in press).
- <sup>11</sup> D. Drung and H. Koch, *IEEE Trans. Appl. Supercond.* **AS-3**, 2594 (1993).
- <sup>12</sup> S. N. Ern , H.-D. Hahlbohm, H. Scheer, and Z. Trontelj, in *Biomagnetism*, edited by S. N. Ern , H.-D. Hahlbohm, and H. L bbig (de Gruyter, Berlin, 1981), p. 79.

### 5.3 Biomagnetic measurements

Biomagnetism refers to the measurement of magnetic signals produced by biological systems, mainly the human body. The source of these signals are either magnetic materials in the body, e.g. magnetized lung contaminants, or ionic currents in nerve and muscle cells. Because of the weak signal strength and the substantial information content at low frequencies, SQUIDs were employed for the measurements already very shortly after their invention [144,145]. Today, all practical and commercial systems for clinical use are still based on low- $T_c$  SQUIDs with expensive helium cooling. However, the best magnetometers from HTS have almost reached the noise level of the commercial low- $T_c$  sensors and are therefore adequate for clinical magnetocardiography [81,128]. Since heart disease is the most frequent cause of death in the industrial countries, a major interest lies in magnetocardiography systems employing HTS magnetometers. From the cheaper liquid nitrogen cooling and the easier handling, reduced costs for the system and its maintenance are expected. Because of the smaller cold-to-warm distance in liquid nitrogen cryostats, a larger signal can be measured with HTS magnetometers, which may roughly compensate for a higher noise level.

The magnetic equivalent to the more familiar electrocardiogram (ECG) is the magnetocardiogram (MCG) showing the magnetic signal from the heart. A typical real-time MCG recorded with the step-edge multiloop magnetometer WH1-#291 (refer to Section 5.1.3) inside the Berlin Magnetically Shielded Room at the PTB Berlin is shown in Fig. 5.23.

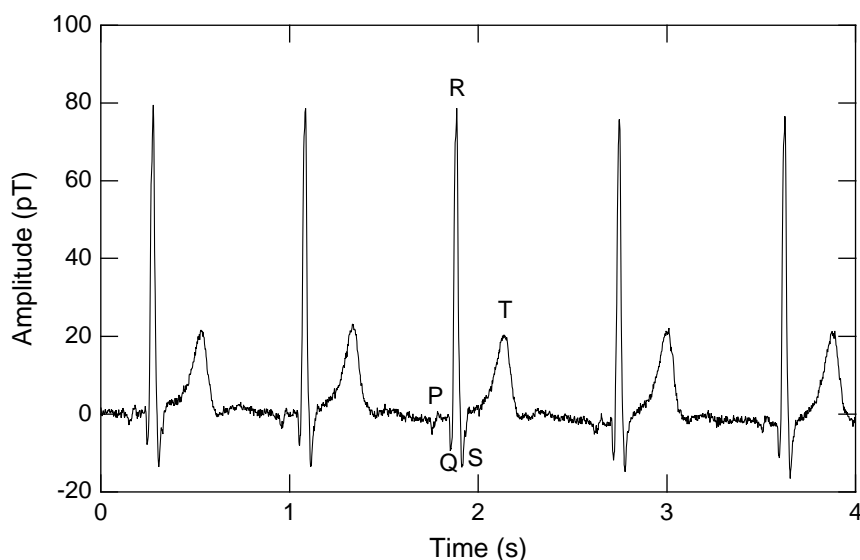


FIGURE 5.23: Real-time magnetocardiogram measured with a multiloop magnetometer at 77 K inside a magnetically shielded room. The measuring bandwidth was 200 Hz and no additional filtering was applied.

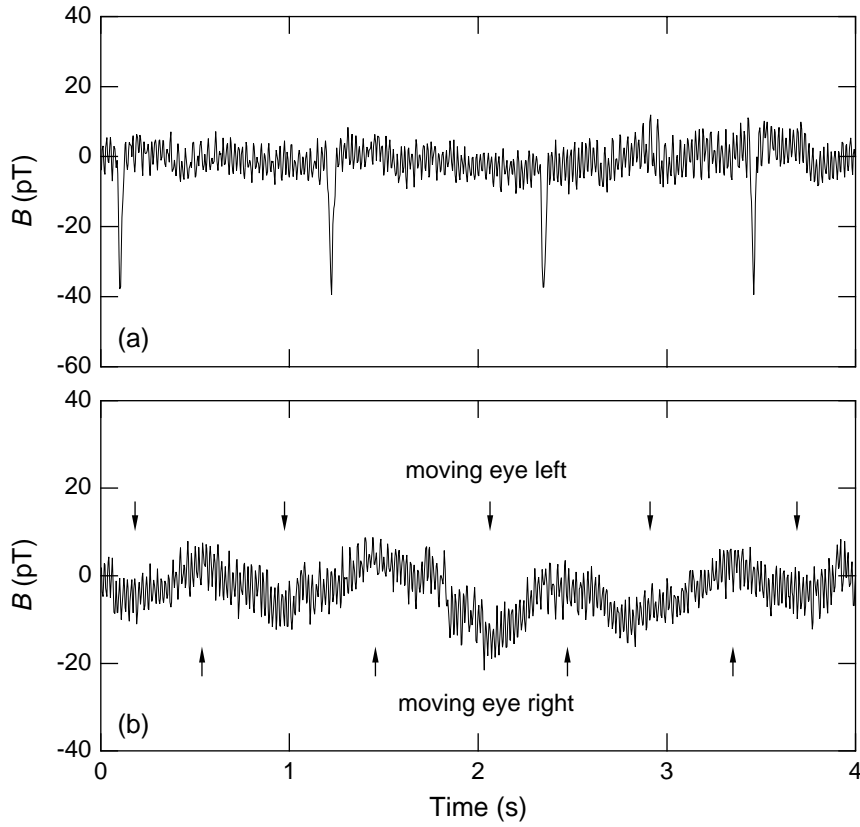


FIGURE 5.24: (a) MCG signal measured through the back of the subject. (b) Magnetic signal from the eye muscle when the eyeball is moved left and right.

It is the same magnetocardiogram as is shown in Fig. 3(b) of publication [P3] included in the previous section. The predominant QRS complex reflects a rapid activation phase, where a wavefront of depolarization caused by ion movement propagates through the cardiac tissue. The T-wave reflects the recovery, i.e. the repolarization [146]. The R-peak has a typical amplitude of roughly 100 pT in a distance of about 2 cm above the chest. Physicians are often more interested in the fine structure of the QRS complex, where the signal has an amplitude of some picotesla. To resolve this, the magnetic field noise of a magnetocardiography system should not exceed  $\sqrt{S_B} = 35 \text{ fT}/\sqrt{\text{Hz}}$  in a measuring bandwidth of 200 Hz, or about  $50 \text{ fT}/\sqrt{\text{Hz}}$ , where a smaller bandwidth of 100 Hz is acceptable. The peak-to-peak field noise level in Fig. 5.23 is about 3 pT, which has been obtained with a magnetometer noise level of  $\sqrt{S_B}(1 \text{ kHz}) = 31 \text{ fT}/\sqrt{\text{Hz}}$  in a 200 Hz measuring bandwidth. This yields an excellent signal-to-noise ratio of 28 for the QRS peak in the magnetocardiogram. The quality of the magnetocardiogram underlines that the noise level of the magnetometer is already adequate for many clinical applications.

Using liquid nitrogen for cooling, the cryostat size can be substantially reduced, which allows for small hand-held SQUID systems. The following publication [P4] describes

biomagnetic measurements made with an IMPUC magnetometer mounted in a miniature cryostat with a content of only 100 cm<sup>3</sup> liquid nitrogen. The MCG measurements were either made with the hand-held cryostat or with the cryostat mounted in a stand. They are compared to measurements with the same magnetometer mounted in a several times larger commercial cryostat. The main difference is a larger pick-up of power-line interference at 50 Hz with the small system. Additional biomagnetic measurements made with the same setup are shown in Fig. 5.24. Figure 5.24(a) depicts the heart signal measured through the back of the subject, and Fig. 5.24(b) shows the magnetic signal from the eye muscle, when the eye is moved from right to left and back again.

Further examples of biomagnetic applications of SQUID magnetometers are the fetal magnetocardiography for the noninvasive observation of the fetal heart [147] and the liver iron susceptometry, i.e. the *in vivo* quantification of the liver iron concentration [148]. Using a HTS SQUID microscope, Lee *et al.* investigated the motion of magnetotactic bacteria, which contain magnetic particles [149]. A comprehensive survey on magnetism in medicine is given by Andrä and Nowak [150].



## Biomagnetic measurements with an integrated $\text{YBa}_2\text{Cu}_3\text{O}_7$ magnetometer in a hand-held cryostat

M. Schilling, S. Krey, and R. Scharnweber<sup>a)</sup>

*Institut für Angewandte Physik und Zentrum für Mikrostrukturforschung, Universität Hamburg,  
Jungiusstraße 11, 20355 Hamburg, Germany*

(Received 23 July 1996; accepted for publication 21 August 1996)

With low-noise magnetometers made from high-temperature superconductors, mobile applications of superconducting quantum interference device (SQUID) magnetometry become possible. Due to the high volume heat of evaporation of liquid nitrogen, a SQUID magnetometer can be operated in a small size cryostat for some hours. For the first time biomagnetic measurements are presented using an integrated  $\text{YBa}_2\text{Cu}_3\text{O}_7$  magnetometer mounted in a hand-held cryostat with a content of  $100\text{ cm}^3$  of liquid nitrogen. These measurements and the noise properties are compared to those made in a conventional cryostat. The low-noise magnetometer consists of a multiloop pick-up coil coupled inductively to a dc SQUID based on ramp-type Josephson junctions with  $\text{PrBa}_2\text{Cu}_3\text{O}_7$  barriers. © 1996 American Institute of Physics. [S0003-6951(96)03544-9]

Biomagnetism is one of the most promising applications of magnetometers using superconducting quantum interference devices (SQUIDs). Aside from the well established use of low-temperature superconductors,<sup>1</sup> SQUIDs based on high-temperature superconductors (HTS) operating at 77 K are also used and biomagnetic measurements for magneto-cardiography have already been demonstrated.<sup>2-4</sup> Relying on grain boundaries of bicrystal substrates as Josephson junctions, the HTS SQUIDs achieve very low magnetic flux density noise<sup>2</sup> down to below  $10\text{ fT}/\sqrt{\text{Hz}}$ , and the use of ramp-type Josephson junctions with  $\text{PrBa}_2\text{Cu}_3\text{O}_7$  barriers in low-noise integrated magnetometers recently has also been demonstrated.<sup>5</sup> Biomagnetic measurements are commonly made in magnetically shielded rooms in order to reduce the electromagnetic noise of the environment. Many new applications arise for SQUID operation in mobile, battery powered magnetometer systems, and mobile operation in an unshielded environment is desirable to simplify the handling and to reduce the costs. Sufficient reduction of external noise by electronic<sup>6,7</sup> or integrated<sup>8</sup> gradiometer arrangements has been demonstrated. When liquid nitrogen with its high volume heat of evaporation is used, the size of a cryostat for hand-held systems can be reduced significantly compared to liquid helium cooled ones for same operation time. We present biomagnetic measurements at 77 K with an integrated  $\text{YBa}_2\text{Cu}_3\text{O}_7$  magnetometer mounted inside a hand-held cryostat. For comparison, these measurements were also performed in a conventional biomagnetic setup with the same magnetometer and flux-locked loop (FLL) electronics in a magnetically shielded environment.

In order to demonstrate the operation of HTS SQUIDs in a hand-held liquid nitrogen magnetometer system, we built a miniature cryostat that fits, together with batteries and the SQUID electronics, into a small hand-held case. The complete system is shown in Fig. 1. At the left-hand side, the SQUID electronics with its two 9 V batteries is shown. In the background a Dewar of  $1000\text{ cm}^3$  content to refill the cryostat, which suffices for 8h operation can be seen. The cry-

ostat consists of two containers thermally insulated by vacuum and six layers of superinsulation foil in between. The magnetometer chip is mounted inside the vacuum avoiding contact to moisture. The inner part of the cryostat containing the liquid nitrogen is made of stainless steel which provides much better durability in mobile applications than glass-fiber epoxy. Because metal usually contributes to the SQUID noise by Johnson noise<sup>9</sup> and externally induced eddy currents, the chip is mounted on a ceramic cold finger 1 cm in distance from any massive metal part of the stainless steel container. For the same reason, the outer, room-temperature container is made from glass-fiber epoxy. Filled with  $100\text{ cm}^3$  liquid nitrogen, the magnetometer is cooled down to a temperature of 77 K. For about 1 h the temperature stays within  $\pm 50\text{ mK}$  if the cryostat is not moved.<sup>10</sup> Moving reduces stability of both the temperature and operation time.

As a magnetometer chip we use an integrated multiloop pick-up coil (IMPUC) magnetometer that was recently demonstrated to operate at 77 K with low noise.<sup>5</sup> In this concept, a multiloop pick-up coil is inductively coupled to a dc SQUID of a small inductance resulting in a high output signal together with a good sensitivity for magnetic fields. The dc SQUID of the IMPUC magnetometer used here has an



FIG. 1. Hand-held SQUID magnetometer system used for biomagnetic measurements. The cryostat can be seen in an additional front part shown in the middle. The complete system is depicted at the right side.

<sup>a)</sup>Electronic mail: scharnweber@physnet.uni-hamburg.de

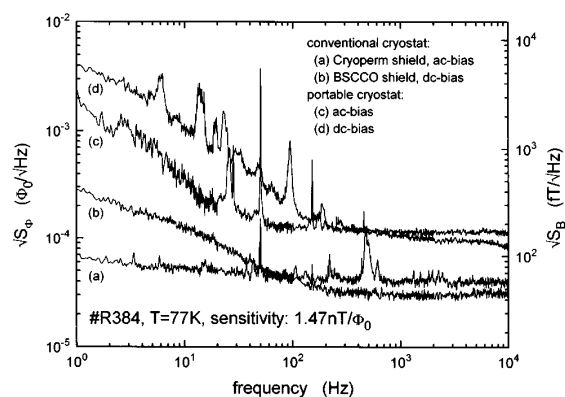


FIG. 2. FLL spectra of flux-density noise in an optimally shielded environment measured in ac-bias (a) and dc-bias modes (b). Flux-density noise of the same magnetometer in the portable cryostat inside a magnetically shielded room measured in FLL mode in ac- (c) and dc-bias modes (d).

inductance of 90 pH, a critical current of 20  $\mu\text{A}$  and a normal state resistance of 2.5  $\Omega$ , and a maximum flux-to-voltage modulation of 2.8  $\mu\text{V}$ . The effective area of the complete IMPUC magnetometer is 1.4  $\text{mm}^2$ . The preparation relies on a multilayer process using KrF-excimer laser deposition of  $\text{YBa}_2\text{Cu}_3\text{O}_7$ ,  $\text{PrBa}_2\text{Cu}_3\text{O}_7$ , and  $\text{SrTiO}_3$  films that are all patterned by conventional photolithography and argon-ion etching.<sup>11</sup> The Josephson junctions of the dc SQUIDs are realized in ramp-type geometry with  $\text{PrBa}_2\text{Cu}_3\text{O}_7$  barriers.<sup>12</sup> For electrical insulation in the crossovers, epitaxial  $\text{SrTiO}_3$  films are employed.<sup>13</sup>

The noise properties of the IMPUC magnetometer were characterized at 77 K in an optimally shielded environment.<sup>5</sup> Operated in a FLL mode, we used a ceramic, superconducting  $\text{Bi}_2\text{Sr}_2\text{CaCu}_2\text{O}_8$  (BSCCO) cylinder for the static bias current mode (dc bias) and a double cryoperm shield for additional bias current modulation (ac bias).<sup>14</sup> Both ac- and dc-bias measurements were made inside a magnetically shielded room in a large commercial liquid nitrogen tank at 77 K. The two flux density noise spectra are depicted in Figs. 2(a) and 2(b), respectively. Here, values of  $\sqrt{S_B}(1\text{Hz}) = 100 \text{ fT}/\sqrt{\text{Hz}}$  and  $\sqrt{S_B}(1\text{kHz}) = 44 \text{ fT}/\sqrt{\text{Hz}}$  in the white noise region are found. We assume these values to be the intrinsic noise level of the magnetometer.

For comparison, we mounted the same magnetometer chip No. R384 inside the portable cryostat and operated it attached to a stand in a fixed position. It should be noted that even refilling of liquid nitrogen does not affect the stable FLL operation of the IMPUC magnetometer. Magnetic flux density noise spectra measured in ac- and dc-bias modes are shown in Figs. 2(c) and 2(d), respectively. For operation in the same magnetically shielded room without further magnetic shielding by cryoperm or HTS ceramics, we find in the white noise regime a flux density noise of  $\sqrt{S_B}(77 \text{ K}, 1 \text{ kHz}) = 150 \text{ fT}/\sqrt{\text{Hz}}$  measured in dc-bias mode. At low frequencies, a strong increase of the flux density noise is observed. This noise was only partly suppressed by operation in the ac-bias mode where a value of  $\sqrt{S_B}(1\text{Hz}) = 3.1 \text{ pT}/\sqrt{\text{Hz}}$  was obtained. Furthermore, discrete peaks in the noise spectra were observed especially in this low-frequency region. These

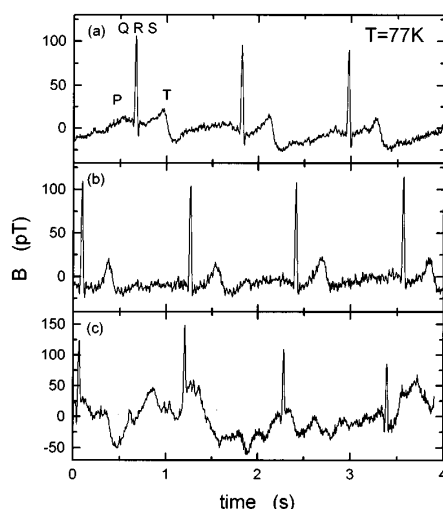


FIG. 3. Biomagnetic measurements of the human heart beat using the IMPUC magnetometer in ac-bias mode at liquid nitrogen temperature. (a) Measured in a conventional setup using a large conventional glass-fiber epoxy cryostat. (b) Measured with the portable SQUID magnetometer system mounted in a stand. (c) Hand-held measurement with the portable SQUID magnetometer system.

peaks were found to be time dependent and are most probably caused by external disturbances penetrating the chamber.

Using the IMPUC magnetometer, we performed biomagnetic measurements in a large conventional glass-fiber epoxy cryostat at 77 K. The magnetic human heart signals were recorded in ac-bias mode. An unfiltered and unaveraged trace measured is shown in Fig. 3(a). The maximum R-peak intensity is about 100 pT while the peak-to-peak noise level of about 8 pT for a measuring bandwidth of 200 Hz is dominated by the 50 Hz signal from the power line. This gives a signal-to-noise ratio of 12.5. The human heart signal of the same person was recorded using the portable SQUID magnetometer system, as depicted in Fig. 3(b). Here, the maximum intensity of the R peak is about 120 pT due to a smaller distance of the magnetometer to the heart. The peak-to-peak noise level for the same measuring bandwidth was determined to about 13 pT resulting in a signal-to-noise ratio of 9.2 which is smaller compared to the conventional cryostat. The performance is somehow degraded, but we believe that the main noise contribution is the again the 50 Hz signal of the power line. Finally, in Figs. 3(c) a real-time trace of the heart signal is depicted where the portable cryostat system was freely handheld over the chest of the person investigated. The FLL operation was observed to be stable but the movement of the cryostat in residual magnetic fields leads to a drift of the zero signal in the same order of magnitude as the intensity of the R peak. The use of two magnetometers in the same cryostat system as the electronic gradiometer is being worked on and it should reduce this drift.

In conclusion we have performed biomagnetic measurements with a low-noise IMPUC magnetometer prepared from  $\text{YBa}_2\text{Cu}_3\text{O}_7$  with ramp-type Josephson junctions containing  $\text{PrBa}_2\text{Cu}_3\text{O}_7$  barriers. Using a hand-held cryostat for

recording human heart traces, we have successfully demonstrated SQUID magnetometer operation in a very small and mobile liquid nitrogen system. This clears the way for new future applications. A further crucial task, operation in a magnetically unshielded environment, is under investigation.

The authors thank the Philips GmbH Forschungslaboratorien, Abteilung Technische Systeme, Hamburg, for the opportunity to perform measurements in their magnetically shielded room. This work was supported by the Bundesministerium für Bildung, Wissenschaft, Forschung und Technologie, Germany, under Contract No. 13N6734-0.

<sup>1</sup>G. L. Romani, S. J. Williamson, and L. Kaufman, *Rev. Sci. Instrum.* **53**, 1815 (1982).

<sup>2</sup>D. Drung, F. Ludwig, W. Müller, U. Steinhoff, L. Trahms, H. Koch, Y. Q. Shen, M. B. Jensen, P. Vase, T. Holst, T. Freltoft, and G. Curio, *Appl. Phys. Lett.* **68**, 1421 (1996).

<sup>3</sup>M. S. Dilorio, K.-Y. Yang, and S. Yoshizumi, *Appl. Phys. Lett.* **67**, 1926 (1995).

<sup>4</sup>B. David, D. Grundler, S. Krey, V. Doormann, R. Eckart, J. P. Krumme, G. Rabe, and O. Dössel, *Supercond. Sci. Technol. A* **9**, 96 (1996).

<sup>5</sup>R. Scharnweber and M. Schilling, *Appl. Phys. Lett.* **69**, 1303 (1996).

<sup>6</sup>R. H. Koch, J. R. Rozen, J. Z. Sun, and W. J. Gallagher, *Appl. Phys. Lett.* **63**, 403 (1993).

<sup>7</sup>Y. Tavrín, Y. Zhang, W. Wolf, and A. I. Braginski, *Supercond. Sci. Technol.* **7**, 265 (1994).

<sup>8</sup>P. Weber, V. M. Zakosarenko, K.-H. Berthel, K. Blüthner, J. Schambach, L. Warzemann, G. Kirsch, T. Döhler, and R. Stolz, *IEEE Trans. Appl. Supercond.* **5**, 2493 (1995).

<sup>9</sup>J. R. Clem, *IEEE Trans. Magn.* **23**, 1093 (1987).

<sup>10</sup>M. Schilling, D. Reimer, R. Scharnweber, K. O. Subke, and U. Merkt, BMBF-Statusseminar Köln, 1996 (unpublished).

<sup>11</sup>D. Reimer, M. Schilling, S. Knappe, and D. Drung, *IEEE Trans. Appl. Supercond.* **5**, 2342 (1995).

<sup>12</sup>M. Schilling, D. Reimer, and U. Merkt, *Appl. Phys. Lett.* **64**, 2584 (1994).

<sup>13</sup>S. Friemel and M. Schilling, *Supercond. Sci. Technol.* **7**, 787 (1994).

<sup>14</sup>O. Dössel, B. David, M. Fuchs, W. H. Kullmann, and K.-M. Lüdecke, *IEEE Trans. Magn.* **27**, 2797 (1991).

## 5.4 Unshielded measurements

The level of environmental magnetic noise signals is usually several orders of magnitude higher than the biomagnetic signals to be measured. Therefore most biomagnetic systems are operated in heavily shielded rooms with several layers of high-permeability material and shielding factors of up to 10000, depending on the frequency. Since the cost for a shielded room can easily take up the major part in the total system cost, biomagnetic SQUID systems will become significantly cheaper, when the operation in unshielded environment is possible. Figure 5.25 shows the magnetic field noise in a laboratory environment compared to the typical magnetic field resolution of HTS SQUID magnetometers. In the low-frequency regime, more than three orders of magnitude lie between the sensor's intrinsic noise level and the ambient noise. The difference to the 50 Hz power line interference and its harmonics is even larger. To overcome this large difference, active noise cancellation methods [151, 152] as well as gradiometer arrangements are employed.

Gradiometers for background noise cancellation can be built in various configurations, as is shown in Fig. 5.26. For low- $T_c$  systems, gradiometric pickup coils are easily fabricated from superconducting wire in many different ways, so that they measure the first spatial derivative of the magnetic field or higher order gradients [145]. For example, a first-order

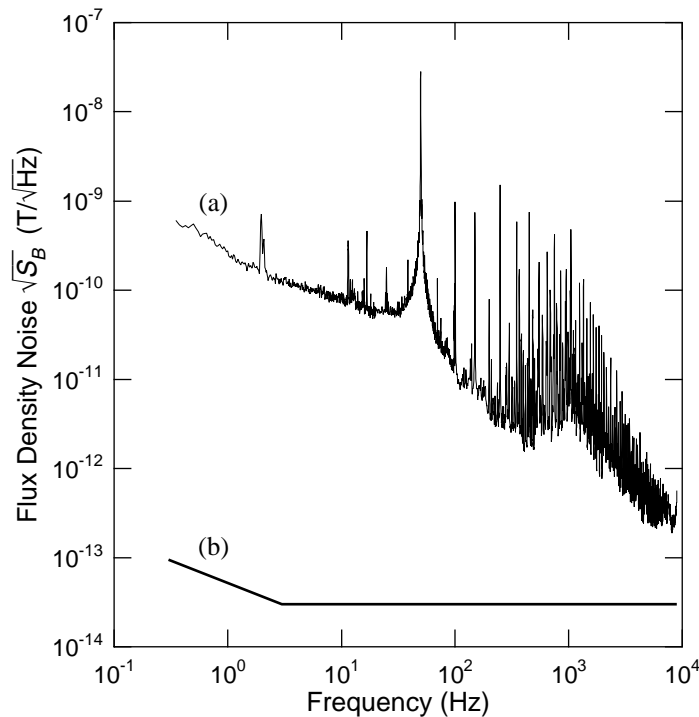


FIGURE 5.25: (a) Ambient magnetic noise in a typical laboratory environment, measured with an unshielded multiloop SQUID magnetometer in comparison with the (b) typical intrinsic noise level of HTS SQUID magnetometers.

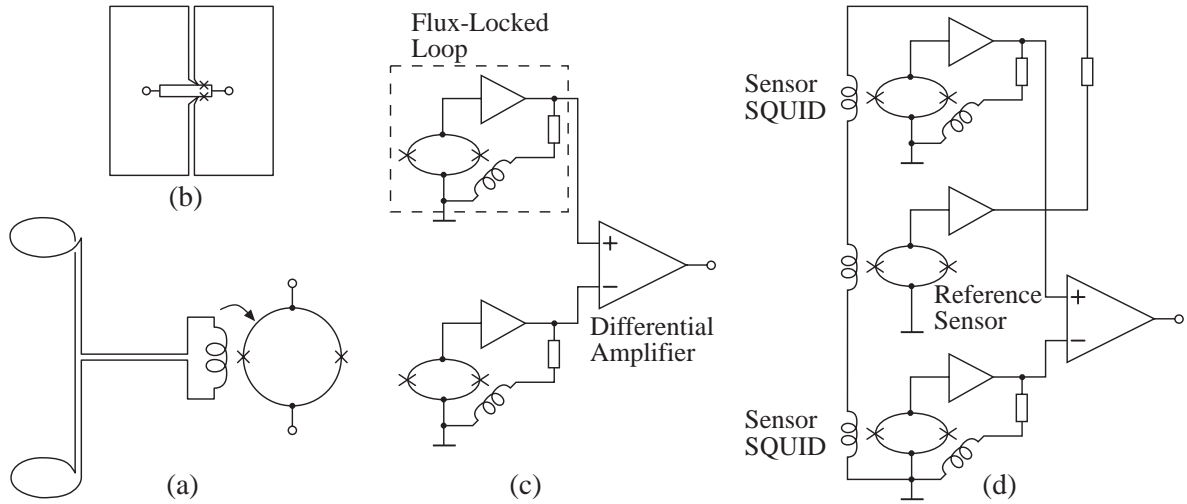


FIGURE 5.26: (a) First order axial gradiometer with wire-wound pickup coil. (b) Single-layer planar gradiometer. (c) First order electronic gradiometer. (d) Three Sensor Gradiometer.

gradiometer consists of two equal coils with opposite winding directions connected in series with the input coil of a SQUID (Fig. 5.26(a)). A homogeneous field will generate opposite shielding currents in both coils which cancel in the input coil. Since the sources of environmental noise are usually located in a much greater distance than the subject under study, the noise signal is largely homogeneous and can be thus rejected to a certain extent. In the case of HTS, integrated planar gradiometers [153–155] or electronic gradiometers must be used, due to the lack of a suitable interconnect technology for HTS wires. The baseline of the integrated planar gradiometer (Fig. 5.26(b)) is limited by the substrate size, which is usually not larger than  $1 \times 1 \text{ cm}^2$ . The sensitivity for deeper sources is accordingly low. An electronic or software gradiometer (Fig. 5.26(c)) consists of two independent SQUID magnetometers with separate FLL electronics, whose output signals are either subtracted electronically or by software after digitization. A big disadvantage of this scheme is that both magnetometers sense the full amplitude of the environmental noise signal, which makes high demands on the slew-rate and linearity of the FLL electronics. For example, the magnetic 50 Hz signal from the power lines may easily be as high as 100 nT peak-to-peak. For a 1 pT resolution in a magnetocardiogram, a difference of 1 part in  $10^5$  has to be measured. Hence, 100 dB of common-mode rejection and linearity range are required, which is at the limit of conventional electronics. Further prerequisites are an equal time delay of both FLL electronics [156] and the stable long-term operation of each sensor in the flux-locked mode. The latter has been exemplarily demonstrated above with the multiloop magnetometer. The measurement of the spectrum in Fig. 5.25 took about one hour without unlocking of the FLL electronics. Measurements employing a planar electronic gradiometer are discussed below. To overcome the drawbacks of the simple



FIGURE 5.27: A multichannel HTS SQUID magnetometer system for unshielded magnetocardiography measurements. The liquid nitrogen cryostat is mounted in a non-magnetic wooden stand. The stand is surrounded by a single wire-wound coil for noise and earth field compensation. A second coil is used as an inductive field sensor for the noise rejection scheme. It surrounds the bottom of the cryostat.

electronic gradiometer, Koch *et al.* [157, 158] proposed the Three Sensor Gradiometer (Fig. 5.26(d)) employing a third sensor. This reference sensor measures the ambient field and compensates it *via* a global feedback loop for all three sensors. The reference sensor may have a reduced field resolution, since its noise signal is coupled equally to both sensor SQUIDs and is thus cancelled for the most part by the differential amplifier. If the reference sensor is sensitive to the absolute magnetic field, like a fluxgate sensor or the Josephson junction array magnetometer described in Chapter 6, the earth's field is simultaneously compensated. A variation of this global feedback scheme employing only two SQUID magnetometers is described by Yokosawa and Kuriki [159].

Different noise compensation methods have been investigated with a prototype of a HTS multichannel system for magnetocardiography in unshielded environment, developed at Philips Hamburg [160]. Figure 5.27 shows a photograph of this system. The liquid nitrogen cryostat is designed for up to 19 magnetometer channels in a planar hexagonal arrangement. The cryostat is mounted in a nonmagnetic wooden stand above the sub-

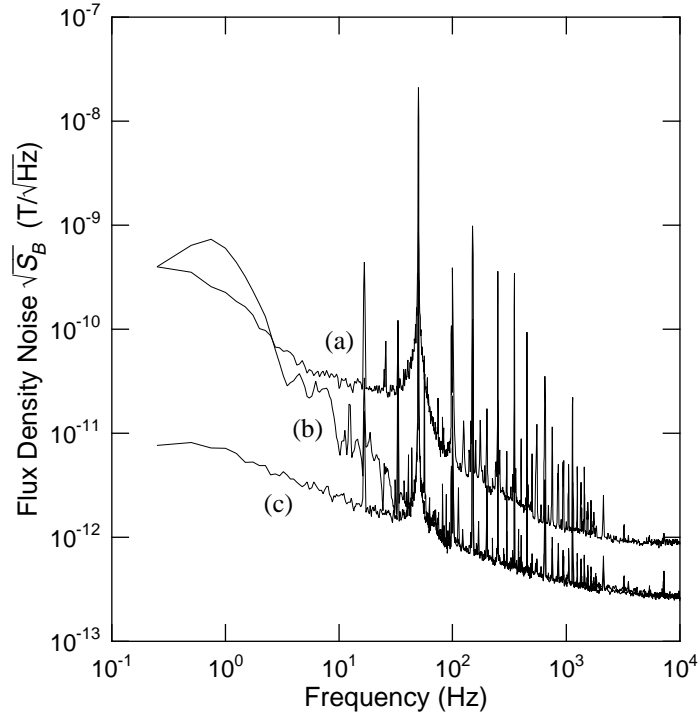


FIGURE 5.28: Noise spectra measured in unshielded environment with different compensation schemes: (a) without compensation, (b) using a sensor coil for the reference, (c) with common-mode rejection.

ject's bed. A new noise suppression method, called planar digital gradiometer, has been proposed, in which the noise field, measured simultaneously by all sensors, is approximated by a Taylor expansion and subtracted from the individual magnetometer signal. First results obtained with this system, including MCG measurements in unshielded environment, are reported by David *et al.* [161]. Since the system was only equipped with 9 sensors, and because of alignment problems of their cardanic suspensions, the digital gradiometer technique could not be applied, but two other methods for the noise reduction have been used. The first one is based on an inductive sensor coil wound around the cryostat at the height of the SQUID magnetometers. It measures a mean noise signal, which is integrated and fed back into a compensation coil for noise rejection. Since the sensor coil is only sensitive at higher frequencies, an additional common-mode rejection has been employed, where the mean signal of all SQUIDs is fed into the compensation coil. These compensation schemes are equivalent to the function of a zero order Taylor expansion spatially across the sensor coil, or a first order gradiometer. The employed magnetometers are directly coupled magnetometers of the type discussed in Section 5.1.1, however step-edge Josephson junctions are used. Figure 5.28 displays noise spectra for the magnetometer channel #2 without noise compensation and for both compensation modes. One finds that the noise reduction by the sensor coil is effective above 3 Hz.

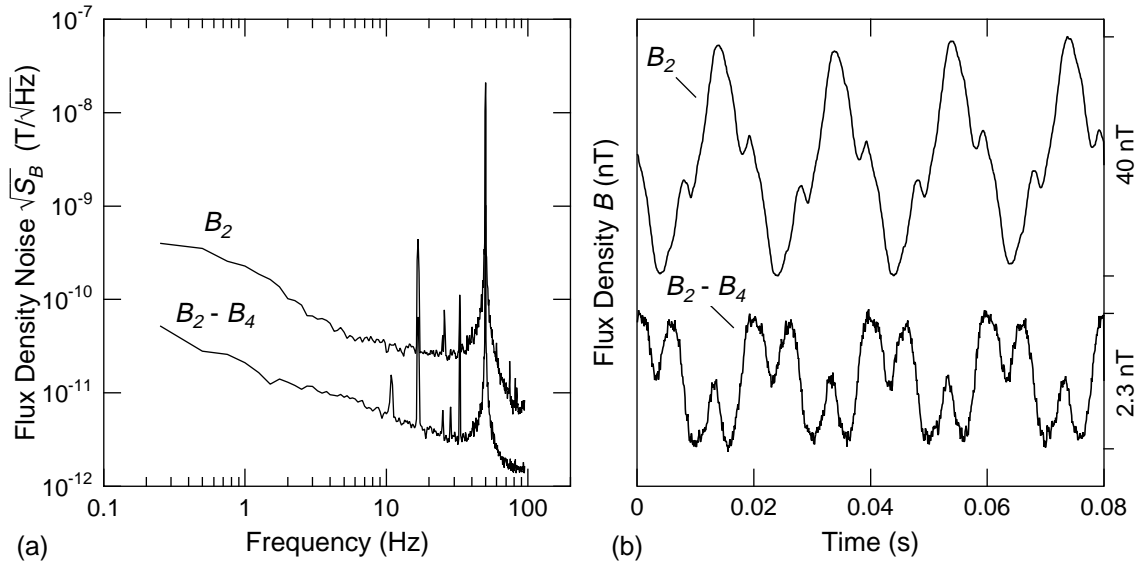


FIGURE 5.29: Noise spectra (a) and magnetic field amplitude (b) for a single sensor ( $B_2$ ) and for the electronic gradiometer output ( $B_2 - B_4$ ) in unshielded environment.

However, a much better noise reduction is obtained with the common-mode compensation. Above 100 Hz, both compensation schemes become similar effective. At 10 Hz, a noise reduction of roughly one order of magnitude is obtained with the common-mode compensation. A slightly better performance with a noise reduction by the factor 40 at 10 Hz could be achieved by selecting only the 7 sensors with lowest  $1/f$  noise for the common-mode compensation. Additional measurements have been performed with an electronic gradiometer, employing two sensors (#2 and #4) in a distance  $\Delta x = 7.5$  cm, whose output signals were electronically subtracted by a differential amplifier. Thus, one measures spatial magnetic field gradients of the form  $\Delta B_z / \Delta x$ . Even though the effective baselength of this gradiometer is much smaller than in the schemes above, no better noise reduction could be achieved. Figure 5.29 depicts the signal from a single sensor and the difference signal of both channels. In both cases, the main signal component is the stray field at 50 Hz from the power lines. Employing the gradiometer, a noise reduction by roughly a factor 20 is obtained. Thus, higher order field gradients must be present on a length scale  $\Delta x$ , which cannot be compensated with the global first order gradiometer schemes described above. Similar results have been obtained by Ludwig *et al.* with a planar gradiometer of 28 mm baselength [162]. All measurements described above have been made without earth field compensation in a harsh industrial environment, which is comparable to an application in a clinic without further precautions for the shielding. It may be concluded that at least a second order gradiometer arrangement is required for unshielded magnetocardiography systems in such an environment.



## 5.5 Noise characterization in static magnetic fields

A severe obstacle for many practical applications of SQUID magnetometers from HTS is often the increase of low-frequency noise that arises, when the magnetometer is operated in an ambient magnetic field, such as the earth's field. According to Section 2.7, this excess noise is caused by the thermally activated random hopping of Abrikosov vortices between their pinning sites. Magnetic flux vortices are either created when the magnetometer is cooled below its critical temperature in an ambient field, or they are introduced into the film by the Lorentz force from shielding currents [163]. Large shielding currents may be induced in the pickup loop of a magnetometer when an ambient magnetic field is changed or when the magnetometer is moved in a static field like the earth's field. The shielding current is of such direction as to induce flux vortices at the edges of the pickup loop. For this reason Koch *et al.* [164, 165] introduced the concept of a flux dam which prevents the shielding current from exceeding a certain level. A flux dam is a weak link of reduced critical current density in the pickup loop. When the shielding current exceeds the critical current of the link, it becomes dissipative and allows flux to enter the loop. Directly coupled magnetometers on bicrystal substrates usually contain a flux dam if the pickup loop crosses the grain boundary. Also the multiloop magnetometer includes an inherent flux dam, since the shielding currents in the loops are forced to flow across the Josephson junctions.

A magnetic flux noise signal from vortex motion may be generated in the SQUID either by directly sensing the flux line motion or by changes in the shielding currents from the displacement of vortices [166]. The pinning energies of the vortices highly depend on the degree of orientation in the superconducting thin-films. Since vortices move along the *ab*-plane comparatively freely, a high degree of *c*-axis orientation is required throughout the whole device [85]. This particularly makes high demands on the preparation of multilayer devices, where the *c*-axis orientation must be maintained in every layer. Additionally, all edges in the bottom layer must be shallow to avoid large-angle grain boundaries at crossovers.

The publication [P7] in the following Section 5.5.1 compares noise measurements on two different multilayer magnetometers and investigates their low-frequency noise as a function of the applied magnetic flux density. Similar measurements on single-layer devices have been reported for bare dc SQUIDs [167, 168], directly coupled magnetometers [164, 165, 167, 169, 170], and rf SQUIDs [171, 172]. Dantsker *et al.* obtained remarkable low noise values in fields up to about  $B_0 = 100 \mu\text{T}$  by reducing the linewidth of the SQUID body [173, 174]. This method has been applied to the pickup loop of a practical directly coupled magnetometer of the type described in Section 5.1.1 [175]. The results of field

dependent noise and linearity measurements on this device are given in Section 5.5.2, which mainly consists of the publication [P11].

In the measurements described below, all devices behaved very stable, even when they were operated in high fields. In particular, no spontaneous flux entry into the Josephson junctions in the form of Josephson vortices, as is reported by Vaupel *et al.* [57] for narrow junctions ( $w < 1 \mu\text{m}$ ), has been observed. Usually, this effect leads to a largely reduced junction critical current and to a large voltage signal when the device is current biased.

### 5.5.1 Low-frequency noise of multilayer $\text{YBa}_2\text{Cu}_3\text{O}_7$ magnetometers in static magnetic fields

The following publication reports the first noise measurements on field-cooled multilayer magnetometers. Two different types of integrated multilayer magnetometers have been investigated in fields up to  $110 \mu\text{T}$ : the inductively coupled magnetometer described in Section 5.1.2 and the WH3 type multiloop magnetometer #366 of Section 5.1.3. The noise measurements on the field-cooled devices were performed either after switching off the magnetic field or in the permanent field. Both devices show only a moderate increase of the low-frequency noise as a function of the applied field, which is attributed to a high quality of the involved thin-films. The flux density noise level of the multiloop magnetometer increases from  $\sqrt{S_B}(5 \text{ Hz}) = 92 \text{ fT}/\sqrt{\text{Hz}}$  at  $B_0 = 0 \mu\text{T}$  to  $308 \text{ fT}/\sqrt{\text{Hz}}$  at  $110 \mu\text{T}$ , and for the inductively coupled device the values  $161 \text{ fT}/\sqrt{\text{Hz}}$  at  $0 \mu\text{T}$  and  $600 \text{ fT}/\sqrt{\text{Hz}}$  at  $110 \mu\text{T}$  are obtained. This increase is comparable to the results obtained with single-layer devices of solid geometry and comparable linewidths [164,165]. A further noise reduction is expected from reduced linewidths in the magnetometer body. However, this has still to be proven for multilayer devices. The subsequent section will show the effect of small linewidths on the low-frequency noise of a single-layer magnetometer.

## Low noise operation of integrated $\text{YBa}_2\text{Cu}_3\text{O}_7$ magnetometers in static magnetic fields

S. Krey<sup>a)</sup>

*Institut für Angewandte Physik und Zentrum für Mikrostrukturforschung, Universität Hamburg, Jungiusstraße 11, D-20355 Hamburg, Germany*

B. David and R. Eckart

*Philips GmbH Forschungslaboratorien, Abteilung Technische Systeme Hamburg, Röntgenstraße 24, D-22335 Hamburg, Germany*

O. Dössel

*Institut für Biomedizinische Technik, Universität Karlsruhe, Kaiserstraße 12, D-76128 Karlsruhe, Germany*

(Received 11 March 1998; accepted for publication 13 April 1998)

The noise of two integrated  $\text{YBa}_2\text{Cu}_3\text{O}_7$ - $\text{SrTiO}_3$ - $\text{YBa}_2\text{Cu}_3\text{O}_7$  multilayer magnetometers in static magnetic fields up to  $110 \mu\text{T}$  is investigated: An inductively coupled magnetometer with integrated flux transformer and a multiloop magnetometer. In both samples, only a moderate increase of the low frequency flux noise is found in high fields, due to the high epitaxial quality of the involved multilayer films. So for moderately shielded or unshielded applications in the earth's magnetic field, high-quality integrated  $\text{YBa}_2\text{Cu}_3\text{O}_7$  magnetometers can be operated with low excess noise.

© 1998 American Institute of Physics. [S0003-6951(98)01924-X]

The most sensitive superconducting quantum interference devices (SQUIDs) from high transition temperature ( $T_c$ ) superconductors are integrated magnetometers from  $\text{YBa}_2\text{Cu}_3\text{O}_7$  (YBCO) multilayers. Today, the noise level of these devices has reached a level close to that achieved with commercial low- $T_c$  systems.<sup>1,2</sup> However, this sensitivity was obtained in heavily shielded settings which often cannot be used for economical or practical reasons. So, for many applications SQUID magnetometers have to be operated in moderately shielded or unshielded environment, where they are influenced by the earth's magnetic field of about  $50 \mu\text{T}$ . The performance of high- $T_c$  devices usually suffers from increased flux noise, if they are cooled through  $T_c$  in a magnetic field  $B_0$ . This causes flux vortices to be trapped in the superconducting thin films, and excess noise is generated by the thermally activated random hopping of the vortices between their pinning sites.<sup>3</sup> The spectral density  $S_\Phi$  of the excess flux noise typically scales with  $1/f$  as a function of the frequency  $f$  and therefore adversely affects low frequency applications such as biomagnetism or geophysical measurements. The number of vortices is proportional to the applied field, and one expects  $S_\Phi(f)$  to scale linearly with  $B_0$  if the vortex motion is uncorrelated.

At present, only measurements on single layer devices in a magnetic field have been reported. Miklich *et al.*<sup>4</sup> investigated the performance of a bare SQUID and a directly coupled magnetometer in static magnetic fields. They found an increase of the  $1/f$  noise at 1 Hz by an order of magnitude for  $B_0 = 50 \mu\text{T}$ . Similar measurements were made by Faley *et al.*<sup>5</sup> and Schmidt *et al.*,<sup>6</sup> but they did not observe any significant increase of flux noise up to  $100 \mu\text{T}$ . Recently, Dantsker *et al.*<sup>7</sup> examined the influence of the device geometry on the excess noise. For washer SQUIDs, they found a

large increase of the flux noise of more than one order of magnitude, if the devices were cooled in fields up to  $60 \mu\text{T}$ . By reducing the washer's linewidth, they could keep the flux noise low up to a threshold field of  $33 \mu\text{T}$ , but at higher fields the noise rapidly increased. In Ref. 8 they further showed that this threshold field can be shifted towards higher values, if the SQUID washer is provided with slots or holes, giving sufficiently small structure widths to prevent vortex penetration.

Here we present the first noise measurements on two integrated multilayer devices operated in static magnetic fields: An inductively coupled magnetometer with integrated flux transformer and a multiloop magnetometer. Each device is patterned on  $10 \times 10 \text{ mm}^2$   $\text{SrTiO}_3$  (STO) substrate and incorporates YBCO step-edge junctions. The YBCO-STO-YBCO multilayer fabrication process is described in detail elsewhere.<sup>9</sup> We deposit the YBCO films and the intermediate STO insulation layer by high oxygen pressure off-axis rf magnetron sputtering and pattern them by standard photolithography and Ar-ion beam etching. The magnitude of the low frequency flux noise in YBCO thin films strongly depends on their epitaxial quality and degree of  $c$ -axis orientation,<sup>10</sup> usually leading to a higher excess noise level in a multilayer device, if the upper film contains areas of lower quality.<sup>11,12</sup> This in mind, we generally pattern the large superconducting areas from the lower YBCO film, directly grown on the substrate. The steep step required for the junctions is milled under normal incidence into the insulation layer and the Josephson junctions are patterned from the upper YBCO film.

The inductively coupled magnetometer is described in detail in Ref. 13. The  $10 \frac{1}{2}$  turn input coil is placed on a  $700 \times 700 \mu\text{m}^2$  square washer and connected to a pickup loop with 8.8 mm outer diameter and a pickup area of  $A_p = 54 \text{ mm}^2$ . The estimated SQUID inductance is  $L_S = 85 \text{ pH}$ . The multiloop layout used in this study is an im-

<sup>a)</sup>Electronic mail: krey@physnet.uni-hamburg.de

TABLE I. Transport properties of the investigated inductively coupled and the multiloop magnetometer measured at the temperature  $T = 77$  K.

Device		Inductively coupled	Multiloop	
Voltage swing	$\Delta V$	6.8	6.9	$\mu\text{V}$
Critical current <sup>a</sup>	$I_0$	42	13	$\mu\text{A}$
Normal resistance <sup>a</sup>	$R_n$	2.6	5.3	$\Omega$
Sensitivity	$B/\Phi$	1.290	0.897	$\text{nT}/\Phi_0$
Effective area	$A_{\text{eff}} = \Phi/B$	1.60	2.31	$\text{mm}^2$

<sup>a</sup>Values given per junction.

proved version of the WH1 layout described in Ref. 14. We enlarged the outer diameter to a value of 8.5 mm and adjusted the pickup coil width  $w_p$  and total spoke width  $D_s$  to give the maximum effective area while keeping the SQUID inductance constant at  $L_S = 145$  pH. With  $w_p = 1095$   $\mu\text{m}$  and  $D_s = 280$   $\mu\text{m}$ , we obtain a measured effective area of  $A_{\text{eff}} = 2.31$   $\text{mm}^2$  in good agreement with the calculated value of 2.35  $\text{mm}^2$ . This is, as far as we know, the largest effective area reported yet for a high- $T_c$  SQUID magnetometer on a  $1 \times 1$   $\text{cm}^2$  substrate. The transport properties of both magnetometers are listed in Table I.

All noise measurements were performed inside a magnetically shielded room, where the magnetometers were installed in a low noise cryostat for biomagnetic measurements, filled with liquid nitrogen. The intrinsic noise characteristic of both devices was measured with an additional Cryoperm shield, using the standard flux locked loop (FLL) technique. For the multiloop magnetometer we found  $\sqrt{S_B}(1 \text{ kHz}) = 39 \text{ fT}/\sqrt{\text{Hz}}$  in the white noise regime and  $\sqrt{S_B}(5 \text{ Hz}) = 92 \text{ fT}/\sqrt{\text{Hz}}$  for the low frequency noise. No further noise reduction with bias current reversal (ac bias) could be achieved at 5 Hz, due to residual ambient noise. Despite a comparable voltage swing  $\Delta V$ , the inductively coupled magnetometer showed a higher white noise level of  $\sqrt{S_B}(1 \text{ kHz}) = 66 \text{ fT}/\sqrt{\text{Hz}}$ , which raised to  $85 \text{ fT}/\sqrt{\text{Hz}}$  with bias current reversal. We attribute this to the resonant flux voltage characteristic of this device, which is often observed for magnetometers with integrated flux transformers.<sup>1</sup> It prevents the optimal adjustment of the flux-modulation scheme, especially with bias reversal. However, with ac bias the low frequency noise was reduced from  $\sqrt{S_B}(5 \text{ Hz}) = 188$  to  $161 \text{ fT}/\sqrt{\text{Hz}}$ , indicating that the former value includes a contribution from critical current fluctuations in the junctions.

For the measurements in static fields, we removed the additional shield. Instead, we centered the magnetometer within a copper coil, fed by a high capacity lead-acid accumulator in series with an appropriate resistor for the field  $B_0$ . For  $B_0 = 0$  but without the extra shield, we found a higher low frequency noise level that increased faster than  $1/f$  with approximately  $S_B \propto f^{-2.4}$  and a corner frequency of about 18 Hz, due to ambient noise penetrating the shielded room. The magnetometers were enclosed in capsules of glasfiber epoxy together with two heating resistors in close contact to the substrate. With a heating power of 0.7 W, we were able to rise the magnetometer's temperature above  $T_c$  in about 2 min. With the magnetometer in normal conducting state, we applied the magnetic field  $B_0$  and subsequently switched off the heating current. In two different experiments we measured the noise of the field cooled magnetometers either after

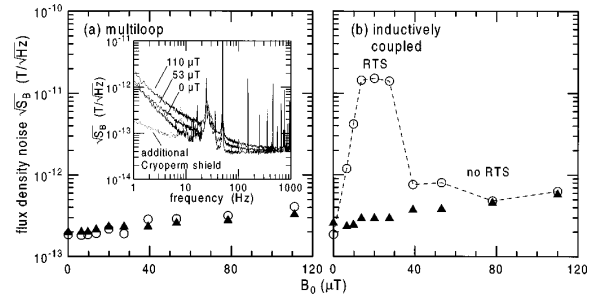


FIG. 1. (a) Flux density noise of the multiloop and (b) the inductively coupled magnetometer as a function of the cooling field  $B_0$ . Filled symbols indicate measurements in the permanent field, open symbols mark measurements with the field switched off. The inductively coupled device shows a random telegraph signal (RTS) for  $B_0 < 40$   $\mu\text{T}$ , induced by the switching transients. The inset of (a) depicts three noise spectra recorded in zero field with the field cooled multiloop magnetometer for  $B_0 = 0, 53$ , and  $110$   $\mu\text{T}$ . The spikes are due to microphonic pickup and power line interference.

switching off the magnetic field or in the permanent field. In the first case, both magnetometers presented here should behave differently. In a changing magnetic field a shielding current is generated in the pickup loop of the device that can induce vortices into the film by the Lorentz force. The multiloop magnetometer contains an *intrinsic* flux dam,<sup>15</sup> limiting the shielding currents in the loops, because they are forced across the Josephson junctions, whereas the current within the flux transformer of the inductively coupled device can become much larger.

Figure 1(a) shows the measured flux density noise  $\sqrt{S_B}(f)$  of the multiloop magnetometer as a function of the cooling field  $B_0$ . For both experiments, a continuous increase in low frequency noise with nearly the same noise levels is found, indicating that our current source for the coil does not contribute significantly to the noise. Also the device's critical currents were not markedly reduced in the field. The inset of Fig. 1(a) depicts three noise spectra recorded in zero field with the field cooled multiloop magnetometer for  $B_0 = 0, 53$ , and  $110$   $\mu\text{T}$ . In the permanent field  $B_0 = 110$   $\mu\text{T}$  we measured  $\sqrt{S_B}(5 \text{ Hz}) = 340 \text{ fT}/\sqrt{\text{Hz}}$ , which includes an environmental contribution of about  $\sqrt{S_{B,\text{env}}}(5 \text{ Hz}) = 144 \text{ fT}/\sqrt{\text{Hz}}$ , yielding a net increase of  $[S_B(B_0) - S_{B,\text{env}}]^{1/2} = 308 \text{ fT}/\sqrt{\text{Hz}}$  at 5 Hz. This is about a factor 3.3 above the value taken with the additional shielding. In zero field, this excess noise could always be removed by the heating procedure. For the inductively coupled device, we found a much stronger increase of the low frequency noise in low fields, if we switched off the field prior the measurements. We measured a random telegraph signal (RTS) that was probably caused by the switching transients.<sup>16</sup> Interestingly, for larger field changes than  $40$   $\mu\text{T}$  this RTS was not observed anymore and the device stayed much quieter. We presume, that the stronger Lorentz force due to the larger shielding currents prevents the vortices from escaping from their metastable pinning sites.

Figures 2(a) and 2(b) show the spectral density of the excess flux noise  $S_{\Phi,\text{exc}}(B_0) = S_{\Phi}(B_0) - S_{\Phi,\text{env}}$  as a function of  $B_0$  in the permanent field, not including the environmental contribution. For both magnetometers we find an overall linear increase of  $S_{\Phi,\text{exc}}$  with  $B_0$ . No threshold field for flux

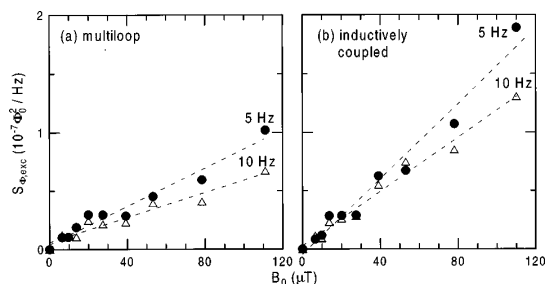


FIG. 2. Spectral density of the excess flux noise  $S_{\Phi, \text{exc}}(B_0) = S_{\Phi}(B_0) - S_{\Phi, \text{env}}$ , due to the cooling field  $B_0$ , not including the environmental contribution  $S_{\Phi, \text{env}}$ . Dashed lines are least-squares fits to the data. Measured at 5 Hz (solid symbols) and 10 Hz (open symbols).

entry is observed, probably due to the large linewidths of the magnetometers. The slope at 5 Hz is about twice as large for the inductively coupled device, what may suggest that the latter is more sensitive to flux entry if we assume the same mechanism for flux noise as in Ref. 4. The main candidate for flux penetration may be the input coil of the flux transformer which is patterned from the upper YBCO layer and which is the most crucial part of the inductively coupled device, due to its many edges and narrow crossovers. Moreover, flux lines moving there couple very effectively into the SQUID. However, both devices show a performance that is not seriously affected by fields up to 110  $\mu\text{T}$ . The induced low frequency flux noise is of the same order as the ambient noise penetrating the shielded room.

In summary, we have measured the noise levels of a multiloop magnetometer and an inductively coupled magnetometer from YBCO-STO-YBCO multilayers in static magnetic fields up to 110  $\mu\text{T}$ . Both devices show only a moderate increase of the low frequency flux noise that underlines the high quality of the involved thin-films. The good performance of both devices in high fields, together with their large

effective area at a small chip size makes multilayer devices attractive for future multichannel applications in moderately shielded or unshielded environment.

This work was supported by the Bundesministerium für Bildung, Wissenschaft, Forschung und Technologie, Federal Republic of Germany under Contract No. 13N6736.

- <sup>1</sup>D. Drung, F. Ludwig, W. Müller, U. Steinhoff, L. Trahms, H. Koch, Y. Q. Shen, M. B. Jensen, P. Vase, T. Holst, T. Freltov, and G. Curio, *Appl. Phys. Lett.* **68**, 1421 (1996).
- <sup>2</sup>D. Drung, E. Dantsker, F. Ludwig, H. Koch, R. Kleiner, J. Clarke, S. Krey, D. Reimer, B. David, and O. Dössel, *Appl. Phys. Lett.* **68**, 1856 (1996).
- <sup>3</sup>M. J. Ferrari, M. Johnson, F. C. Wellstood, J. Clarke, D. Mitzi, P. A. Rosenthal, C. B. Eom, T. H. Geballe, A. Kapitulnik, and M. R. Beasley, *Phys. Rev. Lett.* **64**, 72 (1990).
- <sup>4</sup>A. H. Miklich, D. Koelle, T. J. Shaw, F. Ludwig, D. T. Nemeth, E. Dantsker, J. Clarke, N. McN. Alford, T. W. Button, and M. S. Colclough, *Appl. Phys. Lett.* **64**, 3494 (1994).
- <sup>5</sup>M. I. Faley, U. Poppe, K. Urban, H. Hilgenkamp, H. Hemmes, W. Aarnink, J. Flokstra, and H. Rogalla, *Appl. Phys. Lett.* **67**, 2087 (1995).
- <sup>6</sup>J. M. Schmidt, L. P. Lee, A. Matlashov, M. Teepe, V. Vinetskiy, R. Cantor, and M. S. Dilorio, *Proceedings of Biomag 96*, Santa Fe, NM, 16–21 February, 1996.
- <sup>7</sup>E. Dantsker, S. Tanaka, P.-Å. Nilsson, R. Kleiner, and J. Clarke, *Appl. Phys. Lett.* **69**, 4099 (1996).
- <sup>8</sup>E. Dantsker, S. Tanaka, and J. Clarke, *Appl. Phys. Lett.* **70**, 2037 (1997).
- <sup>9</sup>B. David, D. Grundler, R. Eckart, K. Fanghänel, J. P. Krumme, V. Doormann, and O. Dössel, *Supercond. Sci. Technol.* **7**, 287 (1994).
- <sup>10</sup>M. J. Ferrari, M. Johnson, F. C. Wellstood, J. Clarke, P. A. Rosenthal, R. H. Hammond, and M. R. Beasley, *Appl. Phys. Lett.* **53**, 695 (1988).
- <sup>11</sup>F. Ludwig, D. Koelle, E. Dantsker, D. T. Nemeth, A. H. Miklich, J. Clarke, and R. E. Thomson, *Appl. Phys. Lett.* **66**, 373 (1995).
- <sup>12</sup>R. Scharnweber, N. Dieckmann, and M. Schilling, *Appl. Phys. Lett.* **70**, 2189 (1997).
- <sup>13</sup>B. David, D. Grundler, J. P. Krumme, and O. Dössel, *IEEE Trans. Appl. Supercond.* **5**, 2935 (1995).
- <sup>14</sup>D. Drung, S. Knappe, and H. Koch, *J. Appl. Phys.* **77**, 4088 (1995).
- <sup>15</sup>R. H. Koch, J. Z. Sun, V. Foglietta, and W. Gallagher, *Appl. Phys. Lett.* **67**, 709 (1995).
- <sup>16</sup>M. Mück, S. Schöne, and C. Heiden, *IEEE Trans. Appl. Supercond.* **7**, 3263 (1997).

### 5.5.2 Low-frequency noise and linearity of a directly coupled magnetometer with small linewidths in static magnetic fields

In Refs. [173,174], Dantsker *et al.* have made several suggestions for the design of HTS SQUID devices in order to reduce the amount of trapped flux. They are based on the reduction of the linewidth of the SQUID body, so that it becomes energetically unfavorable for flux to enter the film. An estimation for the threshold field of flux entry is given by

$$B_T = \frac{\pi\Phi_0}{4w^2}, \quad (5.5)$$

where  $w$  is the linewidth of the film. As reported in Ref. [174], bare SQUIDs with slots or holes and linewidths of  $4\mu\text{m}$  showed no excess noise in cooling fields up to about  $100\mu\text{T}$ . For this reason, Cho *et al.* [170] repatterned the pickup loop of a complete directly coupled magnetometer to obtain a mesh of  $4\mu\text{m}$  wide lines. However, the authors found a major noise contribution from the tapered outer edges of their magnetometers. After the removal of these edges, the low-frequency noise remained constant again in cooling fields below  $100\mu\text{T}$  and no further effect from the mesh pattern was observed. This is attributed to the narrow linewidth of their SQUID loop and the large inductance mismatch between pickup loop and SQUID.

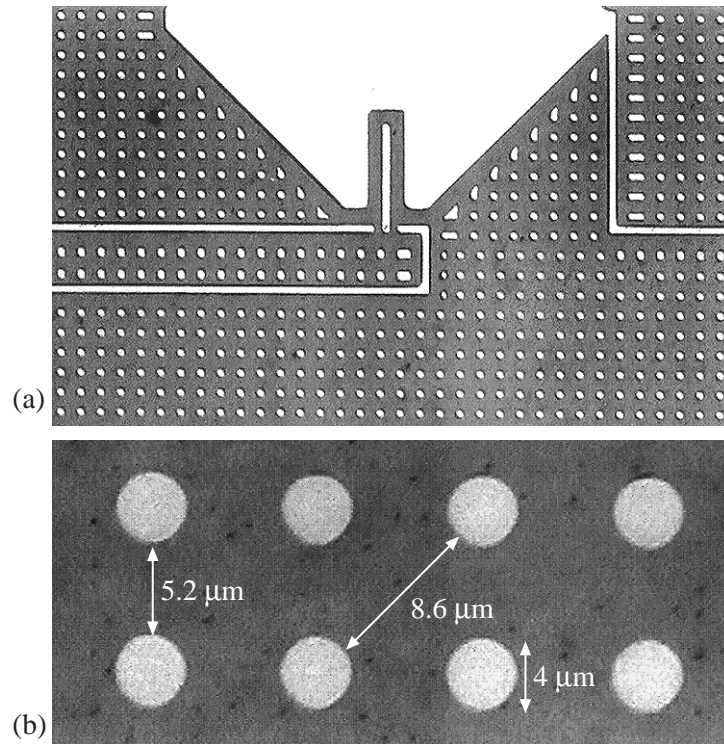


FIGURE 5.30: (a) Micrograph of the magnetometer part around the SQUID loop after it was completely patterned with holes. (b) Dimensions.

TABLE 5.6: Transport properties of the directly coupled magnetometer at  $T = 77$  K in zero magnetic field, before and after the patterning of the holes.

		Before	After	
Voltage swing	$\Delta V$	26	27	$\mu\text{V}$
Critical current	$I_0$	107	76.5	$\mu\text{A}$
Normal resistance	$R_n$	2.1	2.8	$\Omega$
Effective area	$A_{\text{eff}}$	0.225	0.230	$\text{mm}^2$
$B/\Phi = 1/A_{\text{eff}}$		9.203	8.980	$\text{nT}/\Phi_0$

In the following, noise measurements on a similar directly coupled magnetometer are presented, both before and after it was patterned with holes to reduce the maximum structural width of the pickup loop. The effects of the patterning are directly compared for the same device, since the comparison of different devices may be misleading, because of a variable microstructural or epitaxial quality of the involved superconducting thin-films. When considering the unshielded operation of a HTS magnetometer system, the linearity of the system becomes a further important issue, since small signals have to be resolved at a high level of ambient noise. To characterize the magnetometer linearity, the total harmonic distortion (THD) has been measured in different cooling fields. Furthermore, the dependence of the effective flux sensing area on the cooling field is discussed.

After the first characterization of the magnetometer with solid pickup loop, it was patterned a second time using a net-like photomask. A linewidth of about  $5.2\mu\text{m}$  and circular holes with a diameter of about  $4\mu\text{m}$  across the whole pickup loop has been obtained. Figure 5.30 depicts a micrograph of the region around the SQUID loop after the patterning. All measurements have been performed in liquid nitrogen inside of a triple mumetal shield. The magnetic field  $B_0$  is applied with a Helmholtz coil that is supplied by a large capacity lead-acid battery and an appropriate resistor. The flux density noise, resulting from the current noise in the coil, is less than  $85\text{ fT}/\sqrt{\text{Hz}}$  at 3 Hz and  $B_0 = 100\mu\text{T}$ , and does not significantly contribute to the measured noise values. The experimental setup is schematically shown in Fig. 5.31. The noise measurements have been made in flux-locked loop mode with bias current reversal to reject the low-frequency noise from critical current fluctuations in the junctions. In all field dependent measurements, the magnetic field is applied while the magnetometer is heated above  $T_c$ , and it remains on during the cooling and the measurements. Hence, no shielding currents are generated as in a switching process. The magnetometer properties in the zero field cooled case, before and after the second patterning step for the holes, are listed in Table 5.6. After the treatment,  $I_0$  and  $R_n$  were somewhat changed, presumably due to

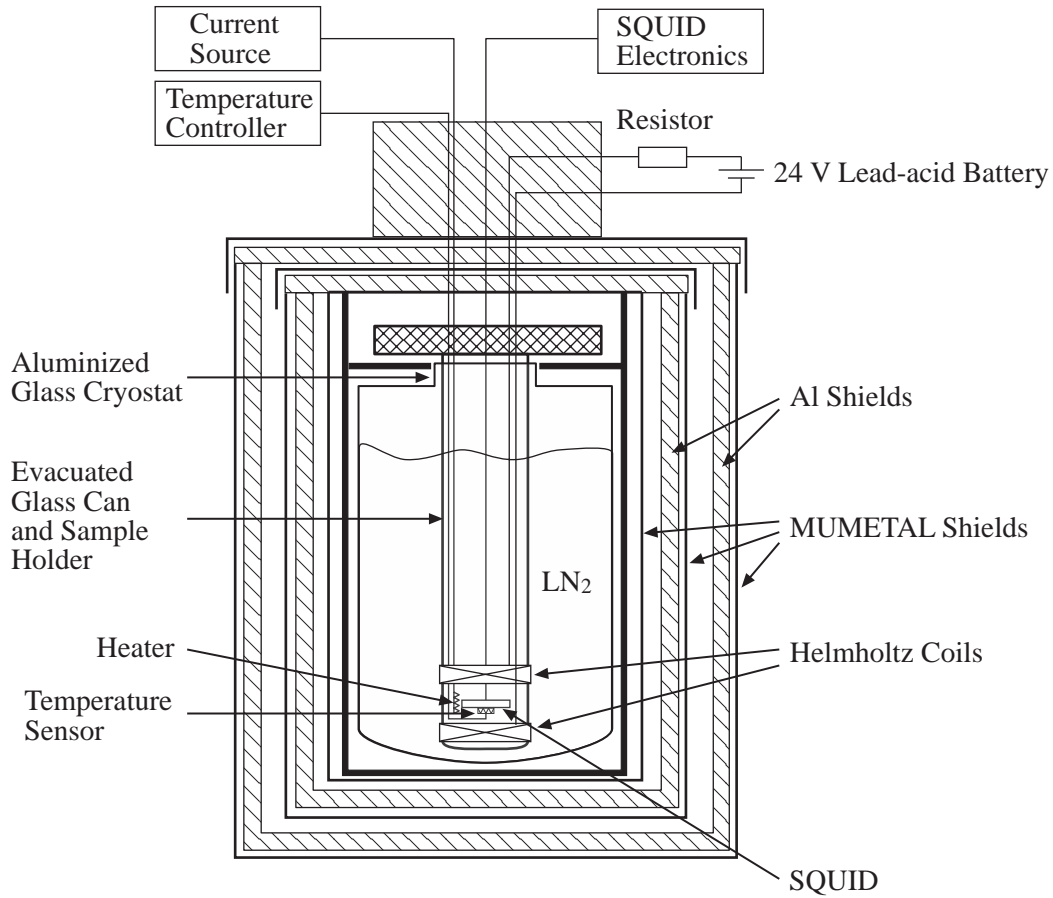


FIGURE 5.31: Experimental setup for the characterization of SQUID magnetometers in static magnetic fields.

a slight oxygen loss in the junctions, since no second oxygen plasma oxidation was carried out to preserve the silver contact pads. The patterning had only a minor effect on the sensitivity of the device. The effective area increased by about 2%, although the character of input coupling completely changed. With the solid pickup loop, flux is focused to some extent into the loop by the Meissner-Ochsenfeld effect. In the patterned device however, this effect is replaced by the flux quantization, which keeps the flux in the holes constant at integer flux quanta. Thus, flux changes must be partly focused into the pickup loop again. One flux quantum in a hole corresponds to an external field of about  $125 \mu\text{T}$ , considering a London penetration depth of about  $300 \text{ nm}$  for  $\text{YBa}_2\text{Cu}_3\text{O}_7$  at  $77 \text{ K}$ . Obviously, there is no significant quantitative difference between both effects in zero field. Somewhat larger differences have been found for magnetometers with several narrow pickup loops connected in parallel, as is described by DiIorio *et al.* [176]. However, a qualitative difference between the solid and the patterned layout is found in field dependent measurements of the effective area, whose results are depicted in Fig. 5.32. For the solid device, the effective area increases with  $B_0$  above roughly  $B_0 = 100 \mu\text{T}$ , whereas it decreases with nearly the



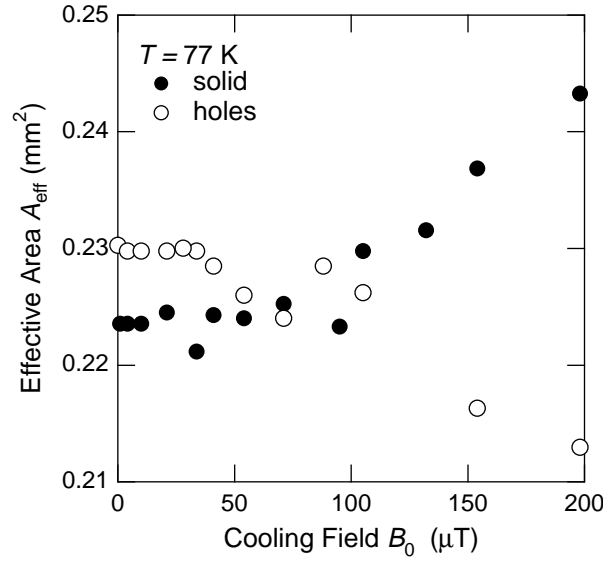


FIGURE 5.32: Effective area as a function of the cooling field for the unpatterned (solid) and the patterned (holes) magnetometer. The jump at  $B_0 = 80 \mu\text{T}$  in the data of the patterned device is attributed to an accidental position change of the magnetometer in the Helmholtz coil.

same variation for the patterned device. Hence, the sensor's calibration is affected by larger cooling fields. This is an important issue for the design of multichannel biomagnetic systems intended for unshielded operation, since their signal processing demands an exact knowledge of each sensor's effective area, but this is usually measured inside a shield. The effect is small for the earth's magnetic field, but it might be larger for a different magnetometer layout. The reason for the dependence of the effective area on the cooling field is not yet clear and is under further investigation. A detailed investigation of the influence of slots in washer SQUIDs on their effective area and inductance has been made by Jansman *et al.* [177, 178], but unfortunately no field dependent calculations are shown.

Figure 5.33 depicts several flux density noise spectra for the unpatterned magnetometer in different cooling fields  $B_0$ . An increasing low-frequency noise is found as a function of  $B_0$ , due to the growing number of trapped vortices in the film. The spectra for  $B_0 = 41 \mu\text{T}$  and  $198 \mu\text{T}$  include additional Lorentzian contributions caused by the random telegraph signal from a predominant two-level fluctuator. Figure 5.34(a) shows the noise values at the frequency 3 Hz as a function of  $B_0$ , before and after the holes were patterned into the pickup loop. In the unpatterned case, the low-frequency noise increases with  $B_0$  even for the lowest cooling fields, whereas it remains approximately constant below a threshold field  $B_T \simeq 35 \mu\text{T}$  in the patterned case. Moreover, it is found that for all values of  $B_0$ , the magnetometer with holes remains markedly less noisy than with solid pickup loop. In the unpatterned case, the noise below  $B_T$  presumably results from the motion of vortices near

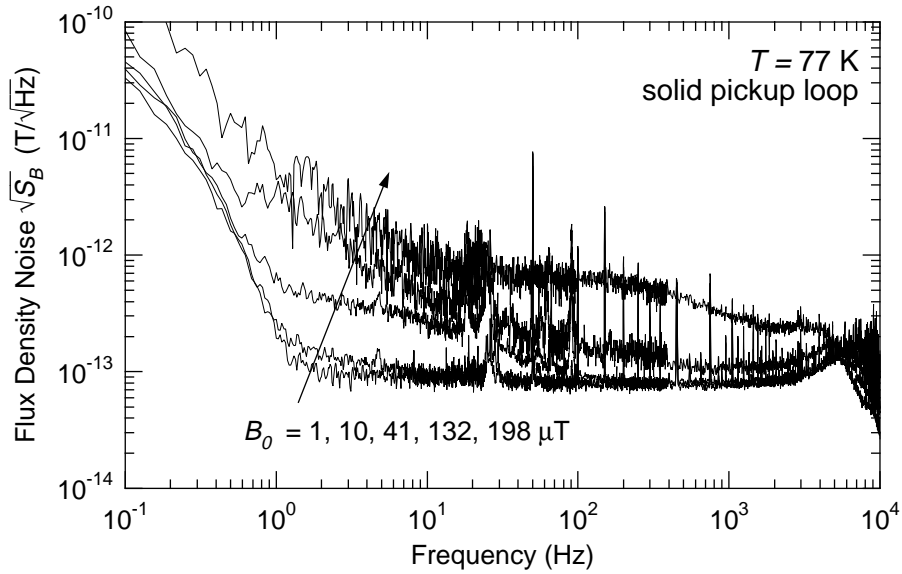


FIGURE 5.33: Flux density noise spectra of the unpatterned magnetometer for different cooling fields  $B_0$ .

the SQUID loop, which is directly coupled into the SQUID, since the indirect component from noise currents in the pickup loop is strongly suppressed by the poor coupling between the inductances of pickup loop and the SQUID. In both cases, a significant increase of noise above  $B_T$  is observed. This is attributed to the flux entry into the SQUID loop, although a somewhat larger threshold field of  $42 \mu\text{T}$  for the measured width  $w = 6.2 \mu\text{m}$  is expected from (5.5). Particularly in the unpatterned case, the noise values above the threshold field remain nearly constant up to  $B_0 \simeq 80 \mu\text{T}$ . This noise is caused by the dominating RTS from a single fluctuator and therefore does not scale with  $B_0$ . For higher values of  $B_0$ , it is covered by the noise of the remaining vortices.

Nonlinear behavior of a SQUID magnetometer can result from the inelastic motion of vortices in the magnetometer body [179]. Thus, the degree of nonlinearity is expected to depend on the number of vortices and on the cooling field. To measure the magnetometer linearity, a sinusoidal magnetic test signal with a peak-to-peak amplitude of  $20 \text{ nT}$  and the frequency  $f = 518 \text{ Hz}$  was applied. The output voltages from the signal source and the FLL electronics were electronically subtracted to obtain a maximum suppression of the harmonics of the test signal. The residual signal has been measured with a FFT signal analyzer. A schematic of the THD measuring system is given in Fig. 5.34(c). Figure 5.34(b) shows the amount of THD of the patterned magnetometer as a function of the cooling field. The THD values show a very similar dependence on  $B_0$  as is found in the noise measurements. The THD remains nearly constant for fields below a threshold and increases for cooling fields beyond this value. The observed threshold field agrees well with the value found in the noise measurements.

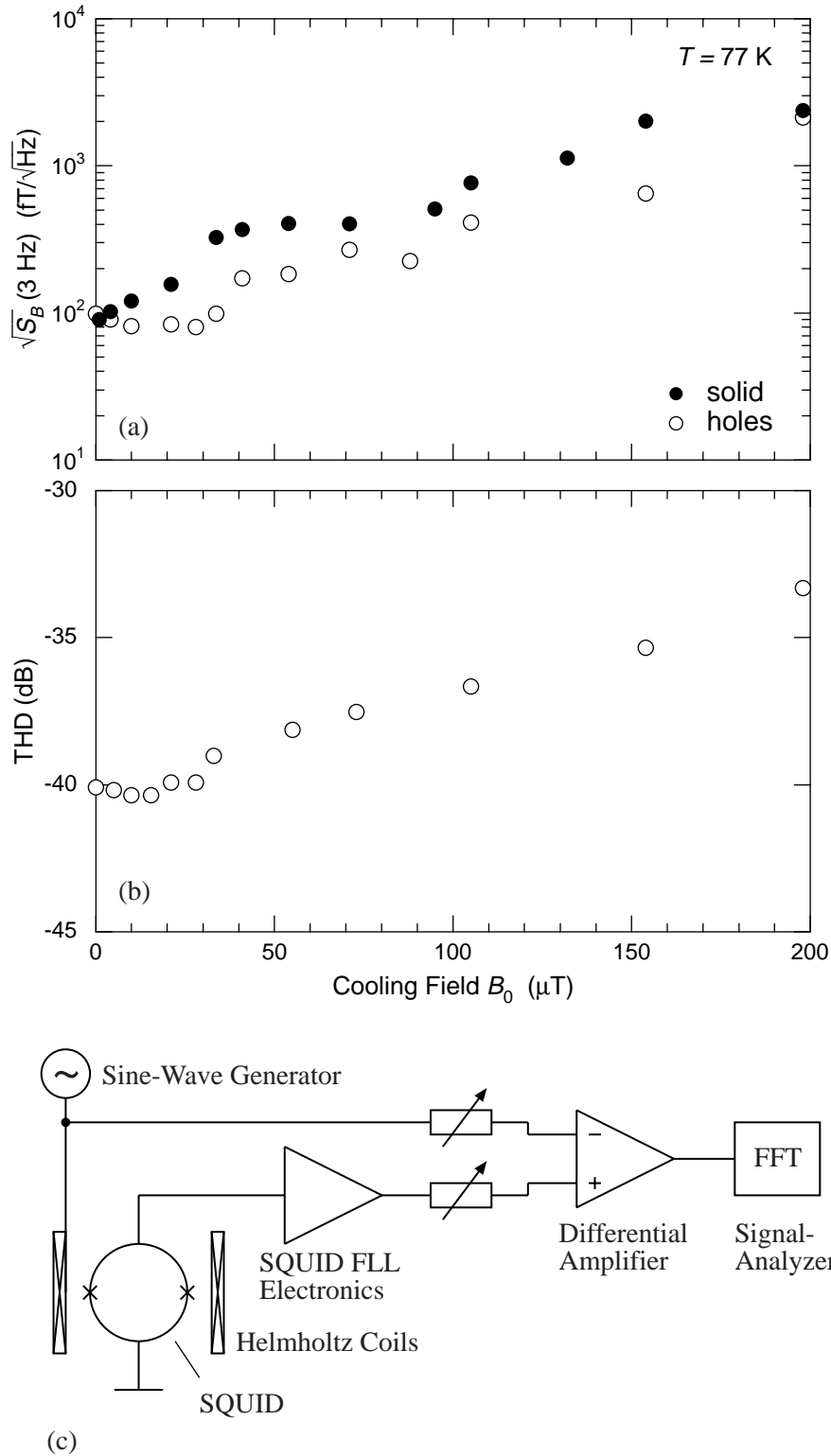


FIGURE 5.34: (a) Flux density noise at 3 Hz vs cooling field for the directly coupled magnetometer, before (●) and after it was completely patterned with holes (○). (b) Total harmonic distortion (THD) of the patterned magnetometer depending on the cooling field. (c) Schematic drawing of the THD measuring setup.



## 6 Josephson junction serial array magnetometers

In the previous chapters only dc SQUIDs have been discussed for magnetometer applications. But also a single Josephson junction can be used as a magnetometer if one takes advantage of the Fraunhofer pattern of the junction's critical current. Although the underlying field period of this pattern is in general much larger than a typical SQUID modulation period due to the small effective junction area, a large sensitivity enhancement can be obtained with additional flux concentrating structures. Here, bicrystal junctions are favorable, because flux can easily penetrate the junction area, and the junction's electrodes cause additional flux focusing [27, 180]. To obtain a maximum critical current modulation, the junction must have a large critical current with a low amount of excess current. In contrast to SQUID devices, the response of a magnetometer based on the Fraunhofer pattern is nonperiodic, thus it can be used where the measurement of absolute magnetic fields is necessary. One possible application is the active shielding of SQUID systems from the earth's magnetic field, where this field is measured and compensated by an

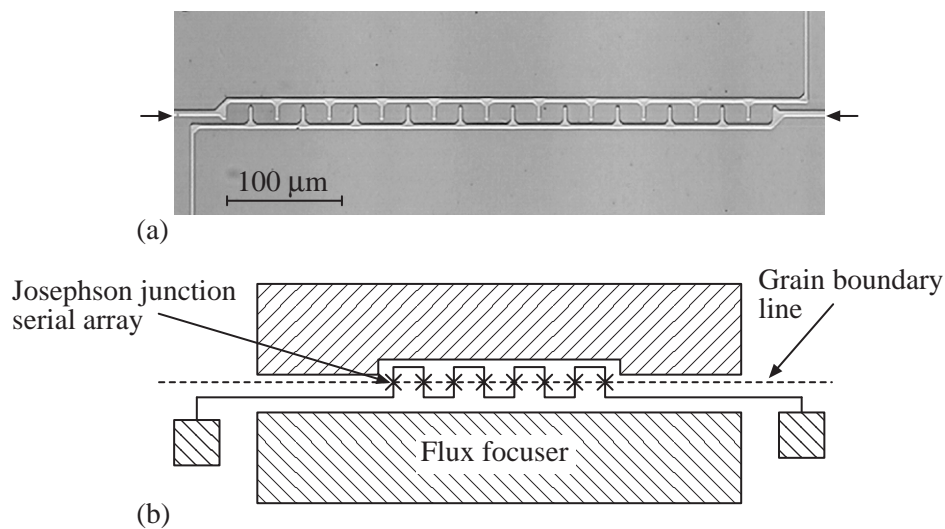


FIGURE 6.1: (a) Microscope image of a 21-junction subarray of bicrystal Josephson junctions embedded in flux focusers. The arrows indicate the grain boundary line. (b) Schematic sketch of the Josephson junction serial array magnetometer.

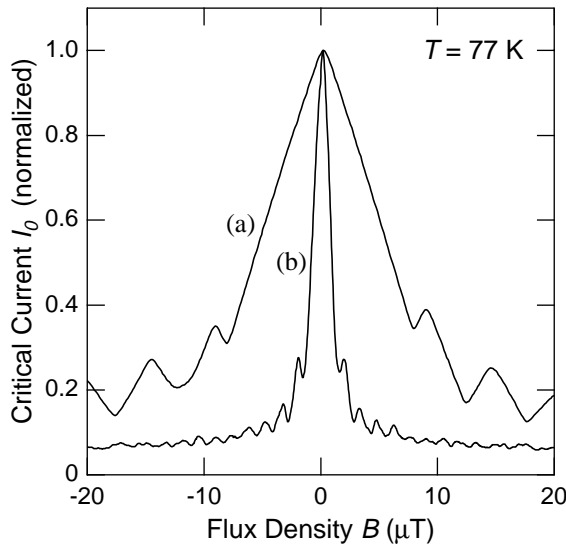


FIGURE 6.2: (a) Fraunhofer pattern of a single bicrystal junction of  $20\text{ }\mu\text{m}$  width without flux focusing and (b) Fraunhofer pattern of the serial array magnetometer of 105 junctions between flux focusers.

appropriate current in a coil around the SQUID system. Similarly, it may be used for the reference magnetometer in the Three Sensor Gradiometer described in Section 5.4. Due to the same preparation process, also an on-chip integration with HTS SQUID devices is easily possible.

Like in the case of SQUIDs, the appropriate figure of merit for a magnetometer based on the junction's Fraunhofer pattern is the amplitude of the voltage modulation depending on the applied field for the current biased device. Hence, the transfer function  $(\partial V / \partial B)_I$  must be large. It can be increased with several junctions in series, since the modulation amplitude scales linearly with the number of junctions  $N$ , when all junctions have similar quality. The voltage noise will only scale with  $\sqrt{N}$  if the noise sources are uncorrelated. Thus, the signal-to-noise ratio should increase with the number of junctions. For this reason, a magnetometer with 105 junctions, equally divided in 5 subarrays of 21 junctions, has been prepared. To obtain a high field sensitivity,  $20\text{ }\mu\text{m}$  wide Josephson junctions are used. The subarrays can be measured independently to reveal the scaling behavior of the magnetometer properties. To further increase the sensitivity, the flux is concentrated at the place of the junctions by the Meissner-Ochsenfeld effect of two large superconducting areas at both sides of the junction array. A photograph and a schematic sketch of this sensor can be seen in Fig. 6.1. It is prepared from a single  $\text{YBa}_2\text{Cu}_3\text{O}_7$  thin-film on a  $24^\circ$  bicrystal substrate [181].

In order to investigate the degree of flux concentration from the flux focusers, the critical current has been measured as a function of the applied magnetic field, both for a single  $20\text{ }\mu\text{m}$  wide junction without flux focuser and for the whole array of equivalent junctions embedded between the superconducting areas. The resulting Fraunhofer patterns are depicted in Fig. 6.2. The triangular shape and the shallow minima of curve (a) indicate

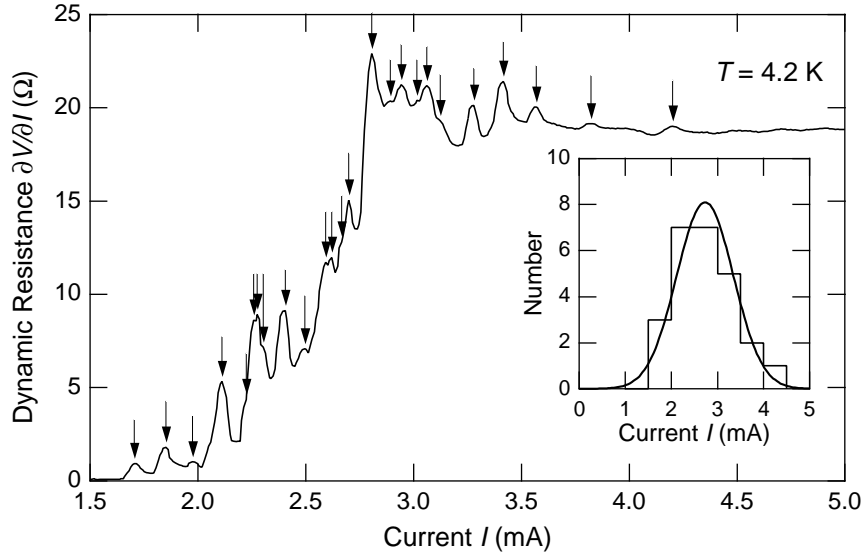


FIGURE 6.3: Dynamic resistance of a serial array from 42 bicrystal Josephson junctions measured at  $T = 4.2$  K. The arrows indicate the positions of the dynamic resistance peaks at the individual critical currents. The inset shows a histogram of the peak positions and the calculated Gaussian distribution.

that the junctions are in the wide limit, i.e. the geometrical junction width is comparable or larger than the Josephson penetration depth  $\lambda_J$ . An estimation of  $\lambda_J$  according to (2.9) yields  $2.4 \mu\text{m}$ . The effective area of the bare junction is about  $350 \mu\text{m}^2$ , i.e. 25 times larger than the geometrical area, due to the flux focusing effect of the junction electrodes. For the junction array embedded between the flux focusers, the sensitivity is further increased by a factor 4.2, as is illustrated by curve 6.2(b). The regular shape of this Fraunhofer pattern, up to the higher order side lobes, emphasizes the high homogeneity of the involved bicrystal Josephson junctions throughout the whole array. At  $T = 77$  K, a maximum field sensitivity of about  $\partial I_0 / \partial B = 130 \text{ A/T}$  is obtained. The excess current for the whole 105-junction array is about 6% of the critical current, as is estimated from the base level of the Fraunhofer pattern.

Additional dynamic resistance measurements have been performed at  $T = 4.2$  K to reveal the distribution of the individual critical currents in the array. The critical currents are hereby identified by the characteristic peaks in  $\partial V / \partial I$  just above  $I_0$ . Figure 6.3 depicts the dynamic resistance of two subarrays with 42 junctions in series and a mean critical current of 2.73 mA. 25 distinct peaks are found, which presumably cover the remaining. The mean square deviation of the revealed critical currents is  $\sigma = 0.62 \text{ mA}$ , i.e. 23% of the mean value, which is in good agreement with data published by Gerdemann *et al.* [65].

Noise measurements on the array have been made at fixed bias current, either with static magnetic flux or with 2 kHz flux modulation. The modulation method is similar to

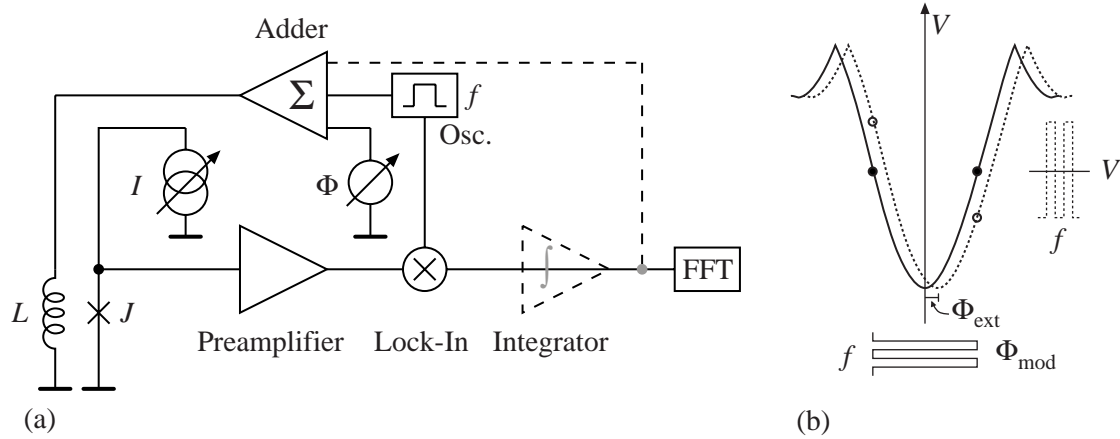


FIGURE 6.4: (a) Schematic of the noise measurement setup.  $J$  denotes the Josephson junction array and  $I$  is the bias current source. The bias flux is adjusted with  $\Phi$ . The flux in  $L$  and  $J$  is modulated with a square-wave oscillator (Osc.) at the frequency  $f$ . The voltage signal of the array is amplified and lock-in detected. Similar to SQUID electronics, a flux-locked-loop feedback control can be used with the parts indicated by dashed lines. (b) shows the measurement principle. An external magnetic flux  $\Phi_{\text{ext}}$  will horizontally shift the Fraunhofer pattern and lead to a signal at the frequency  $f$ . Critical current fluctuations will just displace the pattern vertically and are not mixed up to  $f$ .

the one used in SQUID electronics. However, common SQUID electronics are designed for low-ohmic sources and cannot be used, due to the high impedance of the array. A schematic of the used electronics is given in Fig. 6.4. The amplitude and offset of the square-wave current for the flux modulation is adjusted to switch between the operating points of maximum transfer function on both sides of the central lobe of the Fraunhofer pattern. The preamplifier output is lock-in detected. Thus, no output is generated in zero field and voltage noise due to critical current fluctuations is suppressed. Every magnetic signal will displace the Fraunhofer pattern and leads to a 2 kHz component at the preamplifier output and therefore to an output signal. In the same way as in SQUID FLL electronics, a feedback control may be used to linearize the detector output. This addition is shown with dashed lines in Fig. 6.4. A more detailed description of the scaling behavior of the array parameters and of the noise characteristics is given in the following publication. From the amount of excess low-frequency noise measured with dc flux, the critical current fluctuations are estimated to  $|\partial I_0/I_0| = 6.0 \times 10^{-5}/\sqrt{\text{Hz}}$  referred to a single junction [182], which is in good agreement with data found in the literature (refer to Section 2.4).



## Highly sensitive magnetometers based on $\text{YBa}_2\text{Cu}_3\text{O}_7$ Josephson junction arrays

S. Krey,<sup>a)</sup> O. Brüggmann, and M. Schilling

*Institut für Angewandte Physik und Zentrum für Mikrostrukturforschung, Universität Hamburg,  
D-20355 Hamburg, Germany*

(Received 14 September 1998; accepted for publication 12 November 1998)

The dependence of the critical current of a Josephson junction on the magnetic flux in the junction area can be used for the sensitive detection of external magnetic fields. In contrast to superconducting quantum interference devices, also the measurement of absolute magnetic fields is possible. To increase the transfer function  $\partial V/\partial B$ , we use serial arrays of up to 105 Josephson junctions between flux-concentrating areas on  $24^\circ$   $\text{SrTiO}_3$  bicrystal substrates. We investigate the scaling properties of the critical current  $I_c$ , the normal state resistance  $R_n$  and the flux density noise  $\sqrt{S_B}$  in dependence on the number of Josephson junctions in the serial array. By the use of a magnetic field modulation scheme, the  $1/f$  noise from critical current fluctuations in the junctions can be suppressed. At 77 K, we achieve a white noise level of  $\sqrt{S_B} = 1.2 \text{ pT}/\sqrt{\text{Hz}}$  for a 105-junction array. © 1999 American Institute of Physics. [S0003-6951(99)03902-9]

Currently, the most successful approach in Josephson junction technology for devices from high-temperature superconductors (HTS) is the grain-boundary junction on bicrystal substrates. For magnetic sensors, these junctions are typically used in magnetometers based on superconducting quantum interference devices (SQUIDs), which achieve a field resolution  $\sqrt{S_B}$  of about  $30 \text{ fT}/\sqrt{\text{Hz}}$  in simple single-layer layouts on  $1 \times 1 \text{ cm}^2$  substrates.<sup>1,2</sup> Due to the dependence of the critical current on external magnetic flux, even a single Josephson junction can be used for sensing magnetic fields. In contrast to SQUID magnetometers, the flux-voltage characteristic is nonperiodic, hence, in principle absolute magnetic flux densities can be determined. In bicrystal junctions a high sensitivity is observed, due to the flux focusing effect of the electrodes directly adjoining the grain boundary. Rosenthal *et al.*<sup>3</sup> found a clear  $1/w^2$  dependence for the Fraunhofer field period of biepitaxial grain-boundary junctions of width  $w$ , instead of the classical  $1/w$  relation. This behavior is attributed to corner effects on the current distribution in the electrodes. Martin *et al.*<sup>4</sup> further enhanced the sensitivity of a single  $24^\circ$  bicrystal junction by an additional flux concentrator. With a junction width of  $10 \mu\text{m}$  they achieved a sensitivity  $\partial I_c/\partial B = 176 \text{ A/T}$  and a flux density noise level of  $\sqrt{S_B} = 3.7 \text{ pT}/\sqrt{\text{Hz}}$ . Also, a reduction of low-frequency noise from critical current fluctuations by field modulation was demonstrated.<sup>5</sup> With several junctions in series, the signal-to-noise ratio can be further enhanced since the voltage signal linearly scales with the number  $N$  of junctions, whereas the voltage noise scales with  $\sqrt{N}$  if the noise sources are uncorrelated. Lee *et al.*<sup>6</sup> used a similar approach for a serial array HTS SQUID magnetometer. Here, we present a magnetometer from a serial array of 105 bicrystal Josephson junctions with additional flux focusing areas. Voltage noise due to critical current fluctuations in the junctions is already suppressed by a simple field modulation

scheme. This is in contrast to SQUID-based magnetometers, where the out-of-phase current fluctuations of both junctions have to be suppressed by additional bias current modulation. Due to the high output voltage of the serial array, the demands on the electronics are much lower.

The serial array magnetometers are prepared in a single-layer technology on (100)  $\text{SrTiO}_3$  bicrystals with  $24^\circ$  grain boundaries which are supplied by CrysTec GmbH, Berlin. For the  $\text{YBa}_2\text{Cu}_3\text{O}_7$  thin-film deposition we employ our KrF-excimer laser deposition process that is described elsewhere in detail.<sup>7</sup> We typically use a film of about  $120 \text{ nm}$  thickness. The large number of wide Josephson junctions makes high demands on the large scale quality of the grain boundary and the superconducting film deposited on it. Highly reproducible Josephson junction properties are achieved, since we have no droplets on our films and the outgrowth density is well below  $10^4 \text{ cm}^{-2}$ . After the patterning with conventional photolithography and argon plasma etching, the arrays are treated in an oxygen plasma. To reduce the contact resistance for low noise measurements, the contact pads are covered with  $100 \text{ nm}$  silver. In Fig. 1, an optical micrograph of a 21-junction subarray is depicted. For the whole 105-junction array, five of these subarrays are connected in series. Each Josephson junction has a width of  $20 \mu\text{m}$  to achieve a high sensitivity to external magnetic fields. For a further increase of its sensitivity the array is embedded in flux focusing superconducting areas which cover almost the whole substrate

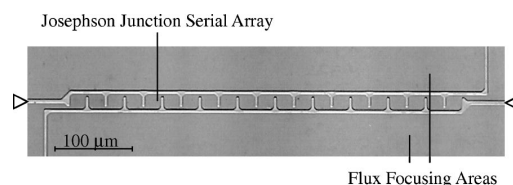


FIG. 1. Optical micrograph of a 21-junction subarray. The figure displays an area of  $570 \times 170 \mu\text{m}^2$ . The position of the bicrystal line is indicated by the arrows.

<sup>a)</sup>Electronic mail: krey@physnet.uni-hamburg.de

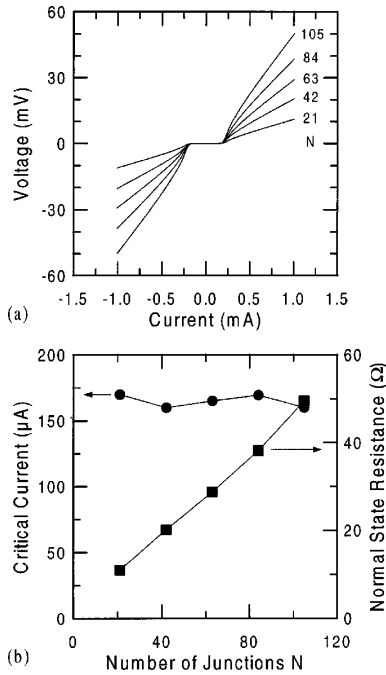


FIG. 2. (a) Current-voltage characteristics for subarrays of a different number of junctions  $N$ . (b) Critical current and normal state resistance for the subarrays vs  $N$ .

of  $1 \times 1 \text{ cm}^2$ . The gaps between these areas and the junctions are  $4 \text{ }\mu\text{m}$  wide.

The arrays are characterized by electrical transport and noise measurements. In Fig. 2(b) we show the scaling properties for both, critical current  $I_c$  and normal state resistance  $R_n$  in dependence on the number  $N$  of junctions in the array. The values for  $I_c$  and  $R_n$  were deduced from the resistively shunted junction-like current-voltage characteristics of the subarrays which are depicted in Fig. 2(a). We find an almost linear increase of  $R_n$  and a constant critical current independent from  $N$  within 5%, resulting in a linear increase of the  $I_c R_n$  product with  $N$ , up to 7.9 mV for 105 junctions. The effective flux collecting area for a single  $20 \text{ }\mu\text{m}$  wide junction, as calculated from the spacing of the minima in the measured Fraunhofer pattern, is about  $350 \text{ }\mu\text{m}^2$ , i.e., 25 times larger than the geometrical area. This is attributed to the flux focusing effect of the junction's electrodes.<sup>8</sup> For the 105-junction array embedded in the flux focusers we find a further increase of the effective area by a factor 4.2. The maximum field sensitivity obtained for this array is  $\partial I_c / \partial B = 130 \text{ A/T}$  at 77 K. In Fig. 3(a) the voltage across the current biased subarrays is shown versus the external magnetic flux density. In each case the bias currents were adjusted to obtain the maximum transfer function. Because the  $I_c R_n$  product scales linearly with  $N$ , we also find a linear increase of the voltage modulation as well as the maximum transfer function  $\partial V / \partial B$  with  $N$ . The latter is illustrated by Fig. 3(b). For the largest array of 105 junctions we measure a voltage modulation of about 7.5 mV that corresponds well with the  $I_c R_n$  product, due to low excess currents. The transfer function of 7500 V/T is comparable to directly coupled SQUID magnetometers from HTS single layers. They typically show

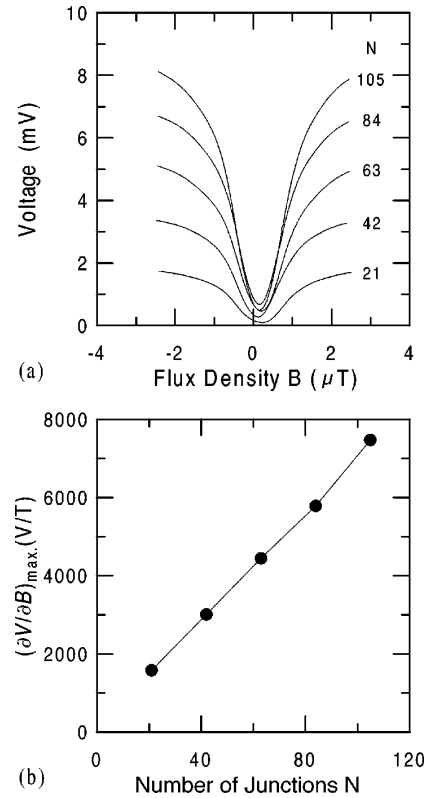


FIG. 3. (a) Voltage across the current biased subarrays vs the external magnetic flux density. (b) Maximum transfer function  $\partial V / \partial B$  in dependence on the number of junctions in the array.

a sensitivity  $\partial B / \partial \Phi$  of about  $10 \text{ nT}/\Phi_0$ , resulting in  $\partial V / \partial B = 6300 \text{ V/T}$  for an assumed sinusoidally voltage modulation of  $20 \text{ }\mu\text{V}$ . The high transfer function of SQUID magnetometers is achieved by their very large effective area  $A_{\text{eff}} = \partial \Phi / \partial B$  of about  $0.2 \text{ mm}^2$  in conjunction with a much smaller voltage modulation. For the junction array we have a very large voltage modulation, but a small effective area.

In the theory of the resistively shunted tunnel junction the voltage noise spectral density of a single junction due to thermal fluctuations is predicted by<sup>9</sup>

$$S_V = \left[ 1 + \frac{1}{2} \left( \frac{I_c}{I} \right)^2 \right] \frac{4k_B T R_D^2}{R_n},$$

where  $R_D$  denotes the dynamic resistance at the bias current  $I$ . Using typical parameters for our bicrystal junctions, a voltage noise level of about  $\sqrt{S_V} = 120 \text{ pV}/\sqrt{\text{Hz}}$  is calculated. If we assume that the noise sources in the junctions are uncorrelated, the noise of the array should increase as  $\sqrt{N}$  and a level of about  $1.2 \text{ nV}/\sqrt{\text{Hz}}$  for 105 junctions is expected. However, a small signal measurement at 2 kHz yielded a total voltage noise of about  $9 \text{ nV}/\sqrt{\text{Hz}}$  that is well above the input voltage noise of the used preamplifier of  $4 \text{ nV}/\sqrt{\text{Hz}}$ . The measurements were made at 77 K at a fixed bias current of  $169 \text{ }\mu\text{A}$  and a fixed bias flux of  $0.75 \text{ }\mu\text{T}$ , which yield the maximum transfer function. The deviation from the theoretical prediction is not yet clear, but it is also observed in SQUIDs from HTS Josephson junctions.<sup>10</sup> Flux density noise

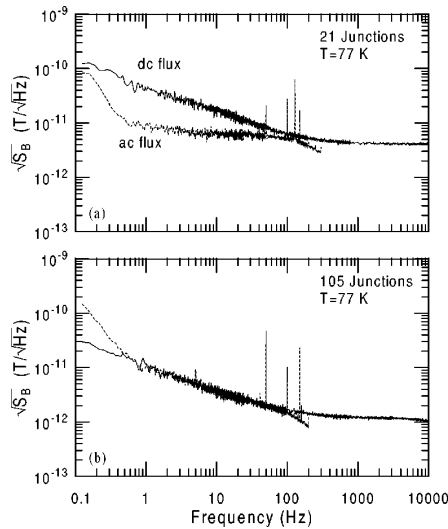


FIG. 4. Noise spectra of the Josephson junction array magnetometers with (a) 21 junctions and (b) 105 junctions. The spectra were measured at 77 K with static bias current either with static flux or with 2 kHz flux modulation (ac flux, dashed line). The cutoff at 100 Hz in the ac spectra is due to the limited bandwidth of the used lock-in amplifier.

spectra for two junction arrays at 77 K are depicted in Fig. 4. They were obtained by dividing the voltage noise spectra by the corresponding transfer function. Figure 4(a) shows two spectra of a 21-junction subarray. They were measured with fixed bias current either with static flux or with 2 kHz flux modulation. The modulation method is similar to that one commonly used in SQUID electronics.<sup>11</sup> The amplitude and offset of the square current for the flux signal is adjusted to switch between the points of maximum sensitivity, so that the ac flux signal is symmetric with respect to the maximum of the Fraunhofer pattern. The preamplifier output signal is lock-in detected. Hence, no signal is measured in zero field and voltage noise due to critical current fluctuations is suppressed. Every external magnetic signal will lead to a 2 kHz component at the preamplifier output and to a lock-in signal. For comparison, in SQUIDs the out-of-phase critical current fluctuations generate flux noise in the SQUID loop that has to be suppressed with additional bias current modulation. As in SQUID systems, a flux locked loop (FLL) circuit can be employed to enhance the linear working range of the array magnetometer.<sup>5</sup> In the static case a frequency-dependent  $1/f$ -noise component with a corner frequency of about 200 Hz was measured. However, this excess noise could be well suppressed to the white noise level of  $\sqrt{S_B} = 4$  pT/ $\sqrt{\text{Hz}}$  using the flux modulation method. Second, the flux density noise spectra for the whole 105-junction array are shown in Fig. 4(b). Here, a white noise level of about  $\sqrt{S_B}(5 \text{ kHz}) = 1.2$  pT/ $\sqrt{\text{Hz}}$  is obtained, however, the apparent  $1/f$  noise was not suppressible. We attribute this excess noise to flux noise from vortex motion in the large flux focusers. A reduction of this flux noise is expected, if the flux focusing areas are provided with slots or holes that prevent the vortex penetration. This was recently demonstrated by Dantsker *et al.*<sup>12</sup> for washer SQUIDs. In Fig. 5 the white flux density noise of the arrays at 2 kHz is shown in dependence on  $N$ . We find a decrease of the noise with an increasing number of junctions

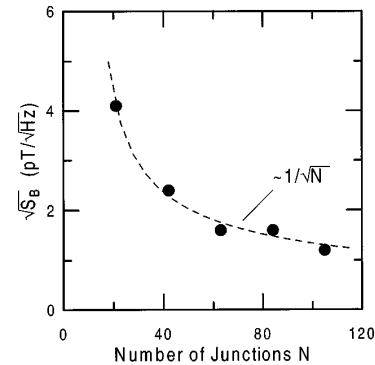


FIG. 5. Flux density noise at 2 kHz of the Josephson junction array magnetometers vs the number of Josephson junctions integrated in the array. The dashed line indicates a  $1/\sqrt{N}$  dependence.

$N$  because the transfer function scales linearly with  $N$  while the voltage noise only increases with  $\sqrt{N}$ . The dashed line in Fig. 5 illustrates the expected decrease with  $\sqrt{N}$ .

In summary, we have fabricated and characterized serial arrays of up to 105 bicrystal Josephson junctions from  $\text{YBa}_2\text{Cu}_3\text{O}_7$  thin films. The measured scaling properties of the critical current  $I_c$  and the normal state resistance  $R_n$  at 77 K demonstrate the high homogeneity throughout the whole array. The serial arrays can be used as highly sensitive magnetometers with a noise level sufficient for many applications. However, highly reproducible Josephson junctions with high  $I_c R_n$  products are necessary for the low noise operation of such magnetometers. The noise values can be further improved by the use of more Josephson junctions in the array and by enhancing the flux focusing into the junctions. The latter can be achieved by a reduced slit width between the array and the flux focusing areas, by an additional flip-chip flux focuser or with multilayer technology.

This work was supported by the Bundesministerium für Bildung, Wissenschaft, Forschung und Technologie, Federal Republic of Germany under Contract No. 13N6734-0.

<sup>1</sup>L. P. Lee, J. Longo, V. Vinetskiy, and R. Cantor, Appl. Phys. Lett. **66**, 1539 (1995).

<sup>2</sup>J. Beyer, D. Drung, F. Ludwig, T. Minotani, and K. Enpuku, Appl. Phys. Lett. **72**, 203 (1998).

<sup>3</sup>P. A. Rosenthal, M. R. Beasley, K. Char, M. S. Colclough, and G. Zaharchuk, Appl. Phys. Lett. **59**, 3482 (1991).

<sup>4</sup>V. Martin, M. Lam Chok Sing, D. Bloyet, D. Robbes, J. Certenais, N. Quéllec, and D. Crete, IEEE Trans. Appl. Supercond. **7**, 3079 (1997).

<sup>5</sup>C. Dolabdjian, P. Poupard, V. Martin, C. Gunther, J. F. Hamet, and D. Robbes, Rev. Sci. Instrum. **67**, 4171 (1996).

<sup>6</sup>S.-G. Lee, Y. Huh, G.-S. Park, I.-S. Kim, Y. K. Park, and J.-C. Park, IEEE Trans. Appl. Supercond. **7**, 3347 (1997).

<sup>7</sup>J.-K. Heinssohn, D. Reimer, A. Richter, K.-O. Subke, and M. Schilling, Physica C **299**, 99 (1998).

<sup>8</sup>R. G. Humphreys and J. A. Edwards, Physica C **210**, 42 (1993).

<sup>9</sup>J. Clarke, W. M. Goubau, and M. B. Ketchen, J. Low Temp. Phys. **25**, 99 (1976).

<sup>10</sup>K. Enpuku, G. Tokita, T. Maruo, and T. Minotani, J. Appl. Phys. **78**, 3498 (1995).

<sup>11</sup>S. Krey, O. Brüggmann, H. Burkhardt, and M. Schilling (unpublished).

<sup>12</sup>E. Dantsker, S. Tanaka, and J. Clarke, Appl. Phys. Lett. **70**, 2037 (1997).



## 7 Summary and conclusions

Three different types of integrated  $\text{YBa}_2\text{Cu}_3\text{O}_7$  SQUID magnetometers incorporating step-edge and bicrystal Josephson junctions have been fabricated and characterized. All devices have been successfully operated at 77 K in liquid nitrogen. From the critical current dependence on the applied magnetic field, it is concluded that the critical current density in bicrystal Josephson junctions is far more homogeneous on a micrometer scale than in step-edge Josephson junctions. This is in agreement with the literature.

Directly coupled magnetometers can be prepared with comparatively low effort from single-layers of  $\text{YBa}_2\text{Cu}_3\text{O}_7$ . The SQUID inductance and effective area of this layout is very sensitive to variations in the thin-film quality and the photolithographic process. Resonances of the Josephson oscillations in the SQUID loop have been identified as a possible reason for a reduced voltage modulation. A substrate material having a smaller dielectric constant than  $\text{SrTiO}_3$  would be helpful to reduce the resonances. The mean characteristic voltage of  $I_0 R_n = 175 \mu\text{V}$  for  $24^\circ$  bicrystal Josephson junctions is in good agreement with data reported in the literature. The observed mean critical current of  $84 \mu\text{A}$  is larger than desirable for SQUID magnetometers operating at 77 K. It has been shown that the device performance can be improved in a limited way by reducing the critical currents through an annealing procedure. However, this may increase the low-frequency noise of the magnetometer. Lower critical currents are expected from symmetrical  $30^\circ$  bicrystals, which are currently under investigation. A maximum voltage modulation of  $\Delta V = 40.5 \mu\text{V}$  has been measured for a device with a calculated SQUID inductance of about  $L = 47 \text{ pH}$ . Noise measurements on this device have yielded  $\sqrt{S_B}(1 \text{ kHz}) = 38 \text{ fT}/\sqrt{\text{Hz}}$  and  $\sqrt{S_B}(1 \text{ Hz}) = 80 \text{ fT}/\sqrt{\text{Hz}}$  for the white noise and the low-frequency noise, respectively. These results meet the current state of technology.

The inductively coupled magnetometer and the multilayer magnetometers have been prepared in a  $\text{YBa}_2\text{Cu}_3\text{O}_7$ - $\text{SrTiO}_3$ - $\text{YBa}_2\text{Cu}_3\text{O}_7$  multilevel process employing step-edge Josephson junctions. Three different multiloop layouts have been investigated. An effective flux capturing area  $A_{\text{eff}} = 2.31 \text{ mm}^2$  at a SQUID inductance  $L = 146 \text{ pH}$  has been obtained by means of an optimization of the pickup loop width and spoke width. This is the largest value reported so far for a HTS SQUID magnetometer on a  $1 \times 1 \text{ cm}^2$

substrate. Furthermore, a very good agreement between the theoretical prediction and the experimental values has been obtained. This results from the direct coupling scheme without inductance mismatch or intermediate flux transformer. Flux density noise values of  $\sqrt{S_B} = 17 \text{ fT}/\sqrt{\text{Hz}}$  in the white noise regime and  $\sqrt{S_B} = 60 \text{ fT}/\sqrt{\text{Hz}}$  at 1 Hz have been measured for a multiloop magnetometer exhibiting a voltage modulation of  $\Delta V = 11.5 \mu\text{V}$ . The noise measurements with the multiloop magnetometers have revealed the limits of the used magnetic shields. The superconducting BSCCO shield generates a large amount of  $1/f$  noise, whereas the metallic shield is a source of Johnson noise.

All investigated types of SQUID magnetometers can show distorted flux-voltage characteristics due to the interaction of the Josephson oscillations with parasitic ac impedances in the pickup loop structures. The distortions will deteriorate the noise performance of the magnetometer when it is operated with a flux modulation type FLL electronics. The strength of the distortion severely depends on the parameters of the Josephson junctions. It has been exemplarily shown that the resonances may be removed by a change of the junction parameters with an annealing procedure. Once more, a different substrate material with lower dielectric constant would be helpful.

The effective area of HTS SQUID magnetometers depends on the temperature and the dependence is different for each layout. In every case, the temperature dependence can be well fitted with a linear dependence on the London penetration depth. The weakest variation with temperature has been found for the multiloop magnetometer and the strongest one for the directly coupled magnetometer. The temperature dependence of the effective area makes demands on the temperature stability when the magnetometer is operating in an ambient magnetic field.

A step-edge multiloop magnetometer has been operated with a direct readout electronics employing the APF method combined with bias current modulation. The noise performance of this device has been compared with multilayer devices employing bicrystal Josephson junctions. Regarding the low voltage modulation of the step-edge device, very competitive noise values of  $\sqrt{S_B} = 30 \text{ fT}/\sqrt{\text{Hz}}$  in the white noise regime and  $\sqrt{S_B}(1 \text{ Hz}) = 94 \text{ fT}/\sqrt{\text{Hz}}$  at low frequencies have been obtained. A real-time magneto-cardiogram with a signal-to-noise ratio of 28 has been recorded, which further illustrates the low noise level and demonstrates that it is adequate for clinical applications.

A demonstration of a practical application and of the advantages of liquid nitrogen refrigeration has been given with biomagnetic measurements performed with a miniature hand-held cryostat.

The unshielded operation in environmental magnetic fields has been successfully demonstrated with a multiloop magnetometer and a prototype multichannel magnetometer system employing single-layer magnetometers. The difference between the magnetic noise

level in an industrial environment and the intrinsic SQUID magnetometer noise is about 3 orders of magnitude and even larger at frequencies of the power line interference. The investigation of several first order gradiometer schemes has yielded a maximum noise reduction by factors of 10...40. Similar results are reported in the literature. It is concluded, that spatial field noise gradients must be present on centimeter lengthscales, which cannot be compensated to a larger extent with the described first order gradiometer schemes.

Detailed investigations have been made on the low-frequency noise of field cooled HTS SQUID magnetometers. The low-frequency noise is generated by the thermally assisted hopping of weakly pinned Abrikosov vortices which are introduced into the device when it is cooled in a static magnetic field. The flux noise increases with increasing cooling fields due to the growing number of vortices. The noise levels of a multiloop magnetometer and an inductively coupled magnetometer have been compared for cooling fields up to  $110\ \mu\text{T}$ . Both devices show only a moderate increase of noise with the applied cooling field indicating a high quality of the involved thin-films. The noise increase is about twice as strong for the inductively coupled device. This is attributed to noise sources in the input coil, which is the most crucial part of the inductively coupled magnetometer due to the narrow linewidth and its fabrication from the top superconducting layer. These are the only field dependent noise measurements that have been reported so far for HTS multilayer magnetometers. The amount of trapped flux in field cooled devices can be reduced by a reduction of the linewidths in the magnetometer. This has been successfully demonstrated by a direct comparison of the noise figures of a directly coupled magnetometer before and after it was completely patterned with holes. Also the linearity of the magnetometer benefits from the patterning. It has been found, that the effective area of a directly coupled magnetometer depends on the cooling field, and that this dependence is different for the solid and the patterned device. The reason for this behavior is still unclear. Further investigations are needed on this topic, since this effect may impair the calibration of multichannel systems in unshielded environment.

A new kind of magnetic field sensor has been introduced. It is based on a serial array of bicrystal Josephson junctions embedded between flux focusers. Detailed investigations of the distribution of the critical currents at low temperatures and the scaling behavior of the electrical characteristics have revealed a high homogeneity of the junction parameters throughout the array. Noise measurements on this magnetometer have yielded a white noise level of  $\sqrt{S_B}(5\text{ kHz}) = 1.2\text{ pT}/\sqrt{\text{Hz}}$ . In contrast to SQUID magnetometers, this sensor detects the absolute magnitude of the magnetic field. A possible application may be the earth field compensation in unshielded SQUID systems, or it may be used for the reference sensor in the Three Sensor Gradiometer.





# Bibliography

- [1] J.G. Bednorz and K.A. Müller, *Possible high  $T_c$  superconductivity in the Ba-La-Cu-O system*, Z. Phys. B **64**, 189 (1986).
- [2] M.K. Wu, J.R. Ashburn, C.J. Torng, P.H. Hor, R.L. Meng, L. Gao, Z.J. Huang, Y.Q. Wang, and C.W. Chu, *Superconductivity at 93 K in a new mixed-phase Y-Ba-Cu-O compound system at ambient pressure*, Phys. Rev. Lett. **58**, 908 (1987).
- [3] J. Bardeen, L.N. Cooper, and J.R. Schrieffer, *Theory of superconductivity*, Phys. Rev. **108**, 1175 (1957).
- [4] F. London, *Superfluids* vol. 1, Wiley, New York, 1950.
- [5] T. Van Duzer and C.W. Turner, *Principles of Superconductive Devices and Circuits*, Elsevier North Holland Inc., New York, 1981.
- [6] D.J. Scalapino, *The case for  $d_{x^2-y^2}$  pairing in the cuprate superconductors*, Phys. Rep. **250**, 329 (1995).
- [7] J.D. Jorgensen, B.W. Veal, A.P. Paulikas, L.J. Nowiki, G.W. Crabtree, H. Claus, and W.K. Kwock, *Structural properties of oxygen-deficient  $YBa_2Cu_3O_{7-\delta}$* , Phys. Rev. B **41**, 1863 (1990).
- [8] A.I. Braginski and J. Talvacchio, *'MBE' Growth of Superconducting Materials in Superconducting Devices*, S.T. Ruggiero and D.A. Rudman, Eds., Academic Press, San Diego (1990), p. 273.
- [9] J.F. Annett, N. Goldenfeld, and S.R. Renn, *The Pairing State of  $YBa_2Cu_3O_{7-\delta}$  in Physical Properties of High Temperature Superconductors*, D.M. Ginsberg, Ed. vol. II, World Scientific, Singapore (1990), p. 571.
- [10] J.Y. Lee and T.R. Lemberger, *Penetration depth  $\lambda(T)$  of  $YBa_2Cu_3O_{7-\delta}$  films determined from the kinetic inductance*, Appl. Phys. Lett. **62** (19), 2419 (1993).
- [11] W.N. Hardy, D.A. Bonn, D.C. Morgan, R. Liang, and K. Zhang, *Precision Measurements of the Temperature Dependence of  $\lambda$  in  $YBa_2Cu_3O_{6.95}$ : Strong Evidence for Nodes in the Gap Function*, Phys. Rev. Lett. **70**, 3999 (1993).
- [12] J. Mao, S.M. Anlage, J.L. Peng, and R.L. Greene, *Consequences of d-Wave Superconductivity for High Frequency Applications of Cuprate Superconductors*, IEEE Trans. Appl. Supercond. **5**, 1997 (1995).

- [13] T. Kisu, T. Iinuma, K. Enpuku, K. Yoshida, and M. Takeo, *Dependence of Magnetic Field Penetration Depth on Resistivity and Critical Temperature in c-Axis Oriented YBaCuO Thin Films*, Jpn. J. Appl. Phys. **31**, L 1027 (1992).
- [14] J.M. Phillips, *Substrate selection for high-temperature superconducting thin films*, J. Appl. Phys. **79**, 1829 (1996).
- [15] H. Töpfer, G. Mäder, and H. Uhlmann, *Accurate calculation of capacitances of grain boundary Josephson junctions in high critical temperature superconductors*, J. Appl. Phys. **77**, 4576 (1995).
- [16] L.P. Lee, J. Longo, V. Vinetskiy, and R. Cantor, *Low-noise YBa<sub>2</sub>Cu<sub>3</sub>O<sub>7- $\delta$</sub>  direct-current superconducting quantum interference device magnetometer with direct signal injection*, Appl. Phys. Lett. **66**, 1539 (1995).
- [17] K. Enpuku, T. Maruo, and T. Minotani, *Effect of large dielectric constant of SrTiO<sub>3</sub> substrate on the characteristics of high T<sub>c</sub> dc superconducting quantum interference device*, J. Appl. Phys. **80** (2), 1207 (1996).
- [18] E.J. Tarte, G.A. Wagner, R.E. Somekh, F.J. Baudenbacher, P. Berghuis, and J.E. Evetts, *The Capacitance of Bicrystal Josephson Junctions Deposited on SrTiO<sub>3</sub> Substrates*, IEEE Trans. Appl. Supercond. **7**, 3662 (1997).
- [19] B.D. Josephson, *Weakly Coupled Superconductors in Superconductivity*, R.D. Parks, Ed. vol. 1, Marcel Dekker, Inc., New York (1969), p. 423.
- [20] B.D. Josephson, *Possible new effects in superconductive tunneling*, Phys. Lett. **1**, 251 (1962).
- [21] R.P. Feynman, R.B. Leighton, and M. Sands, *The Feynman Lectures on Physics* vol. III, Addison-Wesley, 1965.
- [22] S. Shapiro, *Josephson currents in superconducting tunneling: the effect of microwave and other observations*, Phys. Rev. Lett. **11**, 80 (1963).
- [23] J. Halbritter, *Pair weakening and tunnel channels at cuprate interfaces*, Phys. Rev. B **46**, 14861 (1992).
- [24] J. Halbritter, *Extrinsic or intrinsic conduction in cuprates: Anisotropy, weak, and strong links*, Phys. Rev. B **48**, 9735 (1993).
- [25] R. Gross, L. Alff, A. Beck, O.M. Froehlich, R. Gerber, R. Gerdemann, A. Marx, B. Mayer, and D. Koelle, *On the Nature of High-T<sub>c</sub> Josephson Junctions—Clues from Noise and Spatially Resolved Analysis*, in *2<sup>nd</sup> Workshop on HTS Applications and New Materials*, D.A.H. Blank, Ed. Twente, The Netherlands (1995) p. 8.
- [26] R. Gross, L. Alff, A. Beck, O.M. Froehlich, D. Koelle, and A. Marx, *Physics and Technology of High Temperature Superconducting Josephson Junctions*, IEEE Trans. Appl. Supercond. **7**, 2929 (1997).

- 
- [27] P.A. Rosenthal, M.R. Beasley, K. Char, M.S. Colclough, and G. Zaharchuk, *Flux focusing effects in planar thin-film grain-boundary Josephson junctions*, Appl. Phys. Lett. **59**, 3482 (1991).
- [28] W.C. Stewart, *Current-Voltage Characteristics of Josephson Junctions*, Appl. Phys. Lett. **12**, 277 (1968).
- [29] D.E. McCumber, *Effect of ac Impedance on dc Voltage-Current Characteristics of Superconductor Weak-Link Junctions*, J. Appl. Phys. **39**, 3113 (1968).
- [30] A.W. Kleinsasser, *Excess currents and voltages in superconducting junctions*, Appl. Phys. Lett. **62**, 193 (1993).
- [31] V. Foglietti, R.H. Koch, J.Z. Sun, R.B. Laibowitz, and W.J. Gallagher, *Characterizing, modelling, and optimizing high- $T_c$  superconducting quantum interference devices*, J. Appl. Phys. **77**, 378 (1995).
- [32] V. Polushkin, S. Uchaikin, S. Knappe, H. Koch, B. David, and D. Grundler, *Current phase relation of  $Y_1Ba_2Cu_3O_{7-\delta}$  step edge junction*, IEEE Trans. Appl. Supercond. **5**, 2790 (1995).
- [33] E. Il'ichev, V. Zakosarenko, V. Schultze, H.-G. Meyer, H.E. Hoenig, V.N. Glyantsev, and A. Golubov, *Temperature dependence of the current-phase relation for  $YBa_2Cu_3O_{7-x}$  step-edge Josephson junctions*, Appl. Phys. Lett. **72**, 731 (1998).
- [34] E. Il'ichev, V. Zakosarenko, R.P.J. IJsselsteijn, V. Schultze, H.-G. Meyer, H.E. Hoenig, and H. Töpfer, *The Current-Phase Relation in High- $T_c$  YBaCuO Josephson Junctions*, IEEE Trans. Appl. Supercond. **9**, 3994 (1999).
- [35] E. Il'ichev, V. Zakosarenko, R.P.J. IJsselsteijn, V. Schultze, H.-G. Meyer, H.E. Hoenig, H. Hilgenkamp, and J. Mannhart, *Nonsinusoidal Current-Phase Relationship of Grain Boundary Josephson Junctions in High- $T_c$  Superconductors*, Phys. Rev. Lett. **81**, 894 (1998).
- [36] J.W.M. Hilgenkamp, *High- $T_c$  dc SQUID magnetometers*, Ph.D. Thesis, University Twente Enschede (1995).
- [37] S. Goldman, *Frequency Analysis, Modulation and Noise*, MacGraw-Hill, New York, 1948.
- [38] V. Ambegaokar and B.I. Halparin, *Voltage due to thermal noise in the dc Josephson effect*, Phys. Rev. Lett. **22**, 1364 (1969).
- [39] C.M. Falco, W.H. Parker, S.E. Trullinger, and P.K. Hansma, *Effect of thermal noise on current-voltage characteristics of Josephson junctions*, Phys. Rev. B **10**, 1865 (1974).
- [40] R. Gross, P. Chaudhari, D. Dimos, A. Gupta, and G. Koren, *Thermally Activated Phase Slippage in High- $T_c$  Grain-Boundary Josephson Junctions*, Phys. Rev. Lett. **64**, 228 (1990).

- [41] J. Clarke, W.M. Goubau, and M.B. Ketchen, *Tunnel Junction dc SQUID: Fabrication, Operation, and Performance*, J. Low Temp. Phys. **25**, 99 (1976).
- [42] J. Clarke, *SQUIDS: Principles, Noise and Applications in Superconducting Devices*, S.T. Ruggiero and D.A. Rudman, Eds., Academic Press, Inc., San Diego (1990), p. 51.
- [43] K.K. Likharev and V.K. Semenov, *Fluctuation spectrum in superconducting point junctions*, JETP Lett. **15**, 442 (1972).
- [44] F. Ludwig, *Rauschmessungen an dc-SQUID Magnetometern aus  $YBa_2Cu_3O_7$* , Diploma Thesis, Universität Hamburg (1997).
- [45] A. Marx, U. Fath, W. Ludwig, R. Gross, and T. Amreim,  *$1/f$  noise in  $Bi_2Sr_2CaCu_2O_{8+x}$  bicrystal grain-boundary Josephson junctions*, Phys. Rev. B **51**, 6735 (1995).
- [46] A. Marx, U. Fath, L. Alff, and R. Gross, *Correlation of critical current and resistance fluctuations in bicrystal grain boundary Josephson junctions*, Appl. Phys. Lett. **67**, 1929 (1995).
- [47] C.T. Rogers and R.A. Buhrman, *Conductance fluctuations and low frequency noise in Josephson junctions*, IEEE Trans. Magn. **19**, 453 (1983).
- [48] R.H. Koch,  *$1/f$  noise in Josephson junctions—measurements and proposed model in Noise in physical systems*, M. Savelli, G. Lecoy, and J.-P. Nougier, Eds., Elsevier Science Publishers B. V., (1983), p. 377.
- [49] C.T. Rogers, R.A. Buhrman, W.J. Gallagher, S.I. Raider, A.W. Kleinsasser, and R.L. Sandstrom, *Electron trap states and low frequency noise in tunnel junctions*, IEEE Trans. Magn. **23**, 1658 (1987).
- [50] A. Marx and R. Gross, *Scaling behavior of  $1/f$  noise in high-temperature superconductor Josephson junctions*, Appl. Phys. Lett. **70**, 120 (1997).
- [51] D. Grundler, *Rauscharme dc SQUID Magnetometer basierend auf Stufenkontakten aus dem Hochtemperatursupraleiter  $YBa_2Cu_3O_7$* , Ph.D. Thesis, Universität Hamburg (1995).
- [52] A. Marx, U. Fath, L. Alff, R. Gross, T. Amreim, M.A.J. Verhoeven, G.J. Gerritsma, and H. Rogalla,  *$1/f$  Noise Measurements in Different Types of HTS Josephson Junctions*, in *2<sup>nd</sup> Workshop on HTS Applications and New Materials*, D.A.H. Blank, Ed. Twente, The Netherlands (1995).
- [53] L. Hao, J.C. Macfarlane, and C.M. Pegrum, *Comparative noise measurements in YBCO step-edge and bi-crystal grain boundary junctions*, Physica C **232**, 111 (1994).
- [54] L. Hao, J.C. Macfarlane, and C.M. Pegrum, *Excess noise in  $YBa_2Cu_3O_7$  thin film grain boundary Josephson junctions and devices*, Supercond. Sci. Technol. **9**, 678 (1996).

- 
- [55] C.P. Foley, S. Lam, G.J. Sloggett, N. Savvides, A. Katsaros, L. Hao, J.C. Macfarlane, C.M. Pegrum, and J. Kuznik, *Noise Properties of High-Quality Step-Edge YBCO Josephson Junctions*, in *Proceedings of the 5<sup>th</sup> International Superconductive Electronics Conference (ISEC '95)* Nagoya, Japan (1995).
  - [56] F. Ludwig, J. Beyer, D. Drung, S. Bechstein, and T.H. Schurig, *YBa<sub>2</sub>Cu<sub>3</sub>O<sub>7-x</sub> DC Squid Magnetometers with Bicrystal Junctions for Biomagnetic Multichannel Applications*, *Applied Superconductivity* **5**, 345 (1998).
  - [57] M. Vaupel, G. Ockenfuss, and R. Wördenweber, *Magnetic field behavior of small sputtered step-edge junctions*, *Appl. Phys. Lett.* **68**, 3623 (1996).
  - [58] O.M. Froehlich, P. Richter, A. Beck, R. Gross, and G. Koren, *Quasiparticle Tunneling in HTS Grain Boundary Josephson Junctions*, *J. Low Temp. Phys.* **106**, 243 (1997).
  - [59] O.M. Froehlich, P. Richter, A. Beck, D. Koelle, and R. Gross, *Barrier Properties of Grain Boundary Junctions in High-T<sub>c</sub> Superconductors*, *IEEE Trans. Appl. Supercond.* **7**, 3189 (1997).
  - [60] B.H. Moeckly, D.K. Lathrop, and R.A. Buhrman, *Electromigration study of oxygen disorder and grain-boundary in YBa<sub>2</sub>Cu<sub>3</sub>O<sub>7-δ</sub> thin films*, *Phys. Rev. B* **47**, 400 (1993).
  - [61] K.-O. Subke, *Multilayer technology for integrated YBa<sub>2</sub>Cu<sub>3</sub>O<sub>7</sub> magnetometers*, Ph.D. Thesis, Universität Hamburg (1999).
  - [62] C.L. Jia, B. Kabius, K. Urban, K. Herrmann, G.J. Cui, J. Schubert, W. Zander, A.I. Braginski, and C. Heiden, *Microstructures of epitaxial YBa<sub>2</sub>Cu<sub>3</sub>O<sub>7</sub> films on step-edge SrTiO<sub>3</sub> substrates*, *Physica C* **175**, 545 (1991).
  - [63] K. Herrmann, G. Kunkel, M. Siegel, J. Schubert, W. Zander, A.I. Braginski, C.L. Jia, B. Kabius, and K. Urban, *Correlation of YBa<sub>2</sub>Cu<sub>3</sub>O<sub>7</sub> step-edge junction characteristics with microstructure*, *J. Appl. Phys.* **78**, 1131 (1995).
  - [64] F. Lombardi, Z.G. Ivanov, G.M. Fischer, E. Olsson, and T. Claeson, *Transport and structural properties of the top and bottom grain boundaries in YBa<sub>2</sub>Cu<sub>3</sub>O<sub>7-δ</sub> step-edge Josephson junctions*, *Appl. Phys. Lett.* **72**, 249 (1998).
  - [65] R. Gerdemann, K.-D. Husemann, R. Gross, L. Alff, A. Beck, B. Elia, W. Reuter, and M. Siegel, *Spatially resolved analysis of high-T<sub>c</sub> grain boundary Josephson junctions and arrays*, *J. Appl. Phys.* **76**, 8005 (1994).
  - [66] C.P. Foley, S. Lam, B. Sankrithyan, Y. Wilson, J.C. Macfarlane, and L. Hao, *The Effects of Step Angle on Step Edge Josephson Junctions on MgO*, *IEEE Trans. Appl. Supercond.* **7**, 3185 (1997).
  - [67] D. Dimos, P. Chaudhari, J. Mannhart, and K.F. LeGoues, *Orientation dependence of grain-boundary critical currents in YBa<sub>2</sub>Cu<sub>3</sub>O<sub>7-x</sub> bicrystals*, *Phys. Rev. Lett.* **61**, 219 (1988).

- [68] Z.G. Ivanov, P.Å. Nilsson, D. Winkler, J.A. Alarco, T. Claeson, E.A. Stepanov, and A.Ya. Tzalenchuk, *Weak links and dc SQUIDS on artificial nonsymmetric grain boundaries in  $YBa_2Cu_3O_{7-\delta}$* , Appl. Phys. Lett. **23**, 3030 (1991).
- [69] T. Minotani, S. Kawakami, Y. Kuroki, and K. Enpuku, *Properties of Josephson Junction Fabricated on Bicrystal Substrate with Different Misorientation Angles*, Jpn. J. Appl. Phys. **37**, L 718 (1998).
- [70] H. Hilgenkamp, J. Mannhart, B. Mayer, Ch. Gerber, J.R. Kirtley, and K.A. Moler, *Influence of  $d_{x^2-y^2}$  Symmetry on Device Applications of High- $T_c$  Grain Boundary Junctions*, IEEE Trans. Appl. Supercond. **7**, 3670 (1997).
- [71] J. Mannhart and H. Hilgenkamp, *Wavefunction symmetry and its influence on superconducting devices*, Supercond. Sci. Technol. **10**, 880 (1997).
- [72] C.D. Tesche and J. Clarke, *dc SQUID: Noise and Optimization*, J. Low Temp. Phys. **29**, 301 (1977).
- [73] H. Koch, *SQUID Sensors in Sensors—A Comprehensive Survey*, W. Göpel, J. Hesse, and J.N. Zemel, Eds. vol. 5 Magnetic Sensors, R. Boll, K.J. Overshott, Ed., VCH, Weinheim (1989), p. 381.
- [74] J. Clarke, *Superconducting Quantum Interference Devices for Low Frequency Measurements* in *Superconductor Applications: SQUIDS and Machines*, B.B. Schwartz and S. Foner, Eds., Plenum, New York (1977), p. 67.
- [75] J. Knuutila, M. Kajola, H. Seppä, R. Mutikainen, and J. Salmi, *Design, Optimization, and Construction of a DC SQUID with Complete Flux Transformer Circuits*, J. Low Temp. Phys. **71** (5/6), 369 (1988).
- [76] D. Koelle, A.H. Miklich, F. Ludwig, E. Dantsker, D.T. Nemeth, and J. Clarke, *dc SQUID magnetometers from single layers of  $YBa_2Cu_3O_{7-x}$* , Appl. Phys. Lett. **63**, 2271 (1993).
- [77] K. Enpuku, G. Tokita, and T. Maruo, *Inductance dependence of noise properties of a high- $T_c$  dc superconducting quantum interference device*, J. Appl. Phys. **76**, 8180 (1994).
- [78] K. Enpuku, G. Tokita, T. Maruo, and T. Minotani, *Parameter dependencies of characteristics of a high- $T_c$  dc superconducting quantum interference device*, J. Appl. Phys. **78**, 3498 (1995).
- [79] K. Enpuku, Y. Shimomura, and T. Kisu, *Effect on thermal noise on the characteristics of a high  $T_c$  superconducting quantum interference device*, J. Appl. Phys. **73**, 7929 (1993).
- [80] D. Koelle, R. Kleiner, F. Ludwig, E. Dantsker, and J. Clarke, *High-transition-temperature superconducting quantum interference devices*, Rev. Mod. Phys. **71**, 631 (1999).

- 
- [81] D. Drung, F. Ludwig, W. Müller, U. Steinhoff, L. Trahms, H. Koch, Y.Q. Shen, M.B. Jensen, P. Vase, T. Holst, T. Freltoft, and G. Curio, *Integrated  $YBa_2Cu_3O_{7-x}$  magnetometer for biomagnetic measurements*, Appl. Phys. Lett. **68**, 1421 (1996).
  - [82] R.F. Voss, *Noise Characteristics of an Ideal Shunted Josephson Junction*, J. Low Temp. Phys. **42**, 151 (1981).
  - [83] B. Stasik, *DC-SQUIDS aus  $YBa_2Cu_3O_7$ —Modell und Experiment*, Diploma Thesis, Universität Hamburg (1995).
  - [84] G. Hildebrandt, *Modellierung, Optimierung und Parameterbestimmung von supraleitenden Quanteninterferometern unter Gesichtspunkten der Hochtemperatur-Supraleitung*, Ph.D. Thesis, Technische Universität Ilmenau (1997).
  - [85] M.J. Ferrari, M. Johnson, F.C. Wellstood, J.J. Kingston, T.J. Shaw, and J. Clarke, *Magnetic Flux Noise in Copper Oxide Superconductors*, J. Low Temp. Phys. **94**, 15 (1994).
  - [86] G. Jung and B. Savo, *Elementary and macroscopic two-level fluctuations in high- $T_c$  superconductors*, J. Appl. Phys. **80**, 2939 (1996).
  - [87] M.J. Ferrari, M. Johnson, F.C. Wellstood, J. Clarke, P.A. Rosenthal, R.H. Hammond, and M.R. Beasley, *Magnetic flux noise in thin-film rings of  $YBa_2Cu_3O_{7-\delta}$* , Appl. Phys. Lett. **53**, 695 (1988).
  - [88] F. Ludwig, D. Koelle, E. Dantsker, D.T. Nemeth, A.H. Miklich, J. Clarke, and R.E. Thomson, *Low noise  $YBa_2Cu_3O_{7-x}$ - $SrTiO_3$ - $YBa_2Cu_3O_{7-x}$  multilayers for improved superconducting magnetometers*, Appl. Phys. Lett. **66**, 373 (1995).
  - [89] R. Scharnweber, N. Dieckmann, and M. Schilling, *Noise properties and epitaxial quality in low-noise integrated  $YBa_2Cu_3O_7$  magnetometers*, Appl. Phys. Lett. **70**, 2189 (1997).
  - [90] R.H. Koch, J. Clarke, W.M. Goubau, J.M. Martinis, C.M. Pegrum, and D.J. Van Harlingen, *Flicker ( $1/f$ ) Noise in Tunnel Junction DC SQUIDS*, J. Low Temp. Phys. **51**, 207 (1983).
  - [91] V. Foglietti, W.J. Gallagher, M.B. Ketchen, A.W. Kleinsasser, R.H. Koch, S.I. Raider, and R.L. Sandstrom, *Low-frequency noise in low  $1/f$  noise dc SQUID's*, Appl. Phys. Lett. **49**, 1393 (1986).
  - [92] O. Dössel, B. David, M. Fuchs, W.H. Kullmann, and K.-M. Lüdecke, *A modular low noise 7-channel SQUID-magnetometer*, IEEE Trans. Magn. **27**, 2797 (1991).
  - [93] M. Matsuda, Y. Murayama, S. Kiryu, N. Kasai, S. Kashiwaya, M. Koyanagi, and T. Endo, *Directly-coupled dc SQUID magnetometers made of Bi-Sr-Ca-Cu oxide films*, IEEE Trans. Magn. **27**, 3043 (1991).
  - [94] M.B. Ketchen, *DC SQUIDS 1980: The State of the Art*, IEEE Trans. Magn. **17** (1), 387 (1981).

- [95] J.M. Jaycox and M.B. Ketchen, *Planar Coupling Scheme for Ultra Low Noise DC SQUIDS*, IEEE Trans. Magn. **17** (1), 400 (1981).
- [96] M.B. Ketchen, *Integrated Thin-Film dc SQUID Sensors*, IEEE Trans. Magn. **23**, 1650 (1987).
- [97] M.N. Keene, S.W. Goodyear, N.G. Chew, R.G. Humphreys, J.S. Satchell, J.A. Edwards, and K. Lander, *Low-noise  $YBa_2Cu_3O_{7-x}$ - $PrBa_2Cu_3O_7$  multiturn flux transformers*, Appl. Phys. Lett. **64**, 366 (1994).
- [98] E. Dantsker, F. Ludwig, R. Kleiner, J. Clarke, M. Teepe, L.P. Lee, N.McN. Alford, and T. Button, *Addendum: "Low noise  $YBa_2Cu_3O_{7-x}$ - $SrTiO_3$ - $YBa_2Cu_3O_{7-x}$  multilayers for improved superconducting magnetometers" [Appl. Phys. Lett. 66, 373 (1995)]*, Appl. Phys. Lett. **67**, 725 (1995).
- [99] J.E. Zimmerman, *Sensitivity Enhancement of Superconducting Quantum Interference Devices through the Use of Fractional-Turn Loops*, J. Appl. Phys. **42**, 4483 (1971).
- [100] D. Drung, R. Cantor, M. Peters, H.J. Scheer, and H. Koch, *Low-noise high-speed dc superconducting quantum interference device magnetometer with simplified feedback electronics*, Appl. Phys. Lett. **57**, 406 (1990).
- [101] D. Drung, S. Knappe, and H. Koch, *Theory for the multiloop dc SQUID magnetometer and experimental verification*, J. Appl. Phys. **77**, 4088 (1995).
- [102] P. Carelli and V. Foglietti, *Behavior of a multiloop dc superconducting quantum interference device*, J. Appl. Phys. **53**, 7592 (1982).
- [103] P. Carelli, V. Foglietti, R. Leoni, and M. Pullano, *Reliable Low Noise DC-SQUID*, IEEE Trans. Magn. **25**, 1026 (1989).
- [104] R. Scharnweber and M. Schilling, *Integrated  $YBa_2Cu_3O_7$  magnetometer with flux transformer and multiloop pick-up coil*, Appl. Phys. Lett. **69**, 1303 (1996).
- [105] R. Scharnweber and M. Schilling, *A new concept for integrated  $YBa_2Cu_3O_7$  magnetometers*, IEEE Trans. Appl. Supercond. **7**, 3485 (1997).
- [106] K.-O. Subke, C. Hinnrichs, H.-J. Barthelmess, M. Halverscheid, C. Pels, and M. Schilling, *Operation of a  $YBa_2Cu_3O_7$  dc SQUID magnetometer with integrated multiloop pick-up coil in unshielded environment and in static magnetic fields*, in *Proceedings of the 4<sup>th</sup> European Conference on Applied Superconductivity (EUCAS '99) Sitges* (1999).
- [107] K.C. Gupta, R. Garg, and I.J. Bahl, *Microstrip lines and slotlines*, Artech House Inc., Dedham, 1979.
- [108] B.A. Willemsen, T. Dahm, and D.J. Scalapino, *Microwave intermodulation in thin film high- $T_c$  superconducting microstrip hairpin resonators: Experiment and theory*, Appl. Phys. Lett. **71**, 3898 (1997).



- 
- [109] B.C. Wadell, *Transmission Line Design Handbook*, Artech House Inc., Boston, 1991.
- [110] R. Meservey and P.M. Tedrow, *Measurements of the Kinetic Inductance of Superconducting Linear Structures*, J. Appl. Phys. **40** (5), 2028 (1969).
- [111] T. Dahm, *private communication* (1999).
- [112] K. Yoshida, M.S. Hossain, T. Kisu, K. Enpuku, and K. Yamafuji, *Modeling of Kinetic-Inductance Coplanar Stripline with NbN Thin Films*, Jpn. J. Appl. Phys. **31** (12A), 3844 (1992).
- [113] M.B. Ketchen, W.J. Gallagher, A.W. Kleinsasser, S. Murphy, and J.R. Clem, *DC SQUID Flux Focuser in SQUID '85—Superconducting Quantum Interference Devices and their Applications*, H.D. Hahlbohm and H. Lübbig, Eds., Walter de Gruyter, Berlin (1985), p. 865.
- [114] C.D. Tesche, *Quantum Limit Constraints on DC SQUID Amplifiers in Noise in Physical Systems and  $1/f$  Noise*, M. Savalli, G. Lecoy, and J.-P. Nougier, Eds., Elsevier Science Publishers B.V., North Holland, Amsterdam (1983), p. 137.
- [115] R. Cantor, *DC SQUIDS: Design, Optimization and Practical Applications in SQUID Sensors: Fundamentals, Fabrication and Applications*, H. Weinstock, Ed., NATO ASI Series, Kluwer Academic Publishers, Dordrecht, The Netherlands (1996), p. 179.
- [116] W.H. Chang, *The inductance of a superconducting strip transmission line*, J. Appl. Phys. **50** (12), 8129 (1979).
- [117] S. Krey, *Integrierte dc SQUID Magnetometer aus  $YBa_2Cu_3O_7$  mit Stufenkontakten*, Diploma Thesis, Universität Hamburg (1995).
- [118] N. Matsuda, G. Uehara, K. Kazami, Y. Takada, and H. Kado, *Design and Fabrication of a Multi Loop Superconducting Quantum Interference Device, the Clover-Leaf Superconducting Quantum Interference Device*, Jpn. J. Appl. Phys. **34**, L 27 (1995).
- [119] F.C. Wellstood, J.J. Kingston, and J. Clarke, *Thin-film multilayer interconnect technology for  $YBa_2Cu_3O_{7-x}$* , J. Appl. Phys. **75**, 683 (1994).
- [120] B. David, D. Grundler, R. Eckart, K. Fanghänel, J.P. Krumme, V. Doormann, and O. Dössel, *A multi-layer process for the fabrication of HTSC flux transformers and SQUIDS*, Supercond. Sci. Technol. **7**, 287 (1994).
- [121] J.-K. Heinsohn, D. Reimer, A. Richter, K.-O. Subke, and M. Schilling, *Interaction of process parameters in the laser deposition of  $YBa_2Cu_3O_7$  films*, Physica C **299**, 99 (1998).
- [122] K.-O. Subke, S. Krey, H. Burkhardt, D. Reimer, and M. Schilling, *Process Optimization for High Yield of  $YBa_2Cu_3O_7$  Ramp-Edge Josephson Junctions with  $PrBa_2Cu_3O_7$  Barriers*, in *Proceedings of the 6<sup>th</sup> International Superconductive Electronics Conference (ISEC '97)* Berlin (1997).

- [123] K.-O. Subke, S. Krey, H. Burkhardt, A. Bartold, and M. Schilling, *Technology for  $YBa_2Cu_3O_7$  SNS- and SIS-Josephson Junctions*, IEEE Trans. Appl. Supercond. **9**, 3125 (1999).
- [124] D. Drung, *Improved dc SQUID read-out electronics with low  $1/f$  noise preamplifier*, Rev. Sci. Instrum. **68**, 4066 (1997).
- [125] D. Drung, H. Matz, and H. Koch, *A 5-MHz bandwidth SQUID magnetometer with additional positive feedback*, Rev. Sci. Instrum. **66**, 3008 (1995).
- [126] D. Drung, T. Radic, H. Matz, H. Koch, S. Knappe, S. Menkel, and H. Burkhardt, *A 2-Channel Wideband SQUID System for High-Frequency Geophysical Applications*, IEEE Trans. Appl. Supercond. **7**, 3283 (1997).
- [127] D. Drung, *Low-frequency noise in low- $T_c$  multiloop magnetometers with additional positive feedback*, Appl. Phys. Lett. **67**, 1474 (1995).
- [128] D. Drung, E. Dantsker, F. Ludwig, H. Koch, R. Kleiner, J. Clarke, S. Krey, D. Reimer, B. David, and O. Doessel, *Low noise  $YBa_2Cu_3O_{7-x}$  SQUID magnetometers operated with additional positive feedback*, Appl. Phys. Lett. **68**, 1856 (1996).
- [129] D. Drung, *Advanced SQUID Read-Out Electronics in SQUID Sensors: Fundamentals, Fabrication and Applications*, H. Weinstock, Ed., NATO ASI Series, Kluwer Academic Publishers, Dordrecht, The Netherlands (1996), p. 63.
- [130] J. Beyer, D. Drung, F. Ludwig, T. Minotani, and K. Enpuku, *Low-noise  $YBa_2Cu_3O_{7-x}$  single layer dc superconducting quantum interference device (SQUID) magnetometer based on bicrystal junctions with  $30^\circ$  misorientation angle*, Appl. Phys. Lett. **72** (2), 203 (1998).
- [131] K. Enpuku, T. Minotani, A. Kandori, F. Shiraishi, J. Beyer, D. Drung, and F. Ludwig, *Direct-Coupled High  $T_c$  DC Superconducting Quantum Interference Device Magnetometers on  $SrTiO_3$  Substrate: Theoretical Description and Comparison with Experiment*, Jpn. J. Appl. Phys. **37** (9A), 4769 (1998).
- [132] B. David, D. Grundler, S. Krey, V. Doormann, R. Eckart, J.P. Krumme, G. Rabe, and O. Doessel, *High- $T_c$  SQUID magnetometers for biomagnetic measurements*, Supercond. Sci. Technol. **9**, 96 (1996).
- [133] K. Enpuku, T. Maruo, and T. Minotani, *Resonant Characteristics of High  $T_c$  DC SQUID Caused by Large Dielectric Constant of  $SrTiO_3$* , IEEE Trans. Appl. Supercond. **7**, 3355 (1997).
- [134] K. Enpuku and T. Minotani, *Distortion of voltage vs flux relation of dc SQUID coupled to multiturn input coil due to input coil resonance combined with capacitive-feedback effect*, Applied Superconductivity **5**, 419 (1998).
- [135] D. Reimer, M. Schilling, S. Knappe, and D. Drung, *Integrated  $YBa_2Cu_3O_7$  multi-loop magnetometers at 77 K*, IEEE Trans. Appl. Supercond. **5**, 2342 (1995).

- 
- [136] D. Reimer, *Integrierte Mehrschleifen-Magnetometer aus  $YBa_2Cu_3O_7$* , Ph.D. Thesis, Universität Hamburg (1995).
- [137] F. Ludwig, E. Dantsker, R. Kleiner, D. Koelle, J. Clarke, D. Drung, S. Knappe, H. Koch, N. McN Alford, and T.W. Button, *Integrated high- $T_c$  multiloop magnetometer*, Appl. Phys. Lett. **66**, 1418 (1995).
- [138] J. Bock, S. Elschner, and P.F. Herrmann, *Melt Cast Processed (MCP)-BSCCO 2212 Tubes for Power Applications up to 10 kA*, in *Proceedings of the 1994 Applied Superconductivity Conference (ASC '94)* Boston (MA) (1994).
- [139] J.R. Clem, *Johnson Noise from Normal Metal Near a Superconducting SQUID Gradiometer Circuit*, IEEE Trans. Magn. **23**, 1093 (1987).
- [140] H.J.M. ter Brake, W.A.M. Aarnink, P.J. van den Bosch, J.W.M. Hilgenkamp, J. Flokstra, and H. Rogalla, *Temperature dependence of the effective sensing area of high- $T_c$  dc SQUIDs*, Supercond. Sci. Technol. **10**, 512 (1997).
- [141] R. Cantor, L.P. Lee, M. Teepe, V. Vinetskiy, and J. Longo, *Low-Noise, Single-Layer  $YBa_2Cu_3O_{7-x}$  DC SQUID Magnetometers at 77 K*, IEEE Trans. Appl. Supercond. **5**, 2927 (1995).
- [142] S. Krey, K.-O. Subke, D. Reimer, M. Schilling, R. Scharnweber, and B. David, *Integrated  $YBa_2Cu_3O_7$  Magnetometers for Biomagnetic Applications*, Applied Superconductivity **5**, 213 (1998).
- [143] S. Krey, B. David, R. Eckart, and O. Dössel, *Low noise operation of integrated  $YBa_2Cu_3O_7$  magnetometers in static magnetic fields*, Appl. Phys. Lett. **72**, 3205 (1998).
- [144] D. Cohen, E.A. Edelsack, and J.E. Zimmerman, *Magnetocardiograms Taken Inside a Shielded Room With a Superconducting Point-Contact Magnetometer*, Appl. Phys. Lett. **16**, 278 (1970).
- [145] J.P. Wikswo, *SQUID Magnetometers for Biomagnetism and Nondestructive Testing: Important Questions and Initial Answers*, IEEE Trans. Appl. Supercond. **5** (1995).
- [146] D.H. Brooks and R.S. MacLeod, *Electrical Imaging of the Heart*, IEEE Signal Processing Magazine **14**, 24 (1997).
- [147] J.C. Mosher, E.R. Flynn, A. Quinn, A. Weir, U. Shahani, R.J.P. Bain, P. Maas, and G.B. Donaldson, *Fetal magnetocardiography: Methods for rapid data reduction*, Rev. Sci. Instrum. **68**, 1587 (1997).
- [148] D.N. Paulson, R.L. Fagaly, R.M. Toussaint, and R. Fischer, *Biomagnetic Susceptometer with SQUID Instrumentation*, IEEE Trans. Magn. **27**, 3249 (1991).
- [149] T.S. Lee, Y.R. Chemla, E. Dantsker, and J. Clarke, *High- $T_c$  SQUID microscope for Room Temperature Samples*, IEEE Trans. Appl. Supercond. **7**, 3147 (1997).

- [150] W. Andrä and H. Nowak, *Magnetism in Medicine*, Wiley-VCH, Berlin, 1998.
- [151] W.A.M. Aarnink, P.J. an den Bosch, T.M. Roelofs, M. Verbiesen, H.J. Holland, H.J.M. ter Brake, and H. Rogalla, *Active noise compensation for multichannel magnetocardiography in an unshielded environment*, IEEE Trans. Appl. Supercond. **5**, 2470 (1995).
- [152] K. Matsumoto, Y. Yamagishi, A. Wakusawa, T. Noda, K. Fujioka, and Y. Kuraoka, *SQUID-based active shield for biomagnetic measurements in Biomagnetism: Clinical Aspects*, M. Hoke, S.N. Erne, Y.C. Okada, and G.L. Romani, Eds., Excerpta Medica, Amsterdam (1992), p. 857.
- [153] S. Knappe, D. Drung, T. Schurig, H. Koch, M. Klinger, and J. Hinken, *A planar YBaCuO gradiometer at 77 K*, Cryogenics **32**, 881 (1992).
- [154] R. Weidl, S. Brabetz, F. Schmidl, F. Klemm, S. Wunderlich, and P. Seidel, *Heart monitoring with high- $T_c$  d.c. SQUID gradiometers in an unshielded environment*, Supercond. Sci. Technol. **10**, 95 (1997).
- [155] S. Wunderlich, F. Schmidl, H. Specht, L. Dörrer, H. Schneidewind, U. Hübner, and P. Seidel, *Planar gradiometers with high- $T_c$  DC SQUIDs for non-destructive testing*, Supercond. Sci. Technol. **11**, 315 (1998).
- [156] M.A. Espy, R.H. Kraus Jr., and E.R. Flynn, *Two methods for a first order hardware gradiometer using two high temperature superconducting quantum interference devices*, Rev. Sci. Instrum. **69**, 123 (1998).
- [157] R.H. Koch, J.R. Rozen, J.Z. Sun, and W.J. Gallagher, *Three SQUID gradiometer*, Appl. Phys. Lett. **63**, 403 (1993).
- [158] R.H. Koch, G.A. Keefe, and G. Allan, *Room temperature three sensor magnetic field gradiometer*, Rev. Sci. Instrum. **67**, 230 (1996).
- [159] K. Yokosawa and S. Kuriki, *Design and fabrication of direct-feedback gradiometer: Axial gradiometer made of superconductive films and SQUIDs*, Rev. Sci. Instrum. **65**, 3814 (1994).
- [160] O. Dössel, B. David, R. Eckart, D. Grundler, and S. Krey, *High- $T_c$  SQUID Magnetometers for Magnetocardiography*, in *2<sup>nd</sup> Workshop on HTS Applications and New Materials*, D.A.H. Blank, Ed. Twente, The Netherlands (1995) p. 124.
- [161] B. David, O. Dössel, V. Doormann, R. Eckart, W. Hoppe, J. Krüger, H. Laudan, and G. Rabe, *The Development of a High- $T_c$  Magnetocardiography System for Unshielded Environment*, IEEE Trans. Appl. Supercond. **7**, 3267 (1997).
- [162] F. Ludwig, J. Beyer, D. Drung, S. Bechstein, and T. Schurig, *High-Performance High- $T_c$  SQUID Sensors for Multichannel Systems in Magnetically Disturbed Environment*, IEEE Trans. Appl. Supercond. **9**, 3793 (1999).

- 
- [163] J.Z. Sun, W.J. Gallagher, and R.H. Koch, *Initial-vortex-entry-related magnetic hysteresis in thin-film SQUID magnetometers*, Phys. Rev. B **50**, 13664 (1994).
- [164] R.H. Koch, J.Z. Sun, V. Foglietta, and W.J. Gallagher, *Flux dam, a method to reduce extra low frequency noise when a superconducting magnetometer is exposed to a magnetic field*, Appl. Phys. Lett. **67**, 709 (1995).
- [165] F.P. Milliken, S.L. Brown, and R.H. Koch, *Magnetic field-induced noise in directly coupled high  $T_c$  superconducting quantum interference device magnetometers*, Appl. Phys. Lett. **71**, 1857 (1997).
- [166] M.J. Ferrari, J.J. Kingston, F.C. Wellstood, and J. Clarke, *Flux noise from superconducting  $YBa_2Cu_3O_{7-x}$  flux transformers*, Appl. Phys. Lett. **58**, 1106 (1991).
- [167] A.H. Miklich, D. Koelle, T.J. Shaw, F. Ludwig, D.T. Nemeth, E. Dantsker, J. Clarke, N.McN. Alford, T.W. Button, and M.S. Colclough, *Low frequency excess noise in  $YBa_2Cu_3O_{7-x}$  dc superconducting quantum interference devices cooled in static magnetic fields*, Appl. Phys. Lett. **64**, 3494 (1994).
- [168] M.I. Faley, U. Poppe, K. Urban, H. Hilgenkamp, H. Hemmes, W. Aarnink, J. Flokstra, and H. Rogalla, *Noise properties of direct current SQUIDs with quasiplanar  $YBa_2Cu_3O_7$  Josephson junctions*, Appl. Phys. Lett. **67**, 2087 (1995).
- [169] J.M. Schmidt, L.P. Lee, A. Matlashov, M. Teepe, V. Vinetskiy, R. Cantor, and M.S. DiIorio, *Low-Noise Single Layer  $YBa_2Cu_3O_{7-\delta}$  DC SQUID Magnetometers for Shielded and Unshielded Operation*, in *Proceedings of Biomag 96* Santa Fe (1996).
- [170] H.-M. Cho, R. McDermott, B. Oh, K.A. Kouznetsov, A. Kittel, J.H. Miller Jr., and J. Clarke, *Low Frequency Noise in Field Cooled Directly Coupled Magnetometers*, IEEE Trans. Appl. Supercond. **9**, 3294 (1999).
- [171] C.P. Foley, S. Lam, K.E. Leslie, K.-H. Müller, R.A. Binks, L. Macks, and G.J. Sloggett, *Excess low-frequency noise in YBCO rf SQUIDs in weak magnetic fields*, in *Proceedings of the 6<sup>th</sup> International Superconductive Electronics Conference (ISEC '97)* Berlin (1997).
- [172] J. Borgmann, P. David, R. Otto, J. Schubert, and A.I. Braginski, *Characterization of the low-frequency noise in high-temperature radio frequency superconducting quantum interference devices cooled in static magnetic fields*, Appl. Phys. Lett. **74**, 1021 (1999).
- [173] E. Dantsker, S. Tanaka, P.-Å. Nilsson, R. Kleiner, and J. Clarke, *Reduction of  $1/f$  noise in high  $T_c$  dc superconducting quantum interference devices cooled in an ambient field*, Appl. Phys. Lett. **69**, 4099 (1996).
- [174] E. Dantsker, S. Tanaka, and J. Clarke, *High- $T_c$  super conducting quantum interference devices with slots or holes: Low  $1/f$  noise in ambient magnetic fields*, Appl. Phys. Lett. **70**, 2037 (1997).

- [175] H.-J. Barthelmeß, *Rauscheigenschaften direkt gekoppelter dc-SQUID Magnetometer aus  $YBa_2Cu_3O_7$  in statischen Magnetfeldern*, Diploma Thesis, Universität Hamburg (1999).
- [176] M.S. DiIorio, K.-Y. Yang, S. Yoshizumi, S.G. Haupt, D. Haran, R.H. Koch, F.P. Milliken, J.R. Rozen, D.K. Lathrop, S. Kumar, and H.S. Trammel III, *Sensitive High- $T_c$  SQUID Magnetometers for Unshielded Operation*, IEEE Trans. Appl. Supercond. **9**, 4428 (1999).
- [177] A.B.M. Jansman, M. Izquierdo, A. Eiguren, J. Flokstra, and H. Rogalla, *Effective area in slotted high  $T_c$  dc washer superconducting quantum interference devices*, Appl. Phys. Lett. **72**, 3515 (1998).
- [178] A.B.M. Jansman, *High- $T_c$  dc SQUIDs for use in a background field*, Ph.D. Thesis, University Twente, Enschede (1999).
- [179] R.H. Koch, M.B. Ketchen, W.J. Gallagher, R.L. Sandstrom, A.W. Kleinsasser, D.R. Gambrel, T.H. Field, and H. Matz, *Magnetic hysteresis in integrated low  $T_c$  SQUID gradiometers*, Appl. Phys. Lett. **58**, 1786 (1991).
- [180] R.G. Humphreys and J.A. Edwards,  *$YBa_2Cu_3O_7$  thin film grain boundary junctions in a perpendicular magnetic field*, Physica C **210**, 42 (1993).
- [181] O. Brüggmann, *Magnetometer aus Josephson-Kontakt-Serienarrays auf Einkristall-Substraten*, Diploma Thesis, Universität Hamburg (1998).
- [182] S. Krey, O. Brüggmann, H. Burkhardt, and M. Schilling, *Noise Properties of  $YBa_2Cu_3O_7$  Josephson Junction Array Magnetometers*, IEEE Trans. Appl. Supercond. **9**, 3401 (1999).

# Danksagung

Eine Arbeit wie die vorliegende kann nicht ohne die Mithilfe und Unterstützung anderer gelingen. An dieser Stelle möchte ich mich daher ganz herzlich bei all denen bedanken, die hierzu beigetragen haben. Mein besonderer Dank gilt

Prof. Dr. Ulrich Merkt, der mir diese Arbeit ermöglichte und mir immer viel Vertrauen entgegenbrachte,

Dr. habil. Meinhard Schilling für die freundschaftliche Zusammenarbeit. Sein unerschöpflicher Vorrat an Ideen, sein Enthusiasmus und seine Initiative haben maßgeblich zu dieser Arbeit beigetragen.

Ein Teil dieser Arbeit entstand in Zusammenarbeit mit der Abteilung Technische Systeme der Philips Forschungslaboratorien Hamburg. Hiermit möchte ich mich bei allen Philips Mitarbeitern für die nette Arbeitsatmosphäre und die Unterstützung bedanken. Insbesondere danke ich

Dr. Bernd David für die freundschaftliche Zusammenarbeit und seine Unterstützung auch noch nach Beendigung der SQUID-Aktivitäten bei Philips. Prof. Dr. Olaf Dössel für sein großes Interesse, das er meiner Arbeit entgegenbrachte. Sowie Rainer Eckart, Dr. Jens-Peter Krumme, Gerd Rabe und Volker Doormann.

Ein großer Dank geht auch an die Physikalisch Technische Bundesanstalt (PTB) Berlin. Ohne die Möglichkeit zur Nutzung der magnetischen Abschirmkammer und der PTB SQUID-Elektronik wären einige Ergebnisse dieser Arbeit nicht in der vorgestellten Form zustande gekommen. Insbesondere danke ich Dr. Dietmar Drung, Dr. Frank Ludwig und Jörn Beyer für die fruchtbare Zusammenarbeit bei meinen Aufenthalten in Berlin. Dr. Silvia Knappe danke ich für die Erstellung des Maskensatzes für die WH1 und WH2 Mehrschleifen-Magnetometer.

Dr. Dirk Grundler danke ich für die Unterstützung bei meinen ersten Gehversuchen auf dem Gebiet der SQUIDS und für so manchen guten Tip auch noch danach.

Dr. Dirk Reimer und Dr. Ralf Scharnweber danke ich für die freundliche Aufnahme bei meinem Wechsel von Philips in die Gruppe N und für die Einweisung in die ungewohnten Gerätschaften. Ralf war außerdem ein vorzüglicher Reiseleiter mit vielen Insiderkenntnissen auf unserer Tour rund um San Francisco im Sommer '99.

In gleicher Weise danke ich Kai-Olaf Subke. Die hohe Qualität der laserdeponierten Schichten ist zum großen Teil seinem unermüdlichen Einsatz zu verdanken. Außerdem denke ich gerne an unsere gemeinsame Reise durch den westlichen Teil der USA im Sommer '98 zurück. Auch der besonders intensive Eindruck unseres „Schnelldurchgangs“ durch den Grand Canyon wird mir in guter Erinnerung bleiben.

Holger Burkhardt danke ich für die Erstellung einiger Maskenlayouts und für die gute Schreibtischnachbarschaft.

Colmar Hinrichs danke ich für den unvergeßlichen Segeltörn auf der Ostsee im Sommer '97 und für die gute Freundschaft auch außerhalb des Instituts.

Frank Ludwig, mein langjähriger Begleiter durchs Studium, trug immer durch seinen ausgefallenen Humor zum lockeren Arbeitsklima bei.

Weiterhin danke ich den Diplomanden Oliver Brüggemann, Henry-Jobes Barthelmeß und Miriam Halverscheid, die durch ihre Diplomarbeiten wesentlich zu dieser Arbeit beigetragen haben. Ihr Engagement und ihr Sachverstand halfen dabei, so manches experimentelle Problem zu lösen, und ihre vielen kritischen Fragen gaben Anlaß zu wertvollen Diskussionen.

Ich möchte mich außerdem bei allen übrigen Mitarbeitern der Gruppe N für die unbeschreiblich nette Arbeitsatmosphäre bedanken. Gerne denke ich an die vielen gemeinsamen Kinobesuche, Parties, Ausflüge, Konzerte, Kuchenschlachten, usw. zurück.

Ein besonders herzlicher Dank geht an meine Eltern, die mich während meiner Ausbildung immer unterstützten und die mir dieses Studium ermöglicht haben.

Vielen Dank!